A Modeling Analysis Program for the JPL Table Mountain Io Sodium Cloud Data

William H. Smyth

Atmospheric and Environmental Research, Inc.
840 Memorial Drive
Cambridge, Massachusetts 02139

and

Bruce A. Goldberg

Jet Propulsion Laboratory
4800 Oak Grove Drive
Pasadena, California

March 1988

Final Report for Period
June 1, 1984 to November 30, 1987

Prepared for
NASA Headquarters
by AER

TABLE OF CONTENTS

LIST OF FIGURES

LIST OF TABLES

I. Introduction

The goals of this project have been to provide physical insight into the local structure of Io's atmosphere, the manner by which gases escape the gravitational well of the satellite and produce neutral clouds in the circumplanetary space, the nature of east-west and possibly magnetic longitude asymmetries in the plasma torus, and the stability or variability of both the neutral gas clouds and the plasma torus over a several year time period. These goals have been pursued with significant accomplishment achieved in this AER/JPL collaborative effort by studying and modeling the spatial morphology, intensity, and spacetime variability of the Io sodium cloud as preserved in the JPL Table Mountain Io sodium cloud data set, the most complete of the Io sodium cloud data sets currently available. This data set documents the 2-D spatial morphology of the D-line emission intensities of the cloud on the sky plane as a function of both Io geocentric phase angle and the magnetic longitude of Io in the System III coordinate frame over a time period from 1976 to 1981. Highly developed and unique models for the Io sodium cloud at AER have provided the key tool for extracting physical insights from this data set. This method of approach has been proven here and shows great promise for providing even more substantial advances in our understanding through continuing studies of this massive data set and other earlier but less-comprehensive data sets.

The complete JPL Io sodium cloud data set is composed of 1974-1979 spectral data, 1981 spectral data, 1976-1979 Region B/C image data, 1981 Region B/C image data, and 1981 Region A image data. The complete data set was reviewed and assessed in the first project year (see the 1985 Annual Report). From this review, both the quality and quantity of data acquired in 1981 were in general much superior to the earlier observations. Because of this fact, the primary emphasis in the second year (see the 1986 Annual Report) was directed toward the 1981 data set and, in particular, to the 1981 Region B/C images. Second year efforts included three main areas: (1) data quality review for the 1981 Region B/C images, (2) selection and data processing of a subset of 1981 Region B/C images, and (3) physical enhancement of the Io sodium cloud model in preparation for third-year analysis of the data. A major and time-consuming step in the second area was the successful development and

application of software at the Multimission Image Processing Laboratory (MIPL) of JPL to remove distortions present in the brightness distribution of the Region B/C images.

Research efforts in the past project year are divided into three main areas: (1) completion of data processing and calibration for a subset of 34 representative images of the 1981 Region B/C cloud, (2) identification and examination of the basic features and observed changes in the morphological characteristics of the sodium cloud, and (3) physical interpretation of some of these observed characteristics using the highly-developed sodium cloud model. The modeling analysis has led to definite conclusions regarding the flux distribution and density profile of sodium in the exosphere of Io, the level of the collisional exobase in the atmosphere, the nature of the interaction of the corotating plasma torus and the satellite atmosphere/corona, and the presence of both an east-west electric field and an inherent System III longitudinal asymmetry in the planetary magnetosphere. This report, which is organized into the three main areas noted above, summarizes only these third-year accomplishments.

II. Data Processing and Calibration of 1981 Region B/C Images

Observational parameters for the 263 Region B/C images of the 1981 JPL data set acquired in both the D_2 and D_1 emission lines over 14 nights between March 25 and June 14 are summarized in numerical form in Table 1 and in graphical form in Figure 1. Images each night were recorded with an integration time of approximately 10 minutes. Three consecutive images were usually added to improve signal to noise. These added images provide a time-averaged picture of the sodium cloud over an Io phase angle interval of about 4° and an Io System III magnetic longitudinal interval of about 14° and, therefore, reasonably well approximating instantaneous snapshots of the Io sodium cloud. Prior to this project most of these images had been processed only preliminary to remove background signals (see 1985 and 1986 Annual reports for further discussion).

Figure 1 also shows by dots the mid-point locations for 34 representative images which have undergone complete data processing and calibration procedures as part of this project at the Multi-mission Image Processing Laboratory (MIPL) of JPL. The software development and application of these procedures has required a large amount of time and project resources as discussed in the 1986 Annual Report. The observational start, end, and mid-point conditions as well as the Image ID Number for these thirty-four representative images are given in Table 2. Additional information for Io's location in the D_2 image, the spatial scale of the image, and the relative intensity normalization factor for each of these images is given in Table 3. Each of these images is a combination of three (occasionally only two) of the measured ~10 minute images as is reflected in the start and end times and in the number of frames listed in the Image ID Number of Table 2 and Table 3. The final absolutely-calibrated thirty-four images in both the D_2 and D_1 sodium emission lines are ordered by their UT observation date and presented graphically in Appendix I.

Data processing procedures applied to these thirty-four images were discussed in the 1986 Annual Report and have been optimized for the brighter D_2 images. Absolute calibration is achieved by multiplying each processed image array by the relative intensity normalization factor of Table 3 and applying the common conversion factor of 13 DN/kR. The absolute conversion factor is

Table 1

1981 Region B/C Images: Observing Chronology

Date of Observations	Start Conditions			End Conditions		
	Time (UT)	Io Phase Angle (deg)	Magnetic Longitude of Io† (deg)	Time (UT)	Io Phase Angle (deg)	Magnetic Longitude of Io† (deg)
25 March	7:03	25.2	275.3	8:23	36.5	312.7
5 April	5:18	89.6	365.0	7:40	109.5	70.9
6 April	4:33	287.3	290.7	5:52	298.5	327.3
6 April	6:38	305.1	348.5	7:44	314.4	19.1
28 April	4:21	84.0	200.2	8:50	121.9	324.9
29 April	3:18	279.2	117.5	7:15	312.9	227.1
4 May	3:10	215.4	209.2	9:43	271.4	30.8
5 May	3:17	60.0	159.4	9:25	111.7	330.2
6 May	3:07	262.5	101.4	8:27	307.9	249.5
12 May	3:15	44.5	147.5	8:56	92.4	305.7
13 May	3:20	248.9	96.6	8:51	296.0	249.6
4 June	3:34	47.2	377.3	5:48	66.0	79.5
5 June	3:38	251.7	325.6	4:07	255.8	339.1
5 June	5:27	267.2	16.0	5:55	271.1	29.0
6 June	3:48	95.8	278.0	5:56	113.9	337.3
14 June	3:38	282.7	208.4	5:20	297.1	255.7

†System III (1965)

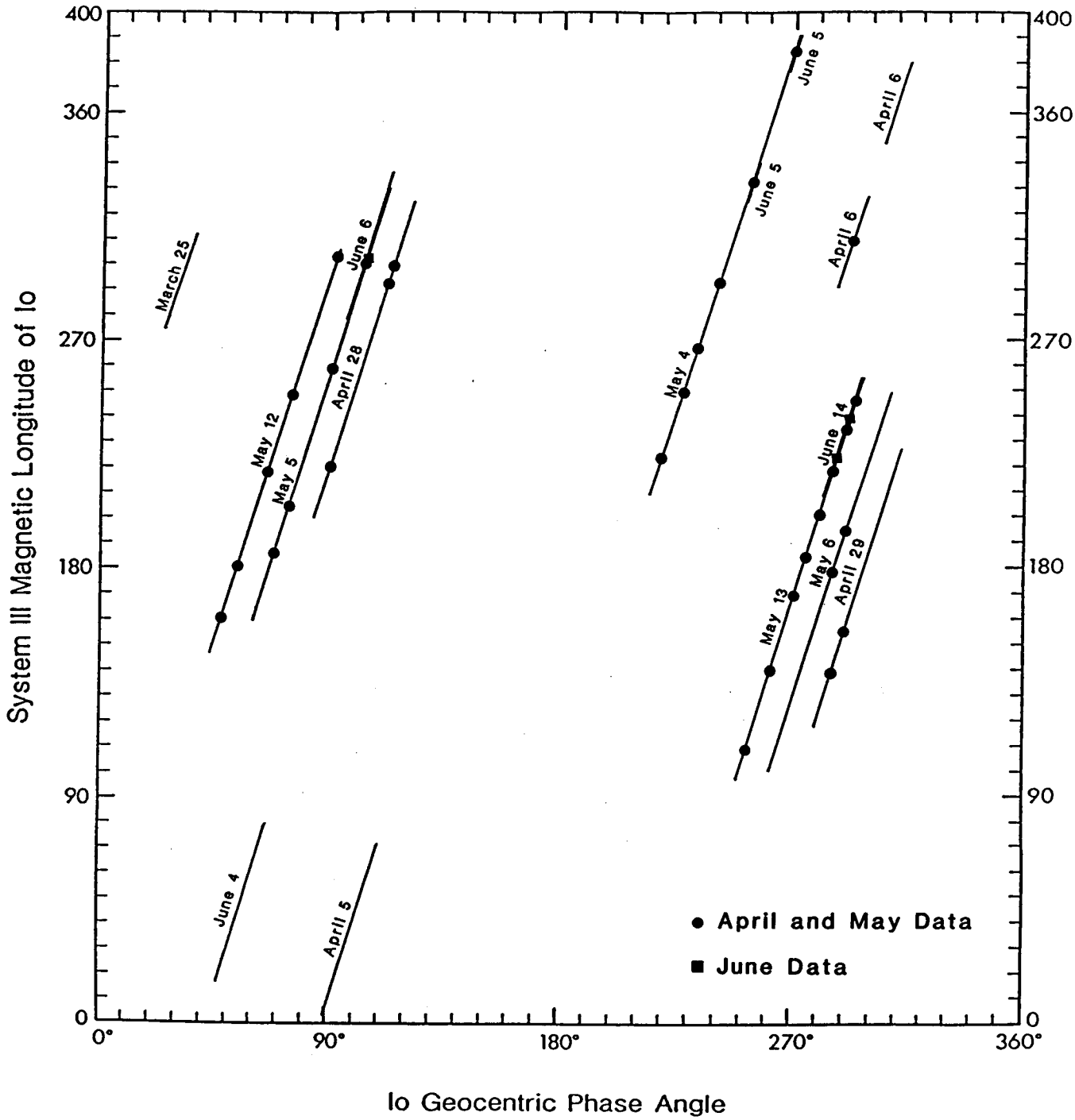

Figure 1. Observing Parameters for the 1981 Io Sodium Cloud Image Data for Table Mountain Observatory. The solid lines show the complete angular coverage for the data as listed in Table 1. The dots and squares show the mid-point conditions for the 34 completely reduced images listed in Table 2.

Table 2

1981 Region B/C Images: Processed by MIPL

Date of Observations	Start Conditions			End Conditions			Mid-Point Conditions		Image ID Number (Tape/frames)
	Time (UT)	Io Phase Angle (deg)	Magnetic Longitude of Io† (deg)	Time (UT)	Io Phase Angle (deg)	Magnetic Longitude of Io† (deg)	Io Phase Angle (deg)	Magnetic Longitude of Io† (deg)	
6 April	5:00	291.1	303.2	5:36	296.3	319.8	293.7	311.5	SIP 410/13-15
28 April	4:49	88.0	213.1	5:24	92.9	229.4	90.5	221.3	SIP 415/27-29
	7:28	110.3	286.9	7:58	114.5	300.8	112.4	293.9	*SIP 415/43-45
	7:39	111.9	292.0	8:07	115.8	305.0	113.9	298.5	*SIP 415/44-46
29 April	3:48	283.5	131.3	4:19	287.9	145.6	285.7	138.5	SIP 416/4-6
	4:22	288.3	147.0	4:53	292.7	161.4	290.5	154.2	SIP 416/7-9
4 May	3:25	217.6	216.2	3:55	221.8	230.0	219.7	223.1	SIP 417/8-10
	4:20	225.4	241.6	4:53	230.1	256.8	227.8	249.2	SIP 417/13-15
	4:56	230.5	258.2	5:33	235.8	275.3	233.2	266.8	SIP 417/16-18
	5:49	238.1	282.7	6:28	243.6	300.7	240.9	291.7	SIP 417/20-22
	7:19	250.9	324.3	7:52	255.6	339.5	253.3	331.9	SIP 417/27-29
	9:06	266.1	13.7	9:50	272.4	34.1	269.3	23.9	SIP 417/36-39
5 May	3:59	65.9	178.9	4:30	70.3	193.3	68.1	186.1	SIP 418/10-12
	4:32	70.5	194.2	5:15	76.6	214.2	73.6	204.2	SIP 418/13-16
	6:34	87.7	250.9	7:10	92.7	267.6	90.2	259.3	SIP 418/24-26
	8:03	100.2	292.2	8:35	104.7	307.0	102.5	299.6	SIP 418/31-33
6 May	5:36	283.6	170.4	6:10	288.5	186.1	286.1	178.3	SIP 419/19-21
	6:11	288.6	186.6	6:43	293.2	201.4	290.9	194.0	SIP 419/22-24
12 May	3:28	46.4	153.5	3:55	50.2	166.0	48.3	159.8	SIP 420/6-8
	4:10	52.3	173.0	4:40	56.5	186.9	54.4	180.0	SIP 420/10-12
	5:05	60.0	198.5	6:28	71.6	237.0	65.8	217.8	SIP 420/15-20
	6:30	71.9	238.0	7:09	77.4	256.1	74.7	247.1	SIP 420/21-23
	8:28	88.5	292.7	9:07	93.9	310.8	91.2	301.8	SIP 420/30-32
13 May	3:28	250.1	100.3	4:03	255.1	116.4	252.6	108.4	SIP 421/21-23
	4:43	260.8	134.9	5:04	263.7	144.6	262.3	139.8	SIP 421/27-28
	5:42	269.1	162.2	6:07	272.7	173.8	270.9	168.0	SIP 421/32-33
	6:09	273.0	174.7	6:47	278.4	192.3	275.7	183.5	SIP 421/34-36
	6:49	278.7	193.2	7:23	283.5	208.9	281.1	201.1	SIP 421/37-39
	7:25	283.8	209.8	7:58	288.5	225.1	286.2	217.5	SIP 421/40-42
	8:00	288.7	226.0	8:35	293.7	242.2	291.2	234.1	SIP 421/43-45
	8:25	292.3	237.6	9:00	297.2	253.8	294.8	245.7	SIP 421/45-47
6 June	4:19	100.2	292.4	4:53	105.0	308.1	102.6	300.3	SIP 424/10-12
14 June	3:47	284.0	212.6	4:28	289.8	231.5	286.9	222.1	SIP 425/6-9
	4:17	288.2	226.5	5:05	295.0	248.7	291.6	237.6	SIP 425/9-12

† System III (1965)
* images processed are redundant

Table 3

1981 Region B/C Images: Pixel and Calibration Information

Date of Observation	Start Time (UT)	End Time (UT)	Image Number Tape/frames	Io's Location in the D_2 Image (Line)	(Sample)	Spatial Scale (km/pixel)	Intensity Normalization Factor
6 April	5:00	5:36	SIP 410/13-15	113	150	2572	0.48†
28 April	4:49	5:24	SIP 415/27-29	128	155	2680	0.80
	7:28	7:58	*SIP 415/43-45	130	154	2680	0.98
	7:39	8:07	*SIP 415/44-46	131	154	2680	1.59†
29 April	3:48	4:19	SIP 416/4-6	128	146	2680	0.93
	4:22	4:53	SIP 416/7-9	128	145	2680	0.87
4 May	3:25	3:55	SIP 417/8-10	140	145	2707	1.04
	4:20	4:53	SIP 417/13-15	141	145	2707	0.85
	4:56	5:33	SIP 417/16-18	141	145	2707	0.78
	5:49	6:28	SIP 417/20-22	142	144	2707	0.86
	7:19	7:52	SIP 417/27-29	144	143	2707	0.92
	9:06	9:50	SIP 417/36-39	145	143	2707	1.04
5 May	3:59	4:30	SIP 418/10-12	143	152	2707	0.97
	4:32	5:15	SIP 418/13-16	143	152	2707	0.94
	6:34	7:10	SIP 418/24-26	145	152	2707	0.80
	8:03	8:35	SIP 418/31-33	146	152	2707	1.00
6 May	5:36	6:10	SIP 419/19-21	143	143	2734	1.24†
	6:11	6:43	SIP 419/22-24	143	143	2734	0.93
12 May	3:28	3:55	SIP 420/6-8	144	152	2761	1.21
	4:10	4:40	SIP 420/10-12	146	153	2761	0.99
	5:05	6:28	SIP 420/15-20	147	153	2761	0.87
	6:30	7:09	SIP 420/21-23	149	153	2761	0.78
	8:28	9:07	SIP 420/30-32	150	153	2761	0.87
13 May	3:28	4:03	SIP 421/21-23	149	145	2761	0.86
	4:43	5:04	SIP 421/27-28	150	144	2761	0.89
	5:42	6:07	SIP 421/32-33	151	144	2761	0.81
	6:09	6:47	SIP 421/34-36	151	143	2761	0.80
	6:49	7:23	SIP 421/37-39	151	143	2761	0.89
	7:25	7:58	SIP 421/40-42	151	143	2761	0.91
	8:00	8:35	SIP 421/43-45	152	144	2761	0.92
	8:25	9:00	SIP 421/45-47	152	144	2761	1.00
6 June	4:19	4:53	SIP 424/10-12	165	159	2951	0.97
14 June	3:47	4:28	SIP 425/6-9	159	149	3032	1.18
	4:17	5:05	SIP 425/9-12	159	149	3032	0.98

*images processed are redundant
†value in error; new value not available at this time

estimated to be accurate to within ~±10%. The image number SIP 418/31-33 was chosen as the standard upon which the absolute conversion factor was established as indicated in Table 3 by the intensity normalization factor of 1.00. The intensity normalization factor contains information to properly correct each image to the standard image for different exposure times, different air masses, different earth-Jupiter distances, and differences in the response of the instrument over the observational period.

In addition to these representative images, these are a large number of partially processed images as noted above that can be used to qualitatively verify and extend the characteristics of the cloud over a larger range of observational parameter space. The representative images, however, provide the best images for quantitative modeling analysis purposes, for comparing images acquired with similar observational parameters but at different times, and for studying the character of the cloud with a minimum amount of instrumental and background distortions.

III. Examination of the Observational Data

3.1 Correlation Studies

In the 1986 Annual Report, five correlation studies for the 1981 Region B/C image data were defined and their potential value evaluated. These five correlation studies are defined in Table 4 and provide a grouping of these images based upon different classifications of their Io geocentric phase angle, ϕ, and their Io System III magnetic longitude angle Ψ. The five studies are important (1) in assessing the stability of the sodium cloud over the two and one-half month observational time interval, and (2) in identifying and studying the effects of solar radiation pressure, the atom source characteristics, and the plasma torus sink characteristics on the morphology of the sodium cloud. These studies together with the data quality reviews undertaken in the first and second project years were used in selecting the thirty-four representative images that were processed and calibrated by MIPL.

The five correlation studies of Table 4 have been applied in the third project year to these 34 fully-reduced and representative 1981 Region B/C images. The representative images, property ordered and compared for each of the five studies, are presented, respectively, in the five appendices I, II, III, IV, and V. The results of these studies are discussed below and form the basis for a number of modeling studies, some of which have been undertaken in this project and are discussed in section IV.

3.2 Stability of the Sodium Cloud

It is important in examining and comparing the 1981 Region B/C images to determine first if the sodium cloud was relatively stable over the ~12 week observing window for observations summarized in Table 1 or more importantly over the ~10 week interval for the selected observations in Appendix I. Since the cloud morphology is time variable and depends upon both the Io geocentric phase angle (~42.5 hour period) and the Io System III longitude angle (~13 hour period), the most appropriate comparison is for images that have a recurrence of these two angle pairs (~32 day period). Fortunately, there are three such occurences in the 1981 Region B/C data set (see Figure 1). Image pairs from two of these occurrences (one east and two west of Jupiter) are compared (study 2 of Table 4) in Appendix II. Comparisons made from the east image

Table 4

1981 Region B/C Images: Five Correlation Studies†

I. Consecutive Image Study: $\phi(t)$, $\Psi(t)$

II. Cloud Stability Study: $(\phi_1, \Psi_1) \approx (\phi_2, \Psi_2)$
image sequences separated by 32 days

III. East/West Image Study: $\phi_W = \phi_E + 180°$

$\Psi_E \approx \Psi_W$	only one image-sequence pair
$\Psi_W \approx \Psi_E + 180°$	no image pairs
$\Psi_E \neq \Psi_W$	many comparison images

IV. System III Variability Study: $\phi_1 = \phi_2$, $\Psi_1 \neq \Psi_2$

V. Io Phase Angle Variability Study: $\phi_1 \neq \phi_2$, $\Psi_1 = \Psi_2$

---

†ϕ = Io Geocentric Phase Angle

Ψ = Io System III Magnetic Longitude Angle

pair (image set 2.A of Appendix II) show that the sodium cloud (apart from some recognized scatter in the data because of signal to noise effects) on May 5 and June 6 are very similar both in absolute intensity and in morphological structure. The same is also true for the two west image pairs (image sets 2.B and 2.C of Appendix II) of May 13 and June 14 for which a System III dependent "bite-out" of the cloud south of Io (to be discussed later) is reproduced in all images.

In order to test more extensively the stability of the sodium cloud for data in Appendix I, the next best comparison of images beyond the one discussed above is that for similar Io geocentric phase angles but different Io System III longitude angles (study 4 of Table 4). This comparison is presented in Appendix IV. To address the question of stability in these images, it is necessary to compare as many images as possbile for different observing dates in order to identify and eliminate System III changes from consideration. Comparison of three image pairs (image sets 4.A, 4.B and 4.C) on March 5 and March 12 all show similar structure, spatial extent and brightness, although a System III correlated asymmetry in the sodium distribution north and south of Io is suggested. This will be discussed further in Section 3.3. An east image (image set 4.C) acquired on April 28 has a similar spatial structure and brightness, but the spatial extent of the forward cloud and the trailing north directional feature are not as pronounced. This does not seem to be due to any observing/reduction problem since it is also presented in other April 28 images (SIP 415/43-45, SIP 415/44-46) at larger east phase angles.

For the sodium cloud west of Jupiter, more extensive image comparisons for similar Io phase angles are possible and are presented in Appendix IV. Inspection of image sets 4.E and 4.F shows similar structure, extent, and brightness of the forward cloud when the expected changing nature of the directional feature in the trailing cloud is considered. The image set 4.G extends the earlier discussed image pair 2.B (May 13, June 14) by adding April 29 and May 6 images. Similarly, image set 4.H extends the earlier discussed image pair 2.C (May 13, June 14) by adding April 29, May 6, another May 13, and April 6 images. In addition to a clearly delineated System III correlated south "bite-out", the images compare very well in both image sets. For image set 4.G, the forward cloud of the April 29 image is not as

extended and the sodium not as bright nearer Io. For image set 4.H, the forward cloud of the April 29 image is of normal length but the cloud is still not as bright near Io, while the April 6 image is generally weaker and may be attributed to data of lesser quality.

In summary, the spatial structure of the sodium cloud appears quite stable over the ~10 week period of data in Appendix I. There is only a hint of weaker sodium brightness in the cloud in April images. The basic structure of the cloud remains the same with the identification of stable features and several time-dependent periodic signatures readily apparent. These features and time-dependent signatures may therefore be safely classified and further studied by additional comparisons of images in Appendix I. The main features and time-dependent signatures of the sodium cloud are discussed below.

3.3 Features and Periodic Signatures of the Sodium Cloud

The main features and periodic signatures of the sodium cloud are listed in Table 5. All of these features and signatures have been either discovered or confirmed in the JPL Table Mountain Io sodium cloud data set. The features and signatures of Table 5 as well as some less stable signatures are discussed separately below.

East-West Intensity Asymmetry

The east-west intensity asymmetry near Io was discovered by Bergstralh et al. (1975, 1977) from the earliest single slit spectrographic observations acquired for the JPL Table Mountain Io sodium cloud data set in 1974 and 1975. These observations showed that the sodium cloud in a 3 x 8 arcsecond slit centered on Io was (on the average) brighter by about 25% when the satellite was east of Jupiter than when it was west of Jupiter. Similar slit spectrographic observations were acquired for the JPL data set in 1976-1981 and were reviewed in the 1985 Annual Report. These observations in addition to 1981 Region A image data are most valuable in extending the results of Bergstralh et al. The spectra and image data have, however, not yet been properly reduced for this purpose.

The spatial region near Io observed by Bergstralh et al. is essentially confined to sodium in the Lagrange sphere (~ 10^4 km in radius) of the satellite. This region is not observed in the 1981 Region B/C images of Appendix I

Table 5

Features and Time-Varying Periodic Signatures of the Sodium Cloud

1. East-West Intenstity Asymmetry near Io
2. Predominance of a Bright Forward Cloud
3. East-West Orbital Asymmetry of the Forward Cloud
4. South Bite-Out in the West Cloud
5. Directional Feature (Trailing Cloud)

because of the larger circular occulting mask (4.5 arcsec in radius and corresponding to a distance varying between 1.46 x 10^4 and 1.71 x 10^4 km) centered on Io. A small increase of order 25% in the cloud brightness east of Jupiter is, however, not readily distinguishable in the 1981 Region B/C cloud at distances from Io of the 1 to 2 kR contour levels when visual comparisons are made between the east-west image sets in Appendix III and when proper account is taken for different Io phase angle and Io System III longitude effects.

To test more quantitatively for a brightness enhancement at distances from Io larger than the occulting mask (i.e. >17,1000 km radius) but smaller than the 1 to 2 kR contour levels, the average D_2 brightness of the cloud in an annulus between 19,000 km and 21,000 km was computed for 31 of the 34 images in Appendix I for which the intensity calibration is established (see Table 3). The results are shown in Figure 2 as a function of the Io geocentric phase angle. From Figure 2, it is immediately apparent that the east cloud is generally brighter just beyond the occulting mask, although there is scatter in the data. For the 12 east images in Figure 2, the average annulus brightness is 3.15 kR while for the 19 west images, the annulus brightness is 2.24. The east cloud annulus is therefore, on average, ~40% brighter than the west cloud annulus. This confirms the east-west asymmetry discovered by Bergstralh et al. (1975, 1977). It also indicates that the east-west brightness ratio at a distance from Io greater than that sampled by Bergstralh et al. is larger than their average 1.25 value and argues that the intensity asymmetric mechanism is primarily sink related in contrast to source related.

Predominant Bright Forward Cloud

The existence of a brighter sodium cloud inside of Io's orbit and ahead of the satellite's location can be traced back to some of the earliest slit observations of the D-line emissions acquired in 1973 and 1974 (i.e. pre- and post-Pioneer 10) by Macy and Trafton (1975a,b) and Münch and Bergstralh (1977). Later two-dimensional image data acquired for the sodium cloud in 1976 and 1977 (Murcray 1978; Matson et al. 1978; Murcray and Goody 1978) first revealed the presence of a bright and predominantly forward sodium cloud. The large number of images in the 1981 portion of the JPL Table Mountain data set provide the first opportunity to refine and examine the spatial character of the forward cloud more quantitatively as discussed in the next subsection.

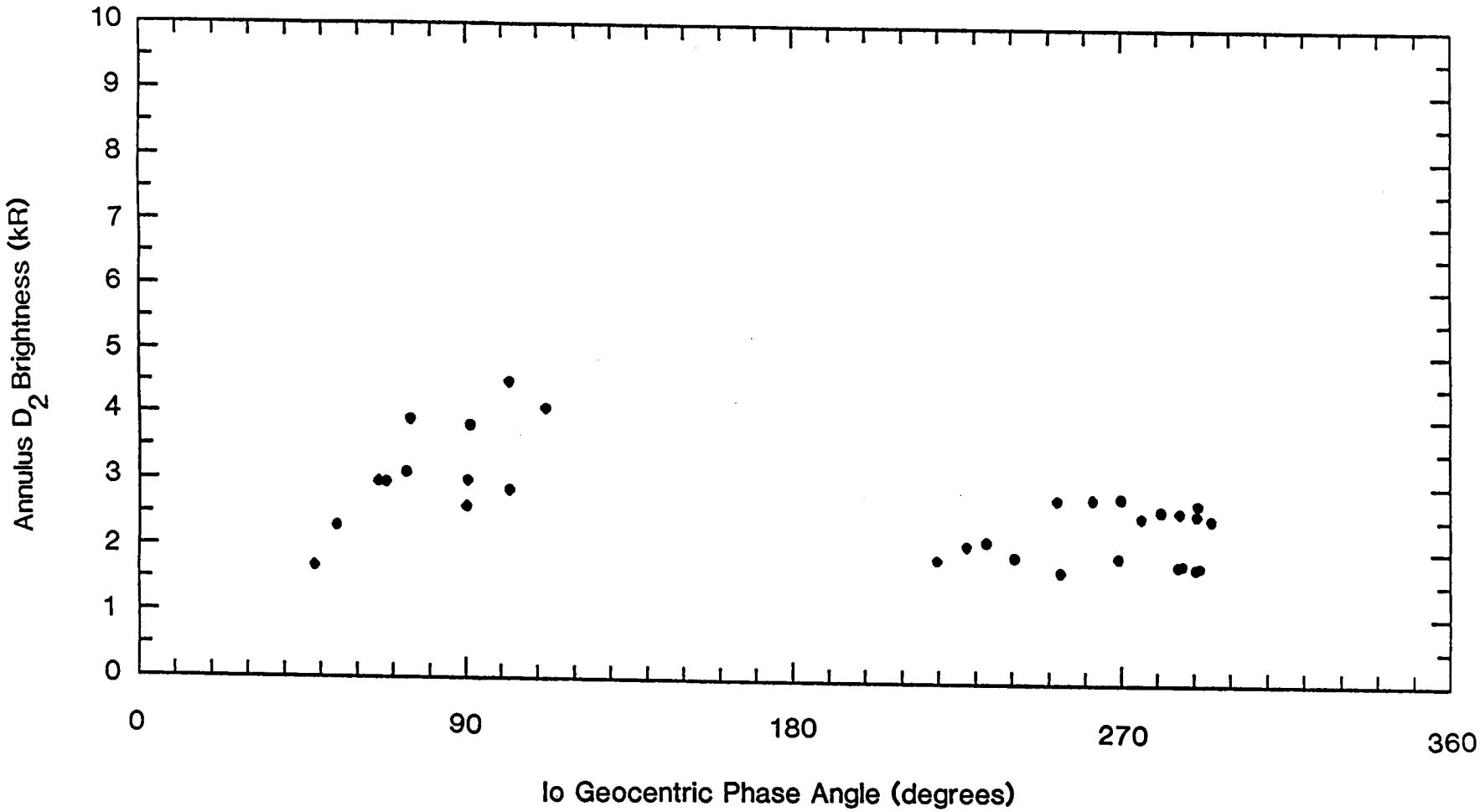

Figure 2. Sodium Cloud D_2 Brightness in an Annulus about Io. The average brightness in an annulus centered on Io with inner radius of 19,000 km and outer radius of 21,000 km is shown for thirty-one of the fully-reduced 1981 Region B/C images in Appendix I.

East-West Orbital Asymmetry of the Forward Cloud

Examination of the fully-reduced 1981 images in Appendix I shows that the forward cloud is always present. The appearance of the forward cloud on the sky plane, however, changes as Io moves about Jupiter. These changes are consistent with changes recognized earlier (Smyth and McElroy 1978; Matson et al. 1978) in 1976 and 1977 images acquired for the JPL data set (Matson et al. 1978) and acquired independently at Harvard University (Murcray 1978; Murcray and Goody 1978). The much larger number of 1981 images in the JPL data set, however, allow one to track these changes in more detail as a function of the satellite phase angle. In particular, the forward cloud on the sky plane can be seen to be approximately parallel to the line of sight at a critical east phase angle of ~65-70° and a critical west phase angle of ~235° from the images of Appendix I. This was first discovered by Goldberg et al. (1978) and later quantified for the 1981 JPL image data by Goldberg, Garneau, and LaVoie (1984). The fact that the east and west critical phase angles do not differ by 180° and furthermore that the forward cloud west of Jupiter is generally significantly longer than the forward cloud east of Jupiter (see images in Appendices I, III and IV) directly indicate an east-west orbital asymmetry in the cloud.

South Bite-Out in the West Cloud

A zone of deficient sodium southwest of Io was noted in the 13 May 1981 Region B/C images in the brief review of the JPL Table Mountain data set conducted by Goldberg, Garneau, and LaVoie (1984). This "bite-out" of a south portion of the west cloud can be seen to develop in time (see images in Appendix I) as a function of the Io System III longitude angle. The "bite-out" is absent for an Io System III longitude angle of 168° (image SIP 421/32-33), is noticeable at an angle of 183.5° (image SIP 421/34-36), is increasing as the angle increases beyond 200°, and is still present near the end of the observational sequence where the angle is 245.7° (image SIP 421/45-47).

Examination of additional images in the 1981 Region B/C data set shows that this south "bite-out" of the west cloud is a normal and periodic feature of the Io sodium cloud for at least a seven week interval. From Figure 1, it

is immediately evident that images on April 29, May 6, and June 14 have similar values for their Io System III longitude and Io geocentric phase angle-pairs. Comparisons of the fully-reduced images on these dates in Appendix I confirm this behavior. Examination of raw data for images on April 29 with Io System III longitude angles larger than 154.2° (image SIP 416/7-9 in Appendix I) also reveals the same behavior.

The south "bite-out" of the west cloud is also a relatively stable feature of the sodium cloud over a several year time frame. The south "bite-out" is consistent with two 1977 images, and one 1979 (Voyager 1 encounter) image of the JPL Table Mountain data set published earlier (Goldberg et al. 1980) even though the integration times for these sets are ~1-2 hours (see the 1985 Annual Report). The south "bite-out" of the west cloud is also present in the very high quality (but unpublished) sodium cloud data acquired on 13 June 1983 and 16 August 1984 by Morgan (1984). The physical meaning of the "bite-out" will be explored and explained in section IV.

Evidence for South Deficiency in the East Cloud

It is natural to ask if there is a sodium deficiency south of Io in the east cloud for the same satellite System III longitude range for which the "bite-out" occurs in the west cloud. From Figure 1, observations obtained on April 28, May 5, and May 12 (seven-day intervals and one day earlier than the west cloud images on April 29, May 6, and May 13 discussed above) are very well suited for such an investigation.

The three fully-processed east images for April 28 in Appendix I have a sodium cloud that is brighter north of Io. The image (SIP 415/27-29) at a satellite System III angle of 221.3° is much more asymmetric north to south than the two similar images (SIP 415/43-45 and SIP 415/44-46) at larger angles near 300°.

The images in Appendix I for May 5 show a fairly symmetric cloud north and south of Io for a satellite System III angle of 204.2° (image SIP 418/13-16) or less, a cloud enhanced north of the satellite for an angle of 259.2° (image SIP 418/24-26), and a cloud symmetric north and south of the satellite for an angle of 299.6° (image SIP 418/31-33). Examination of a number of additional images on May 5 that have not been fully reduced rein-

forces this behavior and indicates that the cloud is symmetric for an Io System III longitude angle of 210°, that it becomes brighter north of Io for larger angles, and that the asymmetry then decreases and is absent by an angle of 294°. The spatial morphology of the south deficient zone of sodium in the east cloud is, however, characterized by a steeper gradient in the brightness for the whole sodium cloud south of Io rather than a sharp and inclined boundary for the deficient zone as is present in the south bite-out of the west cloud. Finally, the image of June 6 (see Appendix II) exhibits only a slight north brightness enhancement when compared with the May 5 image (SIP 418/31-3) at near identical Io phase and Io System III longitude angles.

The images on May 12 do not, however, show the south zone of deficient sodium that is indicated in the May 5 images and suggested by the April 28 images. Examination of May 12 images in Appendix I and additional images that have not been fully reduced shows that the cloud brightness is essentially symmetric north and south of Io for satellite System III longitude angles ranging from ~210° to 302°.

The different north-south behavior of the east cloud images on May 5 and May 12 for the same range of Io System III longitude angles (~180°-300°) is surprising in the light of the consistency and repeatability of the south "bite-out" signature that occur in the west cloud on May 6 and May 13 over this same range of Io System III longitude angles. The long-term stability of the "bite-out" in the west cloud and the temporal or more erratic behavior of the deficient sodium south of Io in the east cloud raise some very interesting questions for Io and the magnetosphere that are discussed in Section IV.

Directional Features

The presence in the trailing cloud of an elongated feature having a changing north/south inclination relative to the satellite plane was discovered in 1980 (January 5 - April 22) and 1981 (March 10 - April 13) image data of Pilcher et al. (1984). The time varying inclination of the directional features was shown to be periodic and correlated with the Io System III longitude angle. In the data of Pilcher et al., the directional feature was inclined north of the satellite orbit plane for Io System III (1965) longitude angles between ~170° and 360°, and south of the orbit plane for longitudes

outside of this range. The south inclination of the feature was observed to decrease to zero as the Io System III longitude angle approached ~150-160°, and the north inclination of the directional feature was observed to increase for larger angles.

To investigate the behavior of the directional features in the JPL data set, the 1981 Region B/C images of Appendix I have been arranged in Appendix V (Study 5 of Table 4) in ascending order of the Io System III (1965) longitude angle for both the east cloud and west cloud separately. Examination of the images in Appendix V shows that the inclination of the directional feature is indeed the same as that discovered in the 1980 and 1981 image data of Pilcher et al. (1984). This north/south correlation of the inclination of the directional feature with the Io System III (1965) longitude angle for images in Appendix V is shown in Figure 3.

As noted in the 1985 Annual Report, the correlation in Figure 3 is also reflected (although not at that time discovered) in 1976-1979 sodium cloud images of the JPL data set published by Goldberg et al. (1980). In particular, comparison of an image on 5 March 1979 (Voyager 1 encounter day) and an image on 5 December 1977 having the same average Io geocentric phase angles (256°) showed that while their forward clouds were similar in length and brightness, their trailing clouds had different brightness distributions north and south of the satellite orbit plane. The trailing cloud of the March 5 image (centered at an average Io System III angle of 34.8°) was distributed south of the satellite orbit plane, while the trailing cloud of the December 5 image (centered at an average Io System III angle of 142°) was distributed symmetrically about the orbit plane. This is the expected behavior based on Figure 3 and implies that the directional feature is a permanent feature of the sodium cloud.

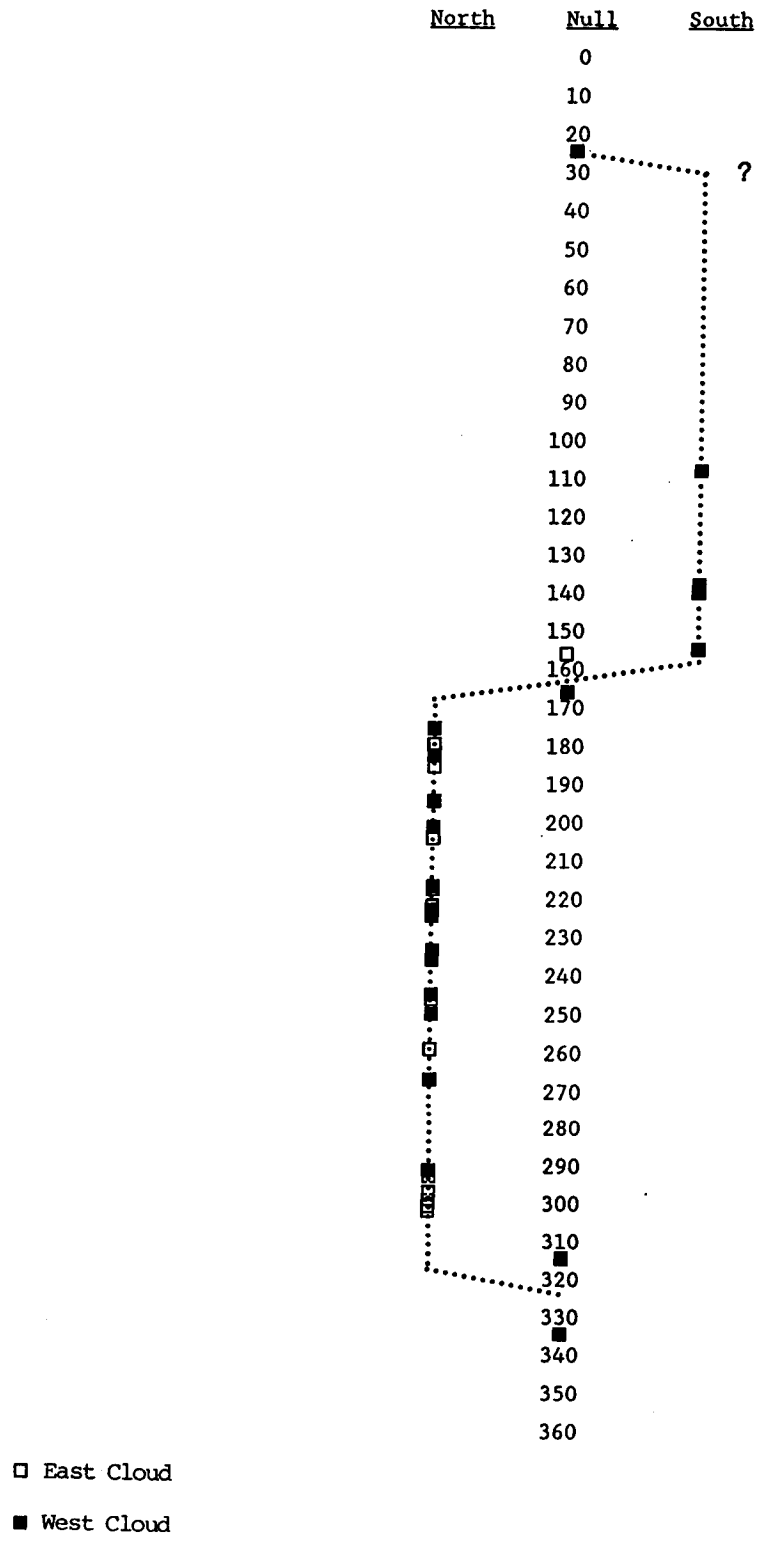

Figure 3. Correlation of the North/South Inclination of the Directional Feature with the Io System III Longitude Angle.

IV. Interpretation of the Observational Data

4.1 Model Development

Overview

In order to analyze effectively the main features and time-varying periodic signatures of the sodium cloud in Table 5, it is necessary to have a model that contains to a reasonable level of accuracy a description of the dynamics, sink processes, and the satellite source mechanism for sodium atoms in the Io-planetary-magnetosphere system. The orbital dynamics of sodium atoms in the cloud model are determined by the gravitational fields of both Io and Jupiter and by the acceleration of solar radiation pressure produced as atoms undergo solar resonance scattering in the D_1 and D_2 emission lines. All three factors were already implemented in the AER sodium cloud model at the beginning of this project. The sink for sodium atoms is determined by their interaction with the plasma torus which is dominated by electron impact ionization. Just prior to the beginning of this project, the spacetime dependent sodium sink produced by the effective oscillation of the plasma torus about the satellite orbit plane was explicitly included in the model. The plasma torus was assumed in this description to be longitudinally symmetric, and its oscillatory motion was based upon a tilled and planet-centered magnetic dipole field with a corotating heavy-ion plasma. A significant number of model improvements for the plasma torus sink have been implemented in this project and are discussed below. The satellite source for the sodium cloud has a most probable speed for the atom flux distribution that has been estimated to be ~3 km sec^{-1}, but the shape of initial velocity dispersion of the flux distribution has remained somewhat uncertain. Particular emphasis in this project has been directed toward more carefully determination of the underlying physical nature of this source and its velocity dispersion as discussed below.

Lifetime of Sodium in the Plasma Torus

The description of the plasma torus in the sodium cloud model to determine the spacetime varying sodium lifetime has been improved. In the first project year, improvements were made in the electron temperature and density by incorporating new results acquired from the analysis of both the Voyager 1

PLS electron data and ion data. These improvements were discussed in the 1985 Annual Report. In the second project year, the lifetime description of sodium in the planetary magnetosphere was improved by including the offset dipole nature of the magnetic field as well as the effects of a constant east-west electric field (Barbosa and Kivelson 1983; Ip and Goertz 1983; Goertz and Ip 1984). These improvements were discussed in the 1986 Annual Report.

A model documentation paper describing a general mathematical formalism for the neutral clouds of Io and including a number of plasma-neutral cloud interactions in the torus was completed in the second year and is included in Appendix VI. This paper (Smyth and Combi 1988a) is scheduled to be published in the 1988 April issue of The Astrophysical Journal Supplement. The general mathematical formalism was applied to the sodium cloud in a second paper (Smyth and Combi 1988b) that was completed in the third project year and that is scheduled to be published in the 1988 May 15 issue of The Astrophysical Journal. This second paper is attached in Appendix VII. The implementation of these improvements in the lifetime description of sodium was driven by the presence of physically based signatures observed in the cloud data and the plasma torus. A paper (Smyth and Combi 1987) correlating east-west asymmetries in the Jovian magnetosphere and the Io sodium cloud that illustrates some of these physical signatures was published in Geophysical Research Letters and is attached in Appendix VIII.

The lifetime description for sodium was further refined in the third project year by including an inherent System III asymmetry in the plasma torus in the longitude range of ~180° to 300°. This addition was required by the presence of the south "bite-out" signature in the west sodium cloud and will be discussed in Section 4.2. A physically corresponding but anticorrelated System III brightness asymmetry in the plasma torus S^+ (6716A° and 6731A°) ion emission has been observed from ground-based telescope since 1976 and was later discovered in the S^{++} (9532Å) ion emission. Pertinent S^+ spectral data for this asymmetry have been acquired from ground-based observations in 1976 (Trafton 1980; Trauger, Münch, and Roesler 1980), in 1977 and 1978 (Trafton 1980; Pilcher and Morgan 1980); in 1979 (Trafton 1980; Morgan and Pilcher 1982), and in 1981 (Morgan 1985a,b). Pertinent image data for S^+ and/or S^{++} emissions have more recently been obtained from ground-based observations in 1980 (Roesler et al. 1982), in 1981 (Trauger 1984; Pilcher and Morgan 1985;

Oliversen et al. 1987), in 1982 (Trauger 1984), in 1983 (Trauger 1984; Pilcher and Morgan 1985) and in 1984 (Trauger, private communication).

A comparison of these plasma observations indicates that two separate longitudinally asymmetric components appear to exist in the torus. The first component is centered at ~180°-200° with an angular width of ~90° or more, and is a permanent feature of the torus. When compared to the normal brightness of the plasma torus at the diametrically opposite magnetic longitude angle, the first component is typically 2-5 times brighter (and at extremes, 10 times brighter) with significant brightness changes occuring on a time scale of months to years. The second component is centered at ~280°-290°, has a comparable angular width to the first component, and is sometimes present and sometimes absent in the torus. The brightness of the second component may be comparable to or less than the brightness of the first component. For the observing time interval of the 1981 Region B/C images in Appendix I, the first and second longitudinally asymmetric components were similar in angular size and brightness, and both of these components had an enhanced brightness of ~4 and a plasma density enhancement of ~2 when compared to the plasma torus at the diametrically opposite longitude location (Morgan 1985a,b; Morgan 1987, private communication).

Initial Flux Distribution for Sodium Atoms at Io

Significant efforts in the third project year have been expended in determining the character of the flux distribution for the upward-moving sodium atoms ejected from Io that is consistent with the general morphology and brightness of the sodium cloud. This work is included in the paper entitled "A General Model for Io's Neutral Gas Clouds. I. Application to the Sodium Cloud" in Appendix VII (see particularly Appendix D of this paper). A modified-sputtering flux distribution to describe the incomplete collisional cascade processes between plasma ions and the atmosphere of Io is formulated and shown in the paper to provide the proper type of nonthermal sodium source required to simulate the morphological characteristics of the cloud.

4.2 Modeling of Sodium Cloud Features and Time Varying Signatures

The modeling analysis of this project has been undertaken in two steps. The first step was to verify the analytic usefulness of the model by successfully establishing an overall consistent and physical explanation for the most basic morphological characteristics of the cloud. The second step was to test and to refine this physical picture by using the model to analyze specific 1981 Region B/C images of the JPL data set. The main features and time-varying periodic signatures of the data set are summarized in Table 5.

Basic Morphological Characteristics of the Cloud

The most basic morphological characteristics of the cloud are (1) the predominance of a bright forward cloud with its east-west orbital asymmetry, (2) the presence of a less bright trailing cloud with its north-south alternating directional feature, and (3) an east-west intensity asymmetry near Io such that the D-line emissions are brighter, on average, when the satellite is east of Jupiter. The east-west orbital asymmetry exhibits itself in an east forward cloud which is less extended and is generally only comparable in length to its directional feature, and a west forward cloud which is significantly longer than the east forward cloud and is more inclined toward Jupiter (relative to a tangent line to the satellite orbit at Io's location) by ~10-15°.

The underlying physical explanation for the nature of the forward cloud and the east-west intensity asymmetry of the cloud have been explored extensively in this project. The results of these modeling efforts are presented in papers (Smyth and Combi, 1988b and 1987) attached in Appendices VII and VIII. The significant conclusions and physical insights gained from these modeling efforts for Io's atmosphere and for the plasma torus are briefly summarized later in Section 4.3.

The north-south alternating nature of the directional feature in the JPL data set was shown in Section 3.3 (see Figure 3) to be correlated with the System III longitude angle of Io. This correlation is identical to that determined earlier by Pilcher et al. (1984). For the image data of Pilcher et al., the directional features were analyzed with the 1983 sodium cloud model of AER. The Io System III longitude behavior of these directional features

was adequately explained by Pilcher et al. in terms of a source of high-velocity (~20 km sec^{-1}) sodium and a spacetime dependent sodium sink produced near Io by the effective geometric and periodic oscillatory motion of the plasma torus. The modeling of the directional feature in the JPL data set need not therefore be explicitly considered further in this project. The velocity dispersion for the sodium flux distribution at Io necessary to provide the directional feature, the forward cloud, and the east-west intensity asymmetry in a consistent manner is discussed in Appendix VII.

South Bite-Out of the West Cloud

The Io System III longitude evolution of the south bite-out feature of the west cloud is illustrated in Figure 4 by four Region B/C images of Appendix I obtained on May 13, 1981. This bite-out is not produced by model computations illustrated in Figure 5 using the best sodium lifetime description (case C in Appendix VII) of Smyth and Combi (1988b) and an isotropic sodium source with a flux of 2×10^8 atoms sec^{-1} (referenced to the satellite surface area) ejected monoenergetically (2.6 km sec^{-1}) from the satellite exobase assumed to have a radius of 2600 km. The lifetime description is based upon a tilted and offset magnetic dipole field in the presence of a constant east-west electric field of 2.8 mV/m for a heavy-ion magnetospheric plasma with no inherent System III longitudinal dependence. The less extended trailing cloud beyond Io's orbit in the model results of Figure 5 is understandable due to the absence of higher velocity components in the adopted monoenergetic source. The adopted monoenergetic source is chosen near the most probable speed of the flux distribution and is quite adequate for our present purposes of investigation.

Examination of 1981 plasma torus data (Morgan 1985a,b; Pilcher and Morgan 1985; Oliversen et al. 1987) as discussed earlier in Section 4.1 indicated an S^+ and S^{++} emission enhancement in the torus near Io's orbit in the System III longitudinal region of the ~180°-300°. The brightness enhancement may be attributed primarily to an increase in the electron density of the so-called S^+ "ribbon feature" (Trauger 1984) or "field-aligned feature" of Pilcher, Fertel and Morgan (1985; Pilcher and Morgan 1985; Morgan and Pilcher 1982) that is located inside of Io's L-shell and to a S^{++} plasma extension of this feature beyond Io's orbit. The longitudinal asymmetry in the torus appears to have

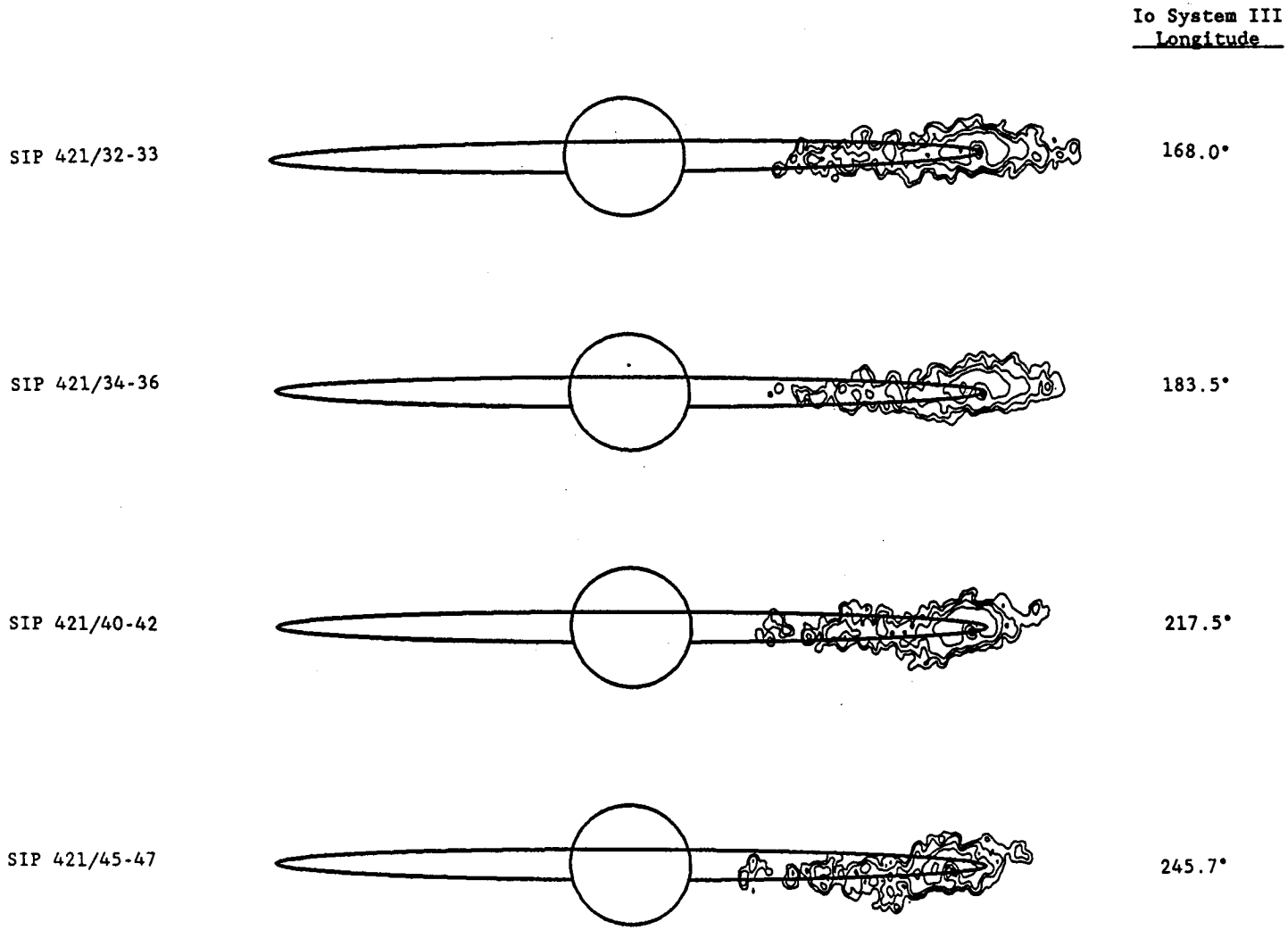

Figure 4. 1981 May 13 Region B/C Image Data. Four D_2 emission images of the sodium cloud as measured on the sky plane from the Table Mountain Observatory are shown in contour plot format and in proper spatial relationship to Jupiter, Io's location, and Io's circular orbit which appears as a thin ellipse. Contour brightness levels in kiloRayleighs, from outside to inside, are spaced as follows: 0.2, 0.5, 1.0, 2.0, 5.0, 10.0, 20.0.

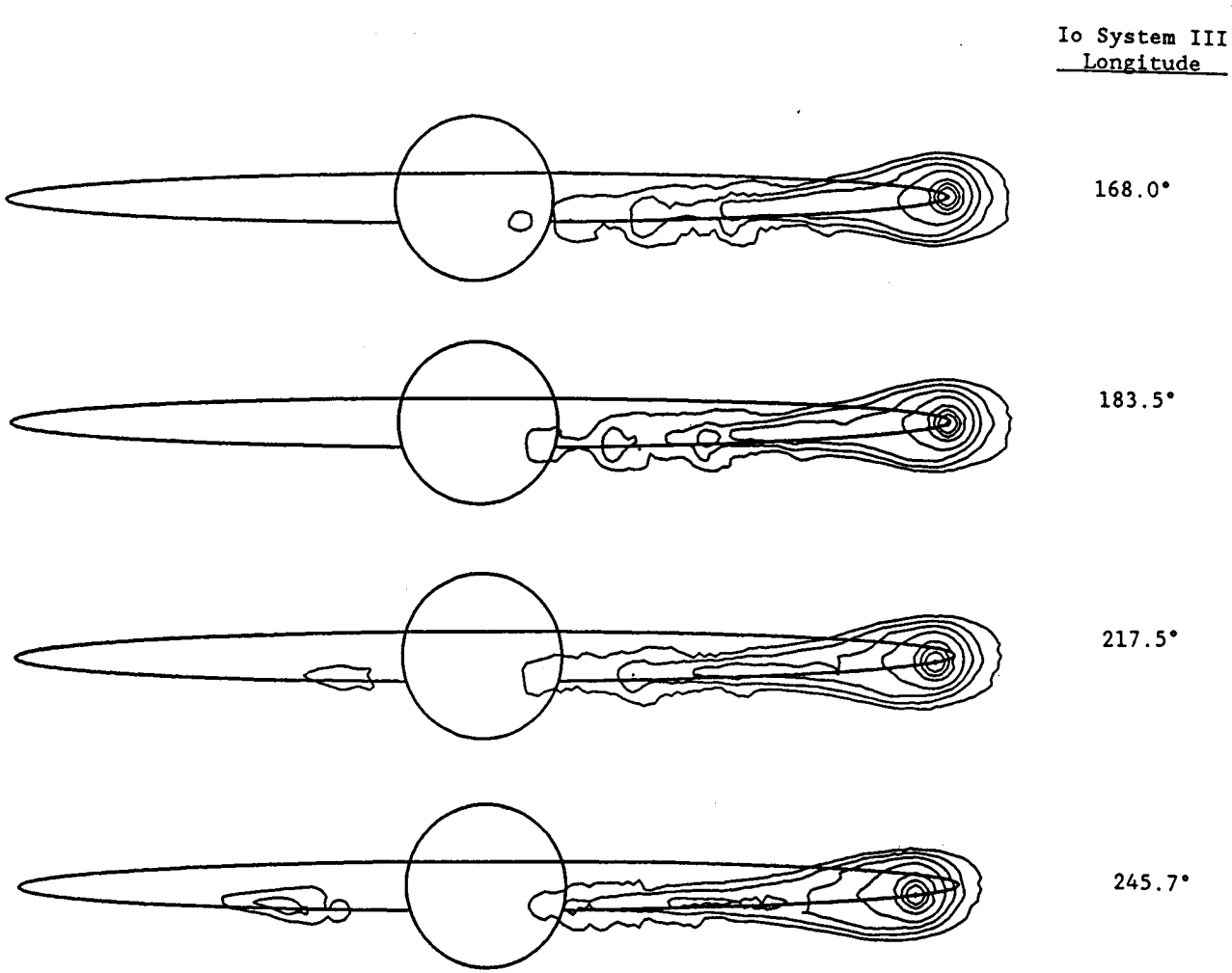

Figure 5. West Cloud Model Calculations for an Isotropic Source and a Longitudinally Symmetric Plasma Torus Sink. Model calculations for the D_2 emission brightness of the four images in Figure 4 are shown with the same adopted contour levels. An inherently longitudinally symmetric sodium sink (case C), an isotropic and monoenergetic (2.6 km sec^{-1}) sodium source with an exobase of 2600 km in radius, and a uniform sodium flux of 2 x 10^8 atoms cm^{-2} sec^{-1} (referenced to the satellite surface) were assumed.

two components, the first one centered at a System III longitude angle $\lambda_{III}^{(1)}$ (~180-200°) and the second one centered at $\lambda_{III}^{(2)}$ (~280-290°). The lifetime of sodium through electron impact ionization then has an inherent longitudinal dependence.

An explicit functional dependence of the sodium lifetime τ on the atom's System III longitude angle, λ_{III}, and radial position r in the plasma torus coordinate frame was therefore adopted in the sodium cloud model. This new lifetime description is given by

$$\frac{1}{\tau} = \nu_o \left\{ 1 + \left[\sum_{j=1}^{2} \alpha_j e^{-\left[\frac{\lambda_{III} - \lambda_{III}^{(j)}}{\sigma_j}\right]^2} \right] R(r) \right\} \tag{1}$$

where

$$R(r) = \begin{cases} e^{-\left[\frac{r - r_o}{\sigma_{inner}}\right]^2} & \text{for } r - r_o < 0 \\ e^{-\left[\frac{r - r_o}{\sigma_{outer}}\right]^2} & \text{for } r - r_o > 0 \end{cases} \tag{2}$$

and was suggested by more recent plasma torus models of Morgan (1987, private communication). Here $\tau_o = \nu_o^{-1}$ is the lifetime description for sodium determined by case C of Smyth and Combi (1988b). The parameters α_j determine the relative longitudinal strength of the two asymmetric plasma torus components while the parameters σ_j determine their relative angular width. The radial dependence R(r) of the asymmetry is centered at $r = r_o$ and has an inner scale length σ_{inner} that differs from its outer scale length σ_{outer}. During the 1981 JPL observations of the sodium cloud, best estimated values for these parameters are given as follows

$$\begin{array}{lll} \lambda_{III}^{(1)} = 180^0 & \lambda_{III}^{(2)} = 280^0 & r_o = 5.65\ R_j \\ \alpha_1 = 1 & \alpha_2 = 1 & \sigma_{inner} = 0.125 \\ \sigma_1 = 45^0 & \sigma_2 = 45^0 & \sigma_{outer} = 1.0 \end{array} \tag{3}$$

Using the parameter values given by (3), the electron density is enhanced in the active longitudinal region by a factor of two (as in the best plasma torus models of Morgan 1985b) over the Voyager 1 value it has at the diametrically opposite longitudinal angle in the plasma torus. The sodium lifetime is correspondingly reduced by the same factor.

New model calculations for the four observations in Figure 4 were performed using the asymmetric longitudinal sodium lifetime description given by the expressions (1), (2), and (3), but using the same satellite source adopted in Figure 5. These results are shown in Figure 6 and clearly simulate the basic character of the Io System III longitude evolution of the south bit-out feature. Comparison of model results in Figure 5 and Figure 6 also shows that the increased sink active in Figure 6 has reduced the size of the forward cloud so that it is now only a little longer than in the data of Figure 4. The 1 kR and 2 kR level contours of the forward cloud in Figure 6 are, however, located at a similar distance from Io as in the data in Figure 4. Reducing only the active flux region of the model exobase to a band source (which excludes a portion of the leading and trailing hemispheres, used in the paper in Appendix VII) and adopting the asymmetric longitudinal sodium lifetime description, monoenergetic model calculations for the first and third images of Figure 4 are shown in Figure 7. Comparison of appropriate images in Figure 4 and Figure 7 shows that the forward cloud lengths at the 0.2 kR level are similar in length, but that the model results for the forward cloud closer to Io are not bright enough by approximately a factor of 2. This suggests that a more correct specification of the source would lie somewhat immedately between the band and isotropic ejection condition. This is similar to the conclusion reached in the paper in Appendix VII from modeling the east-west intensity asymmetry measured by Bergstralh et al. (1975, 1977). The appropriate sodium source may then correspond to a flux of $\sim 2 \times 10^{8}$ cm^{-2} sec^{-1} for isotropic ejection or a slightly larger flux for band ejection which both lead to a total source strength of $\sim 1 \times 10^{26}$ atoms sec^{-1}.

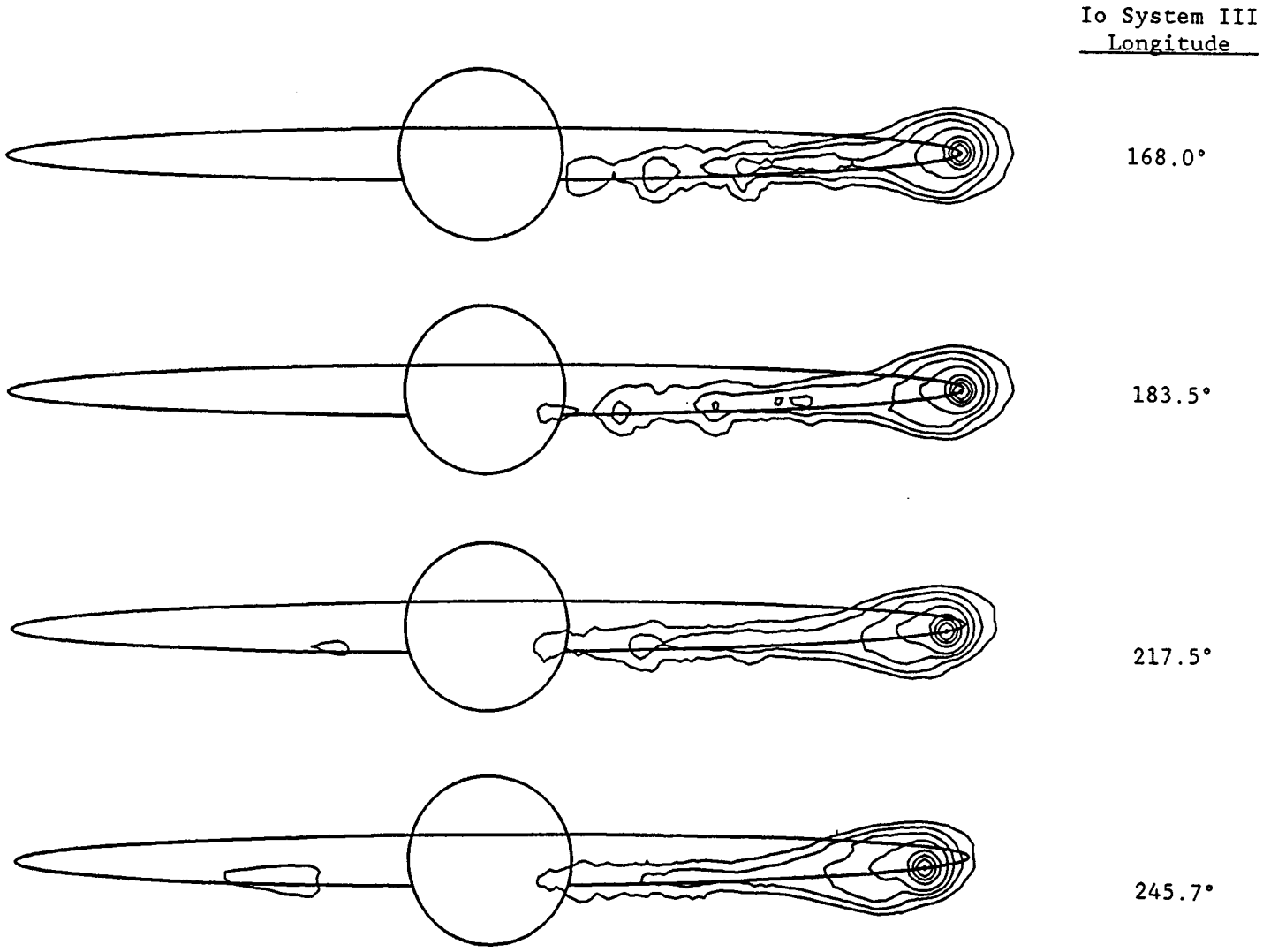

Figure 6. West Cloud Model Calculations for an Isotropic Source and a Longitudinally Asymmetric Plasma Torus Sink. Same description as Figure 5 with the exception that the longitudinally asymmetric plasma torus sink for sodium (see text) has now been assumed.

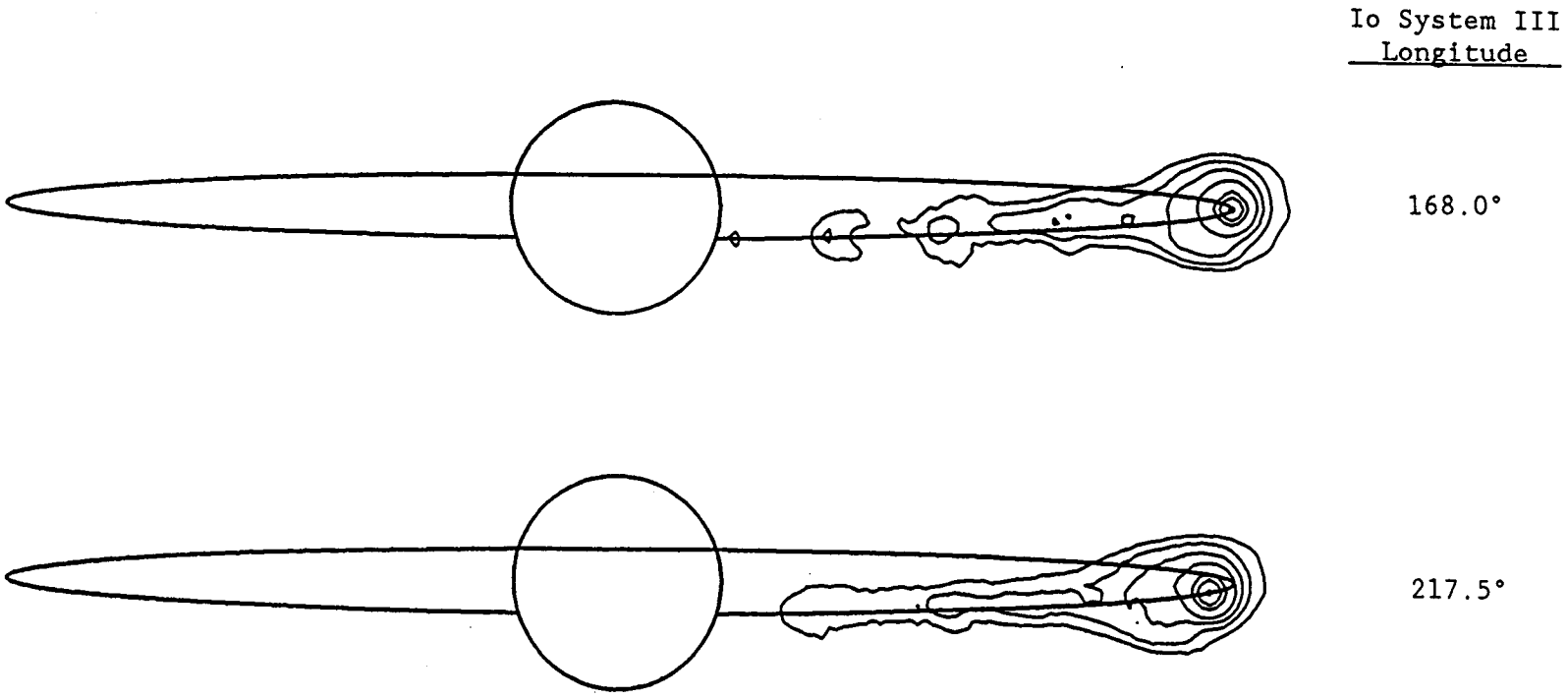

Figure 7. West Cloud Model Calculations for a Band Source and a Longitudinally Asymmetric Plasma Torus Sink. Model calculations for the D_2 emission brightness of two of the four images in Figure 4 are shown with the same adopted contour levels. The plasma torus sink and sodium source are the same as in Figure 6 with the exception that the active exobase area has now been reduced to a band source.

East Cloud Analysis

Two model calculations for the sodium cloud at an Io geocentric phase angle of 90.5° and an Io System III angle of 221.3° assuming the longitudinally asymmetric plasma torus sink given by expressions (1), (2), and (3) and the two previously adopted source conditions with a flux of 2 x 10^8 atoms cm^{-2} sec^{-1} are shown in Figure 8. The Io geocentric phase and Io System III longitude angles for the model results are identical to the April 28 image SIP 415/27-29, and differ only appreciably for the latter angle from the May 5 image SIP 418/24-26 (i.e. 90.2°, 259.3°) and the May 12 image SIP 420/30-32 (i.e. 91.2°, 301.8°). Comparison of the two model results in Figure 8 illustrates how the band source reduces both the length and brightness of the forward cloud (as also noted in the paper in Appendix VII) substantially from that of an isotropic source. Comparison of the band source results in Figure 8 with the three images noted above, however, indicates that the forward cloud predicted by the model, although only slightly longer, is too bright at the 1 to 2 kR level by at least a factor of two. This is in contrast to the model results for the west cloud at comparable Io System III angles in Figure 6 and Figure 7, where the isotropic source matches these observed 1-2 kR brightness levels and the band source produces a cloud that is too dim at these observed brightness levels by a factor of ~2.

The ability of the cloud model for the band source to reasonably match the west cloud shape but underestimate its brightness, and to reasonably match the length of the east forward cloud but overestimate its brightness is most interesting. This likely indicates that the angular distribution of the sodium source is oriented more in the vector direction of motion of the satellite in the east than in the west. Such an east-west asymmetry in the source would not appreciably alter the brightness of the cloud near Io (where it is constrained by the east-west intensity asymmetry observations) but would change the orbital trajectories of sodium atoms at larger distances from the satellite so that not as many atoms would be able to populate the east forward cloud and more atoms would be able to populate the west forward cloud. The comparison of the isotropic and band source in Figure 8 is a simple example where the angular distribution has been changed, but in this case the same reduced angular distribution (i.e. the band source) has been assumed for all

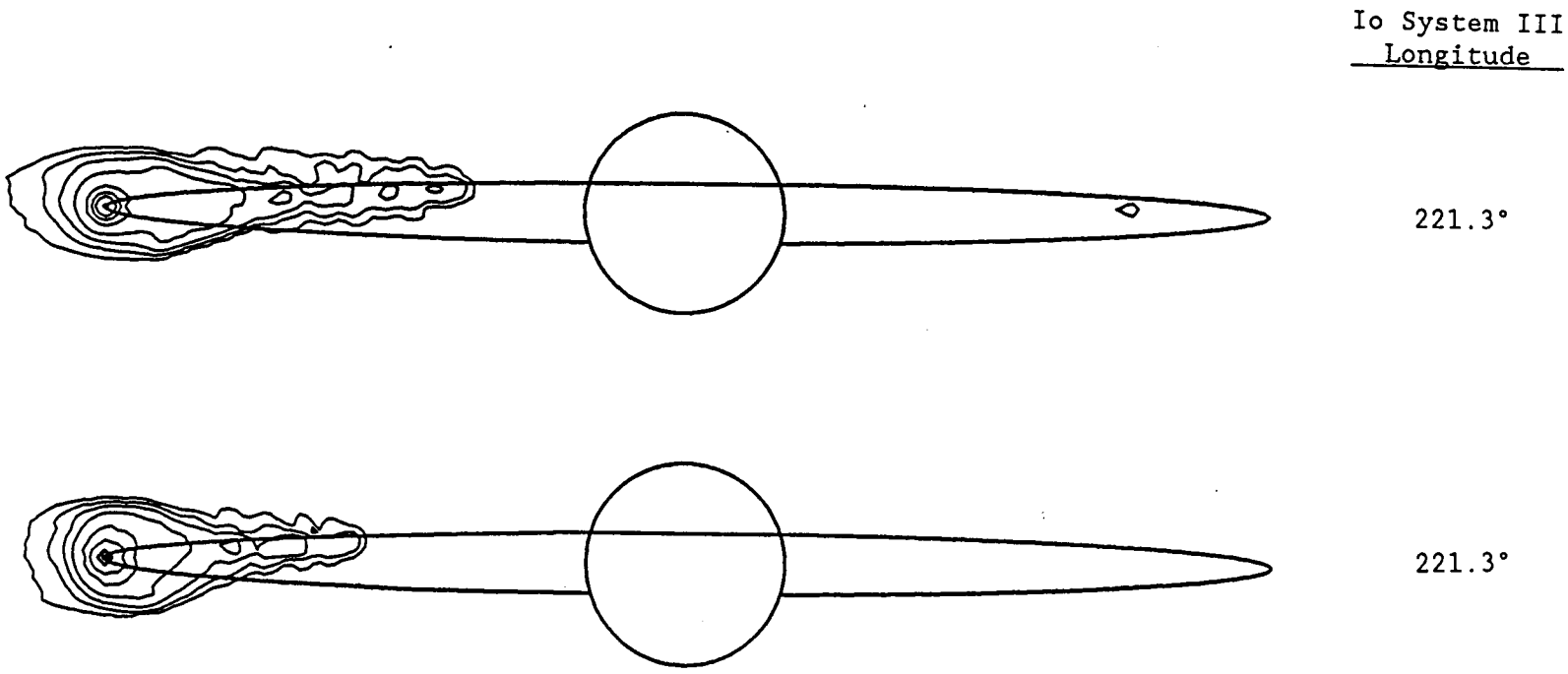

Figure 8. East Cloud Model Calculations for a Longitudinally Asymmetric Plasma Torus Sink. Model calculations for the D_2 emission brightness of the 1981 April 28 image (SIP 415/27-29) are shown on the sky plane with the same contour levels adopted in Figure 4. The plasma torus sink for sodium is the same as in Figure 6. For both the isotropic and band sources, monoenergetic (2.6 km sec^{-1}) ejection of sodium was assumed with the same exobase radius and uniform flux as adopted in Figure 5.

east and west Io geocentric phase angles. The east-west asymmetry in the angular distribution of the source that is suggested might be produced by the interaction of the plasma torus ions with Io's local atmosphere if the atmosphere were enhanced above the sunlit hemisphere of the surface. The investigation of this very interesting possibility, however, requires additional support for research beyond that available in this project.

The model results of Figure 8 show an east cloud that exhibits little or no asymmetric distribution of sodium north and south of Io, in contrast to the south bite-out feature present in the model results for the west cloud (Figure 6 and Figure 7). Additional model results (not shown) for the May 5 east image (SIP 418/24-26) and the May 12 east image (SIP 420/30-32) that cover the Io System III longitude angle range of the asymmetric sink substantiate the results of Figure 8. The reason there is no deficient sodium signature south of Io in the east cloud model is because the east-west electric field has displaced Io radially inward from the location of the asymmetric sink and thereby has literally removed the sodium from the spatial region of enhanced ionization. This is readily apparent by studying Figure 9 where the sodium lifetime (case C of Smyth and Combi 1988b) in the plasma torus at eastern and western elongation is shown in relationship to Io's motion (dark oval) during one Io System III longitude period. The Io System III longitude angle on the oval in the centrifugal equator plane at the smaller radial displacement is 110° and increases as the satellite moves upward along the oval and reaches 200° at the top of the oval. The longitudinally asymmetric plasma torus sink for sodium is centered on the centrifugal plane at a radial distance of 5.65 R_j near the middle of the oval at eastern elongation and somewhat to the left of the oval at western elongation. The small inner radial scale height (σ_{inner} = 0.125 R_j) of the inherent System III enhancement causes the enhancement to decay so rapidly that it is unable to reach Io's location in the 110°-200° sector in the east, while the outer radial scale height (σ_{outer} = 1.0 R_j) of the inherent System III enhancement allows the enhancement to be felt at almost full force at Io's location in the 110°-290° sector in the west.

The north-south symmetry of the east cloud model results in Figure 8 is similar to the Region B/C images observed on March 12, but not the images observed on March 5 and April 28 which show some deficiency in the sodium

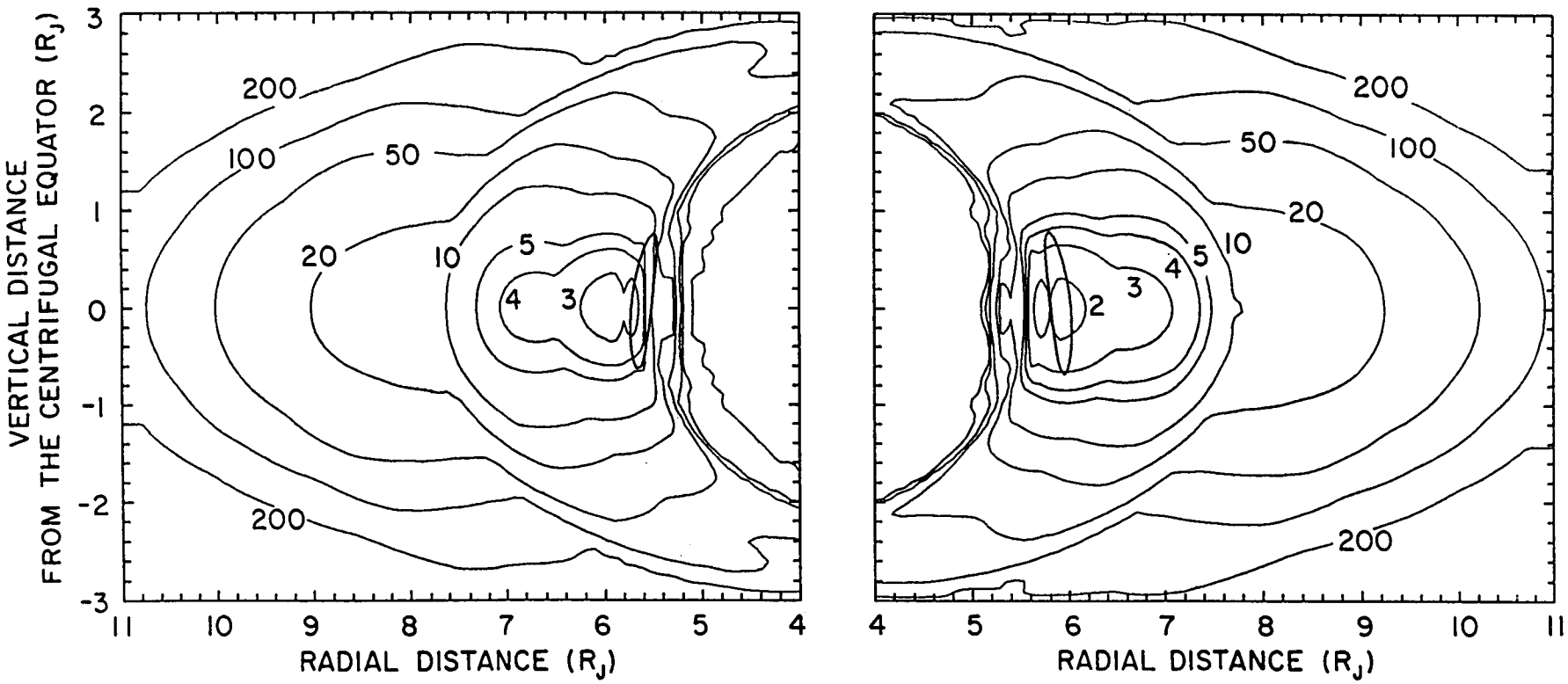

Figure 9. Electron Impact Lifetime of Sodium in the Plasma Torus. The lifetime in units of hours is shown at eastern and western elongation in the coordinate frame of the plasma torus (case C) that is tilted by 7°, has a magnetic dipole offset and is in the presence of an east-west electric field of 2.8 mV/m. The lifetime at Io's location in the plasma torus for these two elongation pictures varies periodically as a function of the System III magnetic longitude of the satellite and is shown by the dark oval.

brightness south of Io as discussed earlier in Section 3.2. The apparent time variability or erratic behavior of the east cloud and the stability of the west cloud regarding a zone of deficient sodium south of Io are likely to be related to a difference (or time variability) in the strength of the east-west electric field east and west of Jupiter. It is clear from Figure 9 that the west cloud is in a rather stable relationship with the location of the inherent System III plasma torus enhancement for small modulations of the electric field strength west of Jupiter. This is not, however, true for the east cloud because of the very small scale height σ_{inner} and the rather close radial proximity of Io's orbit to the System III enhancement in the plasma torus. Small changes in the east-west electric field east and west of Jupiter can therefore modulate the radial inward displacement of Io relative to the location of the longitudinally asymmetric plasma torus sink and hence modulate the sodium population south of the satellite accordingly.

In the sodium lifetime description of Figure 9 (case C of Smyth and Combi 1988b), the east-west field has been assumed simply to be constant. Studies of Voyager EUV ion emission data (Sandel 1985), however, suggest that the electric field may be time variable, but that it also has a preferred time-average value directed from east-to-west, as assumed in Figure 9. More recent studies of the plasma ion emission data (Sandel and Dessler 1987) show that these emissions exhibit a clear and persistent dual periodicity (System III, and a new System IV differing by almost exactly 3% in period). Sandel and Dessler propose that (1) the convection electric field across Jupiter's magnetotail is limited primarily to the west side of the planet, where the overflow of plasma from the Io torus occurs, and (2) that this electric field is stronger and also modulated at the System IV period west of Jupiter, but is weaker and shows little System IV modulation east of Jupiter. This causes the plasma torus west of Jupiter (as is evident in ion emission data) to be shifted on average closer to the dipole offset of the magnetic field by ~0.3 R_j (similar to the case C in Figure 9) but shifted in a different manner than by equal radial contributions by a constant electric field east and west of Jupiter. The assumption of a constant electric field as adopted in Figure 9 would then need to be modified to properly include one shift contributed by the electric field west of Jupiter and a different shift contributed by the electric field east of Jupiter. The presence of an unequal

electric field strength east and west of Jupiter would then change the absolute location of the dark ovals in Figure 9 but not their time-average relative separation. Small changes in the absolute location of the east dark oval could then produce different modulations of the sodium abundance south of Io and thereby provide an explanation for the apparent erratic behavior of the east image data. The investigation of these physical processes is, however, beyond the scope of the present project and should be undertaken in future research efforts for Io.

4.3 Summary of Physical Insights

Physical insights that have been gained in this project are briefly summarized below. These advances in our understanding are divided for discussion purposes into three topics: (1) the local structure of Io's atmosphere, (2) the gas escape mechanism at Io, and (3) the properties and stability of Jupiter's magnetosphere.

Local Structure of Io's Atmosphere

From modeling analysis of the basic morphological characteristics of the sodium cloud (Smyth and Combi 1988b, in Appendix VII), a number of conclusions were formed. The collisional exobase for the atmosphere is somewhat below 2600 km in radius (i.e. somewhat below an altitude of 785 km). Such heights for the collisional exobase are nearer the "minimum" SO_2 atmosphere for Io at the Voyager 1 encounter required by photochemical models of Kumar (1984). Above the collisional exobase, the exosphere (or corona) of the satellite is dominated by a nonthermal upward flux distribution with a sodium density of $\sim 3 \times 10^3$ cm^{-3} at a radius of 2600 km and a radial sodium density profile in agreement with recent measurements of Schneider et al. (1987). The nonthermal sodium atoms escape from the Lagrange sphere of the satellite ($\sim 10^4$ km in radius) and populate the sodium cloud. The nonthermal energy is supplied by ion-neutral interactions (described in the following subsection) which occur near the collisional exobase and in the corona. The nonthermal collisional processes will penetrate energetically somewhat below the classical collisional exobase level and may modify significantly the gas density and simple diffusive equilibrium (vertical stratification) assumptions used in photochemical models for Io (Kumar 1984, 1985). In this manner, the simple photochemical

picture could be replaced in the upper atmosphere by a nonthermal heating layer and an effective global atmospheric blowoff process.

From analysis of Smyth and Combi (1988b) and new results presented in this report, additional information about the local atmosphere is suggested. The local atmosphere is likely collisionally thick above the satellite surface because of the nature of the speed of dispersion of the sodium flux distribution. The atmosphere is also likely enhanced on the sunlit hemisphere so as to produce a different angular distribution for the sodium flux distribution east and west of Jupiter as suggested by image data. Additional analysis is required to investigate more fully this very interesting latter point.

Gas Escape Mechanism

The gas escape mechanism at Io is driven by the corotating plasma through ion-neutral momentum transfer. This momentum transfer most likely occurs in a collisional thick atmosphere. In the atmosphere, ion-neutral interactions are characterized by an incomplete collisional cascade process described reasonably well by a nonthermal modified-sputtering flux distribution that has been explicitly developed (see Smyth and Combi 1988b). The nonthermal flux distribution dominates a thermal (1000°-2000°K) flux disbribution by roughly an order of magnitude in the exosphere (or corona), and a thermal flux distribution by itself is incompatible with the sodium cloud data. The most probable speed of the nonthermal flux distribution for sodium atoms is ~3 km sec^{-1}. The speed disperson of the nonthermal flux distribution is more appropriately described by a Thomas-Fermi differential cross section with an incomplete collisional cascade process than by a classical sputtering distributing for a complete collisional cascade process.

The angular distribution of the nonthermal flux distribution is likely intermediate between an isotropic and band source. There also appears to be an east-west asymmetry in the angular distribution of the sodium source such that the distribution is peaked more in the direction of Io's orbital motion in the east than in the west. This accounts for the suggestion above that the atmosphere may well be enhanced more above the sunlit hemisphere. A more exact understanding of the angular distribution of the flux distribution and its east-west asymmetries will require additional modeling of image data. The

total source strength of the upward directed sodium for the nonthermal flux distribution is in the range of ~1-3 x 10^{26} atoms sec^{-1} and depends upon the details of the angular distribution of the sodium source.

Magnetosphere of Jupiter

A 7° tilted and corotating heavy-ion plasma torus with a planetary offset dipole magnetic field and Voyager-like radial profiles from the plasma density and temperatures is essential in understanding the basic morphology of the sodium cloud. The predominance and length of the forward sodium cloud are determined naturally within this plasma torus description by means of the resulting spactime lifetime structure produced for sodium atoms. The north-south alternating nature of the directional feature in the trailing cloud is also naturally explained by this spacetime lifetime behavior and higher speed (~15-20 km sec^{-1}) sodium atoms in the nonthermal flux distributions. The basic structure of the plasma torus can be judged to be reasonably stable for more than ten years by the consistent presence of these identified sodium signatures in the cloud data over this time period.

An east-west electric field with a time-average value of ~2.8 mV/m is present in the magnetosphere. This electric field produces the east-west intensity asymmetry in the sodium cloud near Io (Smyth and Combi 1987, 1988b) and also the anti-correlated east-west intensity asymmetry observed both in optical and ultraviolet ion emissions in the torus (see Smyth and Combi 1987). Both sodium data and ion emission data suggest that the strength of this east-west electric field east and west of Jupiter may be different and may undergo different time variabilities.

The plasma torus contains an inherent System III longitudinally asymmetric enhancement in the active sector (~180°-320°). This has been noted in ground based observations of the torus ion emissions. This System III asymmetric enhancement has been shown to produce a periodic south "bite-out" in the west sodium cloud which has been present in the various sodium data sets for at least seven years. A zone of deficient sodium south of Io in the east cloud is sometimes observed and sometimes not observed. It appears that this time variable or erratic behavior may be linked to a time variability in the east-west electric field as discussed above in Section 4.2.

4.4 Future Studies

As noted in the introduction, the complete JPL Io sodium cloud data set is composed of 1974-1979 spectral data, 1981 spectral data, 1976-1979 Region B/C image data, 1981 Region B/C image data, and 1981 Region A image data. Studies undertaken in this project have considered only a subset of the 1981 Region B/C image data. At this time, a number of very important studies for the 1981 Region B/C image data still remain to be considered. Studies for the other components of the data set have yet to be even initiated. Some important aspects of future studies are briefly described below.

Additional studies of the 1981 Region B/C image data could be most easily undertaken by extending and refining the analysis already begun in this project. For the local structure of Io's atmosphere, the radial density structure of sodium may be readily probed beyond the occulting mask and questions as to the enhancement of the gas density on the sunlit hemisphere straightforwardly investigated by comparison and analysis of east and west images. The effects of unequal east-west electric fields east and west of Jupiter may likewise be pursued by further comparison and analysis of east images acquired on different days. This latter analysis will lead to a better understanding of the structure, stability, and time variability of the planetary magnetosphere and their connection to the Iogenic plasma source.

The analysis of the 1981 Region B/C images may also be readily applied to the 1976-1979 Region B/C images. This will allow us to extend the time line and to test for the stability or time variability of various morphological features of the cloud and their corresponding physical properties and structures in the plasma torus. The 1976-1979 Region B/C data set includes two images on the Voyager 1 encounter day as well as a number of images around this encounter time. Study of these images would be most valuable in linking the whole sodium cloud data set to Voyager 1 encounter conditions determined by the spacecraft.

Analysis of the 1974-1979 spectral data, 1981 spectral data, and the 1981 Region A image data would also be valuable for refining our understanding of Io's local atmosphere and its stability or time variability. Studies of these data can be used to extend the 1974-1975 measurements for the east-west

asymmetry near Io of Bergstralh et al. (1975, 1977) to the 1981 time frame. Radial profiles for the sodium density within the Lagrange sphere and beyond could be extracted from these data and analysis applied. These studies would also be most valuable in understanding the stability of Io's atmosphere, the plasma source, and the magnetosphere over a seven year period.

V. REFERENCES

Barbosa, D. D., and Kivelson, M. G. (1983), Dawn-Dusk Electric Field Asymmetry of the Io Plasma Torus. Geophys. Res. Lett., 10, 210.

Bergstralh, J. T., Matson, D. L., and Johnson, T. V. (1975) Sodium D-Line Emission from Io: Synoptic Observation from Table Mountain Observatory. Ap. J. Lett., 195, L131-L135.

Bergstralh, J. T., Young, J. W., Matson, D. L., and Johnson, T. V. (1977) Sodium D-line Emission from Io: A Second Year of Synoptic Observation from Table Mountain Observatory. Ap. J. Lett., 211, L51-L55.

Goertz, C. K., and Ip, W.-H. (1984) A Dawn-to-Dusk Electric Field in the Jovian Magnetosphere. Planet. Space Sci., 32, 179-185.

Goldberg, B. A., Carlson, R. W., Matson, D. L., and Johnson, T. V. (1978) A New Asymmetry in Io's Sodium Cloud. Bull. AAS, 10, 579.

Goldberg, B. A., Garneau, G. W., and LaVoie, S. K. (1984) Io's Sodium Cloud. Science, 226, 512-516.

Goldberg, B. A., Mekler, Y., Carlson, R. W., Johnson, T. V., and Matson, D. L. (1980) Io's Sodium Emission Cloud and the Voyager 1 Encounter. Icarus, 44, 305-317.

Ip, W.-H., and Goertz, C. K. (1983) An Interpretation of the Dawn-Dusk Asymmetry of UV Emission from the Io Plasma Torus. Nature, 302, 232-233.

Kumar, S. (1984) Sulfur and Oxygen Escape from Io and a Lower Limit to Atmospheric SO_2 at Voyager 1 Encounter. J. Geophys. Res., 89, 7399-7406.

Kumar, S. (1985) The SO_2 Atmosphere and Ionosphere of Io: Ion Chemistry, Atmospheric Escape, and Models Corresponding to the Pioneer 10 Radio Occultation Measurements. Icarus, 61, 101-123.

Macy, W. W., Jr., and Trafton, L. M. (1975a) Io's Sodium Emission Cloud. Icarus, 25, 432.

Macy, W., Jr., and Trafton, L. (1975b) A Model for Io's Atmosphere and Sodium Cloud. Ap. J., 200, 510.

Matson, D. L., Goldberg, B. A., Johnson, T. V., and Carlson, R. W. (1978) Images of Io's Sodium Cloud. Science, 199, 531-533.

Morgan, J. S. (1985a) Temporal and Spatial Variations in the Io Torus. Icarus, 62, 389-414.

Morgan, J. S. (1985b) Models of the Io Torus. Icarus, 62, 243-265.

Morgan, J. S. (1984) Private Communication.

Morgan, J. S. (1987) Private Communication.

Morgan, J. S., and Pilcher, C. B. (1982) Plasma Characteristics of the Io Torus. Ap. J., 253, 406-421.

Münch, G., and Bergstralh, J. T. (1977) Io: Morphology of its Sodium Emission Region. Pub. A. S. P., 89, 232.

Murcray, F. J. (1978) Observations of Io's Sodium Cloud. Ph.D. Thesis, Dept. of Physics, Harvard University, Cambridge, Massachusetts.

Murcray, F. J., and Goody, R. (1978) Pictures of the Sodium Cloud. Ap. J., 226, 327.

Oliversen, R. J., Scherb, F., and Roesler, F. L. (1987) The Io Sulfur Torus in 1981. Preprint.

Pilcher, C. B., Fertel, J. H., and Morgan, J. S. (1985) [SII] Images of the Io Torus. Ap. J., 291, 377.

Pilcher, C. B., and Morgan, J. S. (1980) The Distribution of [SII] Emission Around Jupiter. Ap. J., 238, 375-380.

Pilcher, C. B., and Morgan, J. S. (1985) Magnetic Longitude Variations in the Io Torus. Adv. Space Res., 5, 337-345.

Pilcher, C. B., Smyth, W. H., Combi, M. R. and Fertel, J. H. (1984) Io's Sodium Directional Features: Evidence for a Magnetospheric-Wind-Driven Gas Escape Mechanism. Ap. J., 287, 427-444.

Roesler, F. L. et al. (1982) Fabry-Perot/CCD Observations of [SIII] and [SII] Emissions from the Jupiter Plasma Torus. Ap. J., 259, 900-907.

Sandel, B. R. (1985) Displacement of the Center of the Plasma Torus from Jupiter's Magnetic Dipole. Bull. AAS, 17, 695.

Sandel, B. R., and Dessler, A. J. (1987) Dual Periodicity of the Jovian Magnetosphere. Preprint.

Schneider, N. M., Hunten, D. M., Wells, W. K., and Trafton, L. M. (1987) Eclipse Measurements of Io's Sodium Atmosphere. Science, 238, 55-58.

Smyth, W. H., and Combi, M. R. (1987) Correlating East-West Asymmetries in the Jovian Magnetosphere and the Io Sodium Cloud. Geophys. Res. Lett., 14, 973-976.

Smyth, W. H., and Combi, M. R. (1988a) A General Model for Io's Neutral Gas Clouds. I. Mathematical Description. Ap. J. Supp., in press.

Smyth, W. H., and Combi, M. R. (1988b) A General Model for Io's Neutral Gas Clouds. II. Application to the Sodium Cloud. Ap. J., in press.

Smyth, W. H., and McElroy, M. B. (1978) Io's Sodium Cloud: Comparison of Models and Two-Dimensional Images. Ap. J., 226, 336-346.

Trafton, L. (1980) The Jovian SII Torus: Its Longitudinal Asymmetry. Icarus, 42, 111-124.

Trauger, J. T. (1984) Photometric Images of Sulfur Ions and Sodium Neutrals in the Jupiter/Io Torus. Bull. AAS, 16, 712.

Trauger, J. T., Münch, G., and Roesler, F. L. (1980) A Study of the Jovian [SII] Nebula at High Spectral Resolution. Ap. J., 236, 1035-1042.

Appendix I

Fully Reduced 1981 Sodium Cloud Images: Study 1

Appendix I

For each observation, the D_2 image (upper contour plot) is shown in proper relationship and scale to Jupiter, Io, and Io's orbit (as seen by an Earth observer) while this information is suppressed for the simultaneously measured but dimmer D_1 image (lower contour plot). Eastern elongation for Io is to the left, western elongation is to the right, and north is up. Contour brightness levels, from outside to inside, have increasing values that are spaced as follows: 0.1, 0.2, 0.5, 1, 2, 5, 10 and 20 kiloRayleighs. In all cases the sodium very near Io is occultated by a circular mask (9 arc sec in diameter) centered on the satellite. This mask accounts for the decrease in the brightness of the cloud very near Io.

For each observation, the Image Number (Tape/Frames), UT date, and mid-point condition for the Io geocentric phase angle and the Io System III longitude angle (from Table 2) are given. The number in parentheses following the UT date identifies the first, second, third, etc. image fully reduced on that day as ordered in Table 2 and indicated by dots in Figure 1.

Appendix I

1981 Region B/C Images: Processed by MIPL

Date of Observations	Start Conditions			End Conditions			Mid-Point Conditions		Image ID Number (Tape/frames)
	Time (UT)	Io Phase Angle (deg)	Magnetic Longitude of Io† (deg)	Time (UT)	Io Phase Angle (deg)	Magnetic Longitude of Io† (deg)	Io Phase Angle (deg)	Magnetic Longitude of Io† (deg)	
6 April	5:00	291.1	303.2	5:36	296.3	319.8	293.7	311.5	SIP 410/13-15
28 April	4:49	88.0	213.1	5:24	92.9	229.4	90.5	221.3	SIP 415/27-29
	7:28	110.3	286.9	7:58	114.5	300.8	112.4	293.9	*SIP 415/43-45
	7:39	111.9	292.0	8:07	115.8	305.0	113.9	298.5	*SIP 415/44-46
29 April	3:48	283.5	131.3	4:19	287.9	145.6	285.7	138.5	SIP 416/4-6
	4:22	288.3	147.0	4:53	292.7	161.4	290.5	154.2	SIP 416/7-9
4 May	3:25	217.6	216.2	3:55	221.8	230.0	219.7	223.1	SIP 417/8-10
	4:20	225.4	241.6	4:53	230.1	256.8	227.8	249.2	SIP 417/13-15
	4:56	230.5	258.2	5:33	235.8	275.3	233.2	266.8	SIP 417/16-18
	5:49	238.1	282.7	6:28	243.6	300.7	240.9	291.7	SIP 417/20-22
	7:19	250.9	324.3	7:52	255.6	339.5	253.3	331.9	SIP 417/27-29
	9:06	266.1	13.7	9:50	272.4	34.1	269.3	23.9	SIP 417/36-39
5 May	3:59	65.9	178.9	4:30	70.3	193.3	68.1	186.1	SIP 418/10-12
	4:32	70.5	194.2	5:15	76.6	214.2	73.6	204.2	SIP 418/13-16
	6:34	87.7	250.9	7:10	92.7	267.6	90.2	259.3	SIP 418/24-26
	8:03	100.2	292.2	8:35	104.7	307.0	102.5	299.6	SIP 418/31-33
6 May	5:36	283.6	170.4	6:10	288.5	186.1	286.1	178.3	SIP 419/19-21
	6:11	288.6	186.6	6:43	293.2	201.4	290.9	194.0	SIP 419/22-24
12 May	3:28	46.4	153.5	3:55	50.2	166.0	48.3	159.8	SIP 420/6-8
	4:10	52.3	173.0	4:40	56.5	186.9	54.4	180.0	SIP 420/10-12
	5:05	60.0	198.5	6:28	71.6	237.0	65.8	217.8	SIP 420/15-20
	6:30	71.9	238.0	7:09	77.4	256.1	74.7	247.1	SIP 420/21-23
	8:28	88.5	292.7	9:07	93.9	310.8	91.2	301.8	SIP 420/30-32
13 May	3:28	250.1	100.3	4:03	255.1	116.4	252.6	108.4	SIP 421/21-23
	4:43	260.8	134.9	5:04	263.7	144.6	262.3	139.8	SIP 421/27-28
	5:42	269.1	162.2	6:07	272.7	173.8	270.9	168.0	SIP 421/32-33
	6:09	273.0	174.7	6:47	278.4	192.3	275.7	183.5	SIP 421/34-36
	6:49	278.7	193.2	7:23	283.5	208.9	281.1	201.1	SIP 421/37-39
	7:25	283.8	209.8	7:58	288.5	225.1	286.2	217.5	SIP 421/40-42
	8:00	288.7	226.0	8:35	293.7	242.2	291.2	234.1	SIP 421/43-45
	8:25	292.3	237.6	9:00	297.2	253.8	294.8	245.7	SIP 421/45-47
6 June	4:19	100.2	292.4	4:53	105.0	308.1	102.6	300.3	SIP 424/10-12
14 June	3:47	284.0	212.6	4:28	289.8	231.5	286.9	222.1	SIP 425/6-9
	4:17	288.2	226.5	5:05	295.0	248.7	291.6	237.6	SIP 425/9-12

† System III (1965)
* images processed are redundant

Appendix I

1981 Region B/C Images:

East-West Comparisons on Consecutive Days

East Images	West Images	Set
April 28	April 29	1.A
	May 4	1.B
May 5	May 6	I.B
May 12	May 13	1.C

SIP410/13-15

UT Date: April 6, 1981 (1)

Average Io Phase = 293.7

Average Io Sys III = 311.5

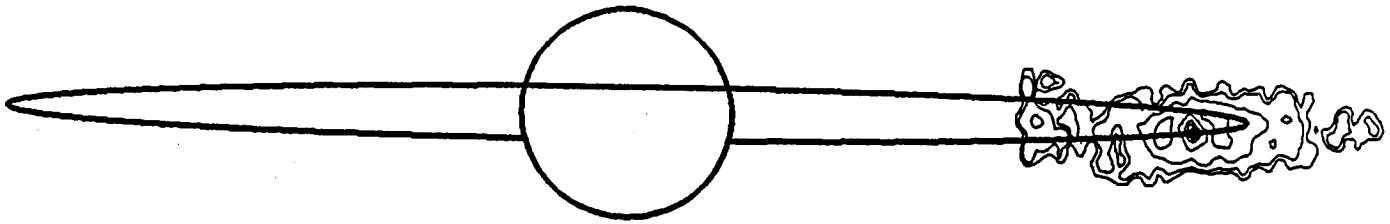

SIP415/27-29

UT Date: April 28, 1981 (1)

Average Io Phase = 90.5

Average Io Sys III = 221.3

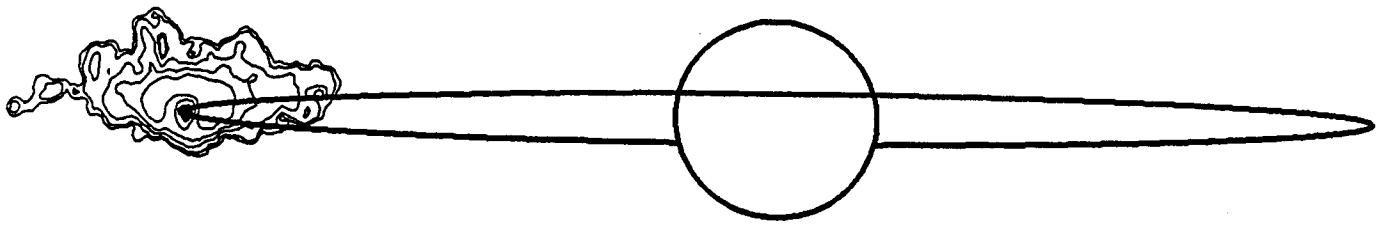

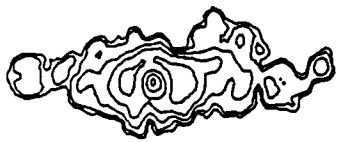

SIP415/43-45

UT DATE: APRIL 28, 1981 (2)

AVERAGE IO PHASE = 112.4

AVERAGE IO SYS III = 293.9

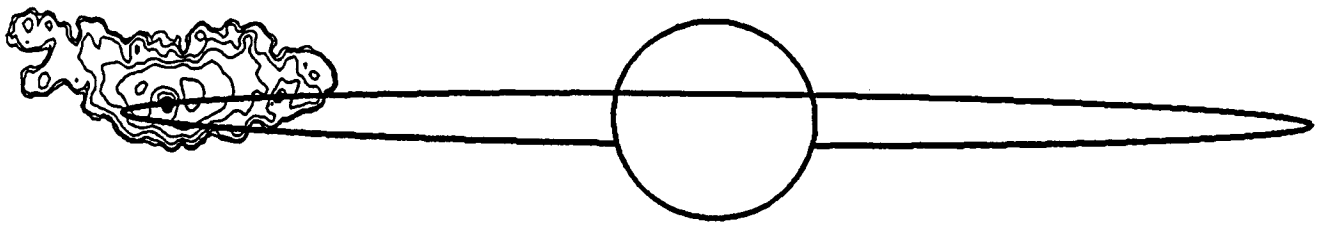

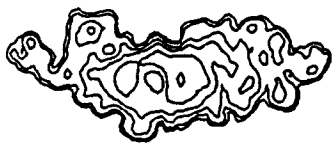

SIP415/44-46

UT Date: April 28, 1981 (3)

Average Io Phase = 113.9

Average Io Sys III = 298.5

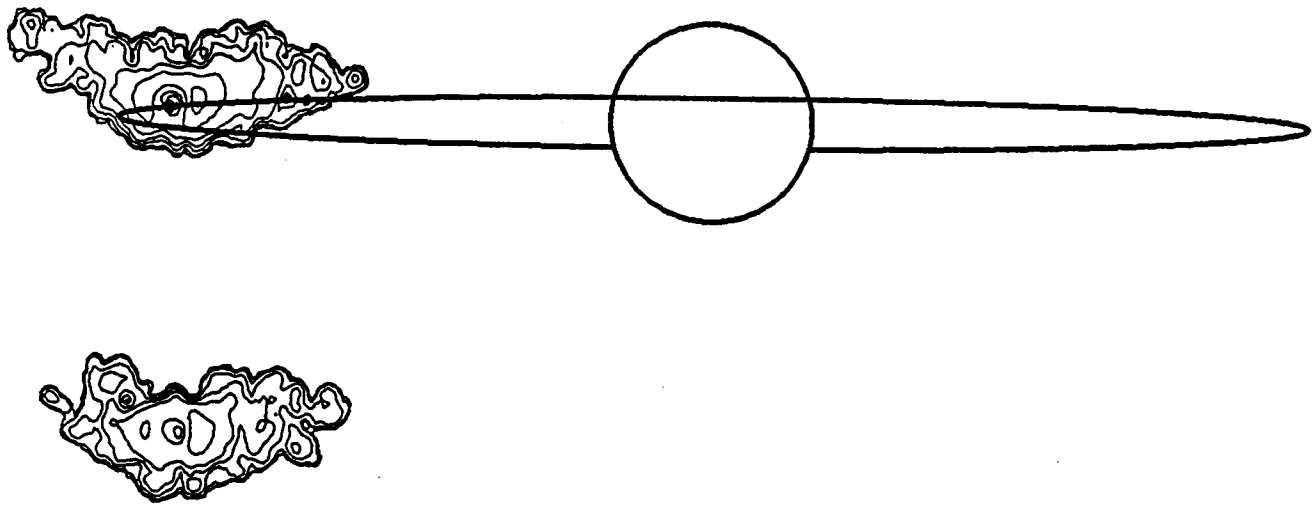

SIP416/4-6

UT Date: April 29, 1981 (1)

Average Io Phase = 285.7

Average Io Sys III = 138.5

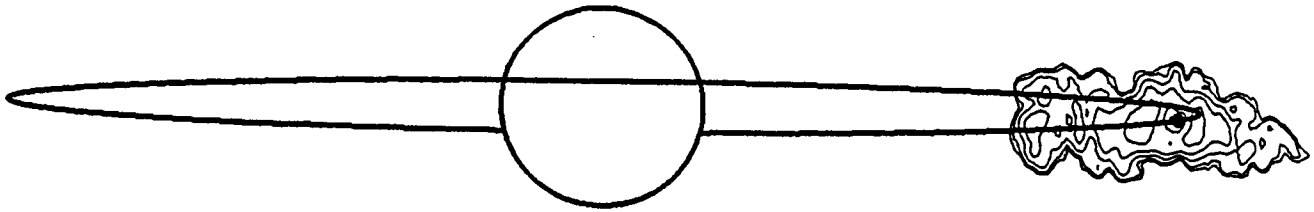

SIP416/7-9

UT DATE: APRIL 29, 1981 (2)

AVERAGE IO PHASE = 290.5

AVERAGE IO SYS III = 154.2

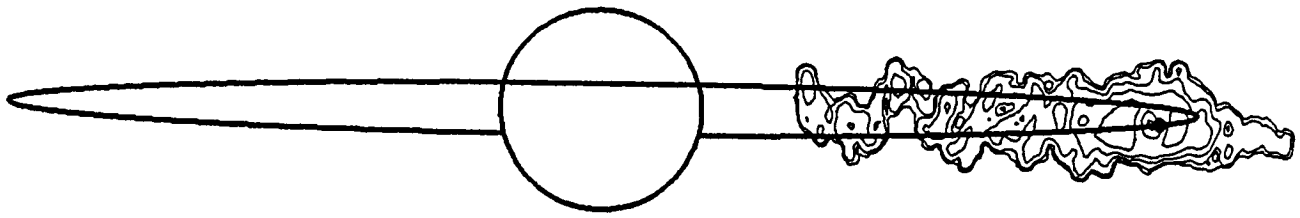

SIP417/8-10

UT DATE: MAY 4, 1981 (1)

AVERAGE IO PHASE = 219.7

AVERAGE IO SYS III = 223.1

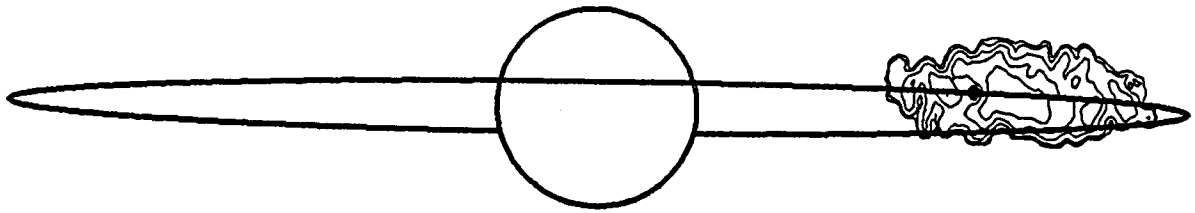

SIP417/13-15

UT DATE: MAY 4, 1981 (2)

AVERAGE IO PHASE = 227.8

AVERAGE IO SYS III = 249.2

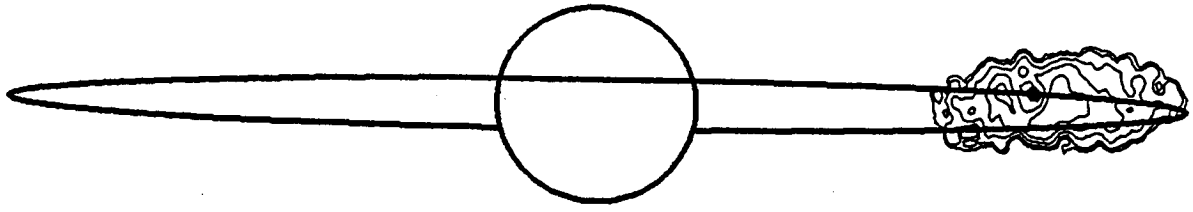

SIP417/16-18

UT Date: May 4, 1981 (3)

Average Io Phase = 233.2

Average Io Sys III = 266.8

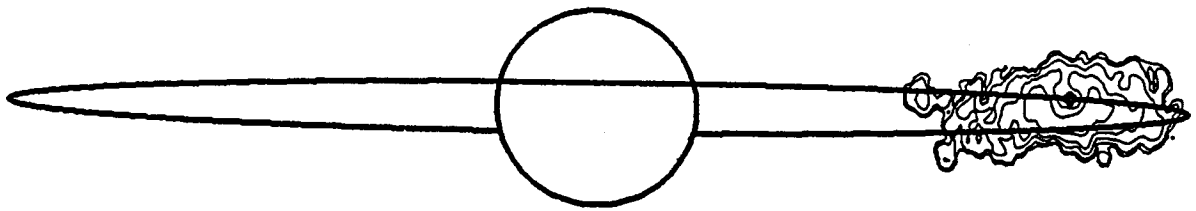

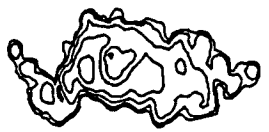

SIP417/20-22

UT Date: May 4, 1981 (4)

Average Io Phase = 240.9

Average Io Sys III = 291.7

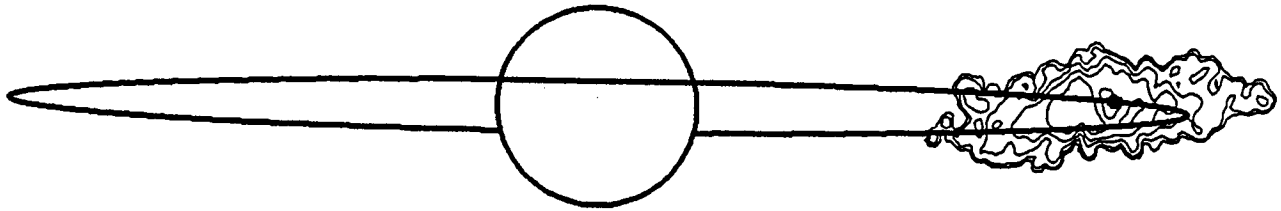

SIP417/27-29

UT Date: May 4, 1981 (5)

Average Io Phase = 253.3

Average Io Sys III = 331.9

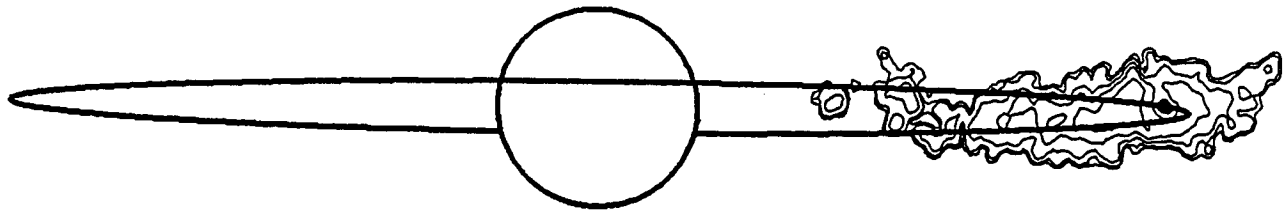

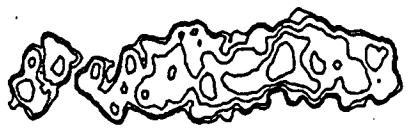

SIP417/36-39

UT Date: May 4, 1981 (6)

Average Io Phase = 269.3

Average Io Sys III = 23.9

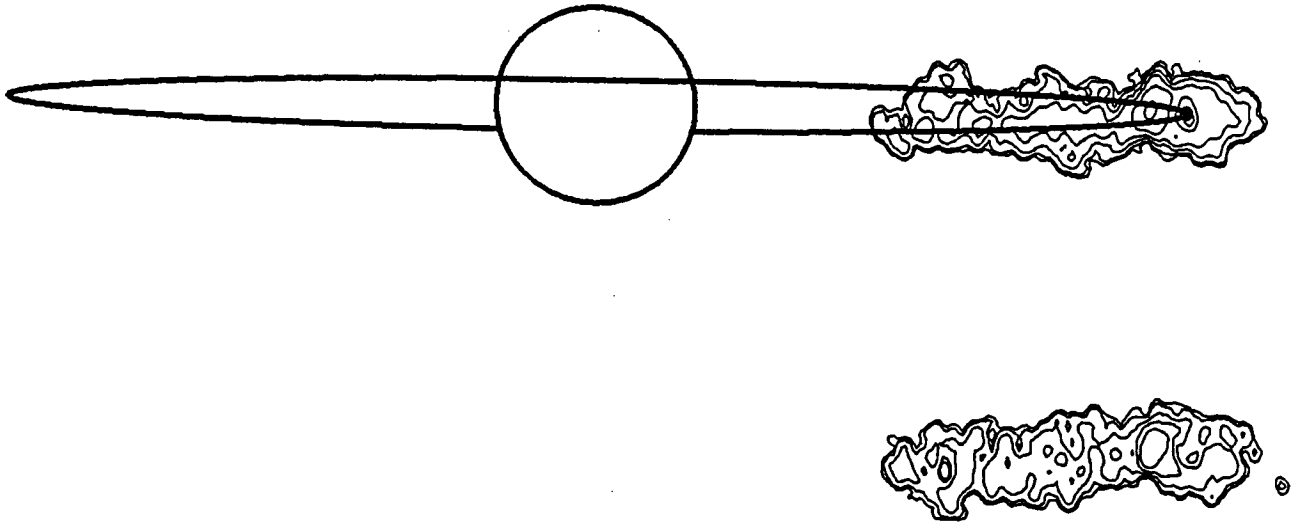

SIP418/10-12

UT DATE: MAY 5, 1981 (1)

AVERAGE IO PHASE = 68.1

AVERAGE IO SYS III = 186.1

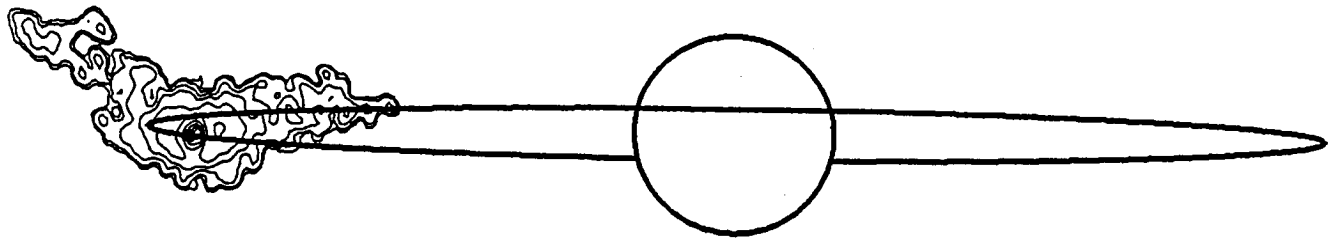

SIP418/13-16

UT DATE: MAY 5, 1981 (2)

AVERAGE IO PHASE = 73.6

AVERAGE IO SYS III = 204.2

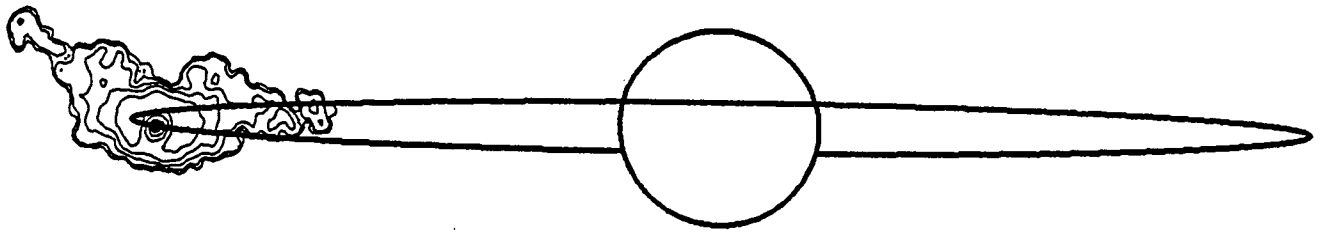

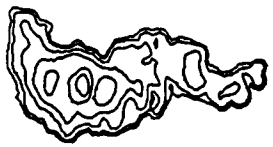

SIP418/24-26

UT Date: May 5, 1981 (3)

Average Io Phase = 90.2

Average Io Sys III = 259.3

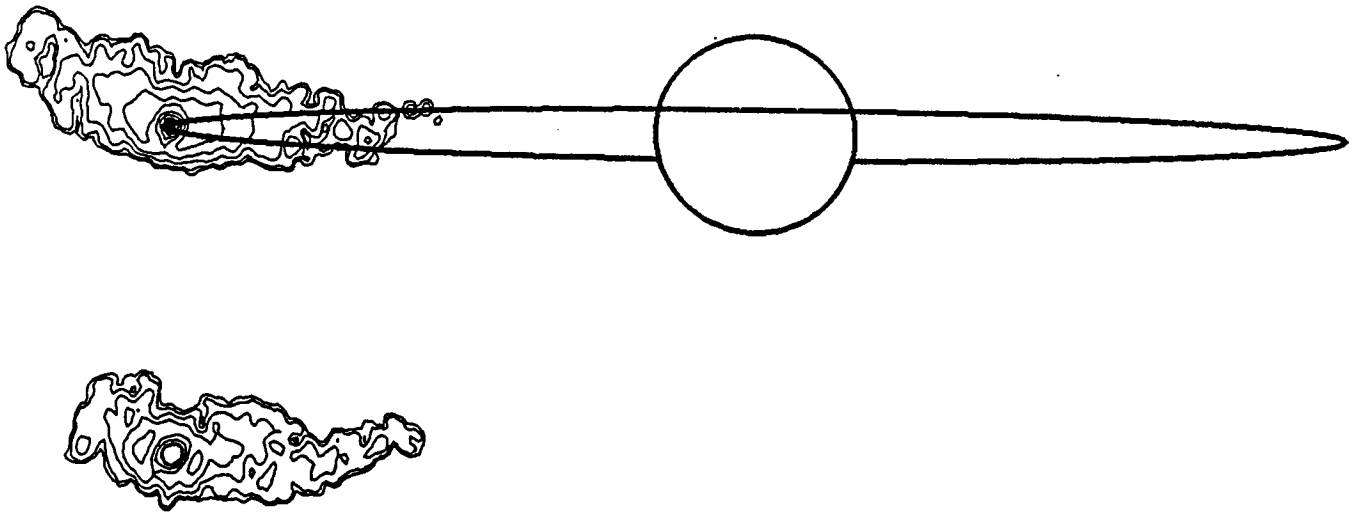

SIP418/31-33

UT Date: May 5, 1981 (4)

Average Io Phase = 102.5

Average Io Sys III = 299.6

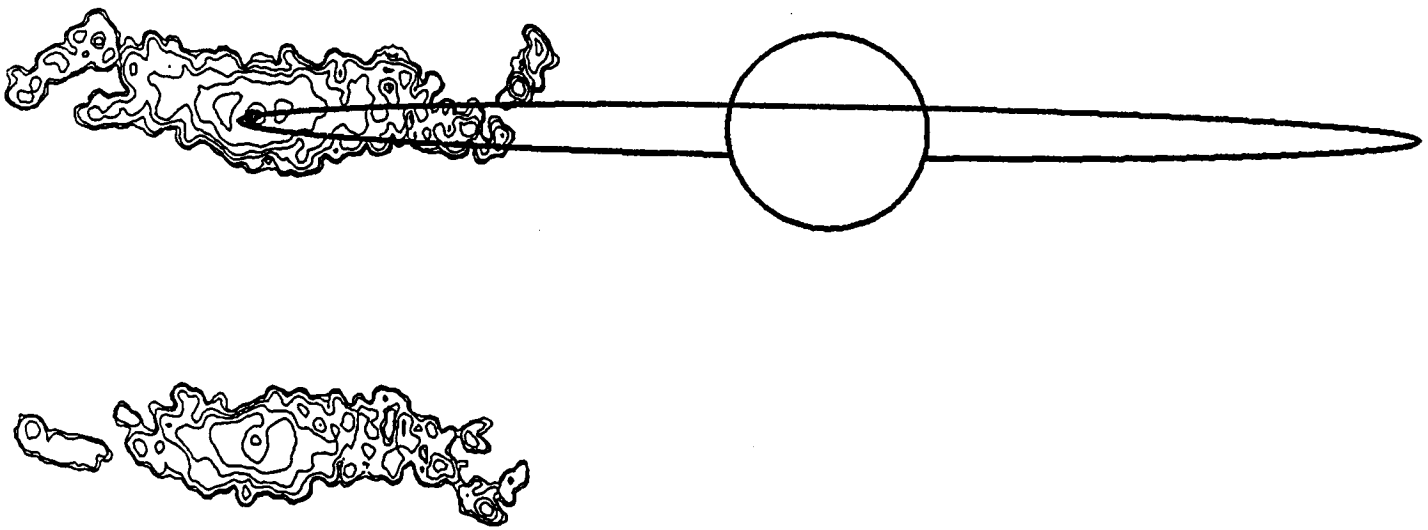

SIP419/19-21

UT DATE: MAY 6, 1981 (1)

AVERAGE IO PHASE = 286.1

AVERAGE IO SYS III = 178.3

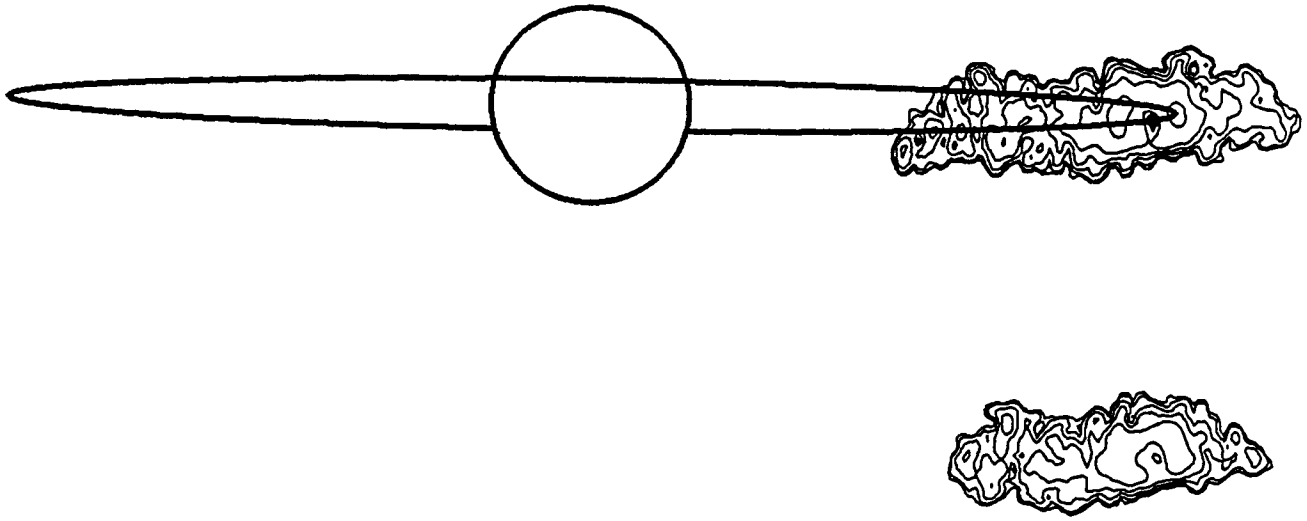

SIP419/22-24

UT DATE: MAY 6, 1981 (2)

AVERAGE IO PHASE = 290.9

AVERAGE IO SYS III = 194.0

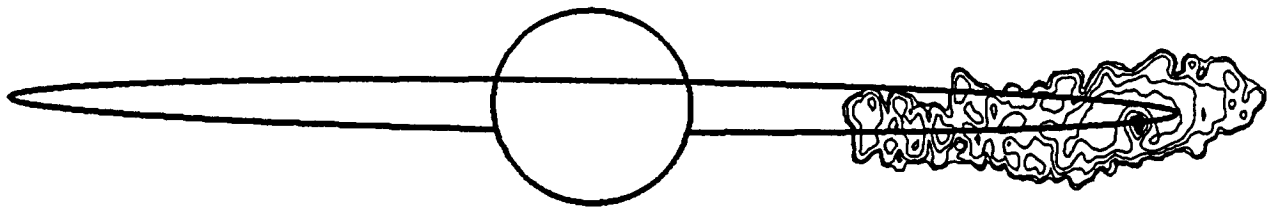

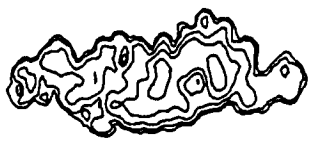

SIP420/6-8

UT DATE: MAY 12, 1981 (1)

AVERAGE IO PHASE = 48.3

AVERAGE IO SYS III = 159.8

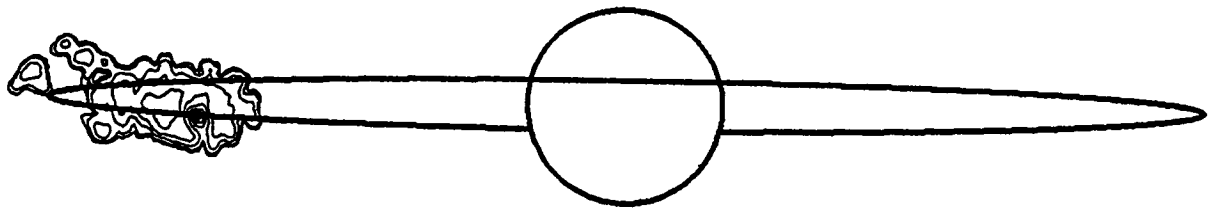

SIP420/10-12

UT DATE: MAY 12, 1981 (2)

AVERAGE IO PHASE = 54.5

AVERAGE IO SYS III = 180.0

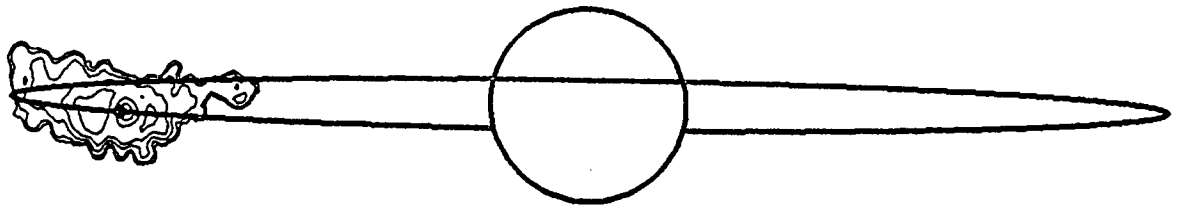

SIP420/15-20

UT DATE: MAY 12, 1981 (3)

AVERAGE IO PHASE = 65.8

AVERAGE IO SYS III = 217.8

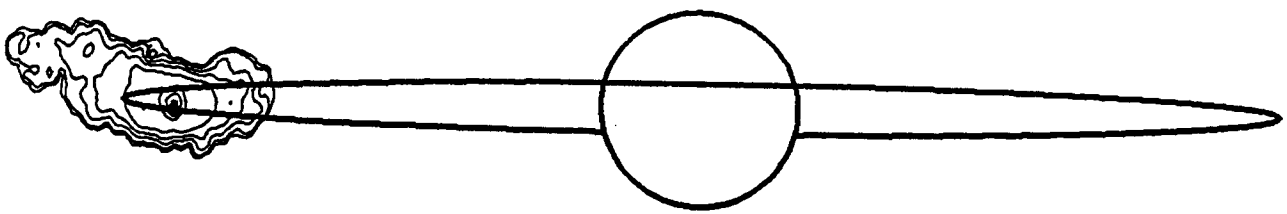

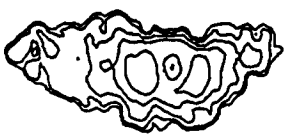

SIP420/21-23

UT DATE: MAY 12, 1981 (4)

AVERAGE IO PHASE = 74.7

AVERAGE IO SYS III = 247.1

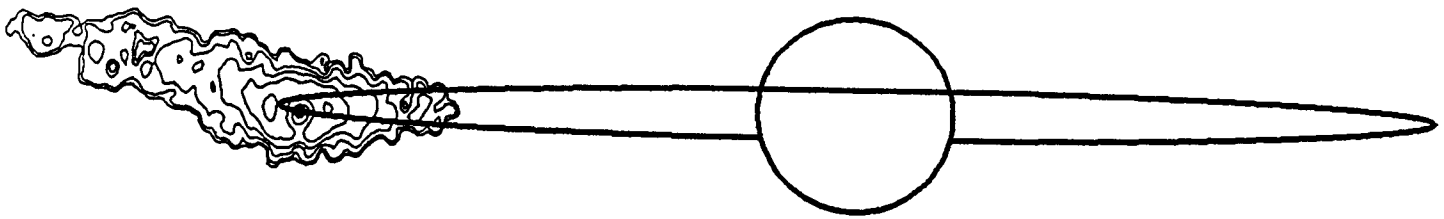

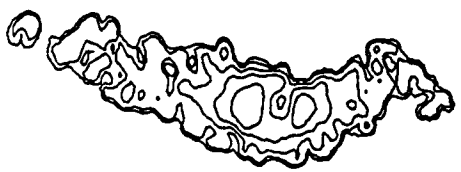

SIP420/30-32

UT DATE: MAY 12, 1981 (5)

AVERAGE IO PHASE = 91.2

AVERAGE IO SYS III = 301.8

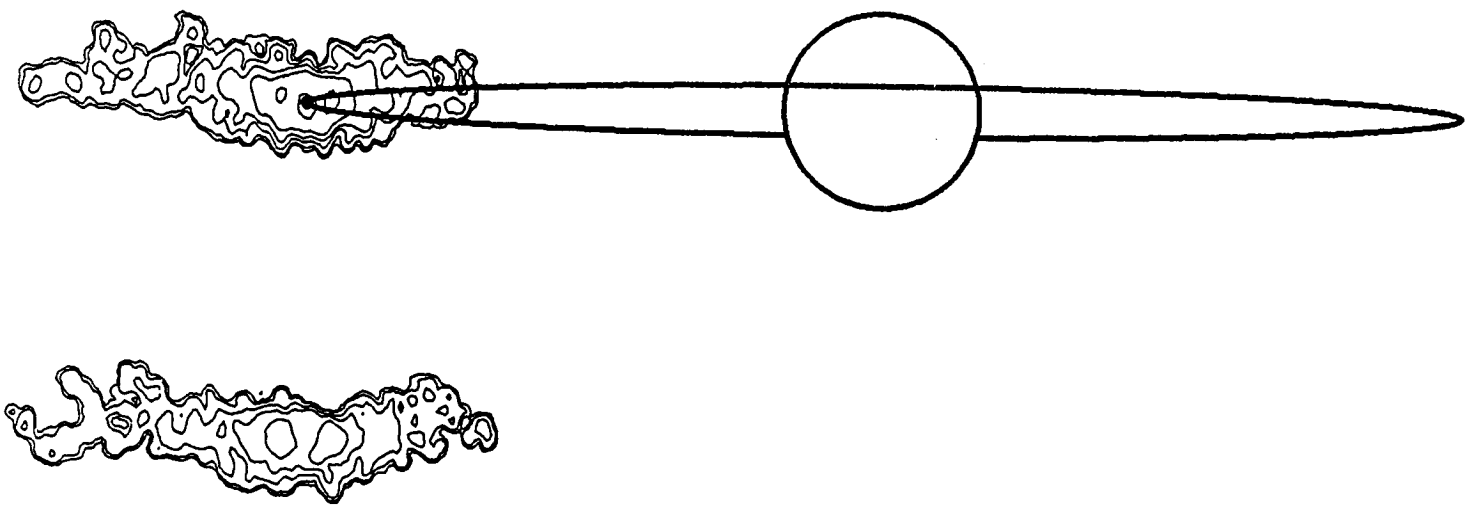

SIP421/21-23

UT DATE: MAY 13, 1981 (1)

AVERAGE IO PHASE = 252.6

AVERAGE IO SYS III = 108.4

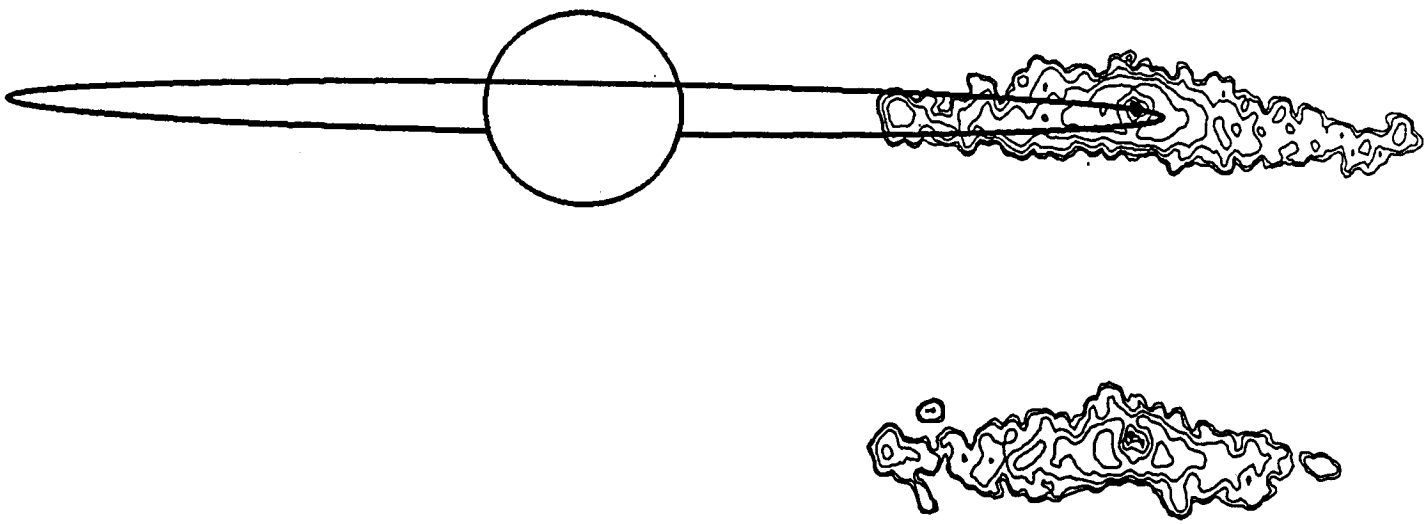

SIP421/27-28

UT DATE: MAY 13, 1981 (2)

AVERAGE IO PHASE = 262.3

AVERAGE IO SYS III = 139.8

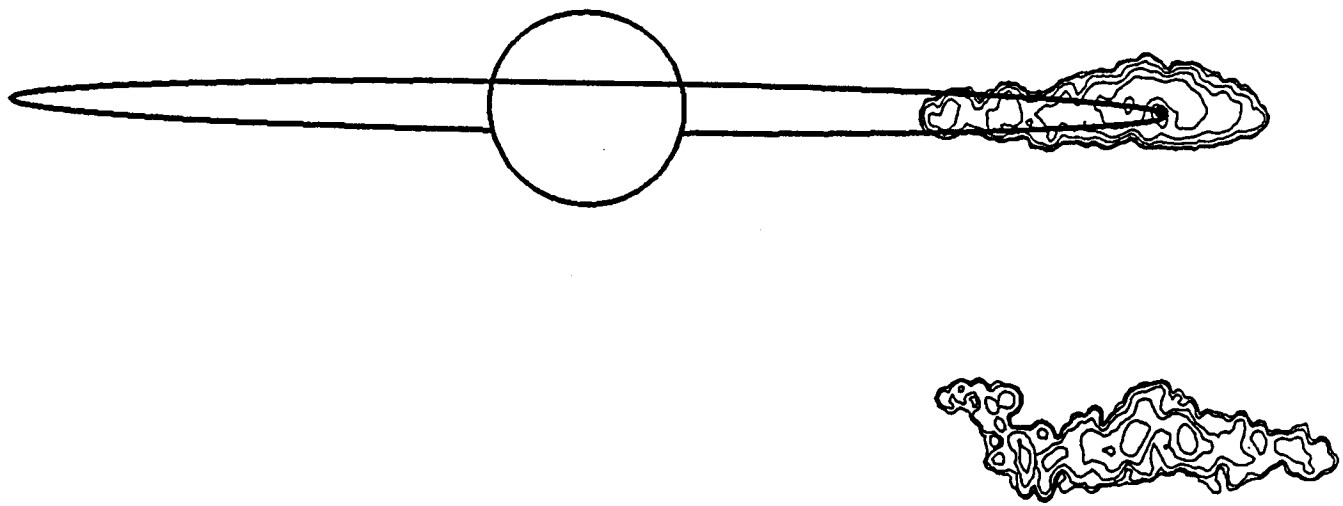

SIP421/32-33

UT Date: May 13, 1981 (3)

Average Io Phase = 270.9

Average Io Sys III = 168.0

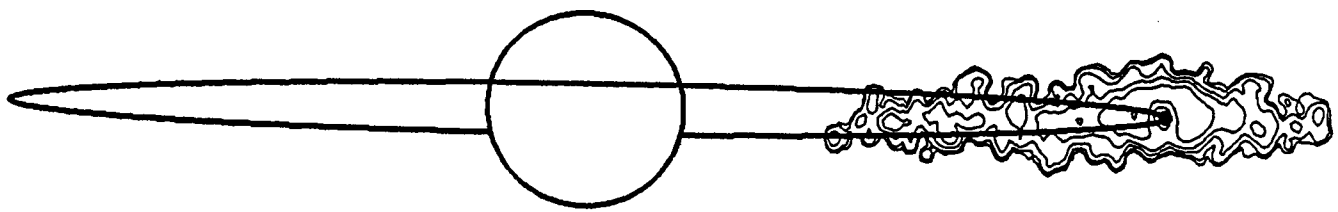

SIP421/34-36

UT DATE: MAY 13, 1981 (4)

AVERAGE IO PHASE = 275.7

AVERAGE IO SYS III = 183.5

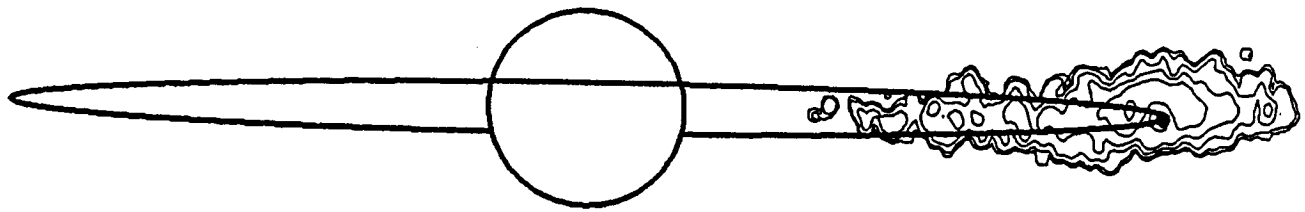

SIP421/37-39

UT DATE: MAY 13, 1981 (5)

AVERAGE IO PHASE = 281.1

AVERAGE IO SYS III = 201.1

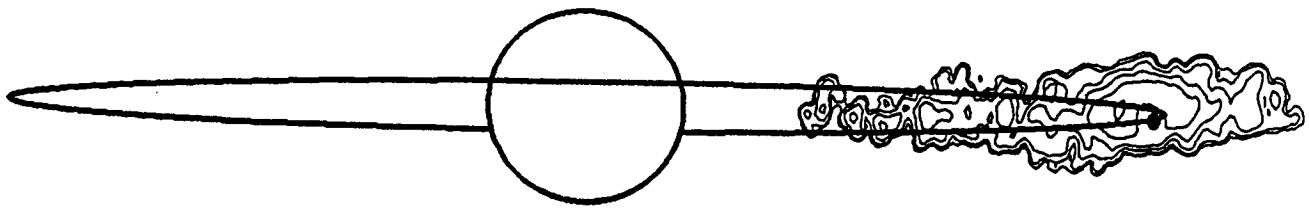

SIP421/40-42

UT DATE: MAY 13, 1981 (6)

AVERAGE IO PHASE = 286.2

AVERAGE IO SYS III = 217.5

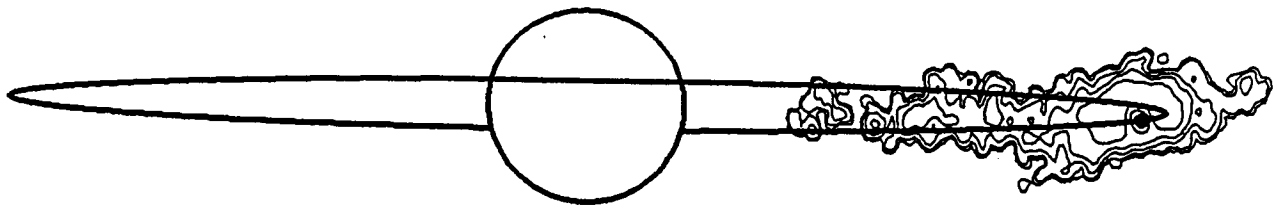

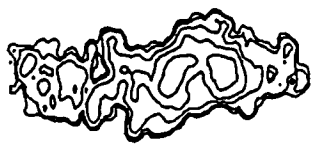

SIP421/43-45

UT Date: May 13, 1981 (7)

Average Io Phase = 291.2

Average Io Sys III = 234.1

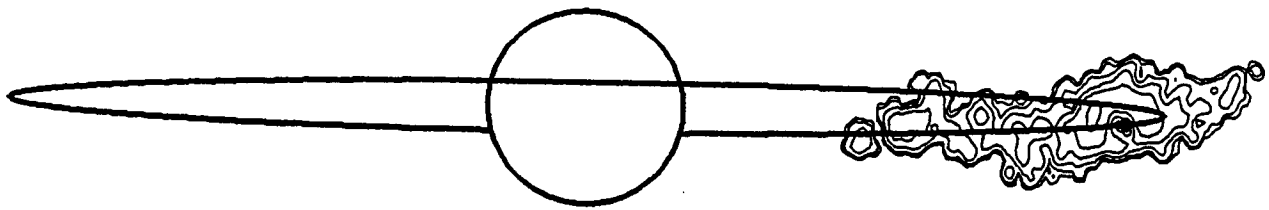

SIP421/45-47

UT DATE: MAY 13, 1981 (8)

AVERAGE IO PHASE = 294.8

AVERAGE IO SYS III = 245.7

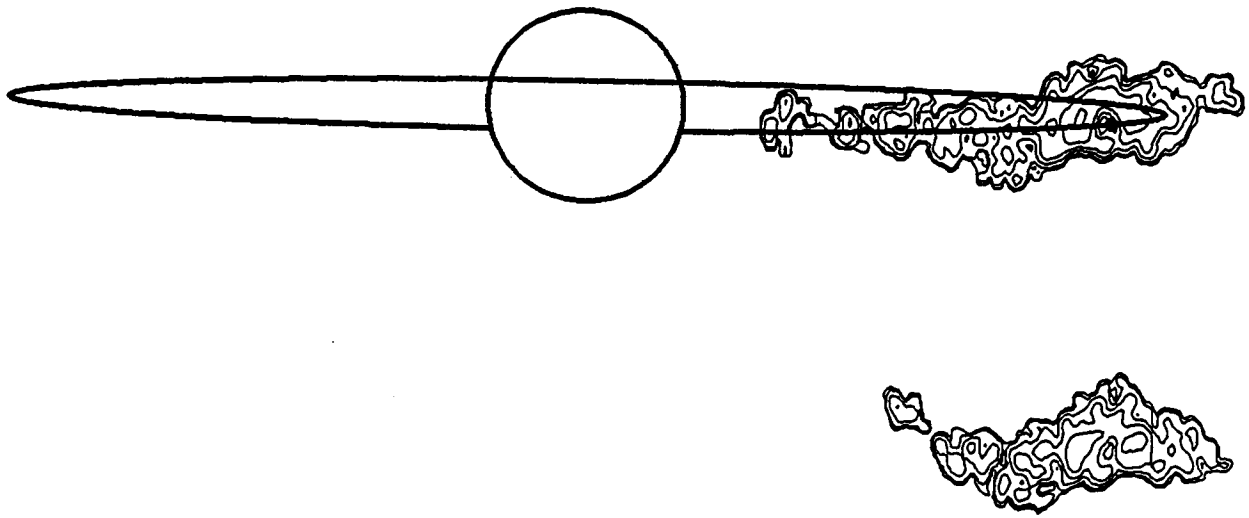

SIP424/10-12

UT DATE: JUNE 6, 1981 (1)

AVERAGE IO PHASE = 102.6

AVERAGE IO SYS III = 300.3

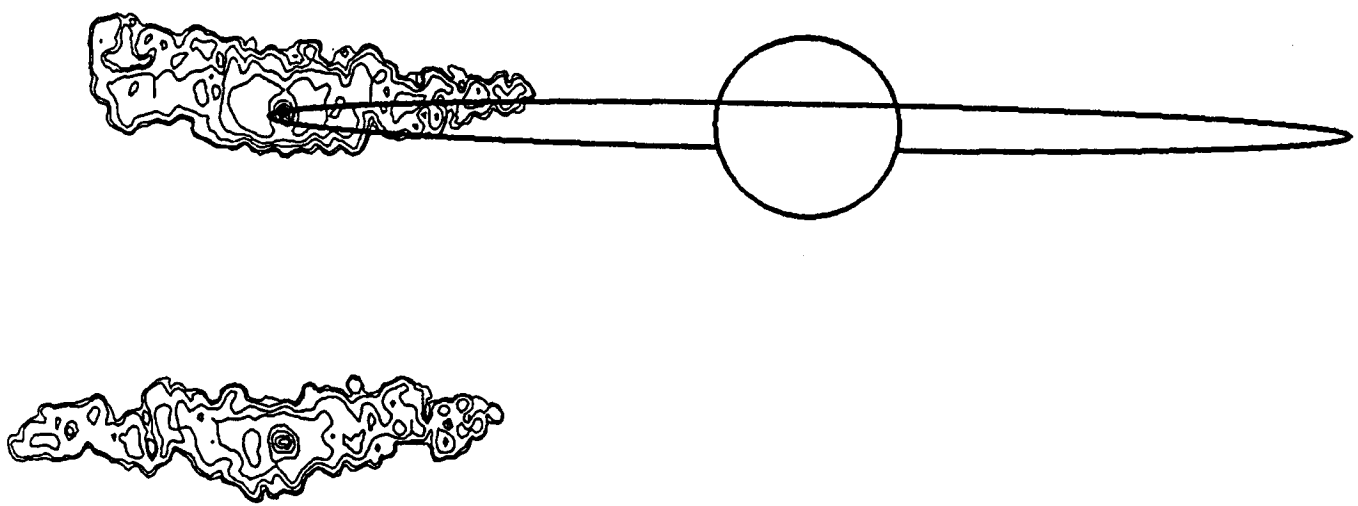

SIP425/6-9

UT DATE: JUNE 14, 1981 (1)

AVERAGE IO PHASE = 286.9

AVERAGE IO SYS III = 222.1

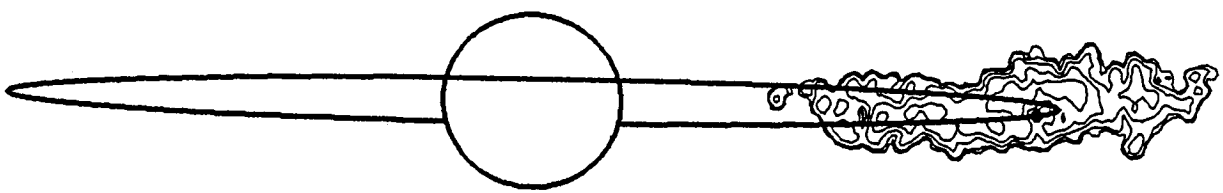

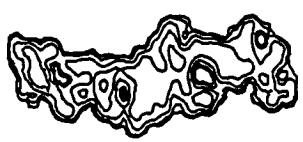

SIP425/9-12

UT DATE: JUNE 14, 1981 (2)

AVERAGE IO PHASE = 291.6

AVERAGE IO SYS III = 237.6

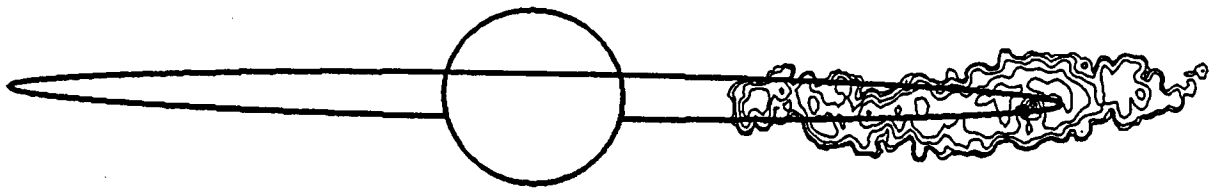

Appendix II

Fully Reduced 1981 Sodium Cloud Images: Study 2

Appendix II

1981 Region B/C Images with Recurrence of Io Geocentric Phase and Io System III Longitude Angles

UT Date	Image ID Number (Tape/Frames)	Mid-Point Condition: Io Phase Angle (deg)	Mid-Point Condition: Io System III Longitude (deg)	Image Set
5 May (4)	SIP 418/31-33	102.5	299.6	2.A
6 June (1)	SIP 424/10-12	102.6	300.3	2.A
13 May (6)	SIP 421/40-42	286.2	217.5	2.B
14 June (1)	SIP 425/6-9	286.9	222.1	2.B
13 May (7)	SIP 421/43-45	291.2	234.1	2.C
14 June (2)	SIP 425/9-12	291.6	237.6	2.C

Image Set: 2A

SIP418/31-33

UT DATE: MAY 5, 1981 (4)

AVERAGE IO PHASE = 102.5

AVERAGE IO SYS III = 299.6

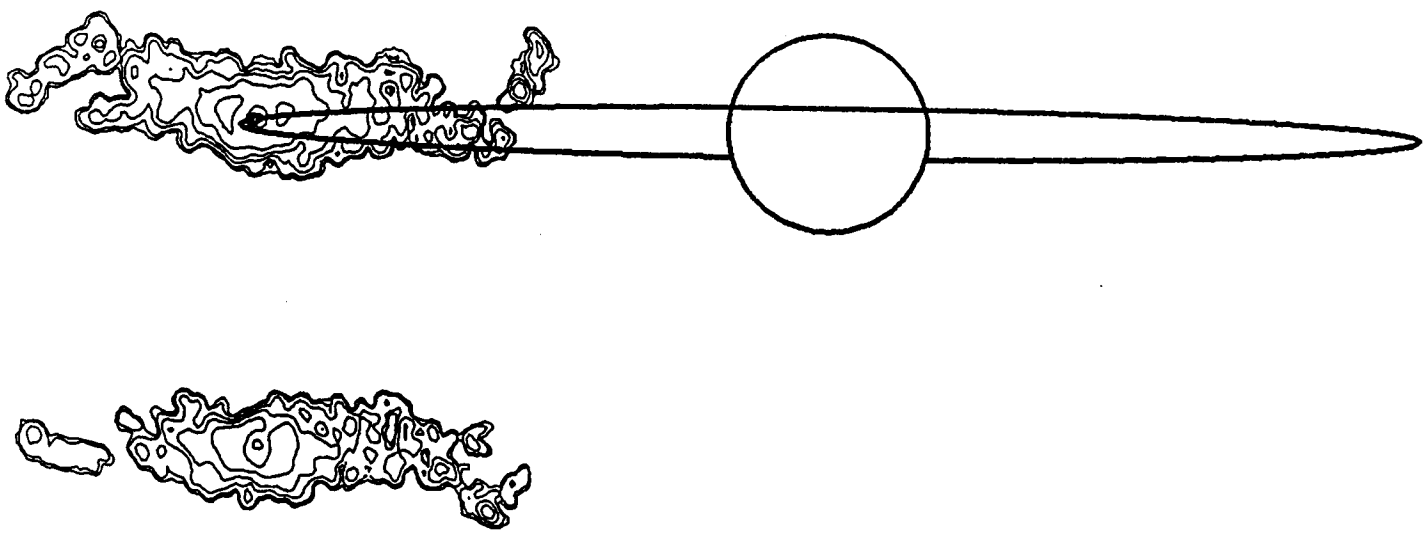

Image Set: 2A

SIP424/10-12

UT DATE: JUNE 6, 1981 (1)

AVERAGE IO PHASE = 102.6

AVERAGE IO SYS III = 300.3

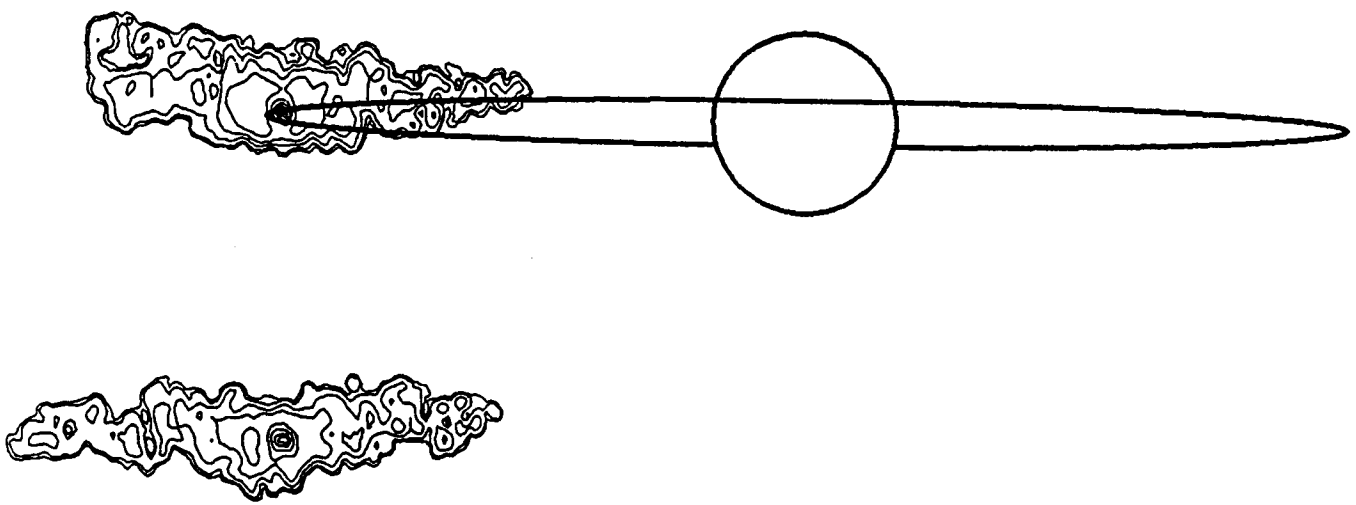

Image Set: 2B

SIP421/40-42

UT DATE: MAY 13, 1981 (6)

AVERAGE IO PHASE = 286.2

AVERAGE IO SYS III = 217.5

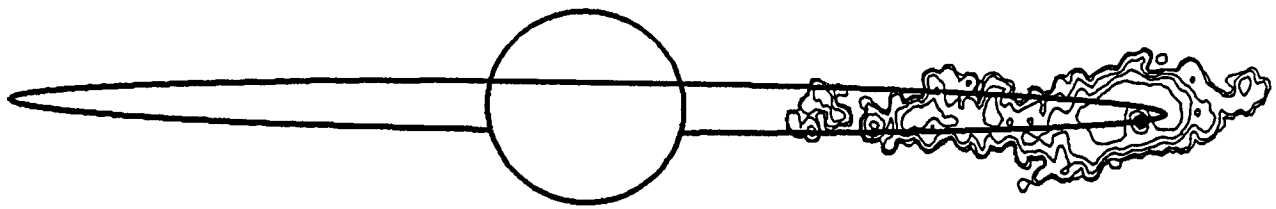

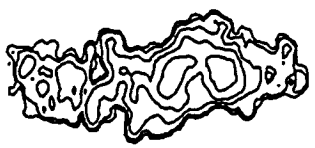

Image Set: 2B

SIP425/6-9

UT DATE: JUNE 14, 1981 (1)

AVERAGE IO PHASE = 286.9

AVERAGE IO SYS III = 222.1

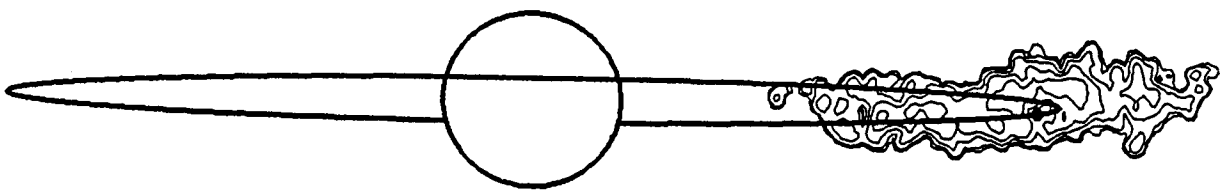

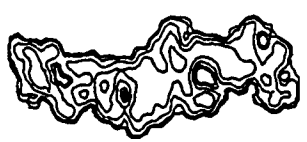

Image Set: 2C

SIP421/43-45
UT DATE: MAY 13, 1981 (7)

AVERAGE Io PHASE = 291.2
AVERAGE Io SYS III = 234.1

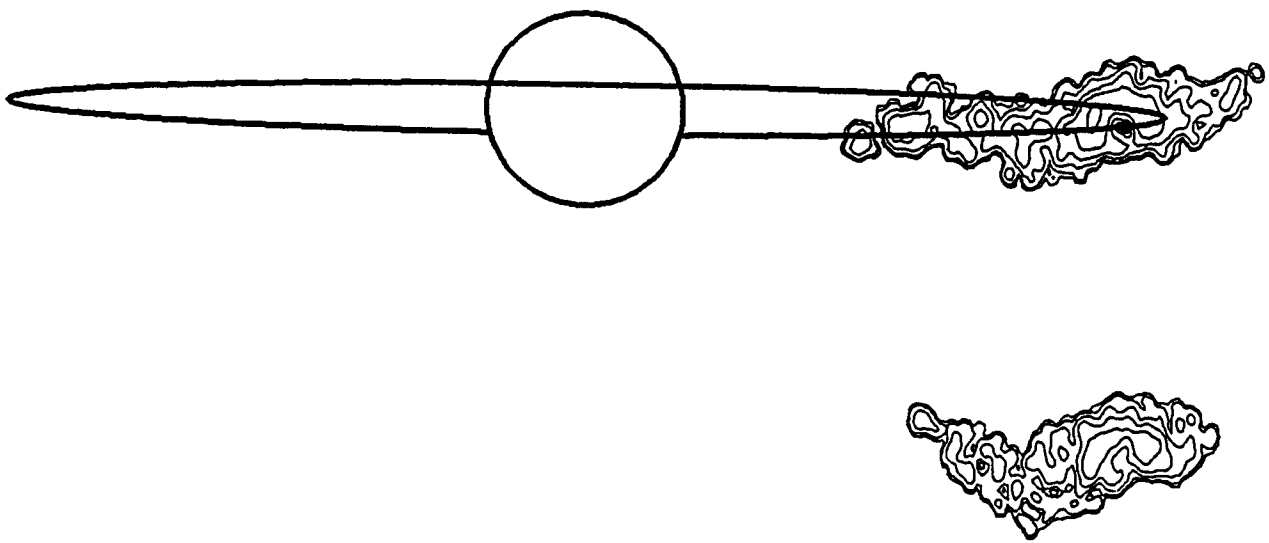

Image Set: 2C

SIP425/9-12

UT DATE: JUNE 14, 1981 (2)

AVERAGE IO PHASE = 291.6

AVERAGE IO SYS III = 237.6

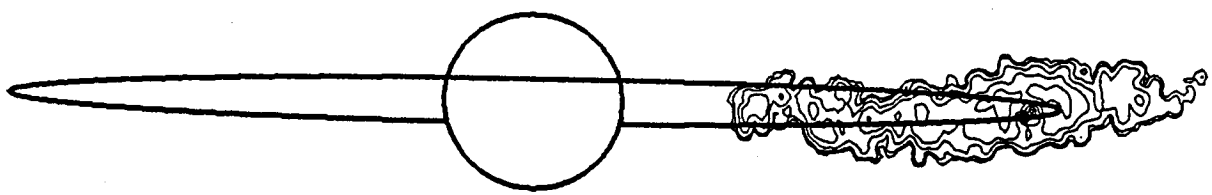

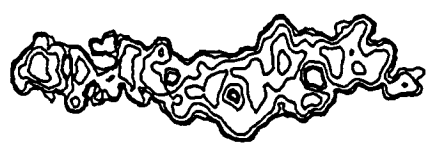

Appendix III

Fully Reduced 1981 Sodium Cloud Images: Study 3

Appendix III

1981 Region B/C Images:
Comparison for Diametrically Opposite Io Phase Angles

UT Date	Image ID Number (Tape/Frames)	Mid-Point Condition: East Io Phase Angle (deg)	Mid-Point Condition: East Io Phase + 180° (deg)	Mid-Point Condition: West Io Phase Angle (deg)	Mid-Point Condition: Io System III Longitude (deg)	Image Set
12 May (1)	SIP 420/6-8	48.3	228.3	-	159.8	3.A
4 May (2)	SIP 417/13-15	-	-	227.8	249.2	3.A
12 May (2)	SIP 420/10-12	54.4	234.4	-	180.0	3.B
4 May (3)	SIP 417/16-18	-	-	233.2	266.8	3.B
5 May (1)	SIP 418/10-12	68.1	248.1	-	186.1	3.C
12 May (3)	SIP 420/15-20	65.8	245.8	-	217.8	3.C
4 May (4)	SIP 417/20-22	-	-	240.9	291.7	3.C
4 May (5)	SIP 417/27-29	-	-	253.3	331.9	3.C
5 May (2)	SIP 418/13-16	73.6	253.6	-	204.2	3.D
12 May (4)	SIP 420/21-23	74.7	254.7	-	247.1	3.D
13 May (1)	SIP 421/21-23	-	-	252.6	108.4	3.D
4 May (5)	SIP 417/27-29	-	-	353.3	331.9	3.D
28 Apr (1)	SIP 415/27-29	90.5	270.5	-	221.3	3.E
5 May (3)	SIP 418/24-26	90.2	270.2	-	259.3	3.E
12 May (5)	SIP 420/30-32	91.2	271.2	-	301.8	3.E
4 May (6)	SIP 417/36-39	-	-	269.3	23.9	3.E
13 May (3)	SIP 421/32-33	-	-	270.9	168.0	3.E
13 May (4)	SIP 421/34-36	-	-	275.7	183.5	3.E
5 May (4)	SIP 418/31-33	102.5	282.5	-	299.6	3.F
6 Jun (1)	SIP 424/10-12	102.6	282.6	-	300.3	3.F
29 Apr (1)	SIP 416/4-6	-	-	285.7	138.5	3.F
6 May (1)	SIP 419/19-21	-	-	286.1	178.3	3.F
13 May (6)	SIP 421/40-42	-	-	286.2	217.5	3.F
14 Jun (1)	SIP 425/6-9	-	-	286.9	222.1	3.F
28 Apr (2)	SIP 415/43-45	112.4	292.4	-	293.9	3.G
28 Apr (3)	SIP 415/44-46	113.9	293.9	-	298.5	3.G
6 May (2)	SIP 419/22-24	-	-	290.9	194.0	3.G
13 May (8)	SIP 421/45-47	-	-	294.8	245.7	3.G
6 Apr (1)	SIP 410/13-15	-	-	293.7	311.5	3.G

48.3° (228.3°)
Image Set: 3.A

SIP420/6-8

UT DATE: MAY 12, 1981 (1)

AVERAGE IO PHASE = 48.3

AVERAGE IO SYS III = 159.8

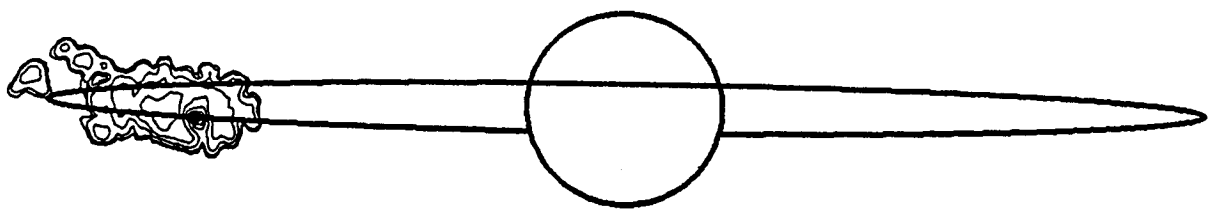

227.8°
Image Set: 3.A

SIP417/13-15
UT DATE: MAY 4, 1981 (2)

AVERAGE IO PHASE = 227.8
AVERAGE IO SYS III = 249.2

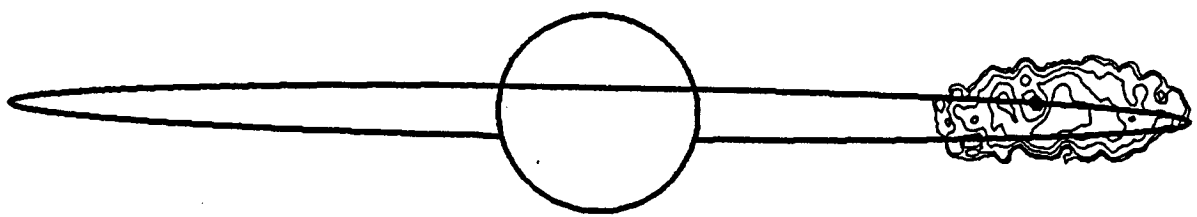

54.4° (234.4°)
Image Set: 3.B

SIP420/10-12
UT DATE: MAY 12, 1981 (2)

AVERAGE Io PHASE = 54.5
AVERAGE Io SYS III = 180.0

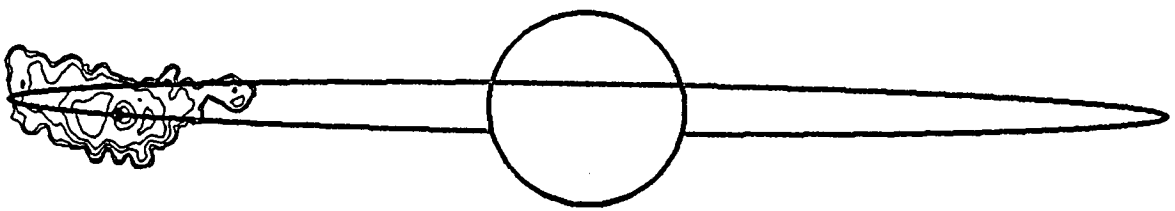

233.2°
Image Set: 3.B

SIP417/16-18
UT DATE: MAY 4, 1981 (3)

AVERAGE IO PHASE = 233.2
AVERAGE IO SYS III = 266.8

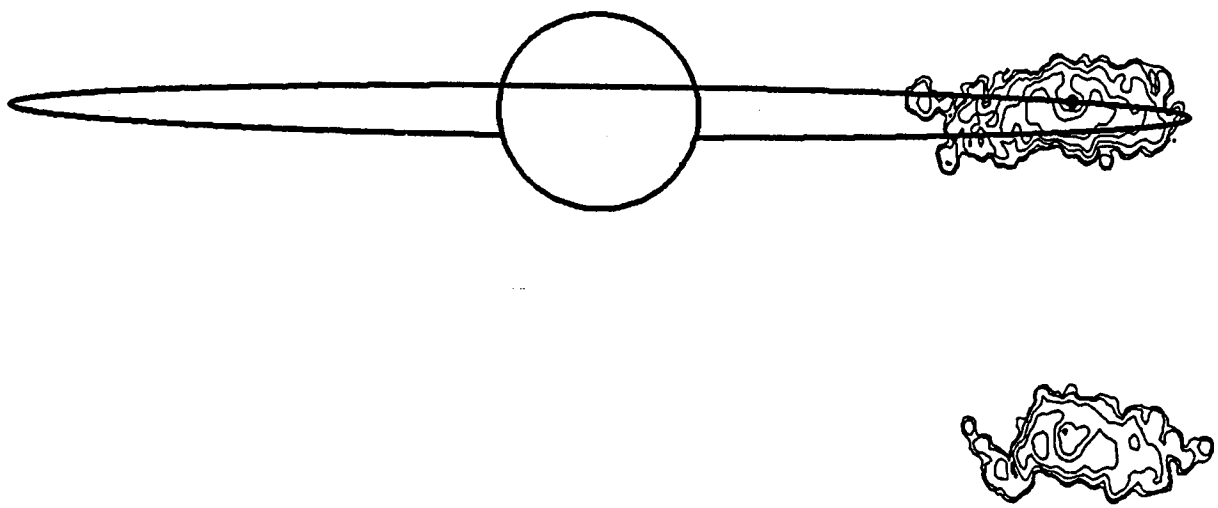

68.1° (248.1°)
Image Set: 3.C

SIP418/10-12
UT DATE: MAY 5, 1981 (1)

AVERAGE IO PHASE = 68.1
AVERAGE IO SYS III = 186.1

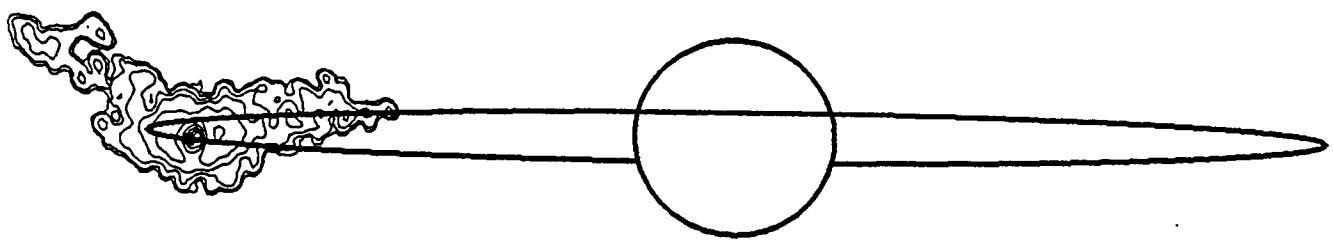

65.8° (245.8°)
Image Set: 3.C

SIP420/15-20

UT DATE: MAY 12, 1981 (3)

AVERAGE IO PHASE = 65.8

AVERAGE IO SYS III = 217.8

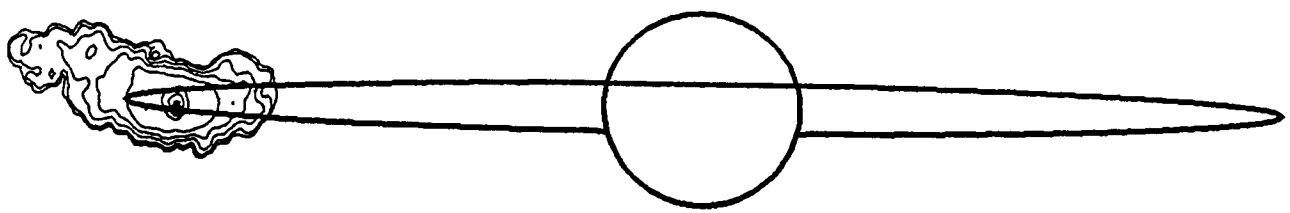

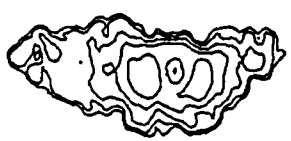

240.9°
Image Set: 3.C

SIP417/20-22

UT DATE: MAY 4, 1981 (4)

AVERAGE IO PHASE = 240.9

AVERAGE IO SYS III = 291.7

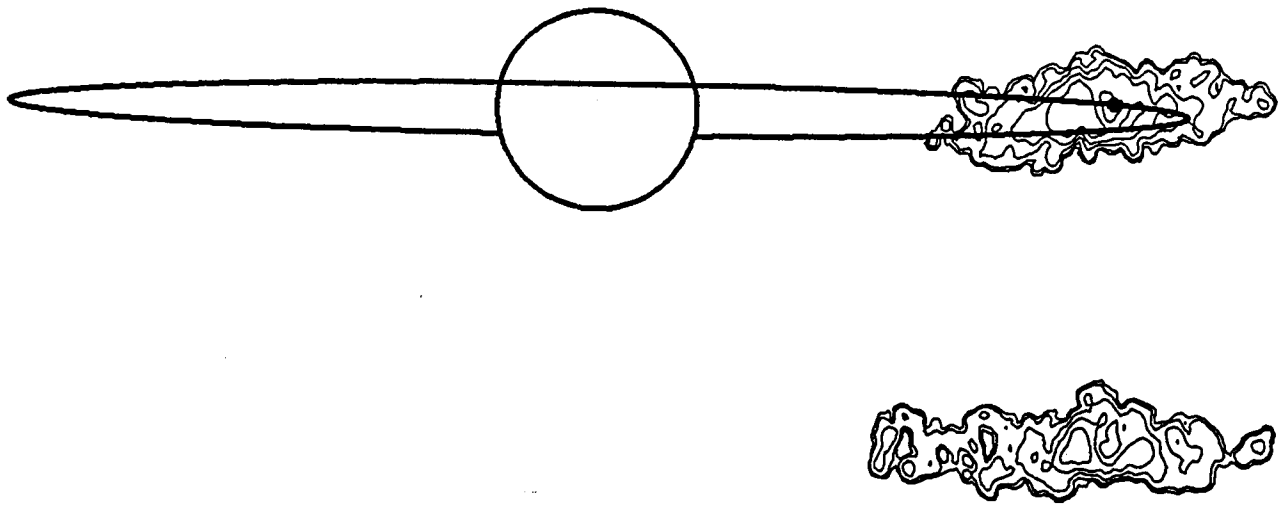

253.3°
Image Set: 3.C

SIP417/27-29
UT DATE: MAY 4, 1981 (5)

AVERAGE IO PHASE = 253.3
AVERAGE IO SYS III = 331.9

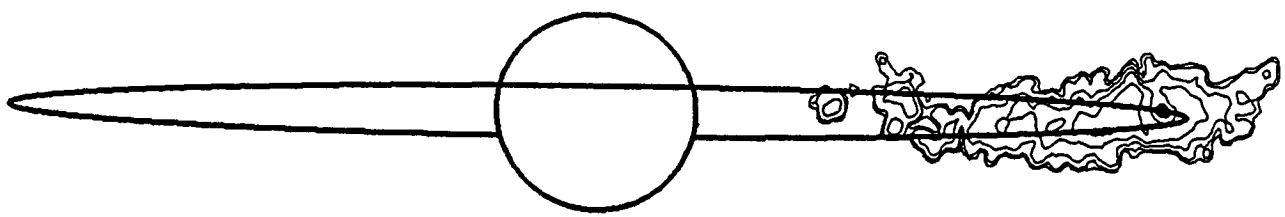

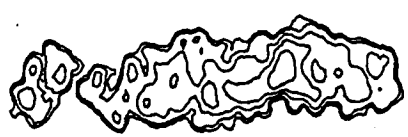

73.6° (253.6°)
Image Set: 3.D

SIP418/13-16
UT DATE: MAY 5, 1981 (2)

AVERAGE IO PHASE = 73.6
AVERAGE IO SYS III = 204.2

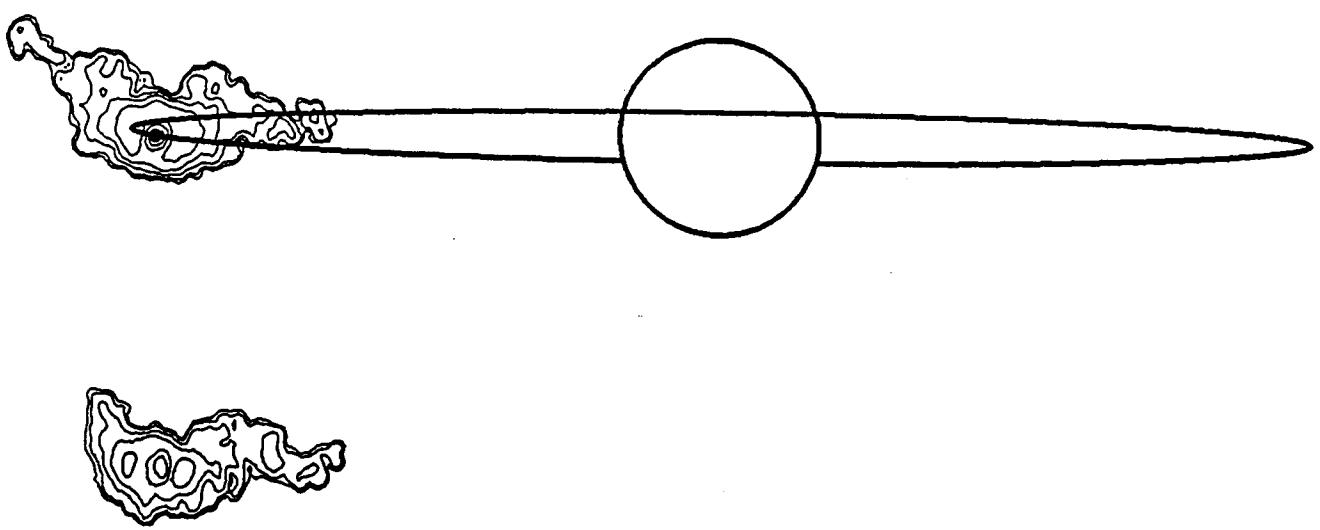

74.7 (254.7°)
Image Set: 3.D

SIP420/21-23

UT DATE: MAY 12, 1981 (4)

AVERAGE IO PHASE = 74.7

AVERAGE IO SYS III = 247.1

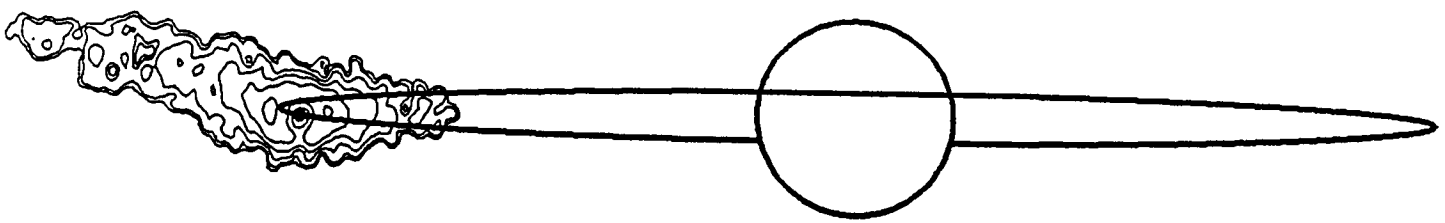

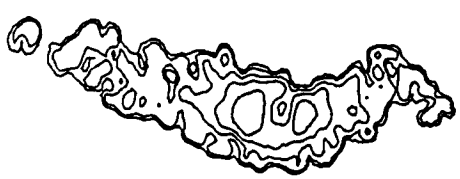

252.6°
Image Set: 3.D

SIP421/21-23
UT DATE: MAY 13, 1981 (1)

AVERAGE IO PHASE = 252.6
AVERAGE IO SYS III = 108.4

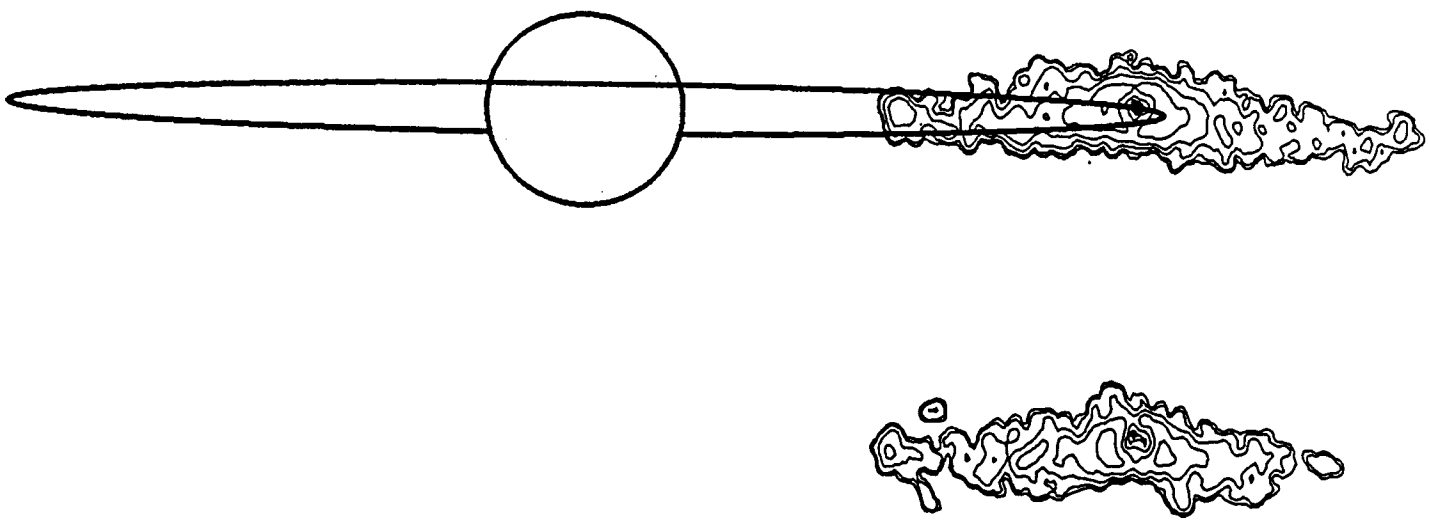

253.3°
Image Set: 3.D

SIP417/27-29

UT DATE: MAY 4, 1981 (5)

AVERAGE IO PHASE = 253.3

AVERAGE IO SYS III = 331.9

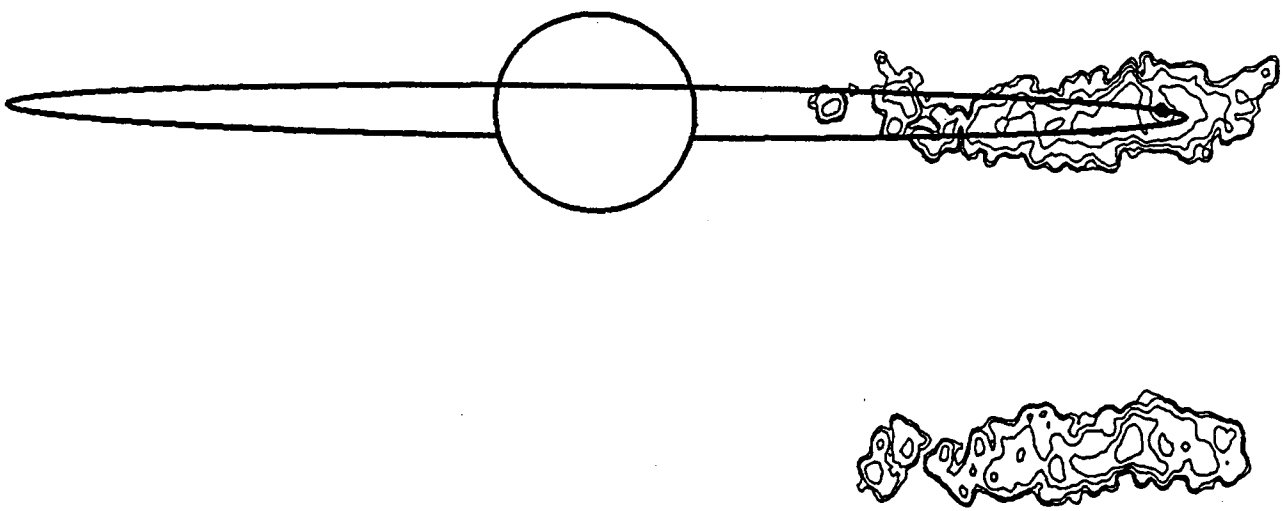

90.5° (270.5°)
Image Set: 3.E

SIP415/27-29

UT DATE: APRIL 28, 1981 (1)

AVERAGE IO PHASE = 90.5

AVERAGE IO SYS III = 221.3

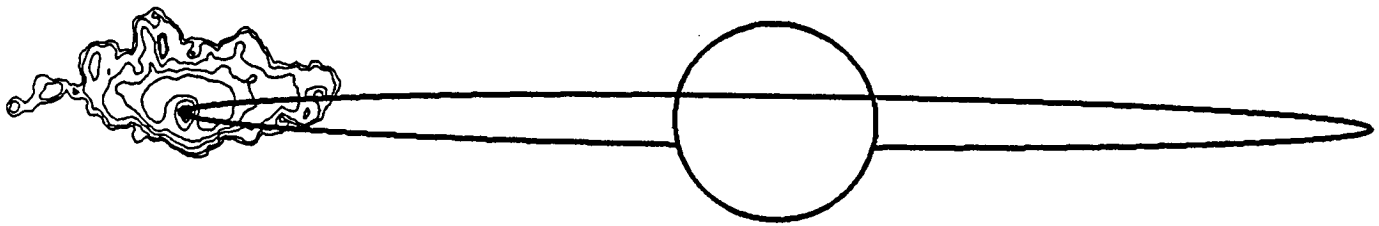

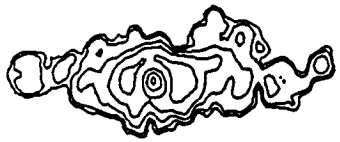

90.2° (270.2°)
Image Set: 3.E

SIP418/24-26

UT DATE: MAY 5, 1981 (3)

AVERAGE IO PHASE = 90.2

AVERAGE IO SYS III = 259.3

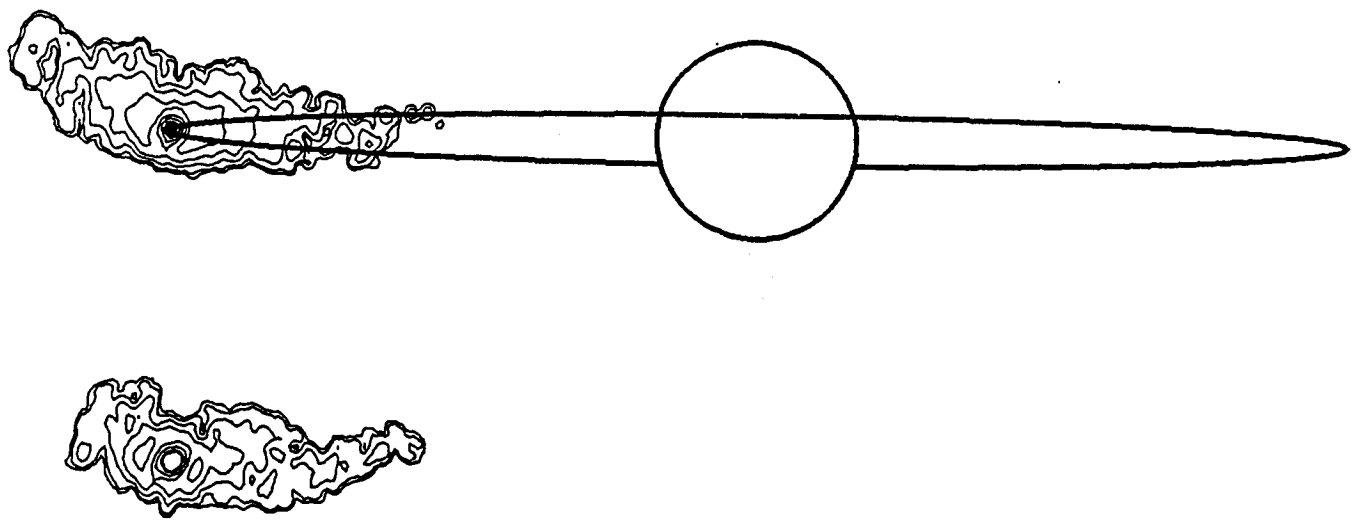

91.2° (271.2)
Image Set: 3.E

SIP420/30-32
UT DATE: MAY 12, 1981 (5)

AVERAGE IO PHASE = 91.2
AVERAGE IO SYS III = 301.8

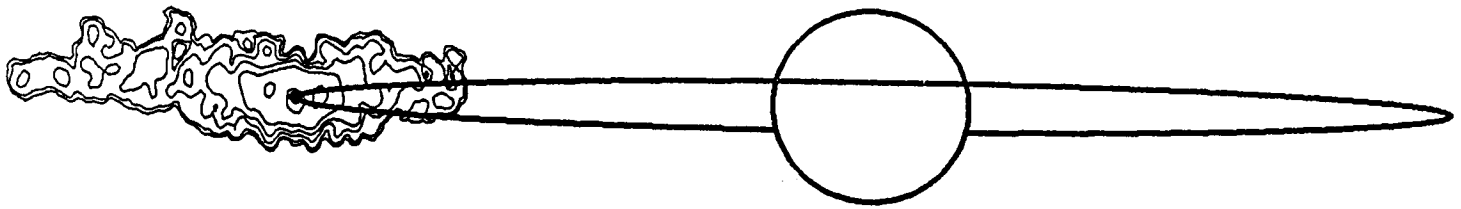

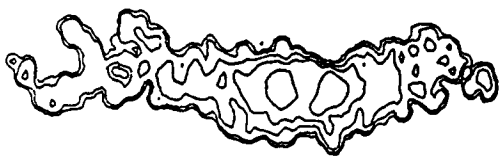

269.3°
Image Set: 3.E

SIP417/36-39
UT DATE: MAY 4, 1981 (6)

AVERAGE IO PHASE = 269.3
AVERAGE IO SYS III = 23.9

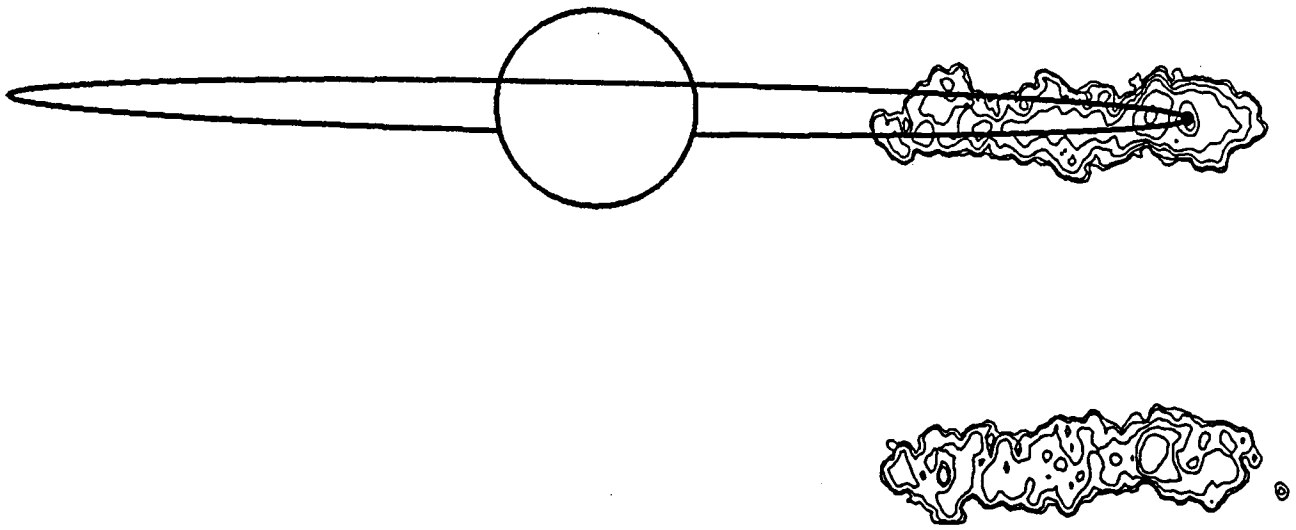

270.9°
Image Set: 3.E

SIP421/32-33
UT DATE: MAY 13, 1981 (3)

AVERAGE IO PHASE = 270.9
AVERAGE IO SYS III = 168.0

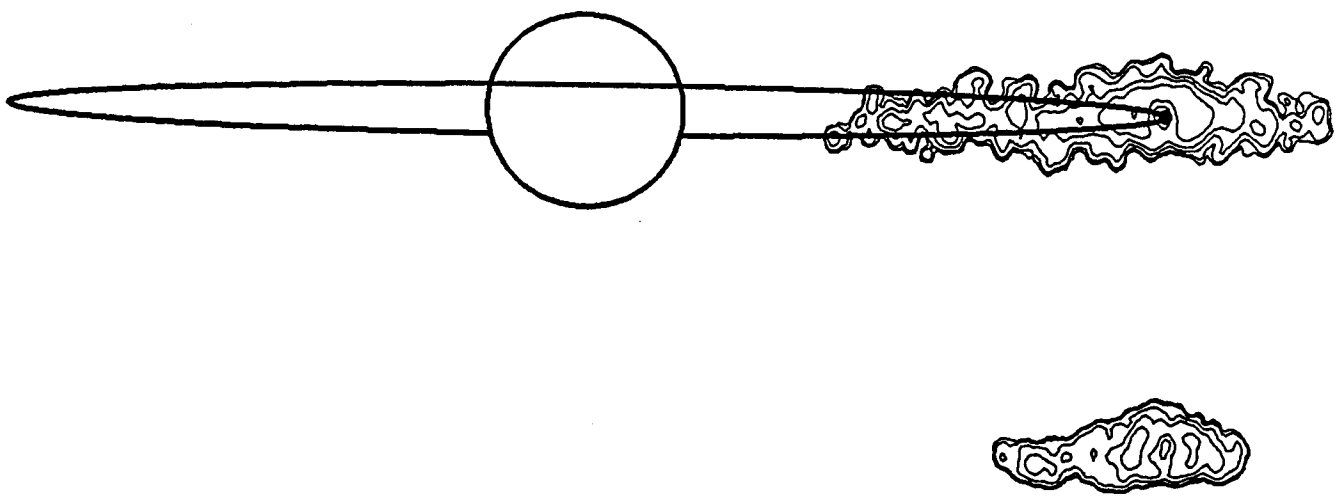

275.7°
Image Set: 3.E

SIP421/34-36
UT DATE: MAY 13, 1981 (4)

AVERAGE IO PHASE = 275.7
AVERAGE IO SYS III = 183.5

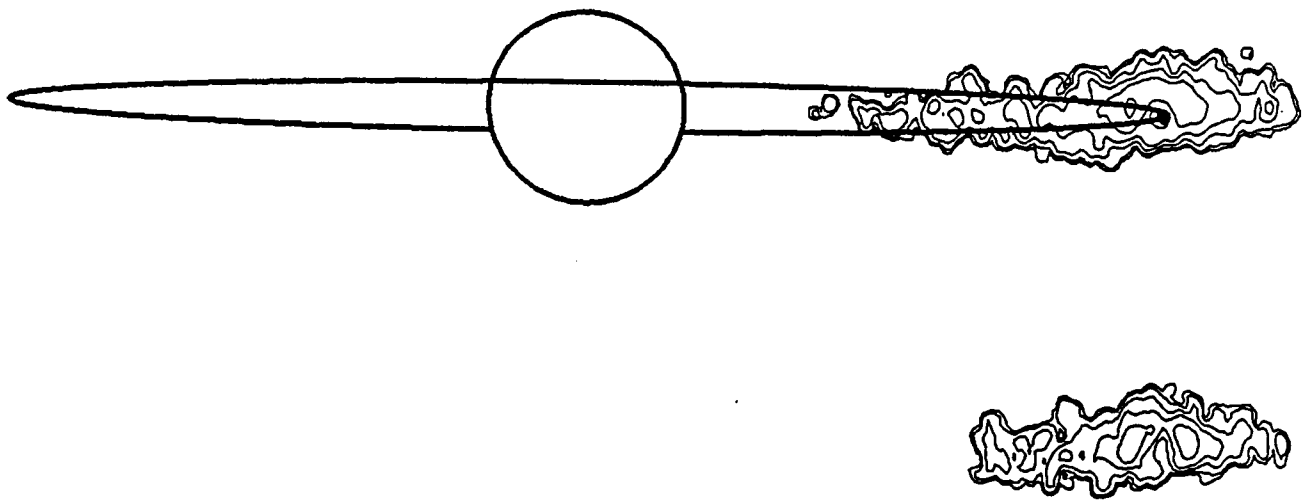

102.5° (282.5°)
Image Set: 3.F

SIP418/31-33
UT DATE: MAY 5, 1981 (4)

AVERAGE IO PHASE = 102.5
AVERAGE IO SYS III = 299.6

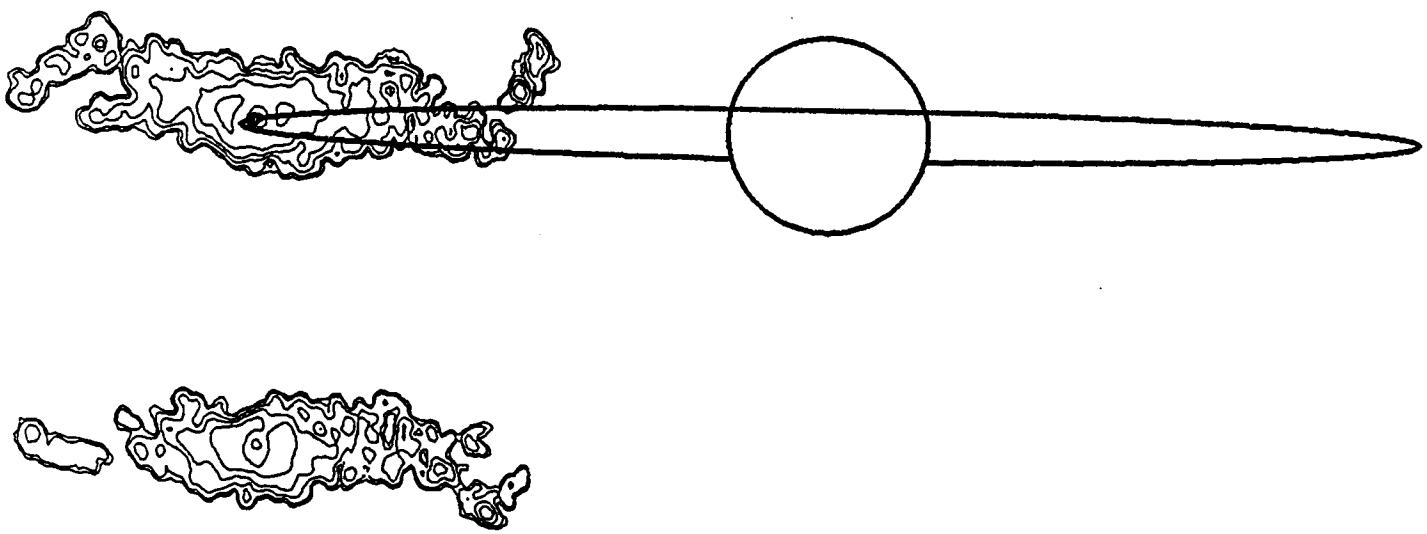

102.6° (282.6°)
Image Set: 3.F

SIP424/10-12
UT DATE: JUNE 6, 1981 (1)

AVERAGE IO PHASE = 102.6
AVERAGE IO SYS III = 300.3

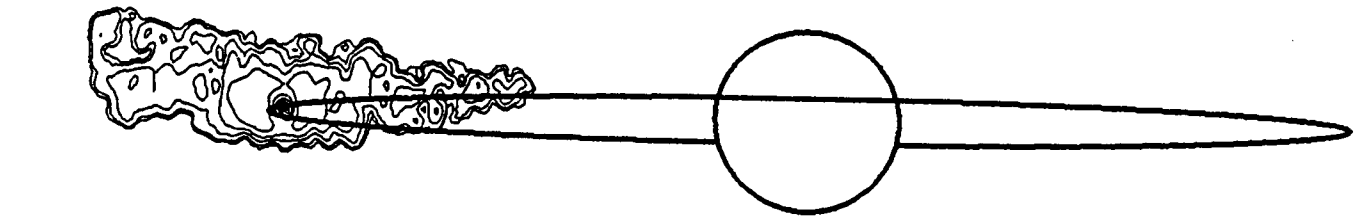

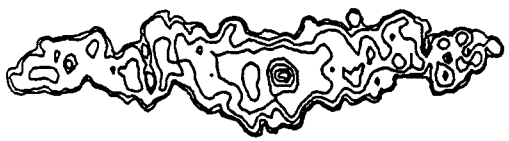

285.7°
Image Set: 3.F

SIP416/4-6

UT DATE: APRIL 29, 1981 (1)

AVERAGE IO PHASE = 285.7

AVERAGE IO SYS III = 138.5

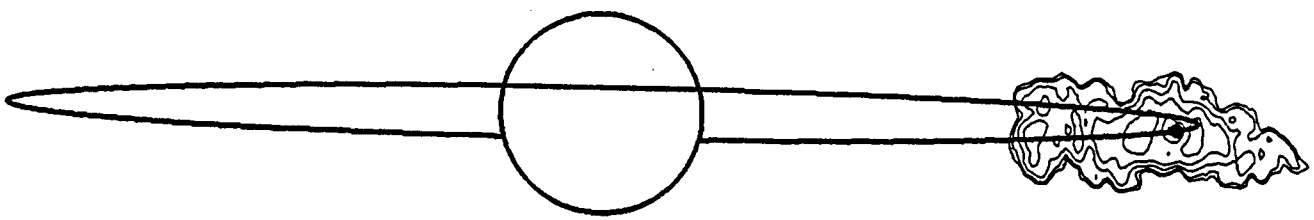

286.1°
Image Set: 3.F

SIP419/19-21

UT DATE: MAY 6, 1981 (1)

AVERAGE IO PHASE = 286.1

AVERAGE IO SYS III = 178.3

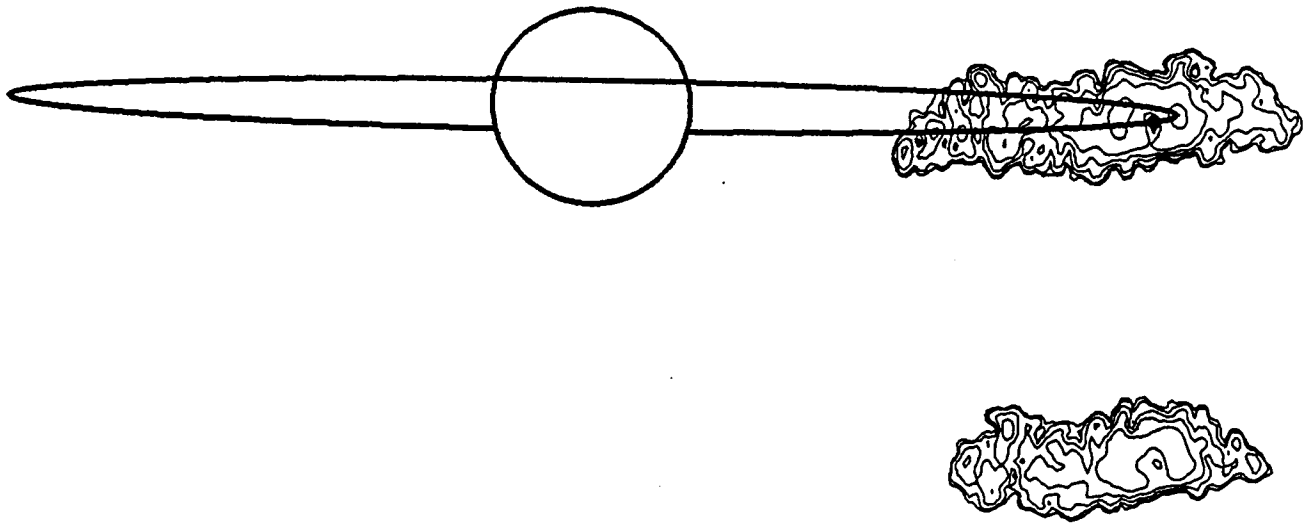

286.2°
Image Set: 3.F

SIP421/40-42
UT DATE: MAY 13, 1981 (6)

AVERAGE IO PHASE = 286.2
AVERAGE IO SYS III = 217.5

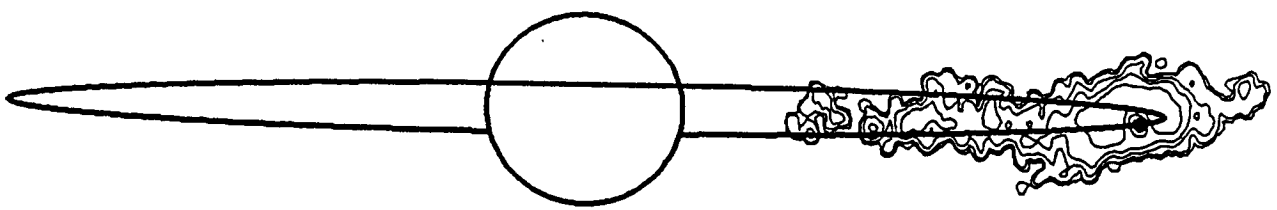

286.9°
Image Set: 3.F

SIP425/6-9

UT DATE: JUNE 14, 1981 (1)

AVERAGE IO PHASE = 286.9

AVERAGE IO SYS III = 222.1

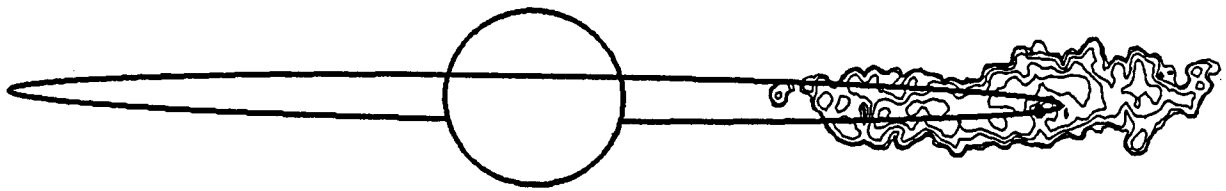

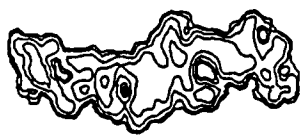

112.4° (292.4°)
Image Set: 3.G

SIP415/43-45

UT DATE: APRIL 28, 1981 (2)

AVERAGE IO PHASE = 112.4

AVERAGE IO SYS III = 293.9

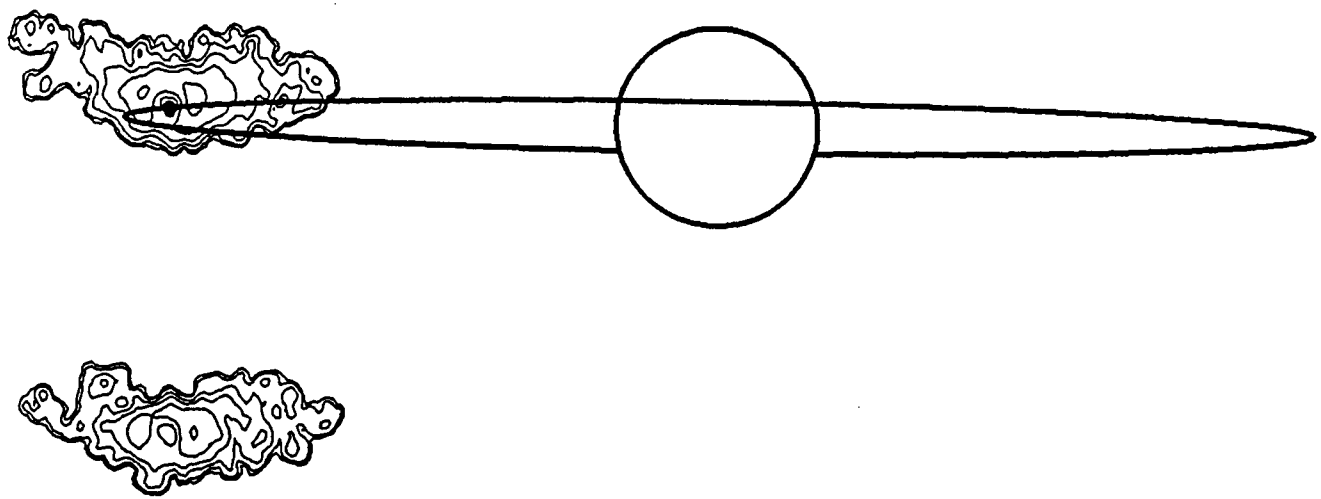

113.9° (293.9°)
Image Set: 3.G

SIP415/44-46

UT DATE: APRIL 28, 1981 (3)

AVERAGE IO PHASE = 113.9
AVERAGE IO SYS III = 298.5

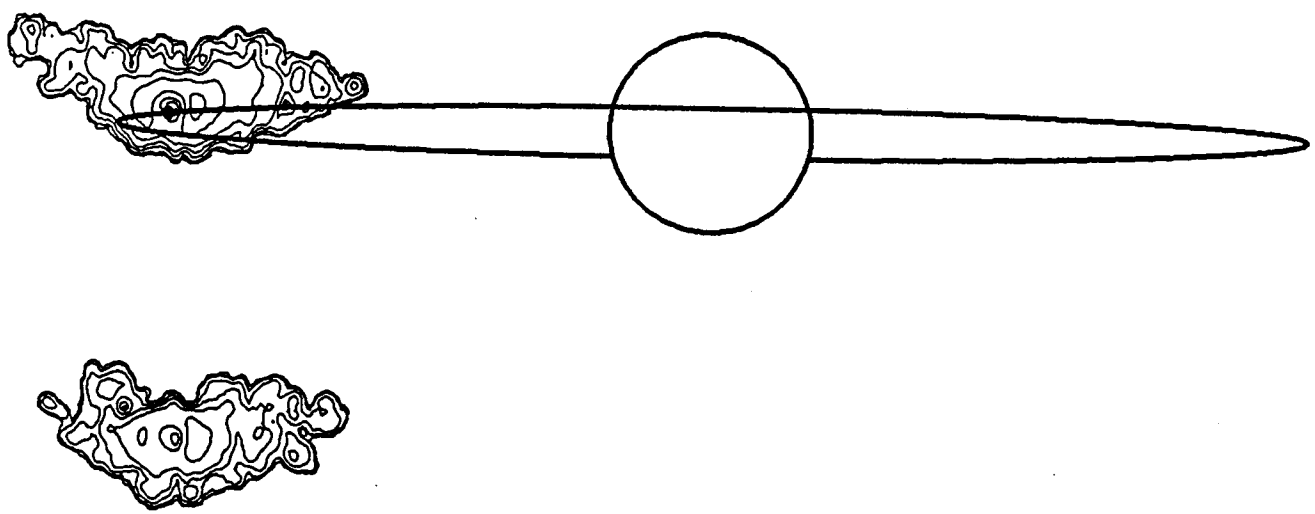

290.9°
Image Set: 3.G

SIP419/22-24

UT DATE: MAY 6, 1981 (2)

AVERAGE IO PHASE = 290.9

AVERAGE IO SYS III = 194.0

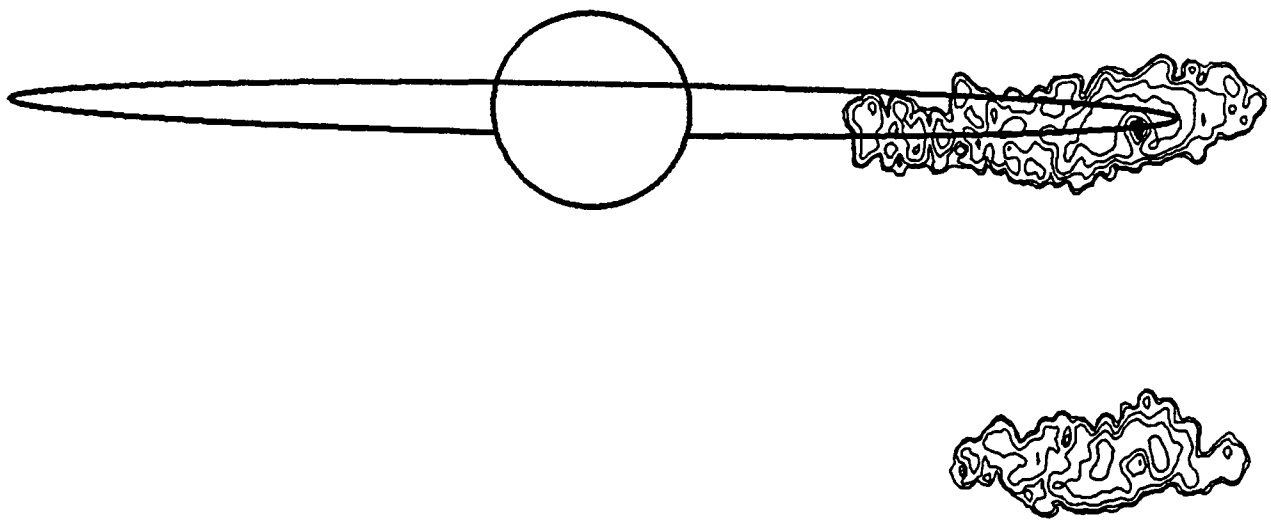

294.8°
Image Set: 3.G

SIP421/45-47

UT DATE: MAY 13, 1981 (8)

AVERAGE Io PHASE = 294.8

AVERAGE Io SYS III = 245.7

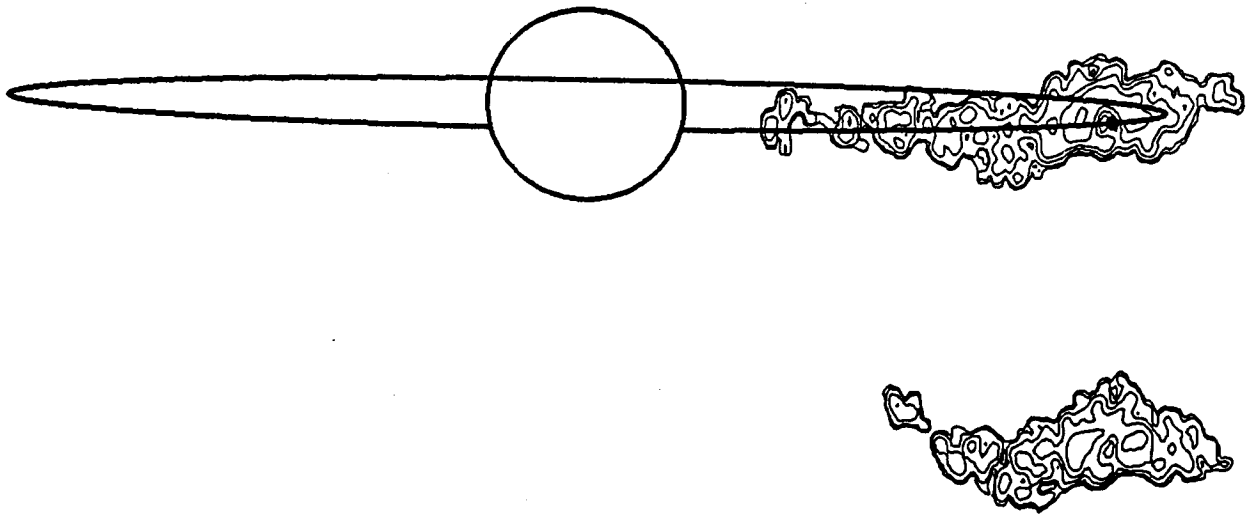

293.7°
Image Set: 3.G

SIP410/13-15

UT DATE: APRIL 6, 1981 (1)

AVERAGE IO PHASE = 293.7

AVERAGE IO SYS III = 311.5

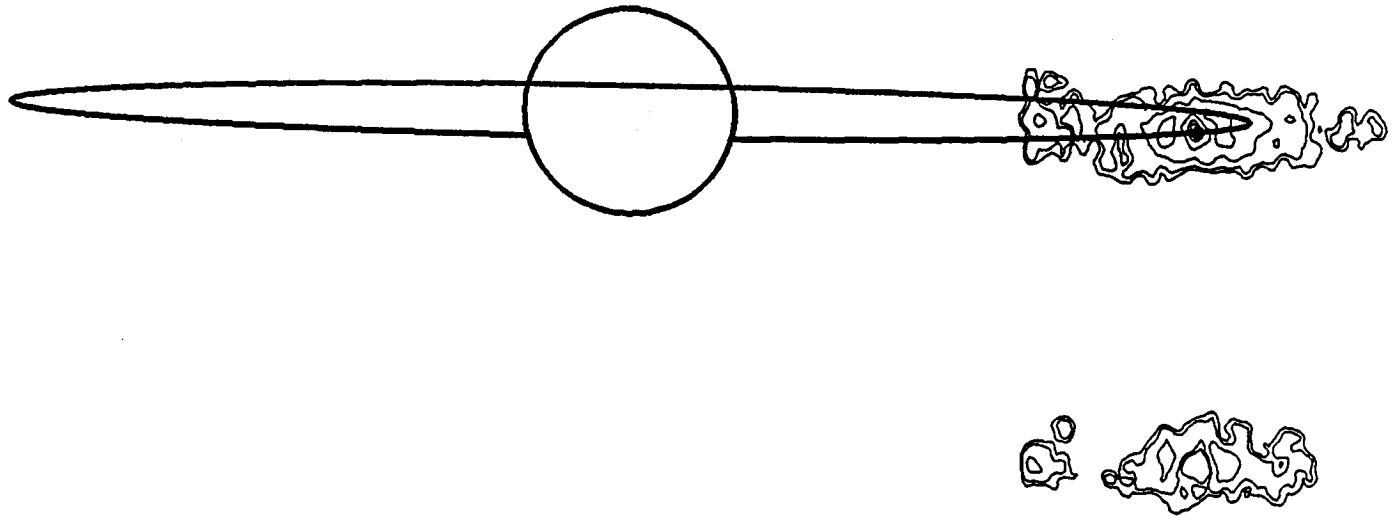

Appendix IV

Fully Reduced 1981 Sodium Cloud Images: Study 4

Appendix IV

1981 Region B/C East Images:
Comparison for Similar Phase Angles

UT Date	Image ID Number (Tape/Frames)	Mid-Point Condition: Io Phase Angle (deg)	Mid-Point Condition: Io System III Longitude (deg)	Image Set
12 May (1)	SIP 420/6-8	48.3	159.8	-
12 May (2)	SIP 420/10-12	54.4	180.0	-
5 May (1)	SIP 418/10-12	68.1*	186.1	4.A
12 May (3)	SIP 420/15-20	65.8*	217.8	4.A
5 May (2)	SIP 418/13-16	73.6	204.2	4.B
12 May (4)	SIP 420/21-23	74.7	247.1	4.B
28 Apr (1)	SIP 415/27-29	90.5	221.3	4.C
5 May (3)	SIP 418/24-26	90.2	259.3	4.C
12 May (5)	SIP 420/30-32	91.2	301.8	4.C
5 May (4)	SIP 418/31-33	102.5	299.6	4.D†
6 Jun (1)	SIP 424/10-12	102.6	300.3	4.D†
28 Apr (2)	SIP 415/43-45	112.4	293.9	-
28 Apr (3)	SIP 415/44-46	113.9	298.5	-

*critical east phase angle
†same as Image Set 2.A

48.3°

SIP420/6-8

UT DATE: MAY 12, 1981 (1)

AVERAGE IO PHASE = 48.3

AVERAGE IO SYS III = 159.8

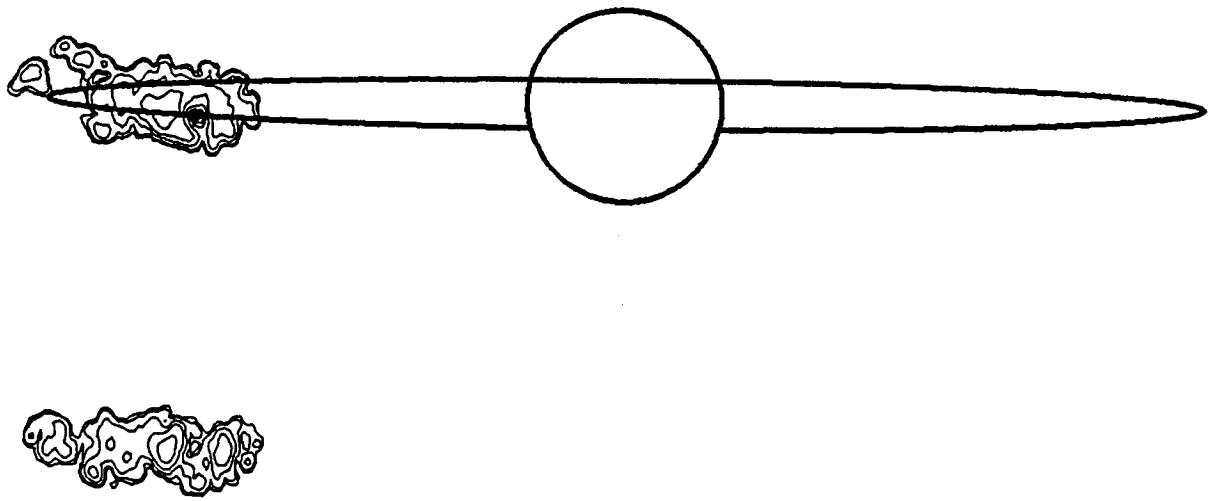

54.4°

SIP420/10-12

UT DATE: MAY 12, 1981 (2)

AVERAGE IO PHASE = 54.5

AVERAGE IO SYS III = 180.0

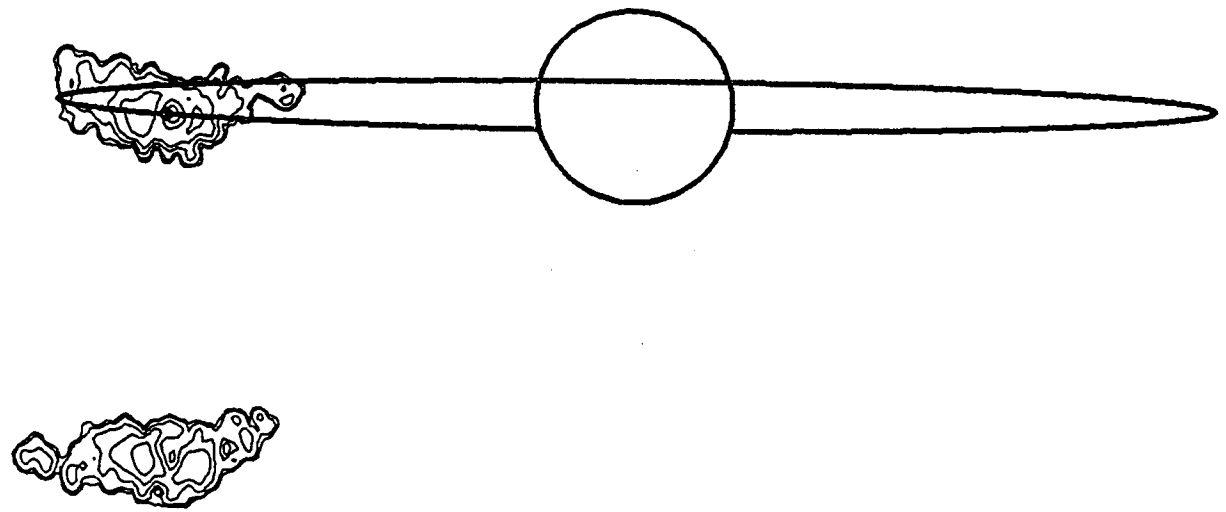

68.1°
Image Set: 4.A

SIP418/10-12
UT DATE: MAY 5, 1981 (1)

AVERAGE IO PHASE = 68.1
AVERAGE IO SYS III = 186.1

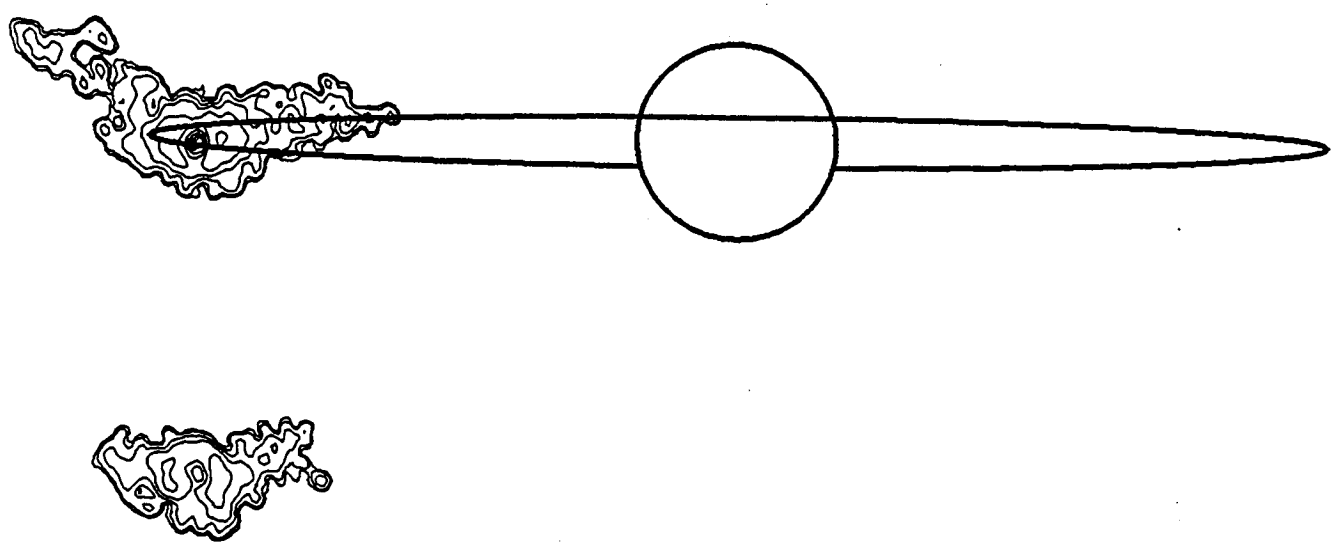

65.8°
Image Set: 4.A

SIP420/15-20
UT DATE: MAY 12, 1981 (3)

AVERAGE IO PHASE = 65.8
AVERAGE IO SYS III = 217.8

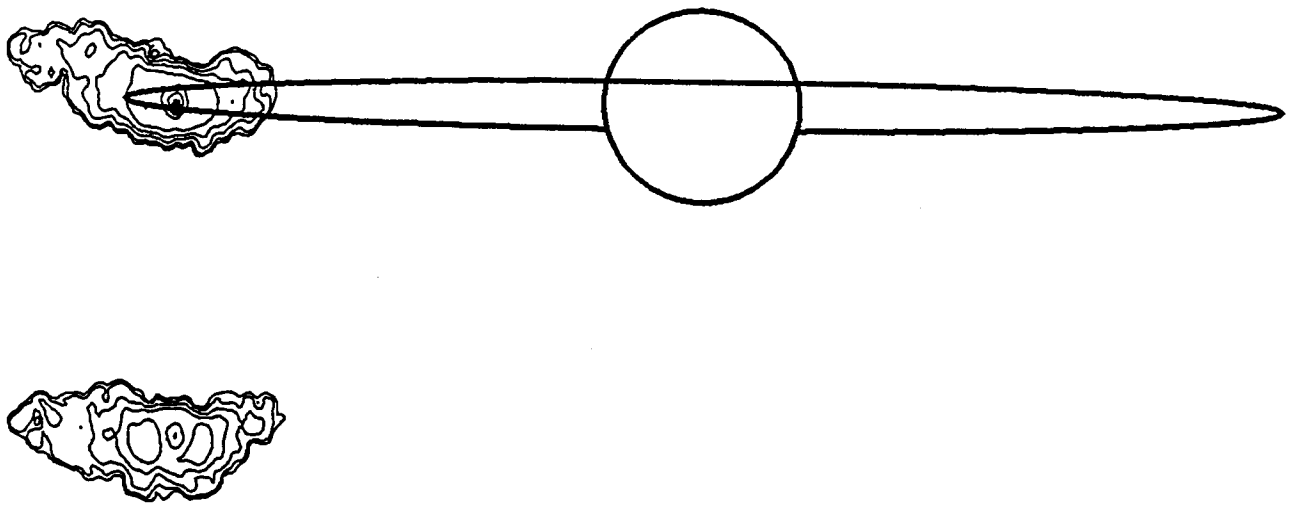

73.6°
Image Set: 4.B

SIP418/13-16
UT DATE: MAY 5, 1981 (2)

AVERAGE IO PHASE = 73.6
AVERAGE IO SYS III = 204.2

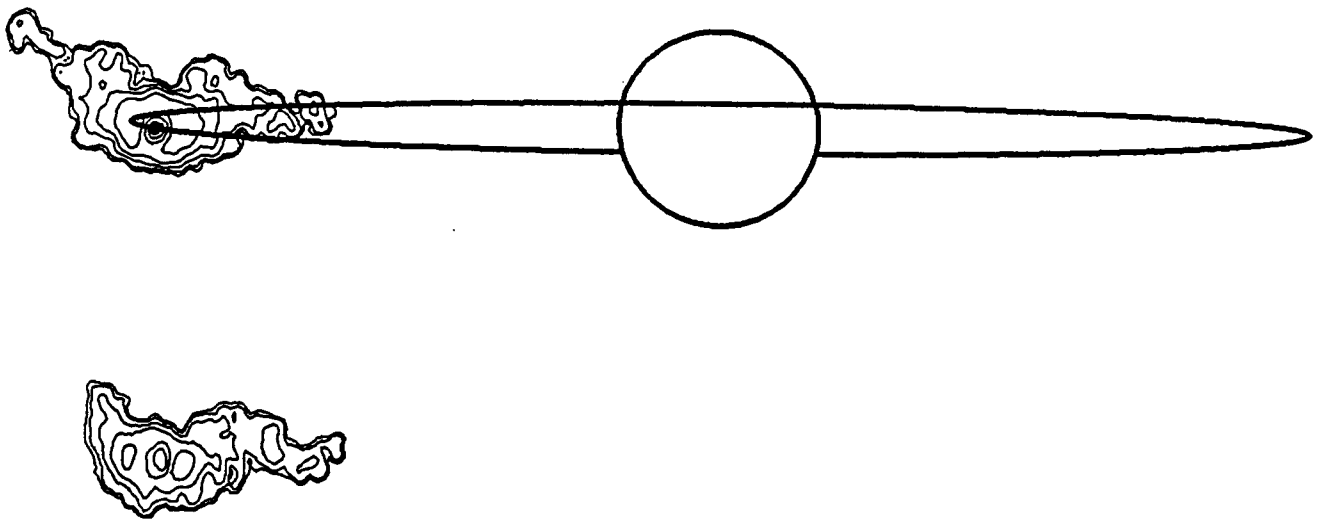

74.7°
Image Set: 4.B

SIP420/21-23
UT DATE: MAY 12, 1981 (4)

AVERAGE IO PHASE = 74.7
AVERAGE IO SYS III = 247.1

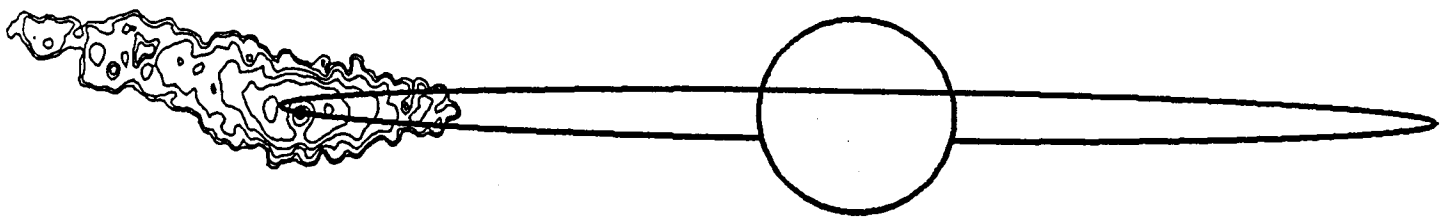

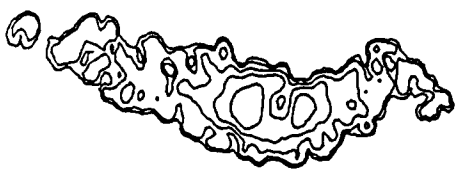

90.5°
Image Set: 4.C

SIP415/27-29
UT DATE: APRIL 28, 1981 (1)

AVERAGE IO PHASE = 90.5
AVERAGE IO SYS III = 221.3

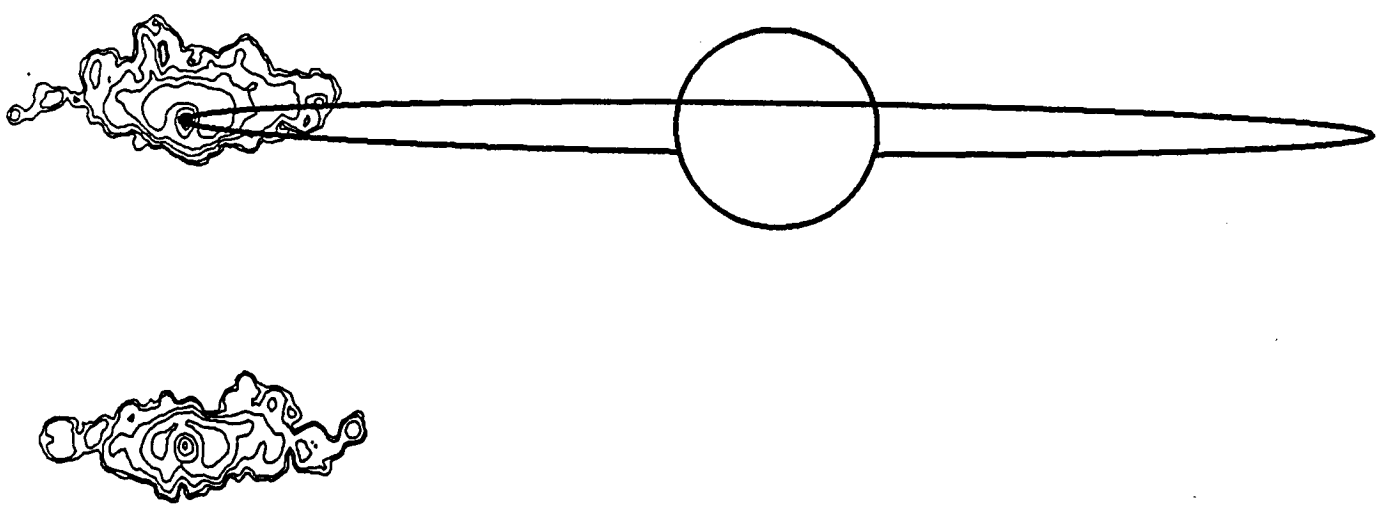

90.2°
Image Set: 4.C

SIP418/24-26
UT DATE: MAY 5, 1981 (3)

AVERAGE IO PHASE = 90.2
AVERAGE IO SYS III = 259.3

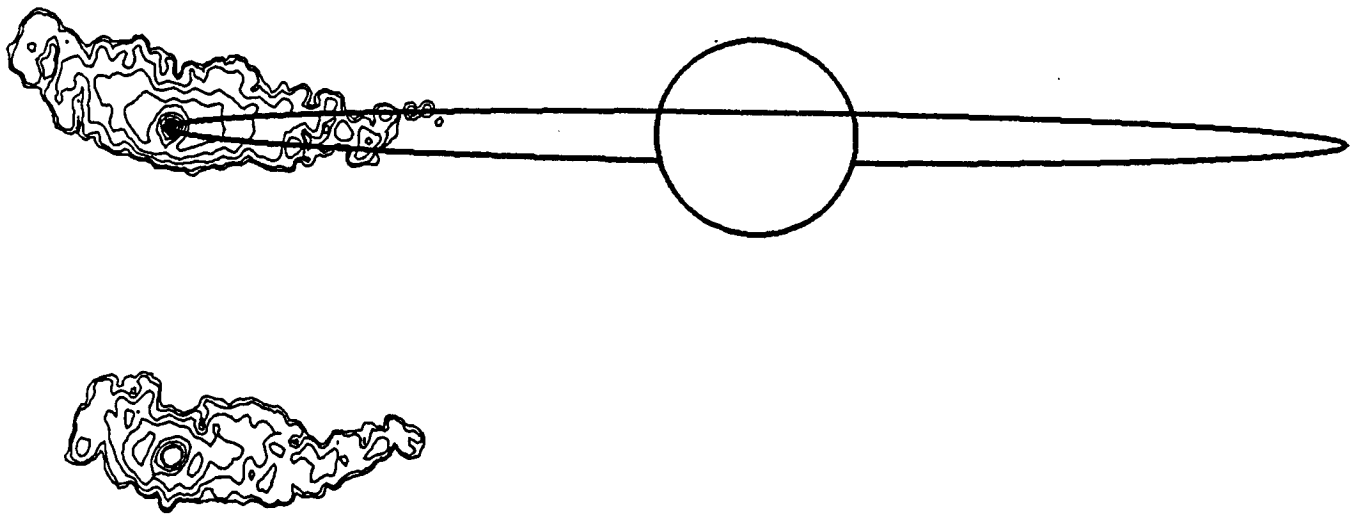

91.2°
Image Set: 4.C

SIP420/30-32
UT DATE: MAY 12, 1981 (5)

AVERAGE IO PHASE = 91.2
AVERAGE IO SYS III = 301.8

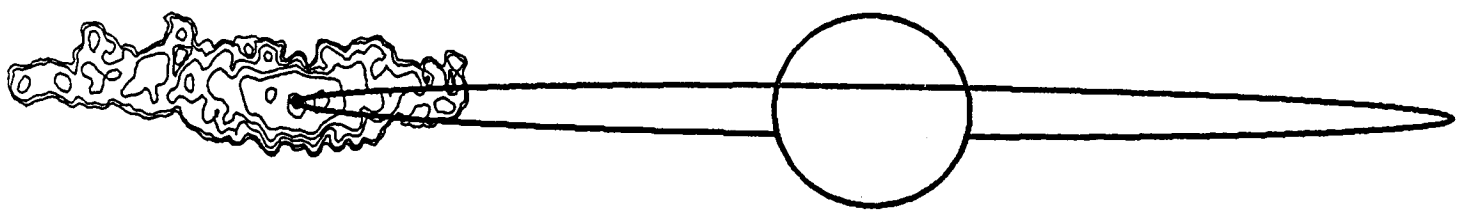

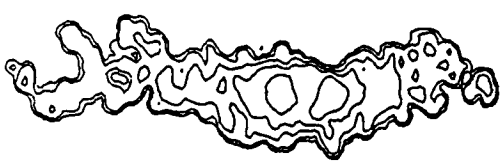

102.5°
Image Set: 4.D
(2.A)

SIP418/31-33

UT DATE: MAY 5, 1981 (4)

AVERAGE IO PHASE = 102.5

AVERAGE IO SYS III = 299.6

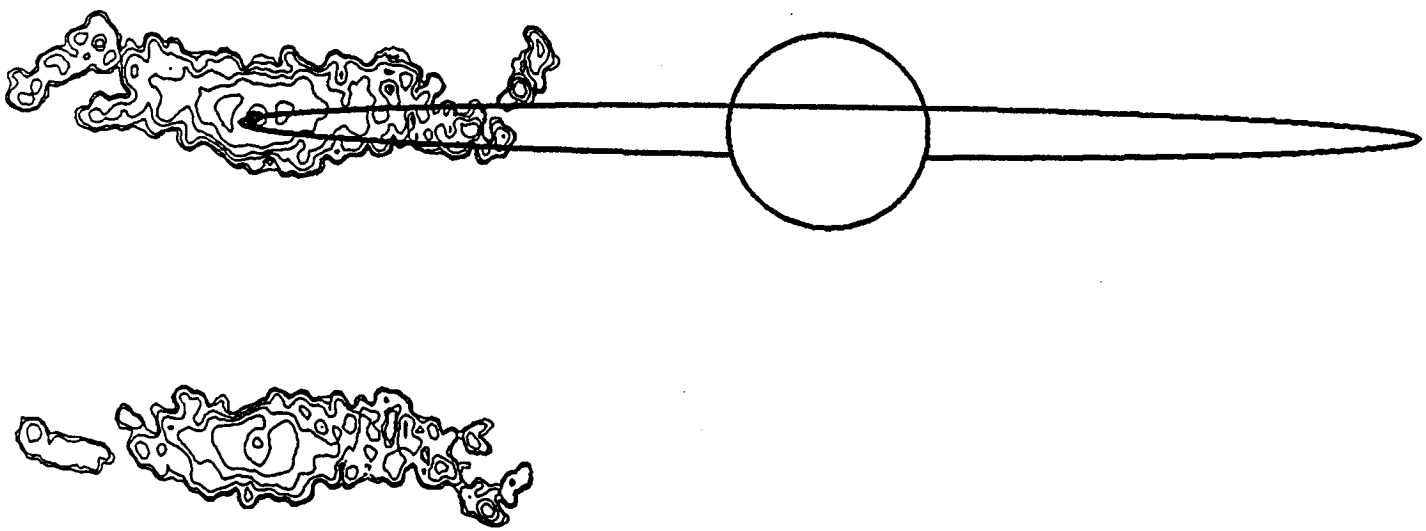

102.6°
Image Set: 4.D
(2.A)

SIP424/10-12

UT DATE: JUNE 6, 1981 (1)

AVERAGE IO PHASE = 102.6
AVERAGE IO SYS III = 300.3

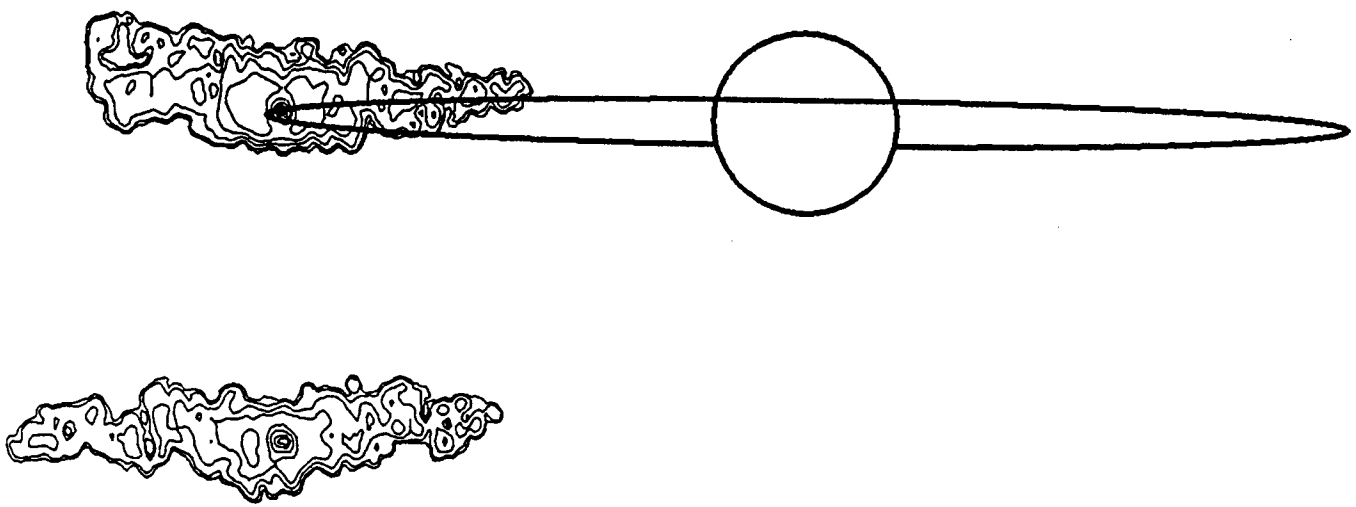

112.4°

SIP415/43-45

UT DATE: APRIL 28, 1981 (2)

AVERAGE IO PHASE = 112.4

AVERAGE IO SYS III = 293.9

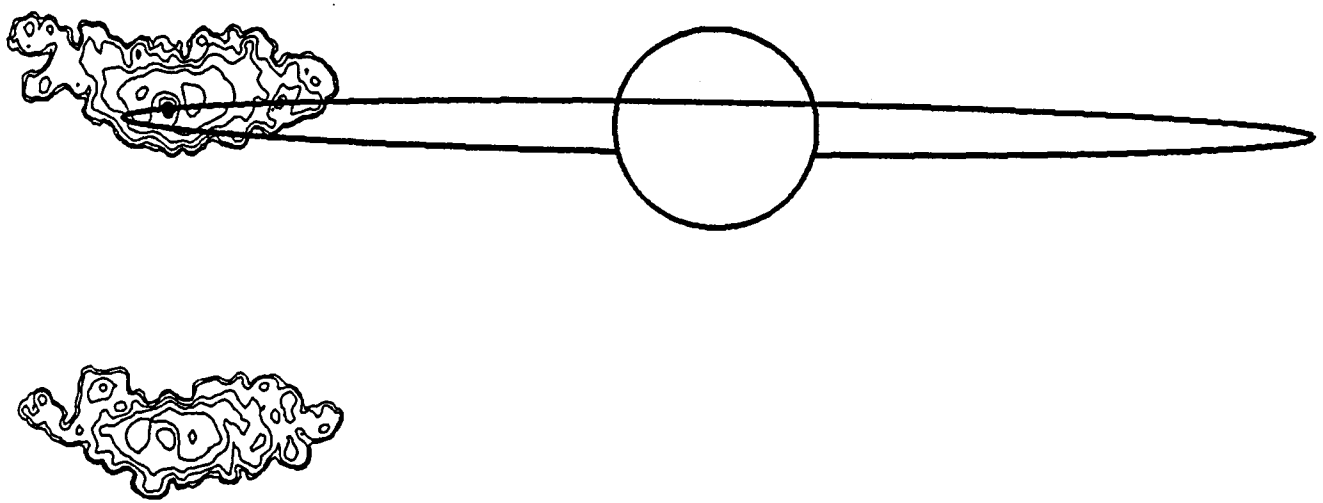

113.9°

SIP415/44-46

UT DATE: APRIL 28, 1981 (3)

AVERAGE IO PHASE = 113.9

AVERAGE IO SYS III = 298.5

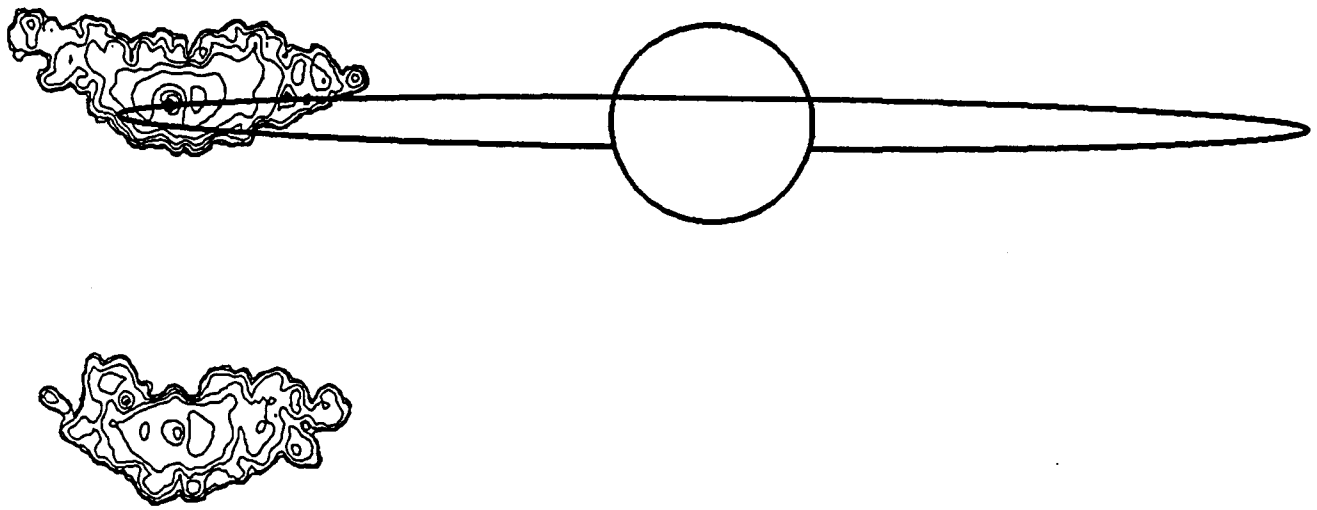

Appendix IV

1981 Region B/C West Images: Comparison for Similar Phase Angles

UT Date	Image ID Number (Tape/Frames)	Mid-Point Condition: Io Phase Angle (deg)	Mid-Point Condition: Io System III Longitude (deg)	Image Set
4 May (1)	SIP 417/8-10	219.7	223.1	-
4 May (2)	SIP 417/13-15	227.8	249.2	-
4 May (3)	SIP 417/16-18	233.2*	266.8	-
4 May (4)	SIP 417/20-22	240.9	291.7	-
13 May (1)	SIP 421/21-23	252.6	108.4	4.E
4 May (5)	SIP 417/27-29	253.3	331.9	4.E
13 May (2)	SIP 421/27-28	262.3	139.8	-
4 May (6)	SIP 417/36-39	269.3	23.9	4.F
13 May (3)	SIP 421/32-33	270.9	168.0	4.F
13 May (4)	SIP 421/34-36	275.7	183.5	-
13 May (5)	SIP 421/37-39	281.1	201.1	-
29 Apr (1)	SIP 416/4-6	285.7	138.5	4.G
6 May (1)	SIP 419/19-21	286.1	178.3	4.G
13 May (6)	SIP 421/40-42	286.2	217.5	4.G†
14 Jun (1)	SIP 425/6-9	286.9	222.1	4.G†
29 Apr (2)	SIP 416/7-9	290.5	154.2	4.H
6 May (2)	SIP 419/22-24	290.9	194.0	4.H
13 May (7)	SIP 421/43-45	291.2	234.1	4.H§
14 Jun (2)	SIP 425/9-12	291.6	237.6	4.H§
13 May (8)	SIP 421/45-47	294.8	245.7	4.H
6 Apr (1)	SIP 410/13-15	293.7	311.5	4.H

*critical west phase angle

†same as image set 2.B

§same as image set 2.C

SIP417/8-10

UT DATE: MAY 4, 1981 (1)

AVERAGE IO PHASE = 219.7

AVERAGE IO SYS III = 223.1

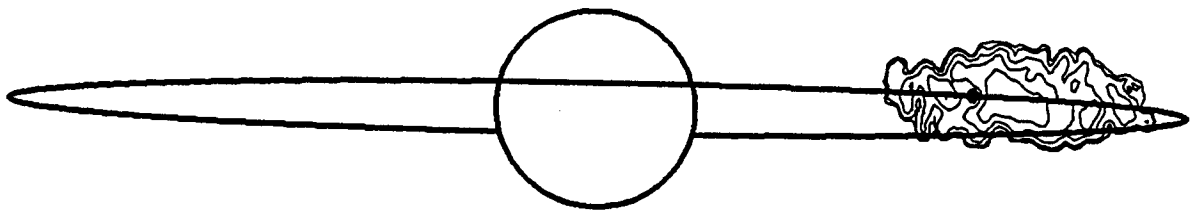

SIP417/13-15

UT DATE: MAY 4, 1981 (2)

AVERAGE IO PHASE = 227.8

AVERAGE IO SYS III = 249.2

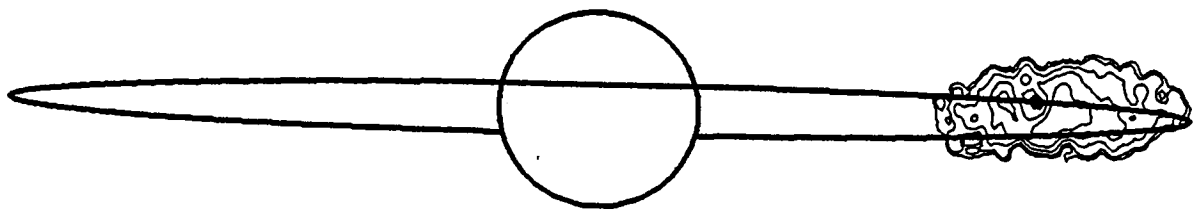

233.2°

SIP417/16-18

UT Date: May 4, 1981 (3)

Average Io Phase = 233.2

Average Io Sys III = 266.8

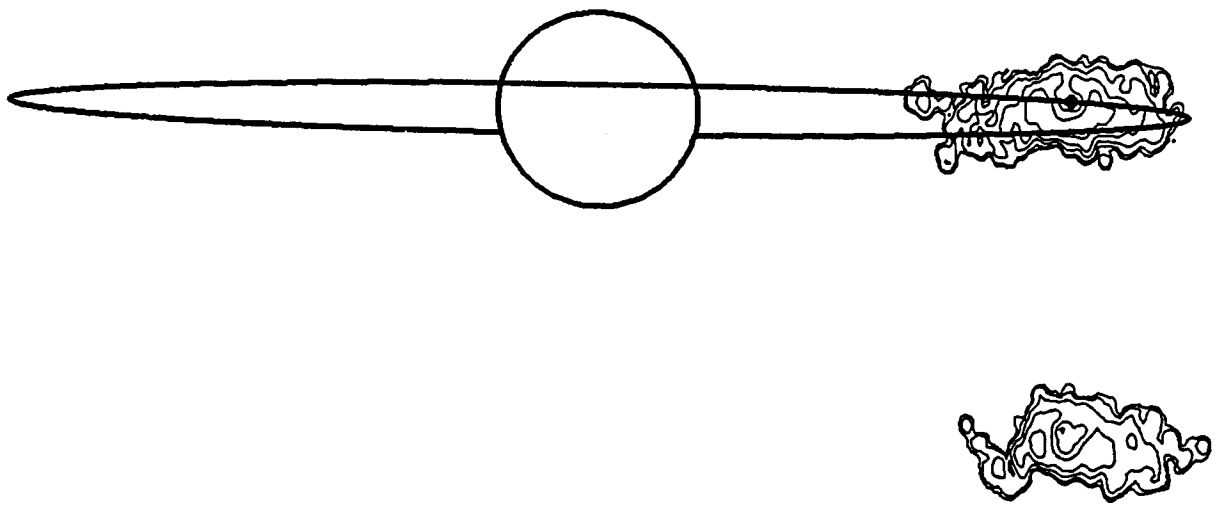

SIP417/20-22
UT DATE: MAY 4, 1981 (4)

AVERAGE IO PHASE = 240.9
AVERAGE IO SYS III = 291.7

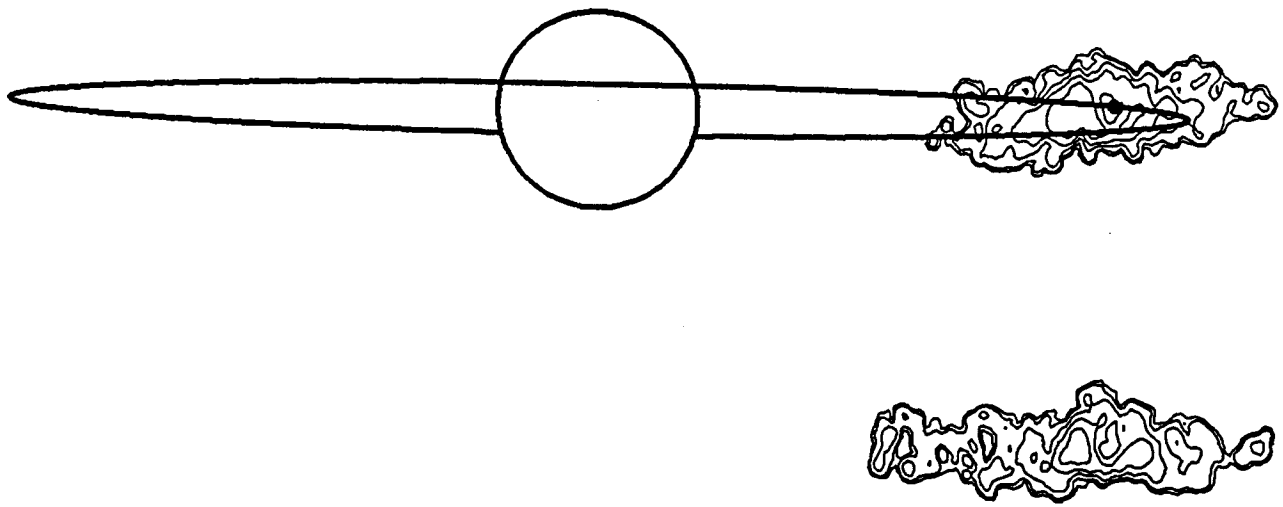

252.6°
Image Set: 4.E

SIP421/21-23
UT DATE: MAY 13, 1981 (1)

AVERAGE Io PHASE = 252.6
AVERAGE Io SYS III = 108.4

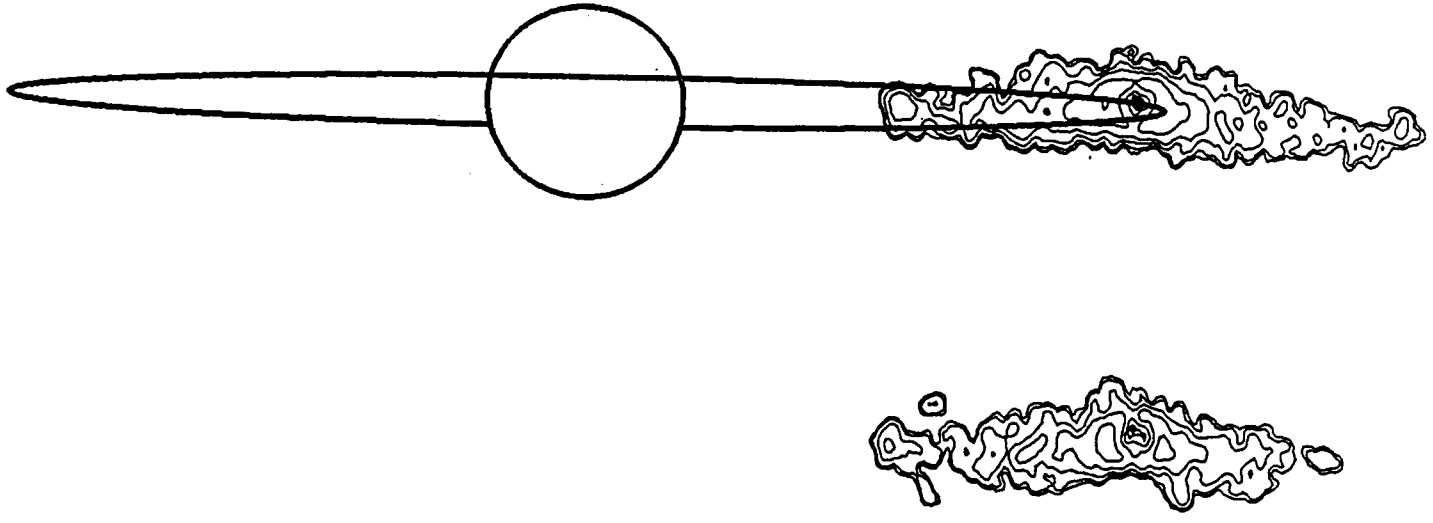

253.3°
Image Set: 4.E

SIP417/27-29

UT DATE: MAY 4, 1981 (5)

AVERAGE IO PHASE = 253.3

AVERAGE IO SYS III = 331.9

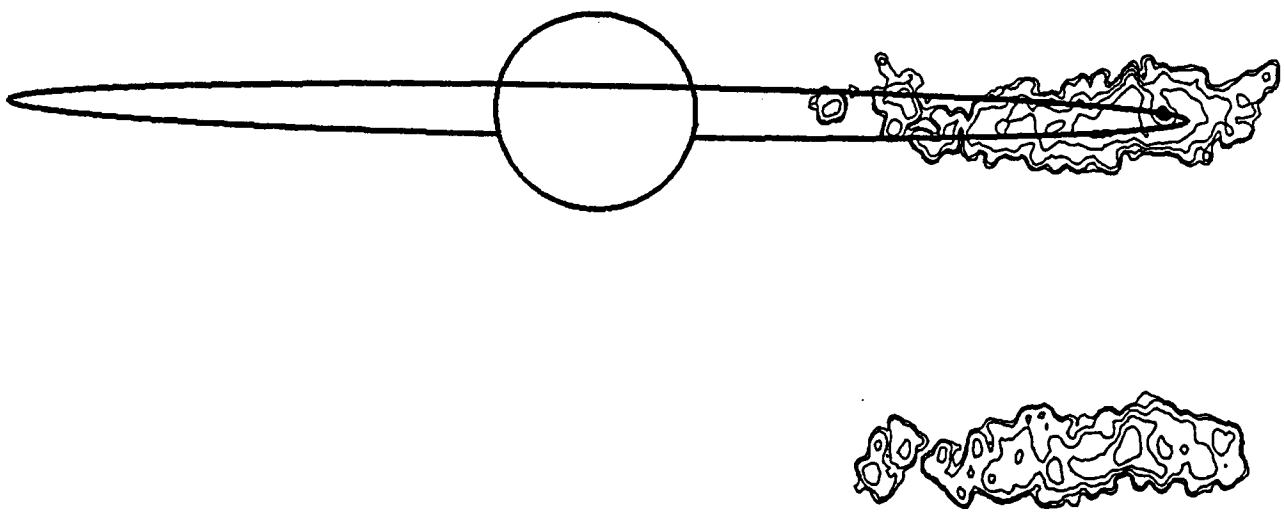

SIP421/27-28
UT DATE: MAY 13, 1981 (2)

AVERAGE IO PHASE = 262.3
AVERAGE IO SYS III = 139.8

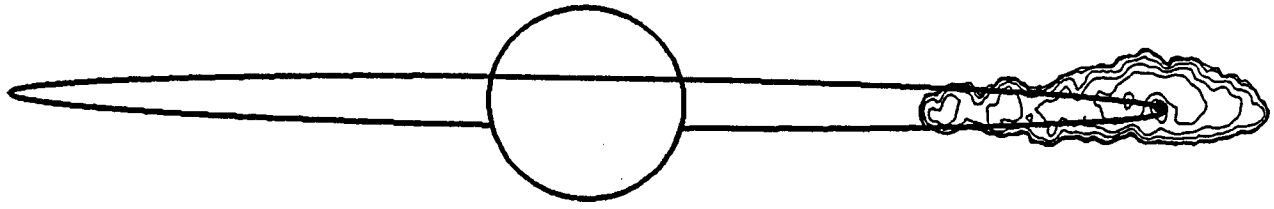

SIP417/36-39
UT DATE: MAY 4, 1981 (6)

AVERAGE Io PHASE = 269.3
AVERAGE Io SYS III = 23.9

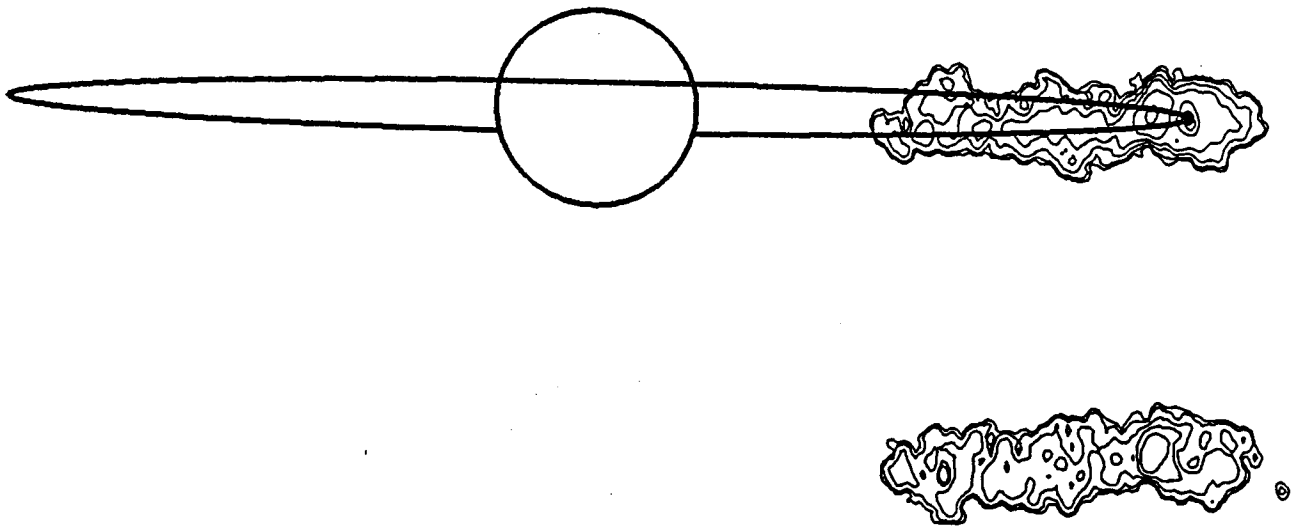

270.9°
Image Set: 4.F

SIP421/32-33
UT DATE: MAY 13, 1981 (3)

AVERAGE IO PHASE = 270.9
AVERAGE IO SYS III = 168.0

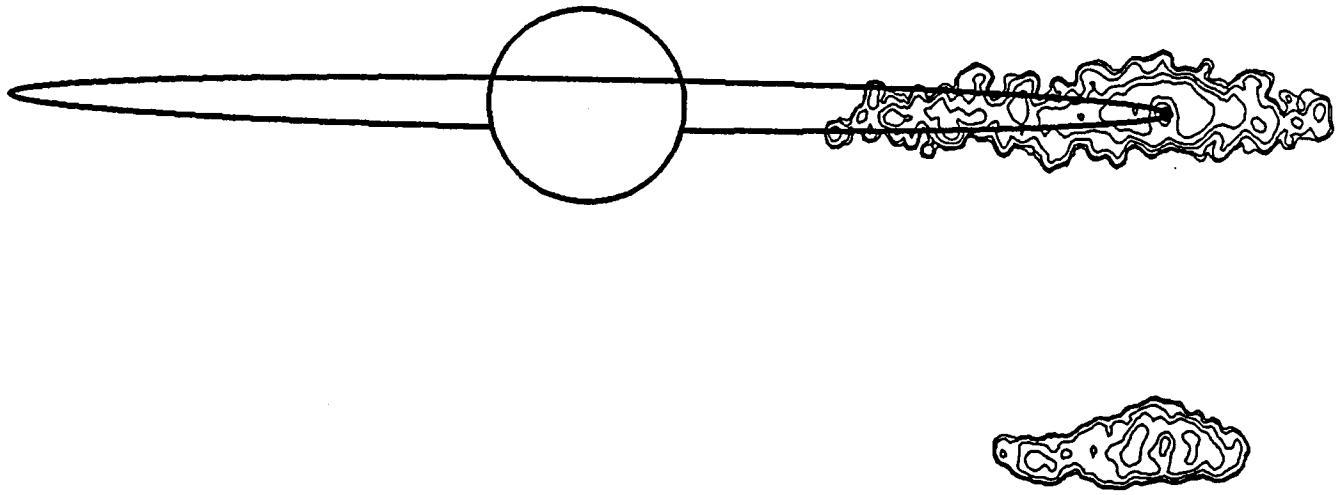

SIP421/34-36

UT DATE: MAY 13, 1981 (4)

AVERAGE IO PHASE = 275.7

AVERAGE IO SYS III = 183.5

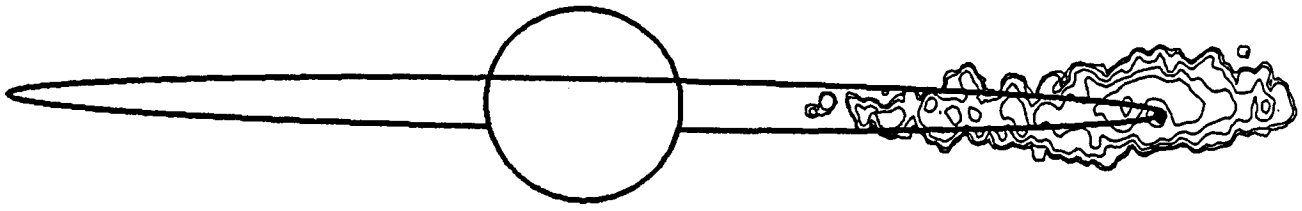

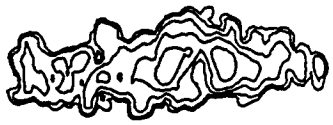

SIP421/37-39

UT DATE: MAY 13, 1981 (5)

AVERAGE Io PHASE = 281.1

AVERAGE Io SYS III = 201.1

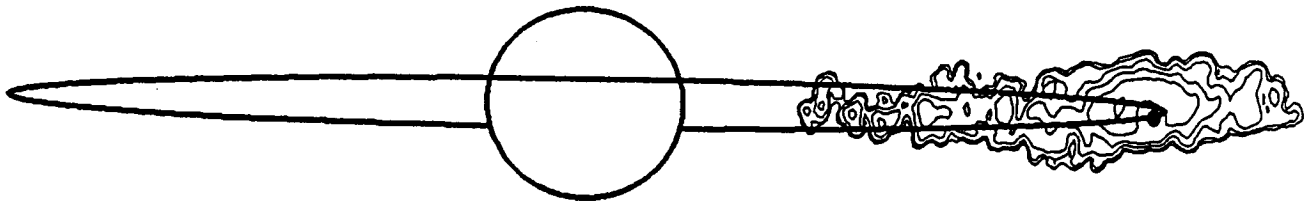

285.7°
Image Set: 4.G

SIP416/4-6

UT DATE: APRIL 29, 1981 (1)

AVERAGE IO PHASE = 285.7
AVERAGE IO SYS III = 138.5

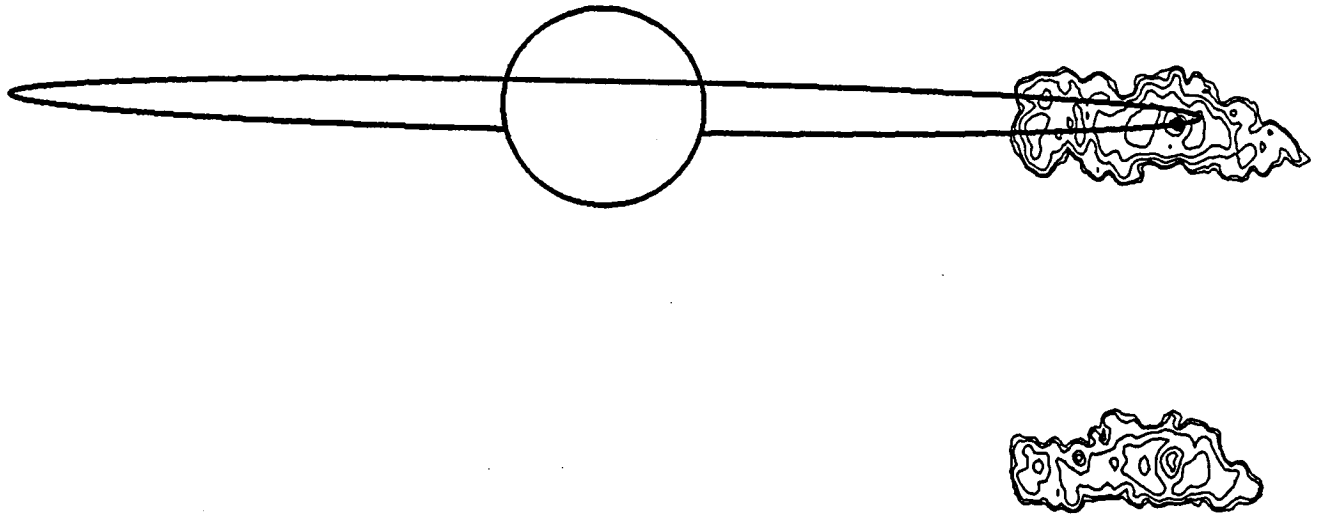

286.1°
Image Set: 4.G

SIP419/19-21

UT DATE: MAY 6, 1981 (1)

AVERAGE IO PHASE = 286.1

AVERAGE IO SYS III = 178.3

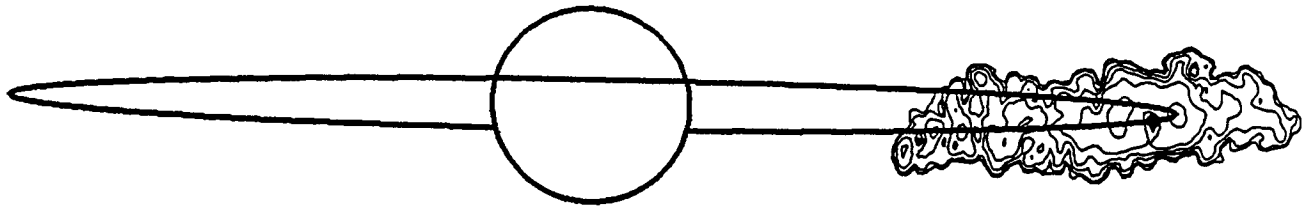

286.2°
Image Set: 4.G
(2.B)

SIP421/40-42
UT DATE: MAY 13, 1981 (6)

AVERAGE IO PHASE = 286.2
AVERAGE IO SYS III = 217.5

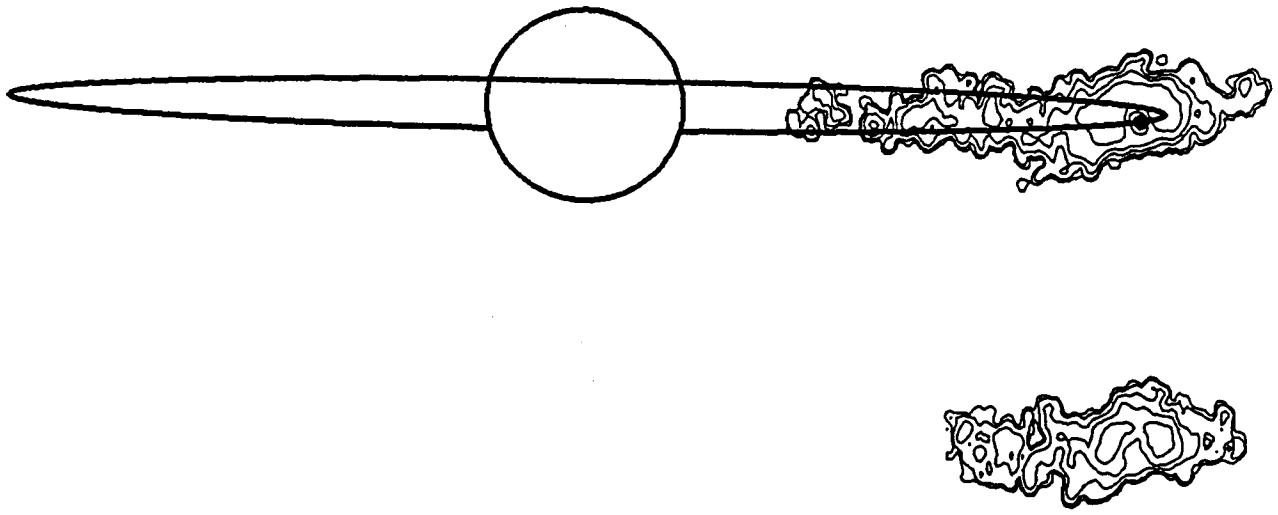

286.9°
Image Set: 4.G
(2.B)

SIP425/6-9

UT Date: June 14, 1981 (1)

Average Io Phase = 286.9
Average Io Sys III = 222.1

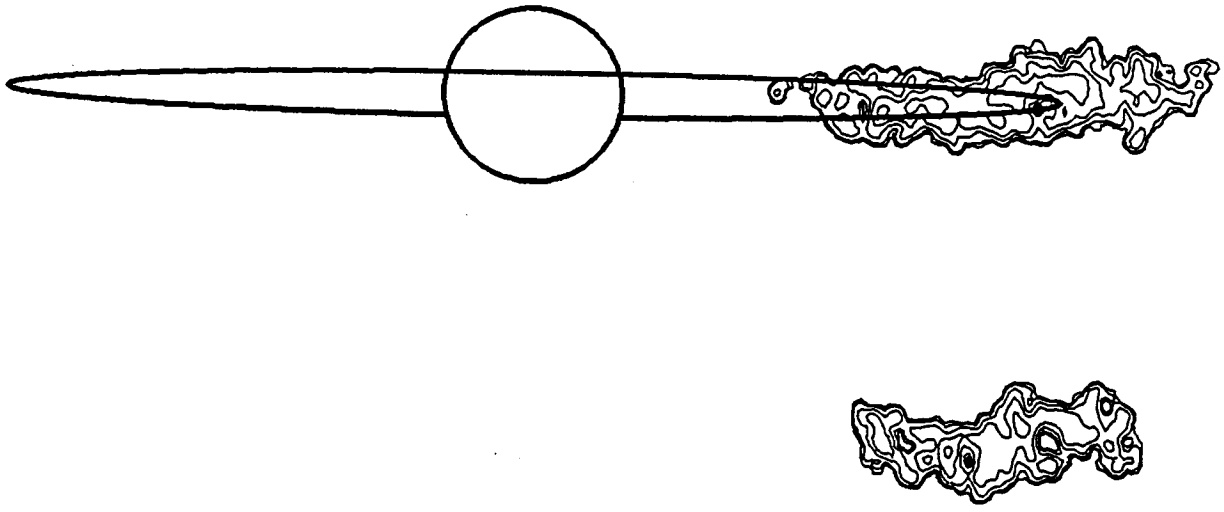

290.5°
Image Set: 4.H

SIP416/7-9

UT DATE: APRIL 29, 1981 (2)

AVERAGE IO PHASE = 290.5

AVERAGE IO SYS III = 154.2

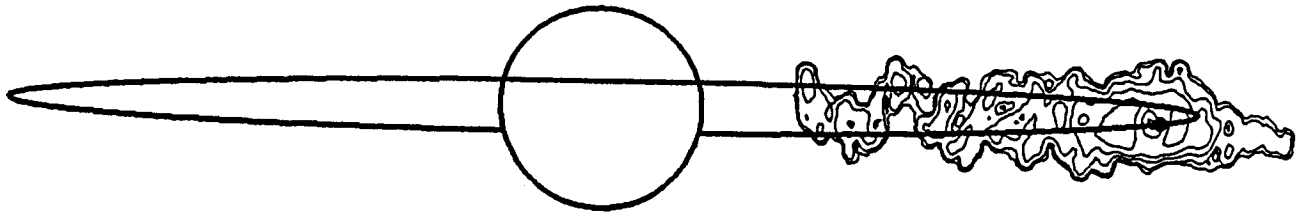

290.9°
Image Set: 4.H

SIP419/22-24

UT DATE: MAY 6, 1981 (2)

AVERAGE IO PHASE = 290.9

AVERAGE IO SYS III = 194.0

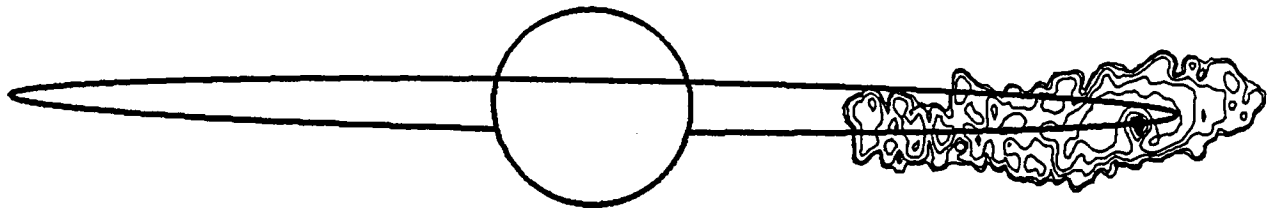

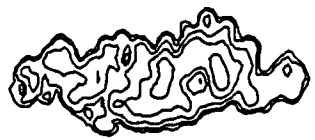

291.2°
Image Set: 4.H
(2.C)

SIP421/43-45

UT DATE: MAY 13, 1981 (7)

AVERAGE IO PHASE = 291.2

AVERAGE IO SYS III = 234.1

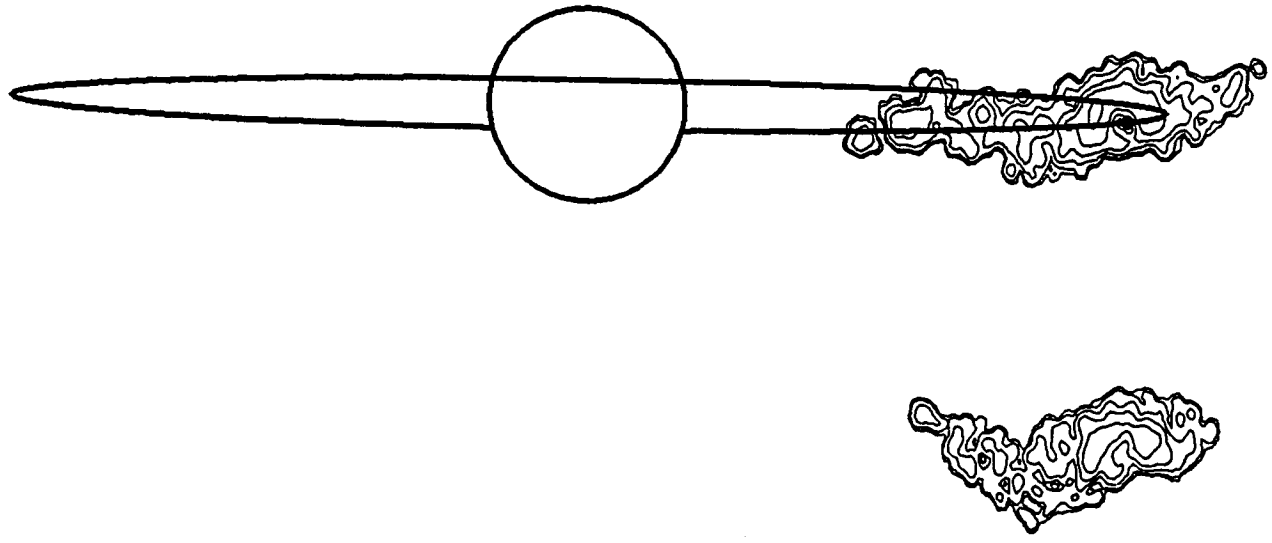

291.6°
Image Set: 4.H
(2.C)

SIP425/9-12

UT DATE: JUNE 14, 1981 (2)

AVERAGE Io PHASE = 291.6

AVERAGE Io SYS III = 237.6

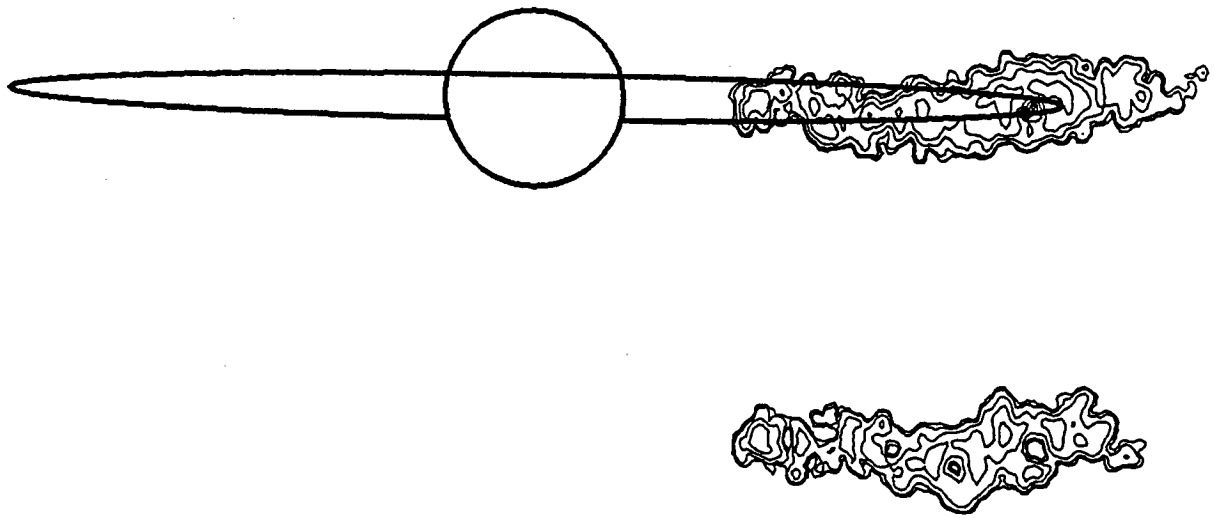

294.8°
Image Set: 4.H

SIP421/45-47
UT DATE: MAY 13, 1981 (8)

AVERAGE Io PHASE = 294.8
AVERAGE Io SYS III = 245.7

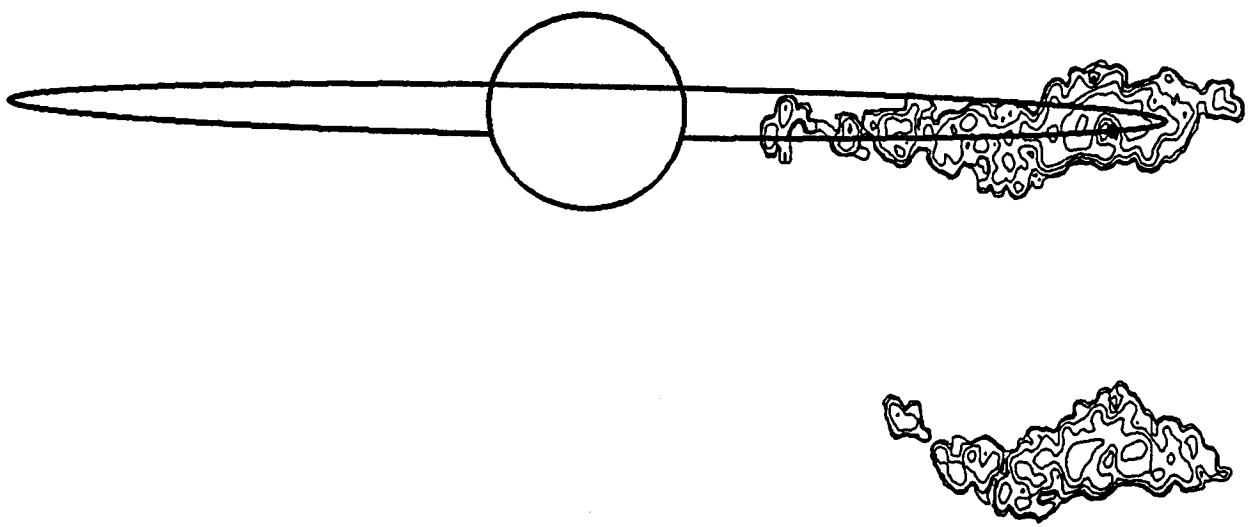

293.7°
Image Set: 4.H

SIP410/13-15
UT DATE: APRIL 6, 1981 (1)

AVERAGE IO PHASE = 293.7
AVERAGE IO SYS III = 311.5

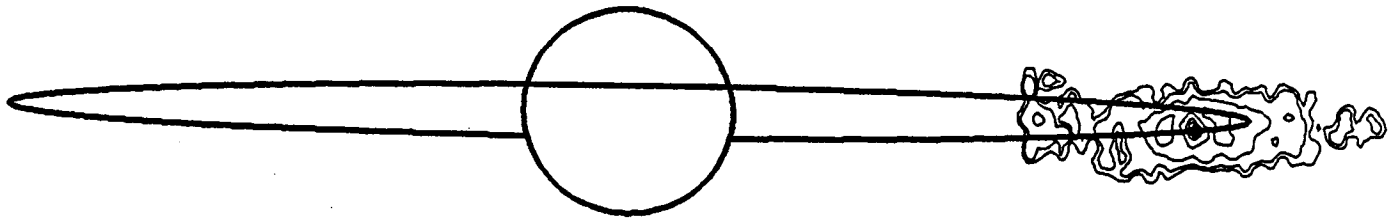

Appendix V

Fully Reduced 1981 Sodium Cloud Images: Study 5

Appendix V

1981 Region B/C East Images:
Comparison for Similar Io System III Longitude Angles

UT Date	Image ID Number (Tape/Frames)	Mid-Point Condition: Io System III Longitude (deg)	Mid-Point Condition: Io Phase Angle (deg)	Image Set
12 May (1)	SIP 420/6-8	159.8	48.3	-
12 May (2)	SIP 420/10-12	180.0	54.4	-
5 May (1)	SIP 418/10-12	186.1	68.1	-
5 May (2)	SIP 418/13-16	204.2	73.6	-
12 May (3)	SIP 420/15-20	217.8	65.8	5.A
28 Apr (1)	SIP 415/27-29	221.3	90.5	5.A
12 May (4)	SIP 420/21-23	247.1	74.7	-
5 May (3)	SIP 418/24-26	259.3	90.2	-
28 Apr (2)	SIP 415/43-45	293.9	112.4	-
28 Apr (3)	SIP 415/44-46	298.5	113.9	5.B
5 May (4)	SIP 418/31-33	299.6	102.5	5.B
6 Jun (1)	SIP 424/10-12	300.3	102.6	5.B
12 May (5)	SIP 420/30-32	301.8	91.2	5.B

159.8°

SIP420/6-8

UT DATE: MAY 12, 1981 (1)

AVERAGE IO PHASE = 48.3

AVERAGE IO SYS III = 159.8

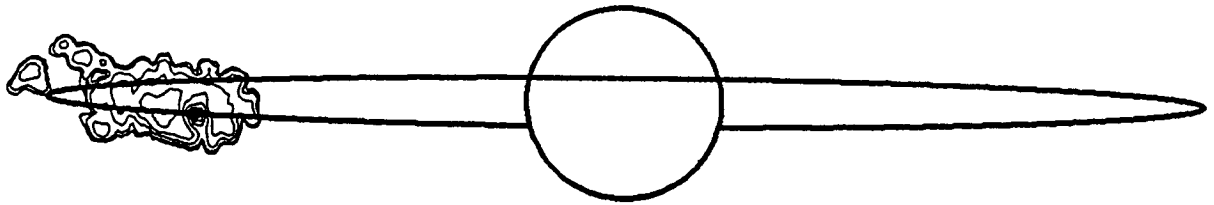

180.0°

SIP420/10-12

UT DATE: MAY 12, 1981 (2)

AVERAGE Io PHASE = 54.5

AVERAGE Io SYS III = 180.0

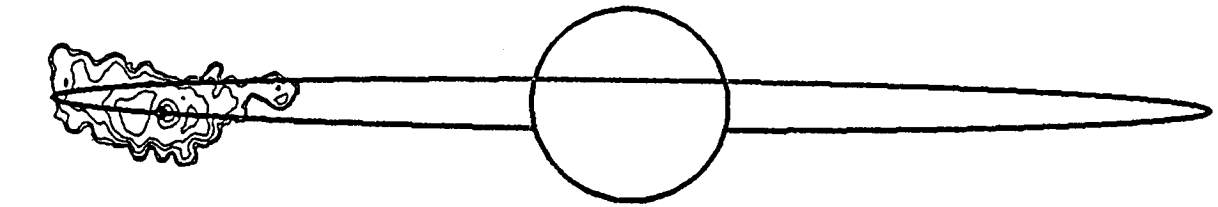

186.1°

SIP418/10-12

UT DATE: MAY 5, 1981 (1)

AVERAGE IO PHASE = 68.1

AVERAGE IO SYS III = 186.1

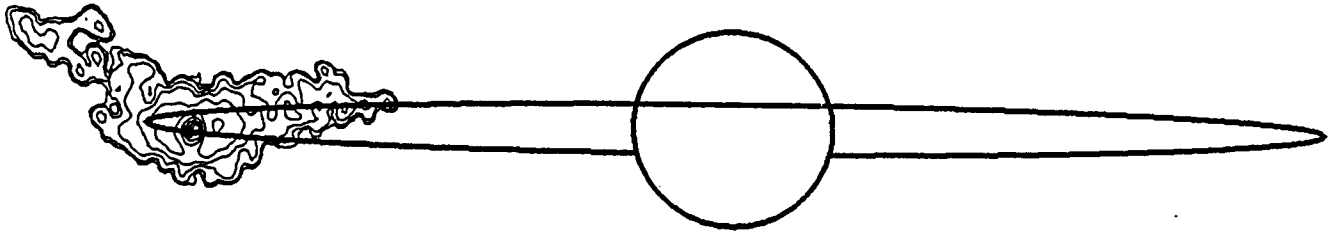

204.2°

SIP418/13-16

UT DATE: MAY 5, 1981 (2)

AVERAGE IO PHASE = 73.6

AVERAGE IO SYS III = 204.2

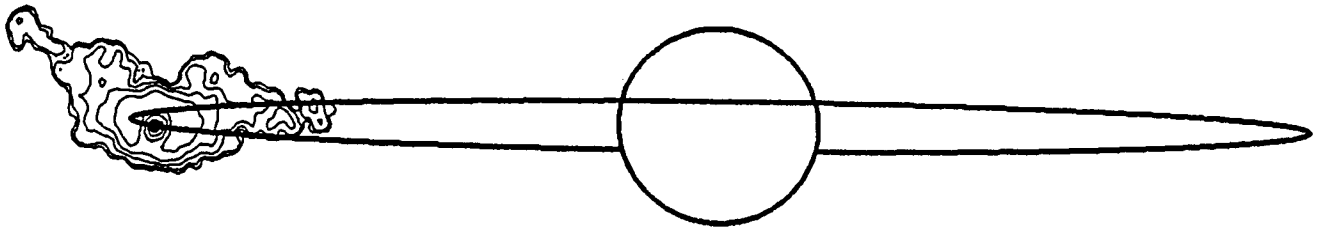

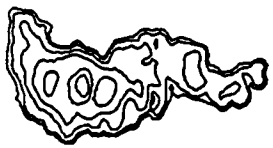

217.8°
Image Set: 5.A

SIP420/15-20

UT DATE: MAY 12, 1981 (3)

AVERAGE IO PHASE = 65.8

AVERAGE IO SYS III = 217.8

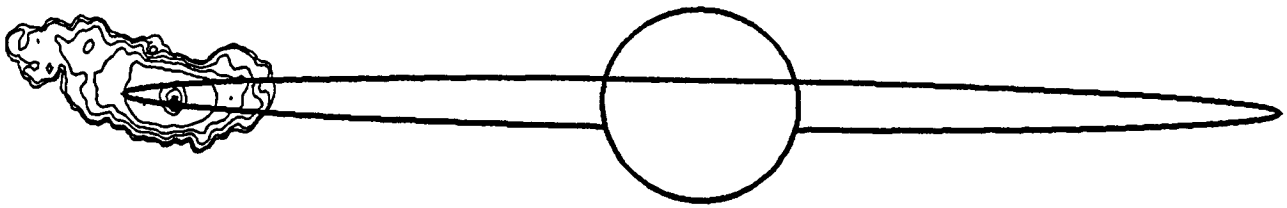

221.3°
Image Set: 5.A

SIP415/27-29

UT DATE: APRIL 28, 1981 (1)

AVERAGE IO PHASE = 90.5

AVERAGE IO SYS III = 221.3

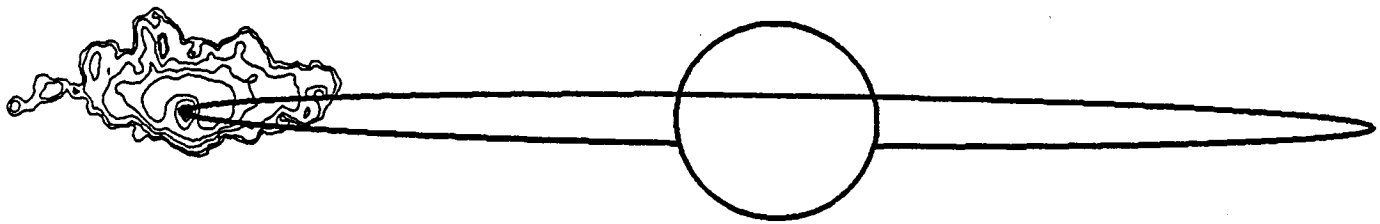

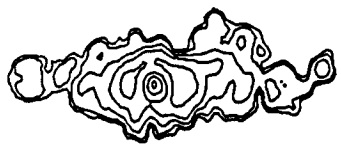

247.1°

SIP420/21-23

UT DATE: MAY 12, 1981 (4)

AVERAGE IO PHASE = 74.7

AVERAGE IO SYS III = 247.1

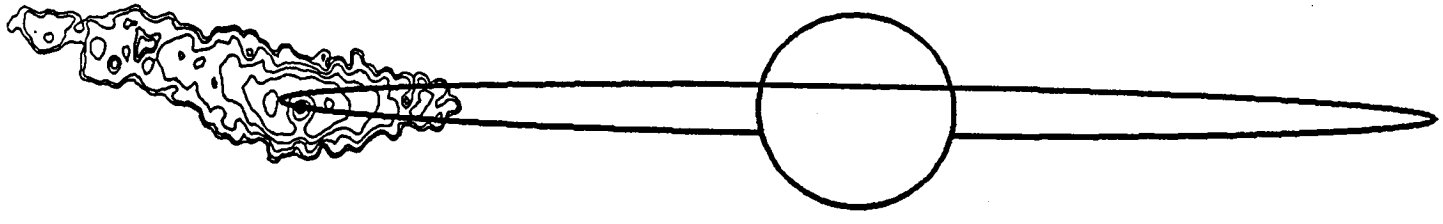

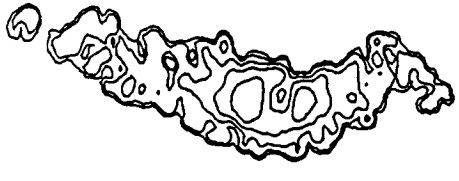

259.3°

SIP418/24-26

UT DATE: MAY 5, 1981 (3)

AVERAGE IO PHASE = 90.2

AVERAGE IO SYS III = 259.3

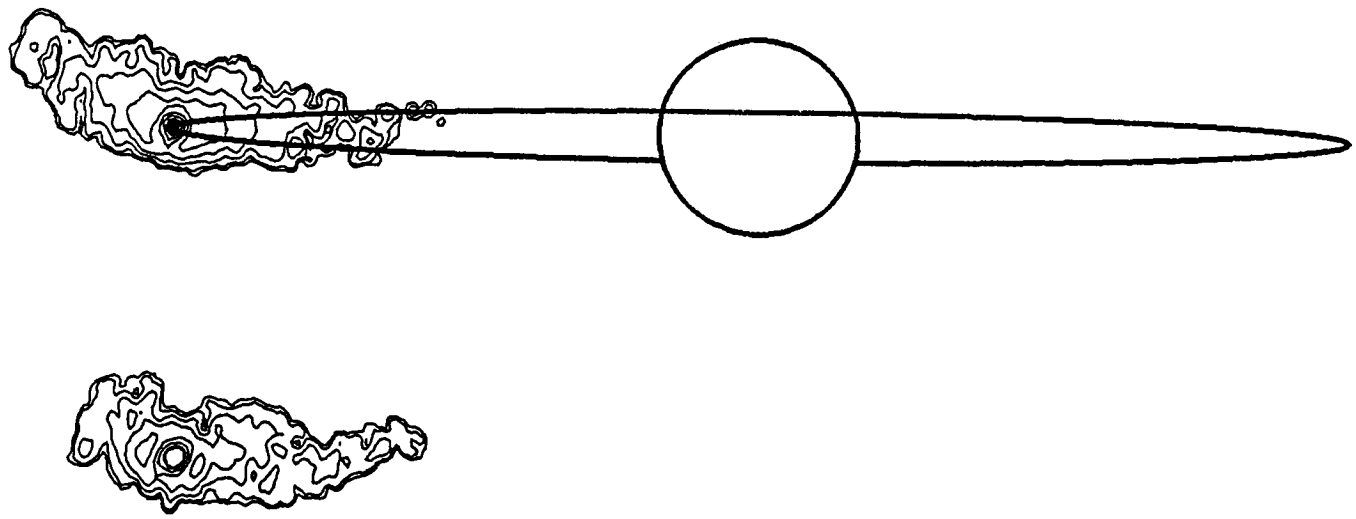

293.9°

SIP415/43-45

UT Date: April 28, 1981 (2)

Average Io Phase = 112.4

Average Io Sys III = 293.9

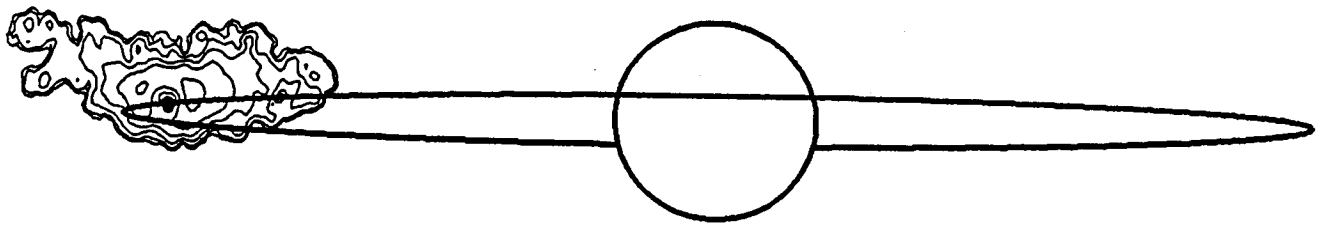

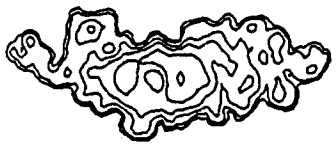

298.5°
Image Set: 5.B

SIP415/44-46

UT DATE: APRIL 28, 1981 (3)

AVERAGE IO PHASE = 113.9

AVERAGE IO SYS III = 298.5

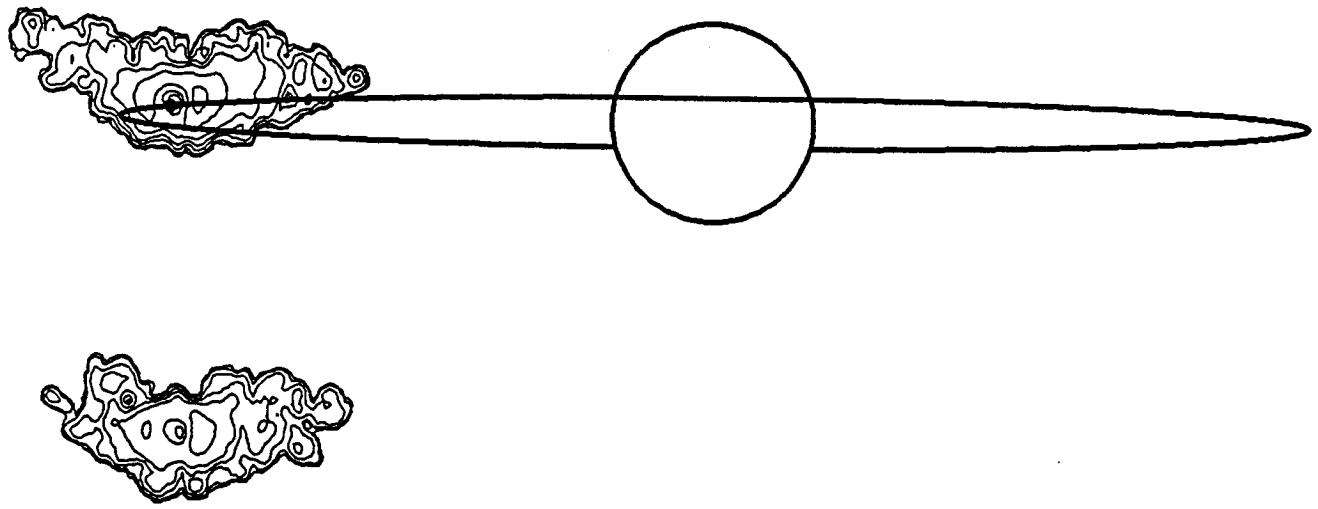

299.6°
Image Set: 5.B

SIP418/31-33
UT DATE: MAY 5, 1981 (4)

AVERAGE IO PHASE = 102.5
AVERAGE IO SYS III = 299.6

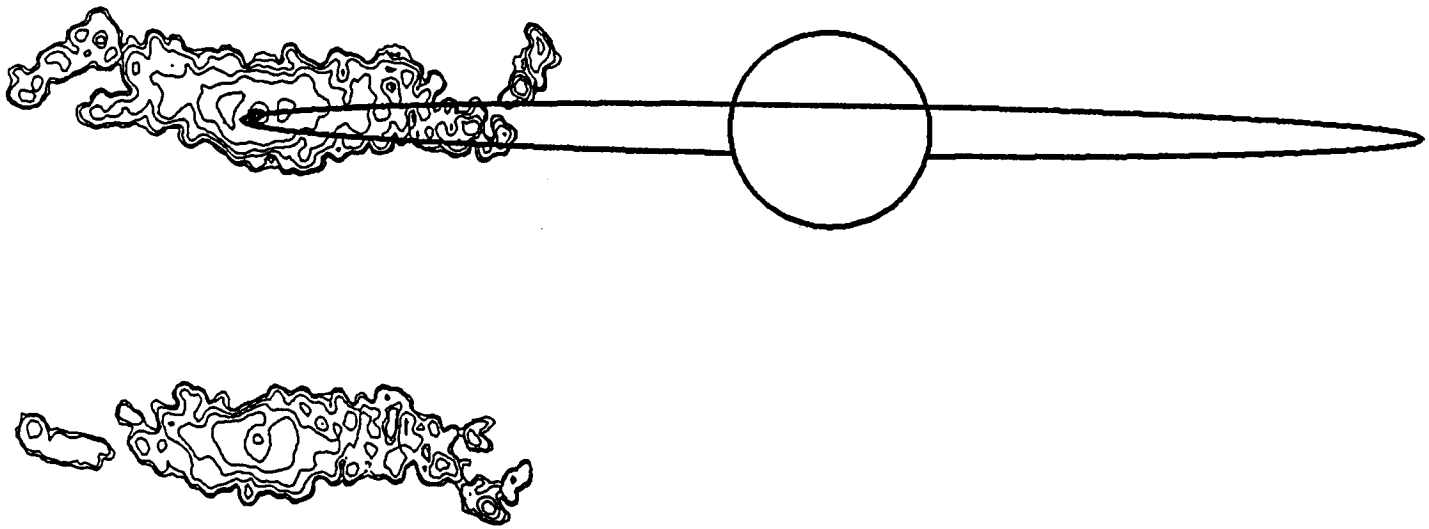

300.3°
Image Set: 5.B

SIP424/10-12
UT DATE: JUNE 6, 1981 (1)

AVERAGE IO PHASE = 102.6
AVERAGE IO SYS III = 300.3

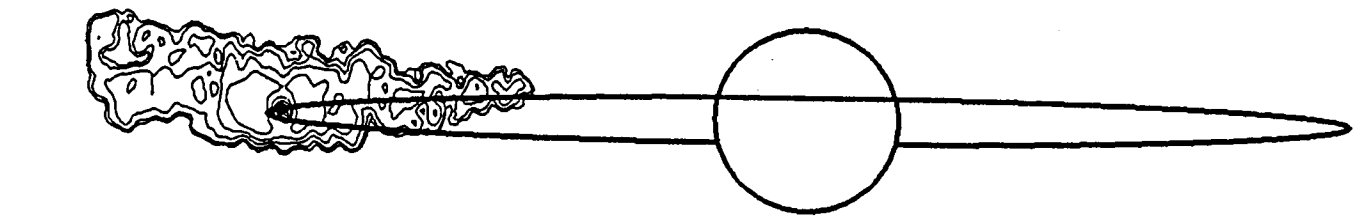

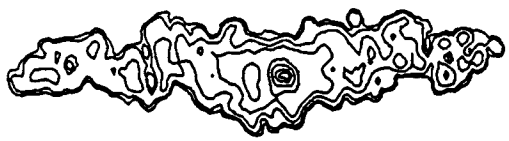

301.8°
Image Set: 5.B

SIP420/30-32
UT DATE: MAY 12, 1981 (5)

AVERAGE IO PHASE = 91.2
AVERAGE IO SYS III = 301.8

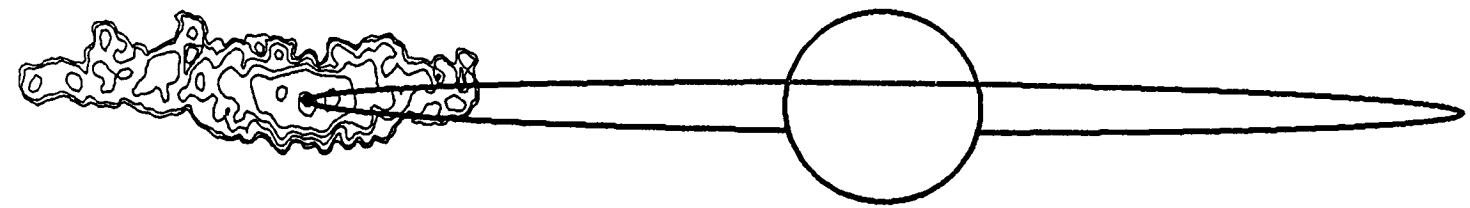

Appendix V

1981 Region B/C West Images: Comparison for Similar Io System III Longitude Angles

UT Date	Image ID Number (Tape/Frames)	Mid-Point Condition: Io System III Longitude (deg)	Mid-Point Condition: Io Phase Angle (deg)	Image Set
4 May (6)	SIP 417/36-39	23.9	269.3	-
13 May (1)	SIP 421/21-23	108.4	252.6	-
29 Apr (1)	SIP 416/4-6	138.5	285.7	5.C
13 May (2)	SIP 421/27-28	139.8	262.3	5.C
29 Apr (2)	SIP 416/7-9	154.2	290.5	-
13 May (3)	SIP 421/32-33	168.0	270.9	-
6 May (1)	SIP 419/19-21	178.3	286.1	-
13 May (4)	SIP 421/34-36	183.5	275.7	-
6 May (2)	SIP 419/22-24	194.0	290.9	-
13 May (5)	SIP 421/37-39	201.1	281.1	-
13 May (6)	SIP 421/40-42	217.5	286.2	5.D
14 Jun (1)	SIP 425/6-9	222.1	286.9	5.D
4 May (1)	SIP 417/8-10	223.1	219.7	5.D
13 May (7)	SIP 421/43-45	234.1	291.2	5.E
14 Jun (2)	SIP 425/9-12	237.6	291.6	5.E
13 May (8)	SIP 421/45-47	245.7	294.8	5.F
4 May (2)	SIP 417/13-15	249.2	227.8	5.F
4 May (3)	SIP 417/16-18	266.8	233.2	-
4 May (4)	SIP 417/20-22	291.7	240.9	-
6 Apr (1)	SIP 410/13-15	311.5	293.7	-
4 May (5)	SIP 417/27-29	331.9	253.3	-

23.9°

SIP417/36-39
UT Date: May 4, 1981 (6)

Average Io Phase = 269.3
Average Io Sys III = 23.9

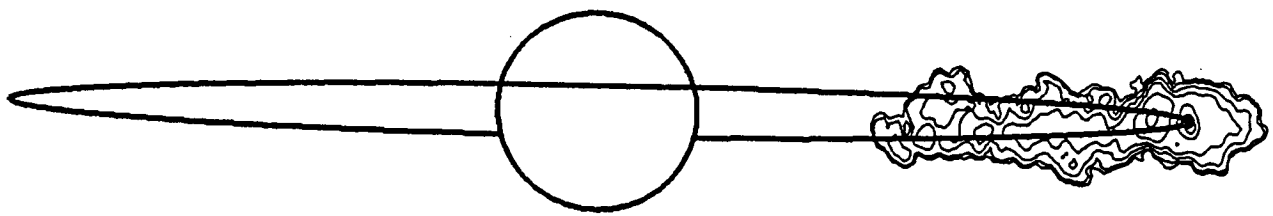

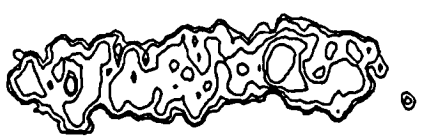

108.4°

SIP421/21-23
UT DATE: MAY 13, 1981 (1)

AVERAGE IO PHASE = 252.6
AVERAGE IO SYS III = 108.4

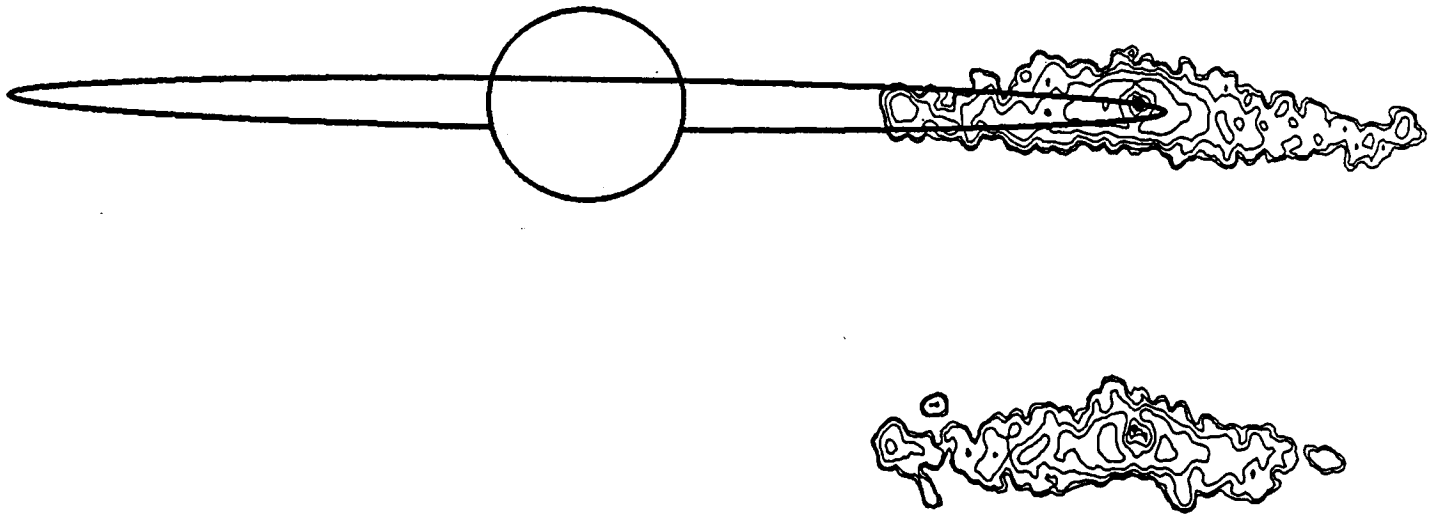

138.5°
Image Set: 5.C

SIP416/4-6
UT DATE: APRIL 29, 1981 (1)

AVERAGE IO PHASE = 285.7
AVERAGE IO SYS III = 138.5

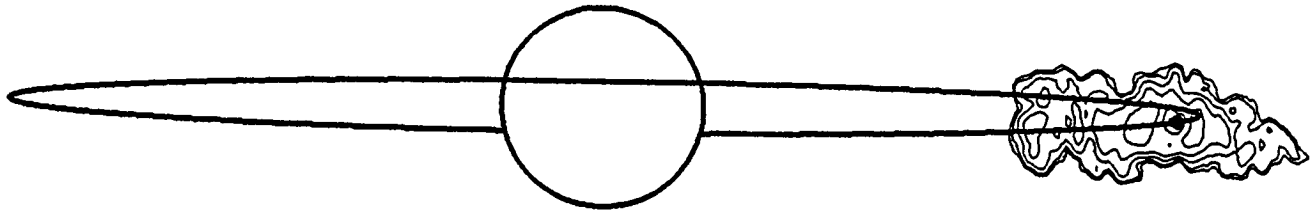

139.8°
Image Set: 5.C

SIP421/27-28
UT DATE: MAY 13, 1981 (2)

AVERAGE IO PHASE = 262.3
AVERAGE IO SYS III = 139.8

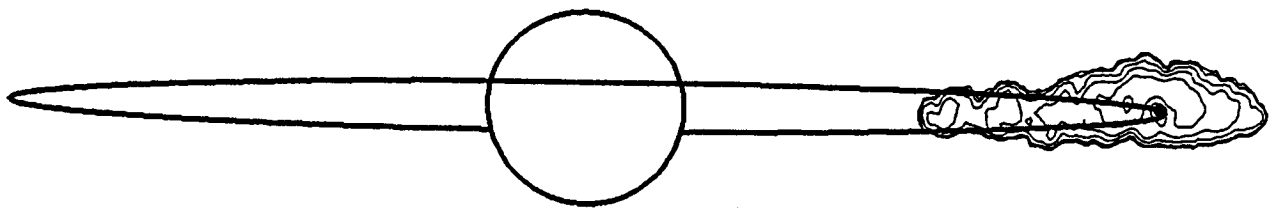

154.2°

SIP416/7-9
UT Date: April 29, 1981 (2)

Average Io Phase = 290.5
Average Io Sys III = 154.2

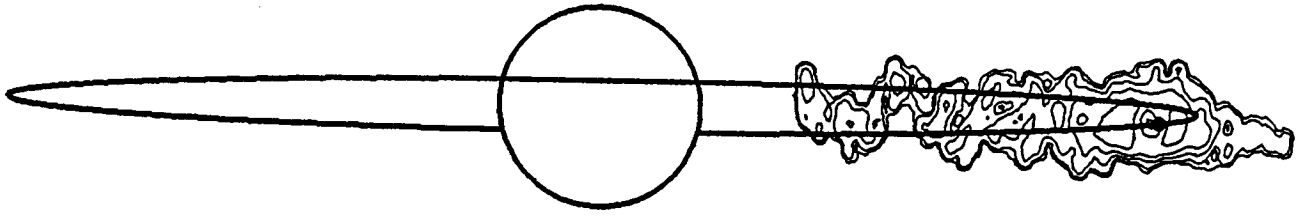

168.0°

SIP421/32-33

UT DATE: MAY 13, 1981 (3)

AVERAGE IO PHASE = 270.9

AVERAGE IO SYS III = 168.0

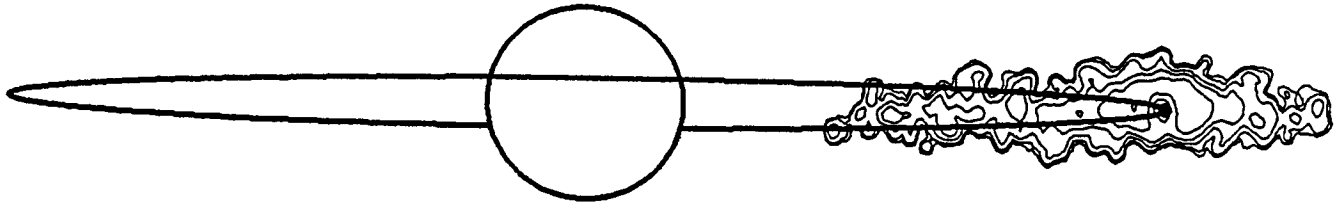

178.3°

SIP419/19-21

UT DATE: MAY 6, 1981 (1)

AVERAGE IO PHASE = 286.1

AVERAGE IO SYS III = 178.3

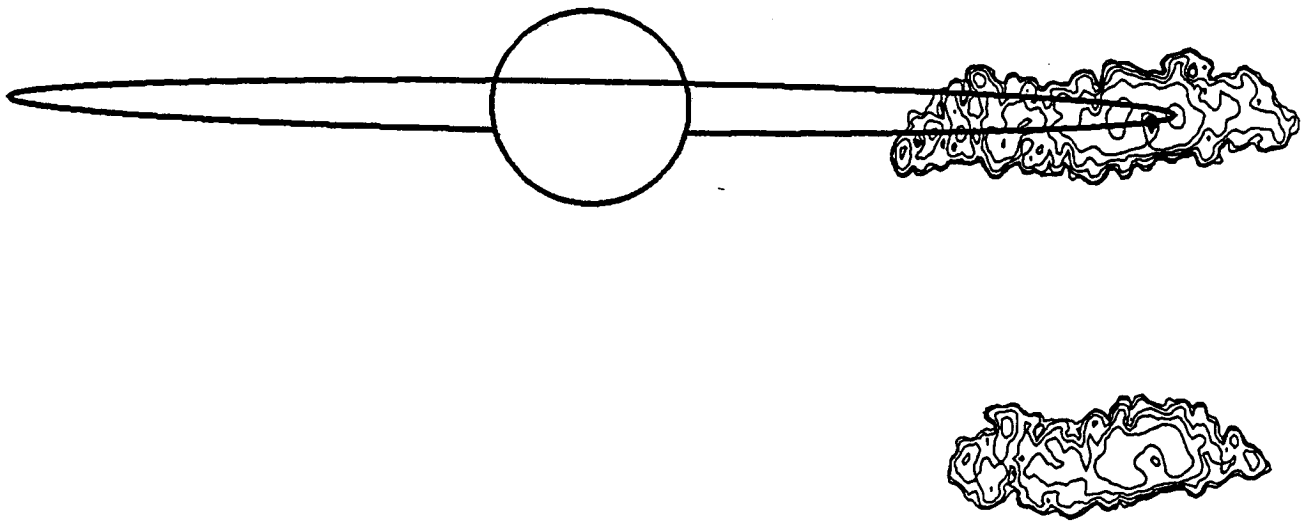

183.5°

SIP421/34-36

UT DATE: MAY 13, 1981 (4)

AVERAGE IO PHASE = 275.7

AVERAGE IO SYS III = 183.5

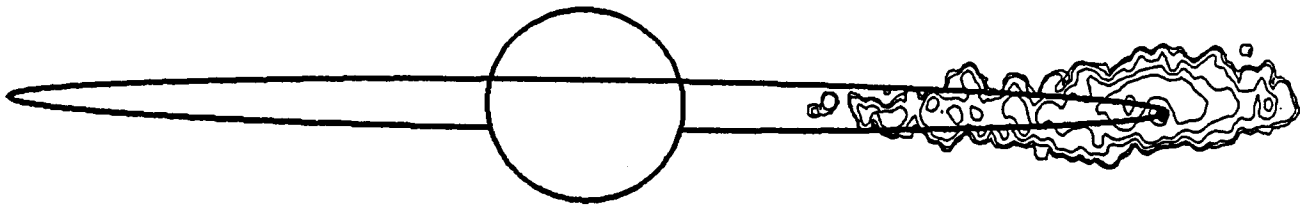

194.0°

SIP419/22-24

UT DATE: MAY 6, 1981 (2)

AVERAGE IO PHASE = 290.9

AVERAGE IO SYS III = 194.0

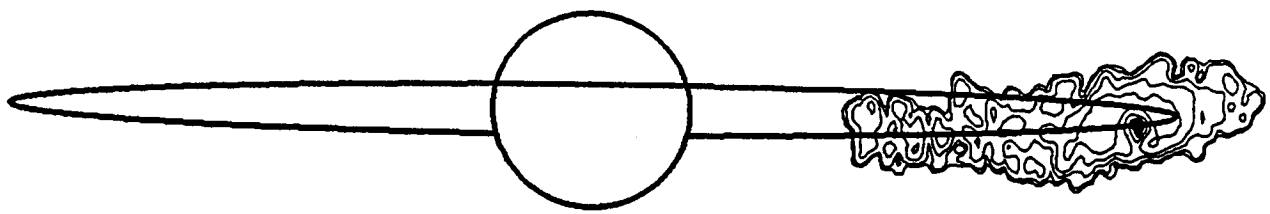

201.1°

SIP421/37-39

UT DATE: MAY 13, 1981 (5)

AVERAGE IO PHASE = 281.1

AVERAGE IO SYS III = 201.1

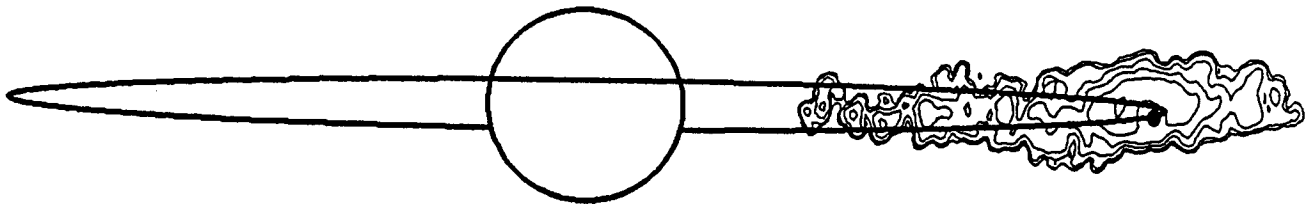

217.5°
Image Set: 5.D

SIP421/40-42
UT DATE: MAY 13, 1981 (6)

AVERAGE IO PHASE = 286.2
AVERAGE IO SYS III = 217.5

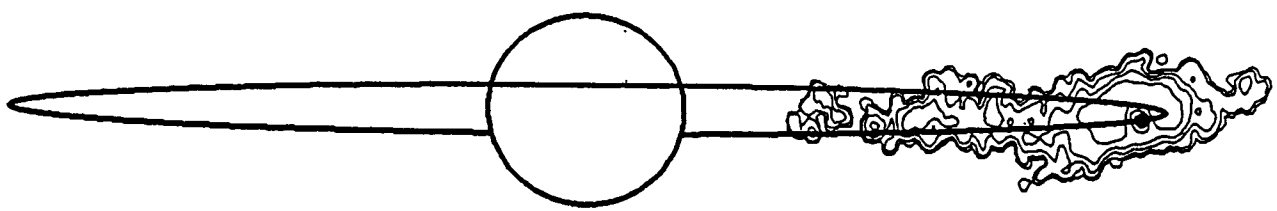

222.1°
Image Set: 5.D

SIP425/6-9
UT DATE: JUNE 14, 1981 (1)

AVERAGE IO PHASE = 286.9
AVERAGE IO SYS III = 222.1

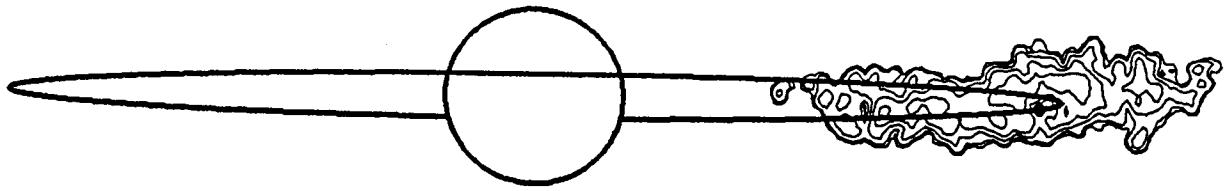

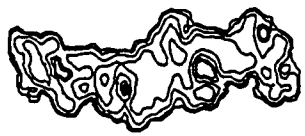

223.1°
Image Set: 5.D

SIP417/8-10

UT DATE: MAY 4, 1981 (1)

AVERAGE IO PHASE = 219.7

AVERAGE IO SYS III = 223.1

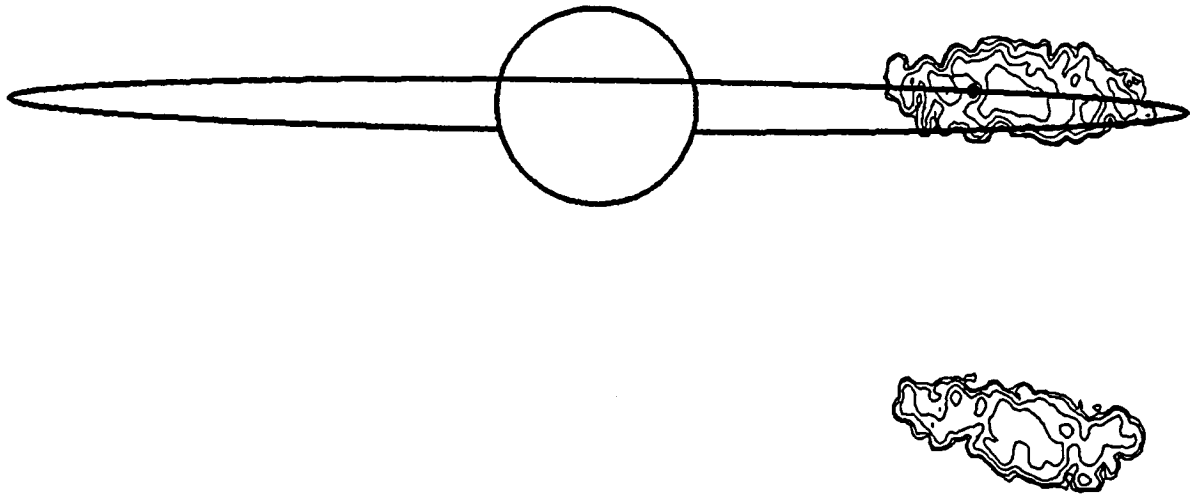

234.1°
Image Set: 5.E

SIP421/43-45
UT DATE: MAY 13, 1981 (7)

AVERAGE IO PHASE = 291.2
AVERAGE IO SYS III = 234.1

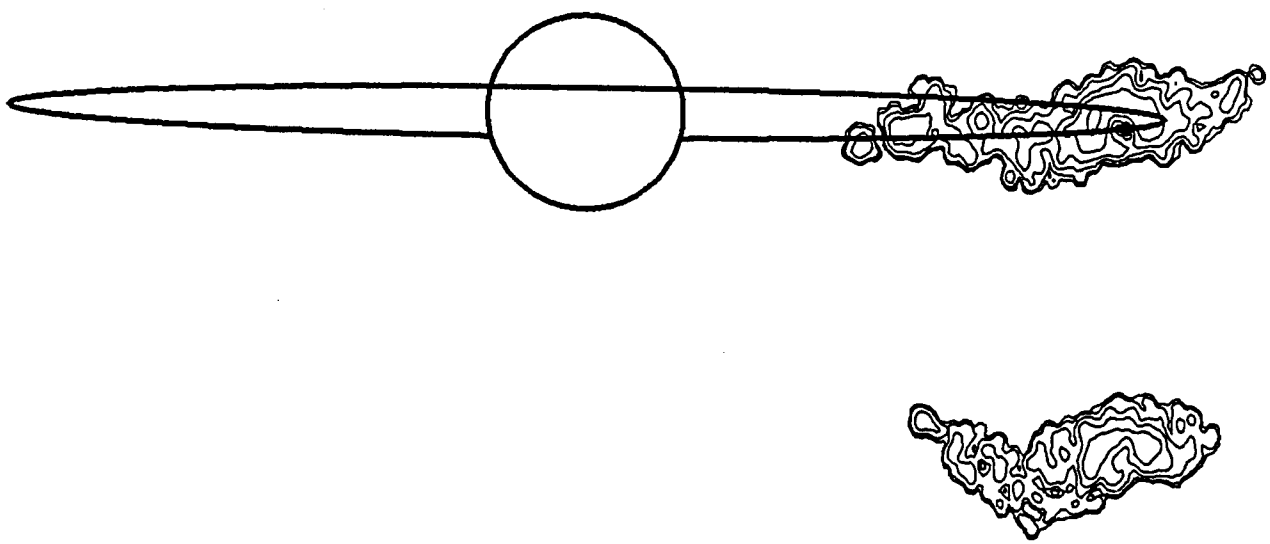

237.6°
Image Set: 5.E

SIP425/9-12
UT DATE: JUNE 14, 1981 (2)

AVERAGE Io PHASE = 291.6
AVERAGE Io SYS III = 237.6

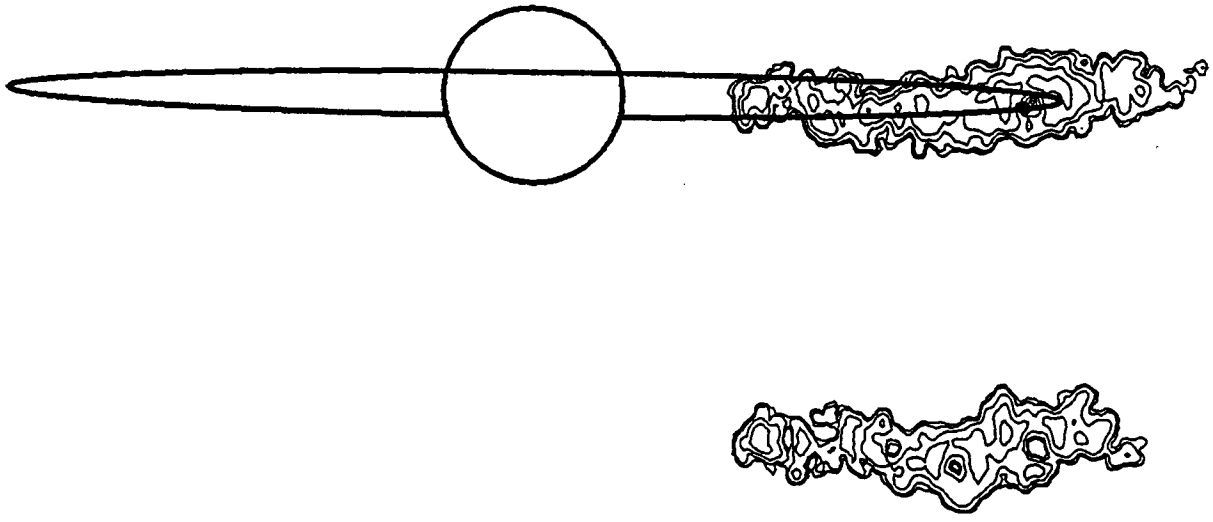

245.7°
Image Set: 5.F

SIP421/45-47
UT DATE: MAY 13, 1981 (8)

AVERAGE Io PHASE = 294.8
AVERAGE Io SYS III = 245.7

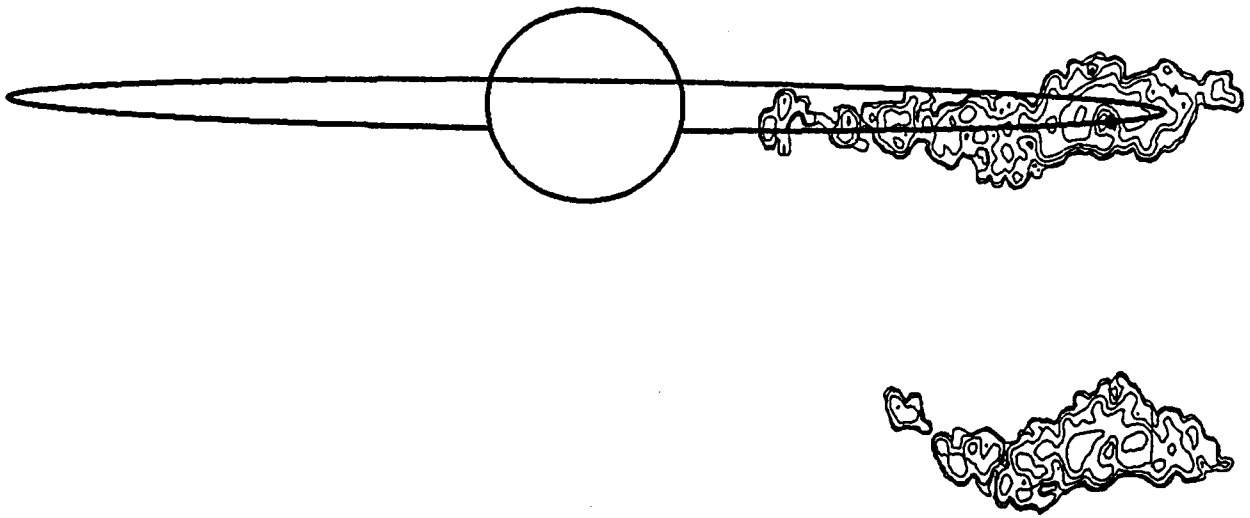

249.2°
Image Set: 5.F

SIP417/13-15
UT DATE: MAY 4, 1981 (2)

AVERAGE IO PHASE = 227.8
AVERAGE IO SYS III = 249.2

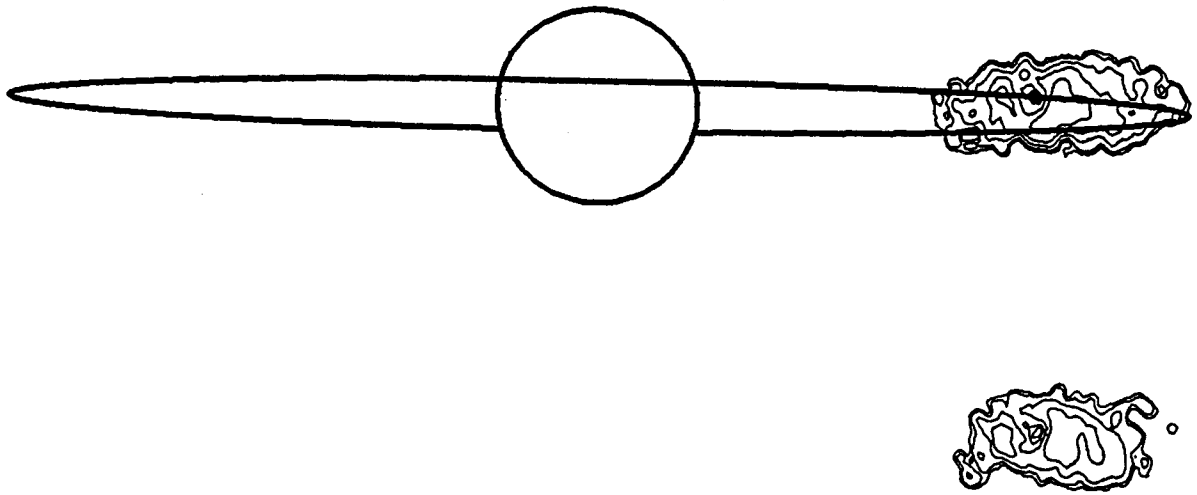

266.8°

SIP417/16-18
UT Date: May 4, 1981 (3)

Average Io Phase = 233.2
Average Io Sys III = 266.8

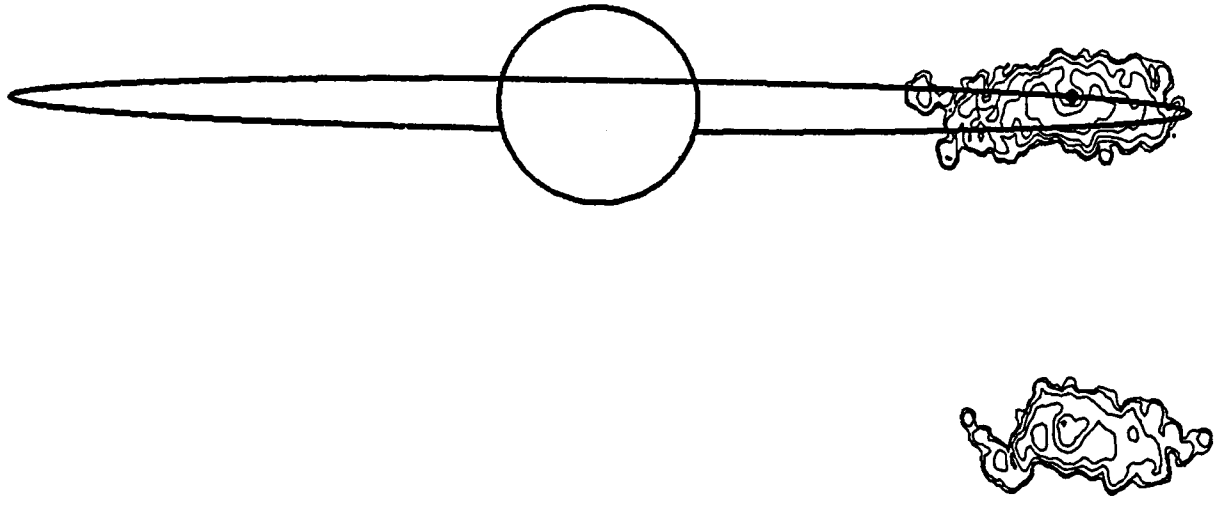

291.7°

SIP417/20-22

UT DATE: MAY 4, 1981 (4)

AVERAGE IO PHASE = 240.9

AVERAGE IO SYS III = 291.7

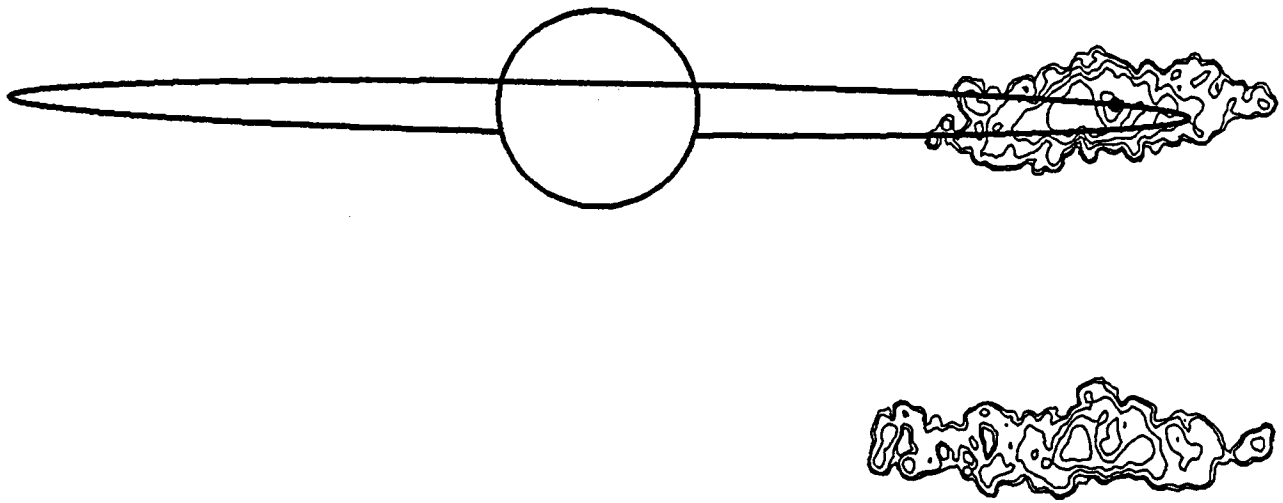

311.5°

SIP410/13-15

UT DATE: APRIL 6, 1981 (1)

AVERAGE IO PHASE = 293.7

AVERAGE IO SYS III = 311.5

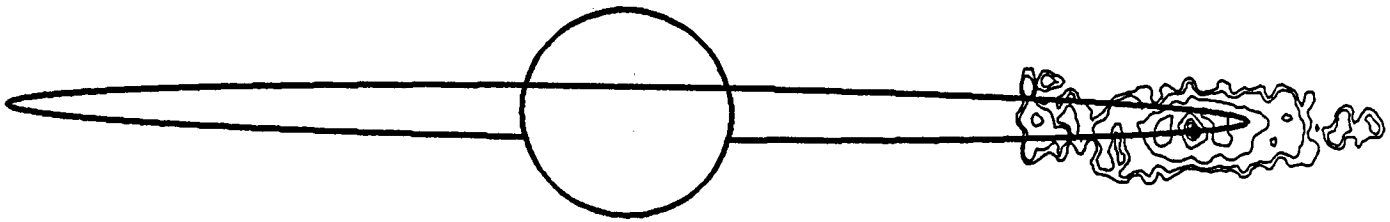

331.9°

SIP417/27-29

UT DATE: MAY 4, 1981 (5)

AVERAGE IO PHASE = 253.3

AVERAGE IO SYS III = 331.9

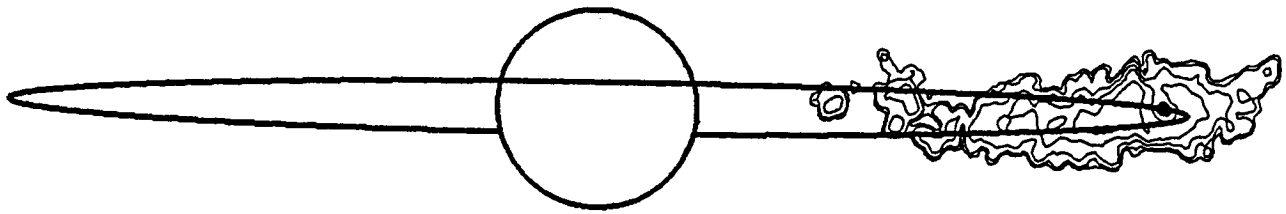

Appendix VI

A General Model for Io's Neutral Gas Clouds.
I. Mathematical Description

A General Model for Io's Neutral Gas Clouds.I. Mathematical Description

by

W. H. Smyth
M.R. Combi

To appear in
The Astrophysical Journal
April 1988

Atmospheric and Environmental Research, Inc.
840 Memorial Drive, Cambridge, Massachusetts

ABSTRACT

A general mathematical formalism for calculating the physical properties of any of Io's neutral gas clouds (Na, K, O, S, SO_2) is presented. The dynamical effects of both the gravitational fields of Io and Jupiter and solar radiation pressure are included, in addition to the many complex space- and time-dependent interactions that occur between the neutral clouds and the plasma torus. Earlier models have not included these complex space- and time-dependent interactions. The importance of this new model in studying both the plasma conditions prevalent in the inner planetary magnetosphere and the nature of Io's local atmosphere is discussed. A numerical method for evaluating the physical properties of the neutral clouds using the new model has been developed and is described. The mathematical formalism and numerical method are applied to a study of the Io sodium cloud in a companion paper.

1. Introduction

During the past two decades, Io, the innermost of the four Galilean satellites of Jupiter, and its profound influence on the planetary magnetosphere have been one of the most exciting and intensely studied subjects in the solar system. The first evidence that Jupiter and Io constituted a complex interactive system was introduced by Bigg (1964), who discovered that some of the decametric radio emission of Jupiter was directly influenced by the satellite's orbital and magnetic location about the planet. Since then, a large information base has been accumulated from ground-based observations, rocket measurements, Earth-orbiting satellites, and four spacecraft encounters with Jupiter: Pioneer 10 (4 December 1973), Pioneer 11 (2 December 1974), Voyager 1 (5 March 1979), and Voyager 2 (9 July 1979).

From ensuing studies of this information base, a picture for the Io-Jupiter system is emerging and slowly coming into focus. Io has a local atmosphere, although it is not well characterized or structurally understood. Io has extended neutral atmospheres or clouds that exist large distances beyond the gravitational grasp of the satellite and fill partial or somewhat incomplete toroidal-shaped volumes around Jupiter. These clouds occupy an overlapping volume with the Io plasma torus - the densest part of the planetary magnetosphere - and interact with it through collisional processes including ionization and charge exchange reactions. These interactions not only shape the spatial morphology of the clouds but also supply heavy ions to the torus and affect the composition, structure, and energy budget of the plasma torus and its extension into the larger magnetosphere. The primary heavy ions that compose the corotating (or nearly corotating) plasma torus are known to be oxygen (O^+, O^{++}) and sulfur (S^+, S^{++}, S^{+++}), although the relative abundances of these ions throughout the torus volume (even for a two-dimensional longitudinally averaged picture) are still not well established. Io and its local atmosphere also interact with the corotating plasma torus and planetary magnetic field in ways that are yet to be fully understood. Some of these interactions almost certainly provide ions and energy directly to the plasma torus as well as drive escape mechanisms for gases in the local atmosphere.

For purposes of this paper, a brief review of Io's local and extended atmospheres and their relevant interactions with the plasma torus will be

given in section 2. This will provide necessary information for understanding the evolution and motivation for developing the new general neutral gas cloud model presented in sections 3 and 4. A more complete discussion of Io may be found in several excellent review articles (Nash et al. 1986; Brown, Pilcher and Strobel 1983; Fanale et al. 1982, 1977; Kumar and Hunten 1982; Pilcher and Strobel 1982; Brown and Yung 1976). The paper concludes with a brief summary in Section 5. The new model is applied to the sodium cloud in a companion paper (Smyth and Combi 1988). In a series of future papers, the new model will also be applied to other neutral clouds of Io (K, O, S, SO_2).

2. Historical Perspective

Our understanding of Io's local atmosphere, although far from complete, has grown steadily since 1964, when Binder and Cruikshank (1964) reported an anomalous brightening of the satellite's surface as it emerged from eclipse. This posteclipse brightening suggested a dynamic and volatile atmosphere for Io, for which in 1971 an upper limit surface pressure of approximately 10^{-7} bars was deduced by Smith and Smith (1972) from occultation of the star β Scorpii by the satellite. In the summer of 1972, the discovery by Brown (1974) of sodium optical emission from Io's vicinity and the subsequent observations in 1973 by Trafton, Parkinson, and Macy (1974) of an extended sodium cloud well beyond the gravitational reach of Io confirmed the presence of a local atmosphere. This discovery also sparked a large number of Earth-based observations of the sodium cloud that have continued over the intervening 16 years. An ionosphere for Io discovered from analyses of Pioneer 10 S-band radio occultation data (Kliore et al. 1974) provided additional information to characterize the satellite's local atmosphere and its possible interactions with the Jovian magnetosphere (Cloutier et al. 1978). A quantum leap forward in understanding Io's local atmosphere was obtained by the Voyager 1 spacecraft's discovery of active volcanic plumes (Morabito et al. 1979) and detection of SO_2 gas ($\sim 10^{-7}$ bars surface pressure) over one of many hot spots on Io (Pearl et al. 1979). Although SO_2 now appears to be the major constituent of the atmosphere (Kumar 1979), the vertical structure, global extent, and surface density variations of the atmosphere still remain uncertain even after much theoretical analysis (Kumar 1980, 1982, 1984, 1985; Matson and Nash 1983; Summers 1984; Ingersoll, Summers, and Schlipf 1985; Lunine and Stevenson 1985; Summers et al. 1986). Insightful information for the density of sodium in Io's local atmosphere is just beginning to emerge, based upon analysis of novel Earth-based observations recently obtained by Schneider et al. (1985, 1987) of absorption signatures at the sodium D-line wavelengths of reflected sunlight from Europa as it was eclipsed by Io.

The discovery of the Io sodium cloud marked the first of four extended atmospheres that have been detected to date for the satellite as summarized in Table 1. The three more recently detected neutral clouds for Io are potassium in 1975 and atomic oxygen in 1980, both from ground-based observations of optical lines, and atomic sulfur in 1981 from rocket-borne instruments

measuring ultraviolet emissions. A fifth cloud of neutral SO_2 is expected, because of the presence of a small amount of SO_2^+ ions measured in the plasma torus (Bagenal and Sullivan 1981; Bagenal 1985), but has not been detected directly. For sodium, more than 1000 observations of its spatial brightness have been made in the last 16 years, with most of the earlier measurements providing only slit-averaged intensity values and most of the more recent measurements providing increasingly higher-quality two-dimensional image data. For the dimmer potassium cloud (about one-twentieth the brightness of the sodium cloud), about 200 slit-averaged observations have been made almost entirely by Trafton (1975, 1981), who presented a survey of this gas cloud that exhibited spatial and temporal variations similar to those documented for the Io sodium cloud. For the much dimmer atomic oxygen and atomic sulfur clouds, only a very few slit-averaged detection observations have been acquired.

The presence of neutral clouds for Io provides a largely unexplored but rich potential for studying both the plasma conditions prevalent in the inner planetary magnetosphere and the nature of Io's local atmosphere. Sodium is by far the best neutral cloud to use as a probe for these purposes, because it is the brightest and most extensively observed and is (together with potassium) sensitive to spatial and temporal changes in the plasma torus because of its small electron impact ionization lifetime (~ 1-2 hours) near Io's orbit. Early observations acquired in 1973 and 1974 (i.e., pre- and post-Pioneer 10) by Macy and Trafton (1975 a,b) and Münch and Bergstralh (1977), for example, first suggested the presence of a magnetospheric sink for sodium near Io's orbit that was both radially asymmetric and oscillatory. The radial asymmetry was suggested by the presence of a predominantly forward sodium cloud, and the oscillatory nature was suggested by time dependent changes in the sodium brightness north and south of the satellite that were correlated with the satellite's magnetic latitude (Trafton and Macy 1975; Trafton 1980). As will be shown in the companion paper, the predominantly forward cloud is indeed naturally produced by the radial asymmetry of the plasma torus for sodium ejected from Io at relatively slow speeds (~ 3 km sec^{-1}) as first suggested from these early observations. These slow speed atoms may be energized by magnetospheric ions both directly through scattering of neutrals from the local atmosphere (or surface, if regions of low density exist) as discussed in

a number of papers (Sieveka and Johnson 1984; Cheng 1984; Lanzerotti and Brown 1983; Brown, Pilcher, and Strobel 1983; Ip 1982; Matson, Johnson, and Fanale 1974), and indirectly through multicollisional processes resulting in atmospheric sputtering (Summers, Yung, and Haff 1983; Haff, Watson, and Yung 1981; McGrath and Johnson 1987) or blowoff (Hunten 1985). More recent observations of the sodium cloud have shown, for example, (1) well-defined spatial zones that become temporally deficient of atoms, perhaps as a result of locally (likely System III) enhanced ionization (Goldberg, Garneau, and LaVoie 1984), (2) directional features produced by high-velocity ($\sim$ 20 km sec^{-1}) sodium driven elastically by the magnetospheric wind from the local atmosphere at near right angles to Io's orbit and preferentially from the equatorial regions (Pilcher et al. 1984), and (3) very fast ($\lesssim$ 60 km sec^{-1}) narrowly collimated jets of sodium driven directly ahead of the satellite by charge exchange reactions with the plasma torus (Trauger 1984, 1985). Although the oxygen and sulfur clouds are only bright enough to be barely detected, physical insight acquired for the bright sodium cloud may be adopted where appropriate in O, S and SO_2 cloud models. These atomic and molecular cloud models so constructed then become enhanced tools themselves to determine ion loading rates, plasma mass loading rates, and ion energy input rates to the plasma torus as well as to specify the character and source rate of neutral gases escaping from Io's local atmosphere (Smyth and Shemansky 1983).

Models for the neutral clouds of Io are essential in probing and recovering physical information from spatial brightness observations of Io's extended atmospheres and relating this information to conditions in Io's local atmosphere and the planetary magnetosphere. The development of cloud models for Io was historically initiated for the sodium cloud in the early 1970's and has evolved during the last decade with progressively more complete descriptions for the source, lifetime, and orbital dynamics of sodium atoms in the Jupiter system. Only in the last few years have models for the Io oxygen and sulfur clouds (Smyth and Shemansky 1983) and the Io potassium cloud (Smyth and Combi 1984) been developed. A general model, appropriate to any of these neutral gas clouds of Io, has now been formulated and is presented in Sections 3 and 4.

3. Mathematical Description for the Io Neutral Gas Clouds

a) Mathematical Approach

The basic mathematical approach is based upon the conservation in phase space of the one-particle distribution function $f(\vec{v},\vec{x},t)$ for a gas species. In brief, if at an initial time $t = t_b$ the distribution function can be specified, then the distribution function at a later time may, under certain circumstances of interest here, be simply related to its initial value by properly mapping its time evolution in phase space and including processes that modify its initial value during this time evolution. This conservation in phase space follows directly from the well-known Liouville theorem for an N-particle system upon integrating over the six phase-space coordinates of N-1 of these particles.

The general approach may be formally understood as follows. The one-particle distribution function in kinetic theory has the physical meaning that

$$f(\vec{v},\vec{x},t)\ d\vec{x}\ d\vec{v} \tag{1}$$

represents the (ensemble-average) number of atoms (or molecules) at time t in a spatial volume element $d\vec{x}$ about position $\vec{x}$, with velocities $d\vec{v}$ about $\vec{v}$. The time evolution of the one-particle distribution function is governed by the kinetic equation

$$\frac{\partial f}{\partial t} + \vec{v} \cdot \frac{\partial f}{\partial \vec{x}} + \frac{\vec{F}}{m} \cdot \frac{\partial f}{\partial \vec{v}} = \left(\frac{\delta f}{\delta t} \right) \tag{2}$$

where $\vec{F}$, which may in general depend on $(\vec{v},\vec{x},t)$, is the force experienced by the gas atoms (or molecules) due to macroscopic internal and external sources and m is the mass of a gas atom (or molecule). Furthermore, $(\delta f/\delta t)$ is the local rate of change of $f(\vec{v},\vec{x},t)$ due to processes such as collisions that may add or remove the (ensemble-average) number of atoms (or molecules) from an element of phase space. For binary collisions in a gas, for example, one obtains the Boltzmann equation when the right-hand side of the kinetic equation is represented by the Boltzmann collision integral (a nonlinear and integral function of the distribution function).

The time evolution or trajectory of a point in phase space $(\vec{v},\vec{x}) = (\vec{v}(t),\vec{x}(t))$ that is initially $(t=t_b)$ at a point $(\vec{v}_b,\vec{x}_b) = (\vec{v}(t_b),\vec{x}(t_b))$ is determined by solving the equations of motion for a gas atom (or molecule) of mass m

$$\vec{v}(t) = \frac{d\vec{x}(t)}{dt} \tag{3.a}$$

$$\frac{\vec{F}(\vec{v}(t),\vec{x}(t),t)}{m} = \frac{d\vec{v}(t)}{dt} \tag{3.b}$$

for this initial value problem. These equations of motion are by construction the characteristic equations of the kinetic equation, so that the left-hand side of the kinetic equation is the total time derivative of the distribution function. The kinetic equation thus reduces to

$$\frac{df}{dt} = \left(\frac{\delta f}{\delta t}\right) . \tag{4}$$

There exists a class of physical problems to which the Io gas clouds may be related in which the gas density is sufficiently low that gas atoms (or molecules) along their phase space trajectories do not collide with each other but may collisionally interact with other material (such as ions and electrons in a rarefied plasma) or photons (i.e., photoionization or photodissociation processes) so as to change the initial ensemble-average number of atoms. In this case, the right-hand side of the kinetic equation is linear in the distribution function and may be expressed in the general form

$$\left(\frac{\delta f}{\delta t}\right) = -\nu f + S , \tag{5}$$

where ν and S are independent of f but may depend in general upon $(\vec{v},\vec{x},t)$. Here ν is an effective loss rate and S is an effective source rate for the ensemble-average number of atoms in an element of phase space. Using expression (5) in equation (4), the kinetic equation can be explicitly integrated along the phase space trajectory to determine the distribution function at time t:

$$f(\vec{v}(t),\vec{x}(t),t) = f(\vec{v}_b,\vec{x}_b,t_b)\ P(t,t_b) + \int_{t_b}^{t} dt'\ S(\vec{v}(t'),\vec{x}(t'),t')\ P(t,t') \ . \tag{6}$$

Here

$$P(t_2,t_1) = \exp\left[-\int_{t_1}^{t_2} dt'\ \nu(\vec{v}(t'),\vec{x}(t'),t')\right] \tag{7}$$

is the probability that an ensemble-average number of gas atoms introduced at a time t_1 exist at a later time t_2 because of the effective loss rate ν. The distribution function at a time $t > t_b$ is then given by the initial distribution function reduced by this probability plus all new source contributions to the initial distribution function that have occurred in the time interval t_b to t with a proper decay loss included for these contributions.

The description of the gas may therefore be constructed in terms of a large number of phase space trajectories along which the ensemble-average number of atoms evolve in time based upon a set of initial conditions for the distribution function which properly simulate the boundary conditions of a particular physical problem. More specifically, the description of the gas can be fundamentally reduced to describing the time evolution of an ensemble packet of gas along its phase space trajectory. An ensemble packet is defined as the infinitesimal volume element containing the ensemble-average number of atoms that initially began its trip along the trajectory in the time interval t_b to $(t_b + dt)$. The physics of an ensemble packet appropriate for the Io neutral gas clouds is described in the next subsection.

The basic principle of the general mathematical approach described above has been employed in planetary science to develop models for a number of studies involving collisionless or nearly collisionless atmospheres. The basic principle has been, in fact, used with increasing regularity in the last two decades. These studies have included cometary atmospheres, planetary atmospheres, and satellite atmospheres for which major references are given in Table 2. A more general review of exospheric theories is given by Fahr and Shizgal (1983). The studies for Io's neutral gas clouds are perhaps the most complex subset of these exospheric problems appropriate to the linear interaction (5). This complexity results because of the inherent velocity, space,

and time dependence of both the force $\vec{F}$ in the equations of motion and the effective loss rate ν of neutrals in the plasma torus and also because of the form of the source term S which is described below.

For the Io neutral gas cloud, the source term S in equation (5) is a spatially distributed source that describes the creation of secondary cloud atoms produced by interactions of the magnetospheric plasma with only the primary gas cloud atoms (or molecules) initially ejected from the satellite. For atomic gas clouds, the distributed source is caused by charge exchange reactions between the extended cloud atoms and the corotating plasma torus ions. Elastic collisions between these ions and extended cloud atoms may also produce a contribution to the source term in equation (5) but this contribution may be significantly less important over the relatively short lifetime of the cloud. Primary cloud atoms have velocities relative to Io that are generally slow compared to the corotational ion speed (~57 km sec^{-1}) and, when removed by the atom-ion charge exchange reactions, create fast secondary cloud atoms that have a rather tightly confined velocity dispersion centered on the corotational speed. The fast secondary cloud atoms are thus created in a velocity volume of phase space that is generally discontinuous with the velocity volume of phase space containing the slow primary cloud atoms. For molecular gas clouds (e.g., SO_2 or SO), electron impact dissociative reactions very rapidly remove the primary cloud molecules (Shemansky 1984) and create other secondary cloud atoms (or molecules) that initially may have additional amounts of kinetic energy as dictated by the energetics of the reaction. Because of the rapid dissociative lifetime of molecules in the plasma torus, these dissociative sources are likely to be heavily confined near Io. A gas cloud of Io for the j^{th} neutral species may therefore be generally described by a primary and a secondary population of cloud atoms (or molecules) by formally dividing the one-particle distribution function (1) into two parts.

$$f_j = f_j^{(primary)} + f_j^{(secondary)} \quad . \tag{8}$$

The kinetic equation (4) with the right hand side given by expression (5) may thus be formally subdivided for the j species into equations for the primary and secondary atom (or molecule) populations

$$\frac{df_j^{(primary)}}{dt} = -\nu_j f_j^{(primary)} \tag{9.a}$$

$$\frac{df_j^{(secondary)}}{dt} = -\nu_j f_j^{(secondary)} + S_j \tag{9.b}$$

where the secondary source term may be written in the form

$$S_j = \sum_k C_{jk} f_k^{(primary)} , \tag{9.c}$$

where C_{jk} describes the creation rate of secondary cloud atoms (or molecules) of the j^{th} species from primary cloud atoms (or molecules) of the k^{th} species. The source term (9.c) therefore represents the secondary cloud atoms (or molecules) produced by all primary cloud atoms (or molecules). More generally, a source term similar to expression (9.c) may likewise be introduced if necessary to include third generation extended source terms produced by dissociation of secondary cloud molecules (e.g. $SO \rightarrow S + O$). Limiting the present development to second generation source terms, the description of a neutral cloud is then obtained by first solving equation (9.a) for the properties of the primary cloud atom (or molecule) population,

$$f_j^{(primary)}(\vec{v}(t),\vec{x}(t),t) = f_j^{(primary)}(\vec{v}_b,\vec{x}_b,t_b)\ P_j(t,t_b) \tag{10.a}$$

and then, second, determining S_j and solving expression (9.b) for the properties of the secondary cloud atom (or molecule) population,

$$f_j^{(secondary)}(\vec{v}(t),\vec{x}(t),t) = \int_{t_s}^{t} dt"\ S_j(\vec{v}(t"),\vec{x}(t"),t")P_j(t,t") \ . \tag{10.b}$$

where $f_j^{(secondary)}(\vec{v}_s,\vec{x}_s,t_s) = 0$ by selecting the initial point of the secondary cloud phase space trajectory $(\vec{v}_s,\vec{x}_s,t_s)$ at a point on the primary cloud phase space trajectory where the secondary cloud distribution originates and is hence zero by definition.

In this paper, a general model for the primary cloud atoms (or molecules) is explicitly developed and will include expressions to calculate the relevant

plasma input rates supplied to the plasma torus by the primary cloud. A model for the secondary cloud atoms (or molecules) is also given but is more briefly outlined. For simplicity, the general model developed will adopt the language appropriate to a gas cloud of atoms but, with slight generalization, will equally well apply to a molecular gas cloud. For a gas cloud of atoms, the primary cloud population is much brighter than the secondary cloud population in the general vicinity of Io's orbit, but the secondary cloud population extends throughout and beyond the planetary magnetosphere and provides a background density and cloud brightness into which the primary cloud population merges.

b) Physics of an Ensemble Packet

A neutral gas cloud of Io may be described for the primary atom population discussed above by following the spacetime history of neutral atoms ejected from the surface of the satellite (in low atmospheric density limit) or from the exosphere of the satellite (in the presence of a substantial atmosphere). Without loss of generality, a spherical exobase of radius R_E centered on Io is adopted. For a differential surface area element $d\Omega$ ($= R_E^2 \sin\Phi \, d\Phi d\Theta$) of the exobase centered on the angular direction $\hat{\Omega} = (\Theta,\Phi)$, let the neutral flux (number of atoms ejected per unit area, per unit initial velocity interval, per unit time) in the initial velocity interval $\vec{\omega}$ to $\vec{\omega} + d\vec{\omega}$ and at the absolute time t_b be denoted by $\phi(\vec{\omega},\hat{\Omega};t_b)$. The rate at which these atoms are ejected from the surface element is then

$$\phi(\vec{\omega}, \hat{\Omega}, t_b) \, d\Omega \, d\vec{\omega}. \tag{11.a}$$

In terms of the one-particle distribution function of the preceding subsection, the flux ϕ is defined by

$$\phi(\vec{\omega}, \hat{\Omega}, t_b) = \vec{\omega} \cdot \hat{\Omega} \, f^{(\text{primary})}(\vec{\omega}, \vec{x}_b, t_b) \tag{11.b}$$

where $\vec{x}_b = (R_E, \Theta, \Phi)$ is the spherical polar coordinate location of the surface area element $d\Omega$.

To describe the neutral cloud and its impact on the planetary magnetosphere, it is sufficient to follow in time an ensemble packet of atoms for

each neutral species initially ejected in an absolute time interval t_b to $t_b + dt'$, where t' is defined at the flight time since the packet was initially ejected from the exobase at time t_b. For one such neutral species, the motion of a packet is depicted in Figure 1. A number of physical quantities will be defined for the packet in this section. The complete description of a neutral cloud for a particular physical quantity is obtained by integrating the packet contribution for this quantity over its complete flight time and over all initial exobase conditions. To develop this description, the location of the center of the packet at flight time t' may be denoted by $\vec{r}(t', |\vec{\omega}, \hat{\Omega})$ in a coordinate system fixed relative to the satellite. In the case of a sodium or potassium cloud, the additional force of solar radiation pressure experienced by the packet atoms as they resonantly scatter sunlight requires a more complex solution for the packet location (see Smyth 1979, 1983) that depends in addition on the present value of the absolute time, $t_b + t'$, and hence must be denoted by $\vec{r}(t', t_b | \vec{\omega}, \hat{\Omega})$. This absolute time dependence is introduced because the magnitude of the solar radiation force is modulated by the Doppler motion that occurs between the Sun and the packet atoms in the satellite frame as Io executes circular motion about Jupiter and as Jupiter moves in its elliptical orbit about the Sun.

As an ensemble packet of atoms moves through the circumplanetary space, it may experience ionization, charge exchange, excitation, and even elastic collisions because of its interactions with the Io plasma torus. Neutral-neutral collisions are generally not important (except for recapture near Io and Jupiter where they are easily included) because the accumulated column density determined by the relatively short lifetime of cloud atoms is small. Electron impact ionization, photoionization, and charge exchange reactions remove atoms from the packet and hence determine its decay lifetime. Ionization processes also supply new ions to the planetary magnetosphere. Charge exchange processes modify the ion composition and energy of the Io plasma torus and also provide a flux of high-speed neutrals that (unless captured in the middle magnetosphere) escape from the planetary system. Electron impact excitation processes for neutral oxygen and sulfur atoms provide a photon emission mechanism for these two neutral gas clouds. Elastic ion-neutral collisions alter the trajectory of atoms in the packet and, if important, require that this momentum transfer information be properly incorporated in

determining the equivalent of $\vec{r}(t',t_b|\vec{\omega},\hat{\Omega})$ for the secondary atom population as described in the previous subsection.

To describe the interactions of the ensemble packet of atoms with the plasma torus, it is necessary at an absolute time t to map a location $\vec{R}$ in the satellite fixed coordinate system where the packet location $\vec{r}(t',t_b|\vec{\omega},\hat{\Omega})$ is specified to a location $\vec{R}$ in the magnetic (or, more correctly and generally, what shall be called the plasma) coordinate frame where the plasma properties are specified. The general transformation for this mapping, which is a function of the absolute time t, will be denoted as follows:

$$\vec{R} = \overleftrightarrow{T}(t)\cdot\vec{R} + \vec{D}(t). \tag{12}$$

The tensor part of the transformation, $\overleftrightarrow{T}(t)$, includes the relative rotational motion and the tilt angle between the satellite coordinate frame and the plasma torus coordinate frame. The vector part of the transformation, $\vec{D}(t)$, includes the more complex mapping required between the satellite frame and the plasma frame for a dipole offset of the origin of the magnetic and planetary spin coordinate frames as well as for the additional shift of the center of the plasma torus produced by an east-west electric field such as proposed by Barbosa and Kivelson (1983) and Ip and Goertz (1983). The location of a packet at flight time t' in the plasma coordinate system is then given as

$$\vec{r}(t',t_b|\vec{\omega},\hat{\Omega}) = \overleftrightarrow{T}(t_b + t') \cdot \vec{r}(t',t_b|\vec{\omega},\hat{\Omega}) + \vec{D}(t_b+t') \ . \tag{13}$$

The velocity of the packet $\vec{v}(t',t_b|\vec{\omega},\hat{\Omega})$ at flight time t' in the plasma coordinate system is then determined directly by time differentiation of equation (13).

In the remainder of this subsection, the ensemble packet contributions for a number of neutral cloud physical quantities of interest (e.g. density, photon emission rate, neutral loss rate, and various plasma input rates to the magnetosphere) are formulated. To facilitate this formulation, a hat "$\hat{}$" notation is adopted to indicate that a physical quantity is described in terms of its phase space representation $(t',t_b|\vec{\omega},\hat{\Omega})$ along its phase space trajectory. Thus, for a general physical quantity Q, its ensemble packet contribution will be denoted by $\hat{Q} = \hat{Q}\,(t',t_b|\vec{\omega},\hat{\Omega})$. For an observer in a

coordinate frame $(\vec{r}_o, t_o)$, the spacetime description of the physical quantity $Q(\vec{r}_o, t_o)$ is then determined, as discussed in a later section, from $\hat{Q}$ by evaluating its ensemble average $< \hat{Q} >$.

The number of atoms in an ensemble packet at flight time t' depend upon the loss processes suffered by the packet since its beginning at time t_b. For an ensemble packet at a location $\vec{r}$ having a velocity $\vec{v}$ in the plasma coordinate frame, the lifetime of cloud atoms is denoted by $\tau(\vec{r}, \vec{v})$. The velocity dependence is required in the lifetime to calculate properly the cloud atom charge exchange reaction rates with the plasma torus ions. The loss collision frequency for the packet is then given by

$$\hat{\nu}(t', t_b | \vec{\omega}, \hat{\Omega}) = [\tau(\vec{r}(t', t_b | \vec{\omega}, \hat{\Omega}), \vec{v}(t', t_b | \vec{\omega}, \hat{\Omega}))]^{-1}, \tag{14}$$

and the probability that the ensemble packet of atoms at flight time t' exists is defined as follows:

$$P(t', t_b | \vec{\omega}, \hat{\Omega}) = \exp\left[-\int_0^{t'} \hat{\nu}(t'', t_b | \vec{\omega}, \hat{\Omega})\, dt''\right]. \tag{15}$$

The number of atoms in the packet at flight time t' is then given by

$$\hat{n}(t', t_b | \vec{\omega}, \hat{\Omega})\, d\Omega\, d\vec{\omega}\, dt' \tag{16}$$

where

$$\hat{n}(t', t_b | \vec{\omega}, \hat{\Omega}) = P(t', t_b | \vec{\omega}, \hat{\Omega}) \phi(\vec{\omega}, \hat{\Omega}, t_b) \tag{17}$$

is the number of atoms per unit surface element $d\Omega$ at the initial surface location $\hat{\Omega}$, per unit initial velocity volume $d\vec{\omega}$ at the initial velocity $\vec{\omega}$, and per unit time interval dt' at the flight time t'.

The number of photons emitted by an ensemble packet at flight time t' depends upon its photon excitation mechanism. The two important mechanisms, electron impact excitation in the plasma torus and solar resonance scattering, are described by an atom excitation rate (i.e., photons per atom per unit time) denoted by $J_\lambda(\vec{r}, v_s)$ for an emission line with wavelength λ. The position vector $\vec{r}$ of the packet in the plasma coordinate frame is required in calculating the electron impact excitation rate for oxygen and sulfur atoms.

The radial speed v_s of the packet relative to the Sun is required in calculating the solar resonance scattering excitation rate for sodium, potassium, oxygen, and sulfur. The photon emission rate (i.e., number of photons emitted per unit time) at wavelength λ for the packet at flight time t' is then given by

$$\hat{I}_\lambda(t', t_b | \vec{\omega}, \hat{\Omega})\ d\Omega\ d\vec{\omega}\ dt' \tag{18}$$

where

$$\hat{I}_\lambda(t', t_b | \vec{\omega}, \hat{\Omega}) = J_\lambda[\vec{r}(t', t_b | \vec{\omega}, \hat{\Omega}),\ v_s(t', t_b | \vec{\omega}, \hat{\Omega})]\ \hat{n}(t', t_b | \vec{\omega}, \hat{\Omega}). \tag{19}$$

The rate at which neutral atoms are lost from the packet at flight time t' is determined from the time derivative of expression (17) and is given by

$$\left[\frac{\partial P(t', t_b | \vec{\omega}, \hat{\Omega})}{\partial t'}\right] \phi(\vec{\omega}, \hat{\Omega}, t_b)\ d\Omega\ d\vec{\omega}\ dt', \tag{20}$$

which may be written in terms of a loss rate

$$\hat{L}(t', t_b | \vec{\omega}, \hat{\Omega})\ d\Omega\ d\vec{\omega}\ dt' \tag{21}$$

where

$$\hat{L}(t', t_b | \vec{\omega}, \hat{\Omega}) = \hat{\nu}(t', t_b | \vec{\omega}, \hat{\Omega})\ \hat{n}(t', t_b | \vec{\omega}, \hat{\Omega}). \tag{22}$$

Loss processes contributing to the collision frequency $\hat{\nu}$ in equation (22) occur for the first four types of neutral reactions summarized in Table 3, where the neutral cloud atoms are denoted by the general chemical symbol Y. (It should be noted in passing that to generalize the collision frequency $\hat{\nu}$ for molecular gas clouds, dissociative reactions would from this point forward have to be properly included.) It should be emphasized that the expression (21) is <u>not</u>, however, the <u>net</u> rate at which ions are deposited into the magnetosphere by the packet, since charge exchange reactions of type C in Table 3, while providing from the packet a new ion (Y^+), simultaneously remove an old ion (X^+) from the magnetosphere by production of a fast escaping neutral.

In general, to determine the impact of the neutral cloud on the magnetosphere, it is necessary to assess simultaneously the contributions of the packets of several neutral clouds on the plasma torus because of reactions of type C in Table 3. It is of interest to determine these contributions not only for the net ion loading rate $\dot{N}$ but also for the plasma mass loading rate $\dot{M}$, and for the ion energy input rate $\dot{E}$. For a mixture of N neutral gas species (j=1,2,...,N), the instantaneous packet contributions to any one of these three input rates can be formulated (see Smyth and Shemansky 1983) and will be denoted by $\hat{\dot{R}}(t',t_b|\vec{\omega},\hat{\Omega})$, where

$$\hat{\dot{R}} = \sum_{j=1}^{N} [\hat{\xi}_j \hat{L}_j - \hat{\eta}_j \hat{P}_j]. \tag{23}$$

Here $\hat{L}_j$ is the loss rate of the packet for the j^{th} species defined in a parallel manner to equation (22), and $\hat{P}_j$ is the production rate of the packet for the j^{th} species as determined from the reactions of type C in Table 3. For the three cases of interest, $\hat{\xi}_j$ and $\hat{\eta}_j$ are defined in Table 4, where V_R is the relative velocity between the neutral atom Y and the plasma coordinate frame at the time the neutral is lost from the packet, and V_T is the thermal velocity of the X^+ ion at the time it is converted to a fast neutral because of reactions of type C in Table 3.

Combining the ionization reactions A and B in Table 3 into a single term, the collision frequency $\hat{\nu}_j(t',t_b|\vec{\omega},\hat{\Omega})$ for the j^{th} species may be divided into a contribution from ionization (I), charge exchange (CE), and charge transfer (CT) as follows:

$$\hat{\nu}_j = \hat{\nu}_j^{(I)} + \hat{\nu}_j^{(CE)} + \hat{\nu}_j^{(CT)}. \tag{24}$$

The charge exchange collision frequency may be further divided into terms

$$\hat{\nu}_j^{(CE)}(t',t_b|\vec{\omega},\hat{\Omega}) = \sum_{k=1}^{N} \hat{S}_j^{(k)}(t',t_b|\vec{\omega},\hat{\Omega}) \tag{25}$$

that describe the individual charge exchange reactions. Here $\hat{S}_j^{(k)}$ is the loss rate for the j^{th} species neutral packet because of the charge exchange reaction that produces a fast k^{th} species neutral (i.e., it is the product of the ion density for the ionized k-species times the reaction rate constant for the

charge exchange reaction). Symmetric charge exchange (k=j) and nonsymmetric charge exchange (k≠j) are included. The production rate $\hat{P}_j(t', t_b|\vec{\omega},\hat{\Omega})$ for all fast neutrals of the j^{th} species that are produced by all neutral packets is then given by

$$\hat{P}_j = \sum_{k=1}^{N} \hat{S}_k^{(j)} \hat{n}_k \tag{26}$$

so that expression (23) may be rewritten as the sum of two different terms

$$\dot{\hat{R}} = \sum_{j=1}^{N} \hat{\xi}_j (\hat{\nu}_j^{(I)} + \hat{\nu}_j^{(CT)}) \hat{n}_j + \sum_{j=1}^{N}\sum_{k=1}^{N} (\hat{\xi}_j \hat{S}_j^{(k)} \hat{n}_j - \hat{\eta}_j \hat{S}_k^{(j)} \hat{n}_k). \tag{27}$$

The contribution of the charge exchange reactions to expression (27) is given by the second term. This second term is zero for $\dot{\hat{N}}$, nonzero for $\dot{\hat{M}}$ because of the nonsymmetric reactions, and nonzero for $\dot{\hat{E}}$ because of every charge exchange reaction.

In the case of $\dot{\hat{N}}$, the number of neutrals lost from the j^{th} species packet, $\hat{L}_j$ is divided between the net ion loading rate, $\dot{\hat{N}}_j$, and the production of new fast neutrals, $\hat{\nu}_j^{(CE)} \hat{n}_j$, that escape from the system because of reactions of type C (Table 3):

$$\hat{L}_j = \dot{\hat{N}}_j + \hat{\nu}_j^{(CE)} \hat{n}_j \tag{28}$$

as expected on physical grounds. The fraction of $\hat{L}_j$ that contributes to $\dot{\hat{N}}_j$ is time dependent because of the oscillation of the plasma torus about the satellite plane and other more complex motions that are contained in the transformation (13). For $\dot{\hat{M}}$ and $\dot{\hat{E}}$, the separate j^{th} species contributions are coupled as described by equation (27). The overall mass and energy conservation is reflected in equation (23), where the first term is the contribution to the plasma torus by the neutrals lost from the packets, and the second term is the contribution produced by new neutrals being created by the packet-plasma reactions of type C in Table 3.

The cumulative value of the instantaneous rate $\dot{\hat{R}}$ supplied to the plasma torus in a time period T by all of the neutral species packets, each of which has a current flight time t', may also equally well be formulated. For the absolute time interval from t_0-T to t_0, this cumulative value is given by

$$\left[\int_{t_\ell}^{t'} \hat{\dot{R}}\,(t'',\, t_o - t' | \vec{\omega}, \hat{\Omega})\, dt''\right] d\Omega\, d\vec{\omega}\, dt' \tag{29}$$

where

$$t_\ell = \left\{ \begin{array}{ll} 0 & \text{if } t' \le T \\ t'-T & \text{if } t' > T \end{array} \right\} . \tag{30}$$

The quantity (29) is useful in that, even though the instantaneous rate $\hat{\dot{R}}$ integrated over all flight time is time dependent, its cumulative value (29) averaged over all flight time t' is not time dependent, if the source and sink processes for the neutral cloud are periodic with the period T. This will be discussed further in a later section. It should be noted here in passing, however, that in addition to the instantaneous contribution (27) or the cumulative contributions (29) of the neutral packets to $\hat{\dot{N}}$, $\hat{\dot{M}}$ and $\hat{\dot{E}}$, the plasma torus may also contribute directly through reactions of type E, F, and G in Table 3. These additional processes are not in the realm of the neutral cloud description and may be treated independently.

Physics of an Ensemble Subpacket

A neutral gas cloud of Io may be described for the secondary atom population by following the spacetime history of all neutral atoms produced by the primary atom population. To accomplish this explicitly, the secondary atom population will be described in terms of an ensemble subpacket in a way analogous to that in which the primary atom population is described in terms of an ensemble packet. The relationship between the packet and the subpacket is illustrated in Figure 2. For a neutral gas subpacket of the j^{th} species, the number of atoms created with initial velocity $\vec{\xi}$ to $\vec{\xi}+d\vec{\xi}$ along the primary packet trajectory $\vec{r}(t', t_b | \vec{\omega}, \hat{\Omega})$ in the time interval t' to $t'+dt'$ is given by

$$\hat{S}_j(t', t_b | \vec{\omega}, \hat{\Omega}, \vec{\xi})\; d\hat{\Omega}\; d\vec{\omega}\; dt'\; d\vec{\xi} \tag{31}$$

where

$$\hat{S}_j(t',t_b|\vec{\omega},\hat{\Omega},\vec{\xi}) = \hat{P}_j(t',t_b|\vec{\omega},\hat{\Omega})\ g_j(\vec{\xi}|\vec{\omega},\hat{\Omega},t',t_b) \tag{32}$$

Here, $g_j(\vec{\xi}|\vec{\omega},\hat{\Omega},t',t_b)$ is the local initial velocity distribution for all secondary atoms created at time t' along this packet trajectory and is normalized to unity,

$$\int g_j(\vec{\xi}|\vec{\omega},\hat{\Omega},t',t_b)\ d\vec{\xi} = 1\ , \tag{33}$$

and $\hat{P}_j$ is given by equation (26) for the case of charge exchange creation of fast secondary neutrals. For a secondary population created by elastic ion-atom or dissociative electron-molecule collisions, the expression for $\hat{P}_j$ must be appropriately generalized. The creation rate (32) in the subpacket formalism occupies a parallel position to the flux (11.b) in the packet formalism.

The location of the center of the subpacket, originally created at a flight time t"=0 with an initial velocity $\vec{\xi}$ at the primary location $\vec{r}(t',t_b|\vec{\omega},\hat{\Omega})$ and corresponding to the primary trajectory time t_b+t', will be denoted for t"$\geq$0 by $\vec{r}(t",\vec{\xi};\ t',t_b|\vec{\omega},\hat{\Omega})$. In the plasma coordinate system, the location of the subpacket at a flight time t" is therefore given by

$$\vec{r}(t",\vec{\xi};t',t_b|\vec{\omega},\hat{\Omega}) = \overleftrightarrow{T}(t_b+t'+t") \cdot \vec{r}(t",\vec{\xi};\ t',t_b|\vec{\omega},\hat{\Omega}) + \vec{D}(t_b+t'+t") \tag{34}$$

in an exactly parallel manner to the packet location (13). The velocity of the subpacket in the plasma coordinate system will be denoted by $\vec{v}(t",\vec{\xi};\ t',t_b|\vec{\omega},\hat{\Omega})$ and is determined by the t" time derivative of expression (34).

The ensemble subpacket contributions for different neutral cloud physical quantities of interest can be formulated as in the previous section for the packet ensemble. To facilitate this formulation, a double hat "$\hat{\wedge}$" notation is adopted to indicate that a physical subpacket quantity is described in terms of its phase space representation $(t",\vec{\xi};\ t',t_b|\vec{\omega},\hat{\Omega})$ along its phase space trajectory. The loss collision frequency for the subpacket of the j^{th} species is given by

$$\hat{\hat{\nu}}_j(t'',\vec{\xi};\ t',t_b|\vec{\omega},\hat{\Omega}) = [\tau_j(\vec{r}(t'',\vec{\xi};\ t',t_b|\vec{\omega},\hat{\Omega}),\ \vec{v}(t'',\vec{\xi};\ t',t_b|\vec{\omega},\hat{\Omega}))]^{-1} \qquad (35)$$

parallel to the packet expression (14), and the probability that the ensemble subpacket of atoms at flight time t'' exist is defined by

$$P_j(t',\vec{\xi};\ t',t_b|\vec{\omega},\hat{\Omega}) = \exp\left[-\int_{t'}^{t''} \hat{\hat{\nu}}_j\ (t''',\vec{\xi};\ t',t_b|\vec{\omega},\hat{\Omega})\ dt'''\right]. \qquad (36)$$

The number of atoms in the subpacket of the j^{th} species at time t'' is then given by

$$\hat{\hat{n}}_j(t'',\vec{\xi};\ t',t_b|\vec{\omega},\hat{\Omega})\ d\Omega\ d\vec{\omega}\ dt'\ d\vec{\xi}\ dt'' , \qquad (37)$$

where

$$\hat{\hat{n}}_j\ (t'',\vec{\xi};\ t',t_b|\vec{\omega},\hat{\Omega}) = \hat{S}_j(t',t_b|\vec{\omega},\hat{\Omega},\vec{\xi})\quad {}_j(t'',\vec{\xi};\ t',t_b|\vec{\omega},\hat{\Omega}). \qquad (38)$$

In a similar manner to the packet quantities defined in the previous section, the subpacket photon emission rate density $\hat{\hat{I}}_\lambda(t'',\vec{\xi};\ t',t_b|\vec{\omega},\hat{\Omega})$, the loss rate density $\hat{\hat{L}}(t'',\vec{\xi};\ t',t_b|\vec{\omega},\hat{\Omega})$, and the plasma input rate densities $\hat{\hat{R}}(t'',\vec{\xi};\ t',t_b|\vec{\omega},\hat{\Omega})$ may be defined parallel to the expressions (18), (21), and (27), respectively.

Kinetic Theory Distribution Function

The kinetic theory distribution function for the neutral gas cloud of the j^{th} species as noted earlier may be divided into contributions from the primary and secondary atom populations

$$f_j(\vec{v}_o,\vec{x}_o,t_o) = \overset{\text{(primary)}}{f_j(\vec{v}_o,\vec{x}_o,t_o)} + \overset{\text{(secondary)}}{f_j(\vec{v}_o,\vec{x}_o,t_o)} \quad . \qquad (39)$$

Here, $\vec{v}_o$ and $\vec{x}_o$ are the velocity and spatial coordinates of phase space for an observation coordinate frame, and t_o is the absolute time in the observation frame. The primary and secondary contributions to equation (39) can be directly expressed, respectively, in terms of the primary packet density

$\hat{n}$ and the secondary subpacket density $\hat{\hat{n}}$ defined in the previous two subsections:

(primary)

$$f_j(\vec{v}_o,\vec{x}_o,t_o) = \int_{\text{exobase}} d\Omega \int_{\text{velocity space}} d\vec{\omega} \int_{\text{flight time}} dt' \; \hat{n}_j(t',t_o-t'|\vec{\omega},\hat{\Omega}) \; \delta(\vec{r}_o,\hat{\vec{r}}_j) \; \delta(\vec{v}_o,\hat{\dot{\vec{r}}}_j) \quad , \quad (40)$$

(secondary)

$$f_j(\vec{x}_o,\vec{v}_o,t_o) = \int_{\text{exobase}} d\Omega \int_{\text{velocity space}} d\vec{\omega} \int_{\text{flight time}} dt' \int_{\text{velocity space}} d\vec{\xi} \int_{\text{flight time}} dt'' \; \hat{\hat{n}}_j(t'',\vec{\xi};t',t_o-t'|\vec{\omega},\hat{\Omega})\delta(\vec{r}_o,\hat{\hat{\vec{r}}}_j)\delta(\vec{v}_o,\hat{\dot{\vec{r}}} \quad (4$$

In equations (40) and (41), $\hat{\vec{r}}$ and $\hat{\dot{\vec{r}}}$ are abbreviated notations for the ensemble packet spatial location and velocity

$$\hat{\vec{r}} = \vec{r}(t',t_o-t'|\vec{\omega},\hat{\Omega}) \quad , \quad \hat{\dot{\vec{r}}} = \left[\frac{d}{dt'}\,\vec{r}(t',t_b|\vec{\omega},\hat{\Omega})\right]_{t_b=t_o-t'} \qquad (42)$$

and $\hat{\hat{\vec{r}}}$ and $\hat{\hat{\dot{\vec{r}}}}$ are abbreviated notations for the ensemble subpacket location and velocity:

$$\hat{\hat{\vec{r}}} = \vec{r}(t'',\vec{\xi}\;;t',t_o-t'|\vec{\omega},\hat{\Omega}) \quad , \quad \hat{\hat{\dot{\vec{r}}}} = \frac{d}{dt''}\left[\vec{r}(t'',\vec{\xi}\;;\;t',t_o-t'|\vec{\omega},\hat{\Omega})\right]. \qquad (43)$$

The quantities $\delta(\vec{r}_o,\vec{r}_j)$ and $\delta(\vec{v}_o,\dot{\vec{r}}_j)$, respectively, are the spatial volume projection operator and the velocity volume projection operator defined as follows:

$$\delta(\vec{r}_o,\vec{r}) = \frac{1}{\Delta^3 r_o} \left\{ \begin{array}{ll} 1 & \text{if } \vec{r}_o < \vec{R}_o < \vec{r}_o + \Delta\vec{r}_o \\ 0 & \text{otherwise} \end{array} \right\} \qquad (44)$$

$$\delta(\vec{v}_o,\dot{\vec{r}}) = \frac{1}{\Delta^3 v_o} \left\{ \begin{array}{ll} 1 & \text{if } \vec{v}_o < \vec{V}_o < \vec{v}_o + \Delta\vec{v}_o \\ 0 & \text{otherwise} \end{array} \right\}. \qquad (45)$$

Here, $\vec{R}_o$ is the location of the ensemble packet (or subpacket) in the observation coordinate frame defined and mapped by an appropriately defined transformation of the form

$$\vec{R}_o = \overleftrightarrow{T}_o(t_o) \cdot \vec{R} \qquad (46)$$

where $\vec{R} = \hat{\vec{r}}$ (or $\hat{\hat{\vec{r}}}$) and $\vec{V}_o = \dot{\vec{R}}_o$ is the velocity of the ensemble packet (or subpacket) in the observation coordinate frame. In addition, the quantities $\Delta^3 r_o$ and $\Delta^3 v_o$ are, respectively, the spatial and velocity volume elements establishing the volume resolution element in the phase space of the observation coordinate system and correspond to the spatial volume $\Delta\vec{r}_o$ about $\vec{r}_o$ and the velocity volume $\Delta\vec{v}_o$ about $\vec{v}_o$.

Spatial Properties of the Neutral Cloud

The spatial properties of the neutral cloud (e.g., the three-dimensional number density or the two-dimensional brightness of the cloud on the sky plane) as well as the physical ion input rates to the planetary magnetosphere can be determined directly from the kinetic theory distribution function (39) or, alternatively, from the expressions derived from the ensemble packet and subpacket in the previous sections. In the former case, one multiplies the distribution function by a physical quantity of interest, which may in general be a function of $(\vec{r}_o, \vec{v}_o, t_o)$, and integrates the product over the velocity coordinate space $\vec{v}_o$. In the latter case, one defines an ensemble average for the packet and subpacket physical quantity of interest, producing a result identical with that obtained by the former method because of the nature of the spatial and velocity volume projection operators (44) and (45). The ensemble average approach will be explicitly developed below and is the description adopted for the numerical evaluation of the neutral cloud model discussed in the next section.

If an ensemble packet quantity (e.g., $\hat{n}$, $\hat{I}_\lambda$, $\hat{\dot{N}}$) and its subpacket quantity (e.g., $\hat{\hat{n}}$, $\hat{\hat{I}}_\lambda$, $\hat{\hat{\dot{N}}}$) are denoted respectively by $\hat{Q}(t', t_b | \vec{\omega}, \hat{\Omega})$ and $\hat{\hat{Q}}(t'', \vec{\xi};\ t', t_b | \vec{\omega}, \hat{\Omega})$, and if the corresponding ensemble-average physical quantity in the observer's coordinate frame at $\vec{r}_o$ and at an absolute time t_o is denoted by $Q(\vec{r}_o, t_o)$, then

$$Q(\vec{r}_o, t_o) = \langle \hat{Q} \rangle + \langle \hat{\hat{Q}} \rangle , \tag{47}$$

where

$$\langle \hat{Q} \rangle = \underset{\text{exobase}}{\int d\Omega} \quad \underset{\text{velocity space}}{\int d\omega} \quad \underset{\text{flight time}}{\int_0^\infty} dt'\ \hat{Q}(t', t_o - t' | \omega, \hat{\Omega}) \delta(\hat{r}_o, \hat{\vec{r}}) , \tag{48}$$

$$<\hat{\hat{Q}}> = \int_{\text{exobase}} d\Omega \int_{\substack{\text{velocity}\\\text{space}}} d\vec{\omega} \int_{\substack{0\\\text{flight}\\\text{time}}}^{\infty} dt' \int_{\substack{\text{velocity}\\\text{space}}} d\vec{\xi} \int_{\substack{0\\\text{flight}\\\text{time}}}^{\infty} dt'' \; \hat{\hat{Q}}(t'', \vec{\xi}; t', t_o - t' | \vec{\omega}, \hat{\Omega}) \delta(\vec{r}_o, \hat{\hat{r}}), \quad (49$$

where $\hat{\hat{r}}$ and $\hat{\hat{\hat{r}}}$ are given by equation (42) and (43), and where the volume projection operator $\delta(\vec{r}_o, \vec{r})$ is defined by equation (44). To project an ensemble average physical quantity $Q(\vec{r}_o, t_o)$ onto the observer's viewing plane, as is appropriate for the gas density to obtain a column density or for the volume photon emission rates to obtain an image of the cloud brightness, an integration along the line of sight in the observer's coordinate frame is required in addition to those specified in equations (48) and (49). For the simple case of no parallax with the z_o-axis along the line of sight, the column integrated quantity is given by

$$Q(x_o, y_o t_o) = \int_{-\infty}^{\infty} Q(\vec{r}_o, t_o) \, dz_o. \quad (50)$$

In this manner, the basic properties of the cloud and also its interactions with the magnetosphere may be calculated.

It should be noted that if the ensemble packet quantity and the packet trajectory are periodic with period T in their initial ejection time t_b, that is, if

$$\hat{Q}(t', t+T | \vec{\omega}, \hat{\Omega}) = \hat{Q}(t', t | \vec{\omega}, \hat{\Omega}) \quad (51a)$$

$$\vec{r}(t', t+T | \vec{\omega}, \hat{\Omega}) = \vec{r}(t', t | \vec{\omega}, \hat{\Omega}), \quad (51b)$$

it then follows that the corresponding ensemble average physical quantities of the neutral cloud (47), although time dependent in general, are also periodic with period T

$$Q(\vec{r}_o, t_o + T) = Q(\vec{r}_o, t_o). \quad (52)$$

In general, the ensemble-average value of the cumulative value [see eqs. (29) and (30)] of any packet quantity $\hat{Q}$ over a time t_o-T to t_o ,

$$< [\int_{t_\ell}^{t'} \hat{Q}(t'', t_o - t | \vec{\omega}, \hat{\Omega})\, dt''] > , \tag{53}$$

is exactly equal to the ensemble average value of the instantaneous packet quantity $\hat{Q}$ integrated over the time interval

$$\int_{t_o - T}^{t_o} < \hat{Q} > dt_o' , \tag{54}$$

as can be readily verified. A similar result also holds for the subpacket quantity. If equations (51) hold, the quantities (53) and (54) are also explicitly independent of the time t_o, as would, of course, be expected purely on physical grounds. For $\hat{Q} = \hat{L}$, this time independence is clearly illustrated in the simple case of a constant flux,

$$\phi(\vec{\omega}, \hat{\Omega}, t_b) = \phi(\vec{\omega}, \hat{\Omega}) , \tag{55}$$

by the obvious result

$$\int_{\substack{\text{all} \\ \text{space}}} d\vec{r}_o \int_{t_o}^{t_o+T} < \hat{L} > dt_o' = T \int_{\text{exobase}} d\Omega \int_{\substack{\text{velocity} \\ \text{space}}} d\vec{\omega}\, \phi(\vec{\omega}, \hat{\Omega}) , \tag{56}$$

developed directly from expressions (20) and (48).

The general periodic relationship (52) and the equality of expressions (53) and (54) are useful in studying the impact of the neutral clouds on the magnetosphere. A period T of approximately 13 hours exists between Io and its location in the oscillating/rotating magnetosphere if east-west torus differences are assumed small or zero. If, on the other hand, east-west torus differences cannot be ignored, a period T of approximately 32 days exists for recurrence of the same east-west position and System III magnetic longitude of Io. To illustrate the impact of the neutral clouds, the packet expression (28) is summed over the various neutral cloud species and its ensemble average is taken to obtain

$$< \hat{L} > = < \dot{\hat{N}} > + < \sum_{j=1}^{N} \hat{\nu}_j^{(CE)} \hat{n}_j >. \tag{57}$$

This expression divides the instantaneous total packet neutral loss rate of the cloud $< \hat{L} >$ into its instantaneous net ion loading rate for the magnetosphere $< \dot{\hat{N}} >$ and its instantaneous production rate of fast neutrals $< \Sigma_j \hat{\nu}_j^{(CE)} \hat{n}_j >$. This partitioning is time- as well as space-dependent. The latter term of equation (57) is, of course, the rate at which subpacket fast neutrals are produced. If the packet periodicity (51) holds, the period averaged value of each term in equation (57) is independent of time, so that the average fractions of neutrals contributing to the net ion loading rate and to the production of fast neutrals are given, respectively, by

$$f^{(\dot{N})}(\vec{r}_o) = \overline{< \sum_{j=1}^{N} (\hat{\nu}_j^{(I)} + \hat{\nu}_j^{(CT)}) \hat{n}_j >} \Big/ \overline{< \sum_{j=1}^{N} \hat{\nu}_j \hat{n}_j >} \tag{58a}$$

and

$$f^{(fast)}(\vec{r}_o) = \overline{< \sum_{j=1}^{N} \hat{\nu}_j^{(CE)} \hat{n}_j >} \Big/ \overline{< \sum_{j=1}^{N} \hat{\nu}_j \hat{n}_j >} \tag{58b}$$

where the angular brackets denote the packet ensemble average and the bar indicates periodic accumulation, that is,

$$\overline{< \hat{Q} >} = \int_{t_o}^{t_o+T} < \hat{Q} > dt_o' = \int_{t_o}^{t_o+T} Q(\vec{r}_o, t_o') \, dt_o' \, , \tag{58c}$$

and where by construction

$$f^{(\dot{N})}(\vec{r}_o) + f^{(fast)}(\vec{r}_o) = 1. \tag{58d}$$

4. Numerical Approach

The ensemble average of a packet and subpacket quantity given by equations (47) - (49) and its column integrated value given by equation (50) may be evaluated numerically. For the packet description, this is accomplished by dividing the exobase into many small area elements. On each area element, the initial velocity distribution as well as the absolute flux are specified independently. For each initial condition specified on an area element, a trajectory $\vec{r}(t', t_b | \vec{\omega}, \hat{\Omega})$ for an ensemble packet is calculated for a sufficiently long flight time t' to determine accurately the cloud properties. Along each trajectory, the packet quantities $\hat{Q}$ of interest are calculated and accumulated in their appropriate spatial volume (or area of the sky plane) in such a way as to determine the packet ensemble average (48) or its contribution to the column-integrated ensemble average (50). For the subpacket description, the source density rate $\hat{S}$ for the subpacket as defined by expression (31) is calculated in the packet description along the packet trajectory and has the analogous role that the flux (11a) has in the packet description. The source density rate $\hat{S}$ is numerically divided into many small packet flight time increments along the packet trajectory and from each increment the subpacket trajectories $\vec{r}(t'', \vec{\xi};\ t', t_b | \vec{\omega}, \hat{\Omega})$ are calculated for sufficiently long flight time t'' to determine accurately the cloud properties. Along each trajectory, the subpacket quantities $\hat{\hat{Q}}$ of interest are calculated and accumulated in the appropriate spatial volume element of the observation coordinate frame.

The packet trajectories $\vec{r}(t', t_b | \vec{\omega}, \hat{\Omega})$ and subpacket trajectories $\vec{r}(t'', \vec{\xi};\ t', t_b | \vec{\omega}, \hat{\Omega})$ may be determined by solving the standard (Smyth and McElroy 1977) or modified (Smyth 1983) circular-restricted three-body equations of motion for each prescribed initial condition. The modified equations are required for the sodium and potassium cloud because of the additional effects of solar radiation pressure (Smyth 1979, 1983) on these atoms. The equations of motion are solved numerically by applying a straightforward Runge Kutta technique. The time steps employed in the numerical solution must be selected small enough not only to determine an accurate trajectory but also to ensure that the space and time resolution of the ensemble average quantities (47), which are quite sensitive to the oscilla-

tional/rotational motion of the plasma torus, are calculated to the level of desired accuracy.

For a particular neutral cloud, calculation of the packet quantity $\hat{Q}$, the subpacket quantity $\hat{\hat{Q}}$, and their ensemble averages (48) and (49) requires first that the relevant reactions and their rates (symbolically indicated by A-D in Table 3) and also the excitation rates (18) be identified and defined, and, second, that the spacetime properties of the plasma torus be specified along the packet and subpacket trajectories. For the sodium cloud, this information is presented in the companion paper (Smyth and Combi 1988).

5. Summary

A brief review of Io's local atmosphere and its extended gas clouds as well as their interactions with the planetary magnetosphere was given in section 2. The Io neutral clouds were seen to occupy a central position in understanding the coupled planet-satellite-magnetosphere system. Analysis of Earth-based, rocket, or Earth-orbiting satellite observations of neutral cloud emissions provides a direct, very promising, and still largely untapped approach for increasing our knowledge and understanding of complex physical phenomena in the system. Physically realistic models for the neutral clouds are essential in this analysis. These models must include the complex space-time interactions that occur between the neutral clouds and the plasma torus which have hitherto not been incorporated. The general Io neutral cloud model developed here includes these interactions and provides a general and solid base for future analysis of cloud data.

A mathematical description for the general neutral cloud model was presented for Io in section 3. For a given neutral gas species, the description is divided into a primary cloud population that is initially ejected from the satellite exobase and a secondary cloud population that is created in a spatially extended volume by the primary cloud population through various time-dependent processes. For simplicity, the mathematical description for the primary and secondary gas populations is explicitly developed for an atomic cloud, although it may be readily generalized for a molecular cloud. The description of the primary gas cloud may be fundamentally reduced to describing the time evolution of an ensemble packet of gas along its phase space trajectory. The description of the secondary gas cloud may likewise be reduced to describing the time evolution of an ensemble subpacket along its phase space trajectory. The physics of an ensemble packet and ensemble subpacket are presented and are also directly related to the kinetic theory distribution function for the gas cloud. The spatial properties of the neutral cloud as well as various ion input rates to the planetary magnetosphere are obtained from their ensemble packet and subpacket values by evaluating their ensemble averages. A straightforward numerical approach for evaluating the model is outlined with appropriate references that define and present a method of solution for the equations of motion of the phase space trajectories for the ensemble packet and subpacket.

As noted earlier, the general model is applied to the Io sodium cloud in a companion paper (Smyth and Combi 1988). The application of the general model to other neutral gas clouds of Io (e.g., K, O, S, SO_2, etc.) will be considered in a series of future papers.

ACKNOWLEDGMENTS

This research was supported by the Planetary Atmospheres Program of the National Aeronautics and Space Administration under grants NASW-3949, NASW-3503, NASW-3387 and NASW-3174. Acknowledgment is also made to the National Center for Atmospheric Research, which is sponsored by the National Science Foundation, for computational time used in implementing the model numerically. W. H. Smyth wishes to thank A. Ezzeddine and K. Burleson for their computational support in the earlier phases of developing this model.

Table 1

Io's Neutral Gas Clouds

Neutral Cloud	First Detection		Cloud Emission		
	Date	Observer	Wavelength (Å)	Intensity (Rayleighs)	Excitation Mechanism
Sodium	1972	R.A. Brown (1974)	5890, 5896	$10^3 - 10^4$	Solar Resonance Scattering
Potassium	1975	L.M. Trafton (1975) J.T. Trauger et al. (1976)	7665, 7699	15 - 300	Solar Resonance Scattering
Oxygen	1980	R.A. Brown (1981)	6300	~ 8	Electron Impact
Sulfur	1981	S.T. Durrance et al. (1983)	1304, 1425	~ 3	Electron Impact

Table 2

Some Studies for Exospheric Problems in Planetary Science

Subject	Reference
1. Cometary Atmospheres	Eddington 1910; Haser 1957, 1966; Keller 1973; Keller and Thomas 1975; Keller and Meier 1976; Combi and Delsemme 1980; Combi 1980; Festou 1981a,b; Combi and Smyth 1985; Combi, Stewart and Smyth 1986; Combi and Smyth 1988a,b
2. Planetary Atmospheres	
• Mercury	Hartle 1971; Hartle, Ogilvie and Wu 1973; Hodges 1974; Hartle, Curtis and Thomas 1975; Smith et al. 1978; Curtis and Hartle 1978; Hodges 1980; Ip 1986; Smyth 1986
• Venus	Penner 1977; Hodges and Tinsley 1981, 1982; Rodriguez, Prather and McElroy 1984; Hodges and Tinsley 1986
• Earth	Chamberlain 1963; Hartle 1973; Bertaux and Blamont 1973; Fahr and Paul 1976; Penner 1977; Hodges, Rohrbaugh and Tinsley 1981; Rodriguez 1983; Bishop 1985
3. Satellite Atmospheres	
• Moon	Hodges 1973; Hartle and Thomas 1974; Hodges 1980
• Titan	Fang, Smyth and McElroy 1976; Smyth and McElroy 1977; Smyth 1981; Shemansky, Smith, Smyth and Combi 1984; Hilton and Hunten 1985; Ip 1985; Hilton 1987
• Io	Carlson, Matson and Johnson 1975; Fang, Smyth and McElroy 1976; Smyth and McElroy 1977, 1978; Matson et al. 1978; Carlson et al. 1978; Smyth 1979; Goldberg et al. 1980; Macy and Trafton 1980; Smyth 1983; Smyth and Shemansky 1983; Sieveka 1983; Pilcher et al. 1984; Smyth and Combi 1983, 1984, 1985; Sieveka and Johnson 1985; McGrath and Johnson 1987; Smyth and Combi 1988.

Table 4

Definition of the Parameters $\hat{\xi}_j$ and $\hat{\eta}_j$

$\dot{\hat{R}}$	$\hat{\xi}_j$	$\hat{\eta}_j$
$\dot{\hat{N}}$	1	1
$\dot{\hat{M}}$	m_j	m_j
$\dot{\hat{E}}$	$\frac{m_j}{2} V_R^2$	$\frac{m_j}{2} V_T^2$

REFERENCES

Bagenal, F. 1985, J. Geophys. Res., 90, 311.

Bagenal, F., and Sullivan, J. D. 1981, J. Geophys. Res., 86, 8447.

Barbosa, D. D., and Kivelson, M. G. 1983, Geophys. Res. Letters, 10, 210.

Bertaux, J. L., and Blamont, J. E. 1973, J. Geophys. Res., 78, 80.

Bigg, E. K. 1964, Nature, 203, 1008.

Binder, A. B., and Cruikshank, D. P. 1964, Icarus, 3, 299.

Bishop, J. 1985, J. Geophys. Res., 96, 5235.

Brown, R. A. 1974, in Exploration of the Planetary System: Proceedings, I.A.U. symposium No. 65, Torun, Poland, 5-8 September 1973. (Eds. Woszczyk and Iwaniszewska). D. Reidel Publishing Co., Dordrecht, Boston, p. 527.

Brown, R. A. 1981, Ap. J., 244, 1072.

Brown, R. A., Pilcher, C. B., and Strobel, D. F. 1983, in Physics of the Jovian Magnetosphere (Ed. A.J. Dessler), Cambridge University Press, New York, NY, p. 197.

Brown, R. A., and Yung, Y. L. 1976, in Jupiter, Studies of the Interior, Atmosphere, Magnetosphere, and Satellites (Ed. T. Gehrels), The University of Arizona Press, Tucson, AZ, p. 1102.

Carlson, R. W., Matson, D. L., and Johnson, T. V. 1975, Geophys. Res. Letters, 2, 469.

Carlson, R. W., Matson, D. L., Johnson, T. V., and Bergstralh, J. T. 1978, Ap. J., 223, 1082.

Chamberlain, J. W., 1963, Planet. Space Sci., 11, 901.

Cheng, A. F. 1984, J. Geophys. Res., 89, 3939.

Cloutier, P. A., Daniell, R. E., Jr., Dessler, A. J., and Hill, T. W. 1978, Astrophys. Space Sci., 55, 93.

Combi, M. R. 1980, Ap. J., 241, 830.

Combi, M. R., and Delsemme, A. H. 1980, Ap. J., 237, 641.

Combi, M. R., and Smyth, W. H. 1985, Bull. AAS, 17, 724.

Combi, M. R., and Smyth, W. H. 1988a, Ap. J, in press.

Combi, M. R., and Smyth, W. H. 1988b, Ap. J, in press.

Combi, M. R., Stewart, A. J. F., and Smyth, W. H. 1986, Geophys. Res. Letters, 13, 385.

Curtis, S. A., and Hartle, R. E. 1978, J. Geophys. Res., 83, 1551.

Durrance, S. T., Feldman, P. D., and Weaver, H. A. 1983, Ap. J. (Letters), 267, L125.

Eddington, A. S. 1910, M.N.R.A.S., 70, 442.

Fahr, H. J. and Paul, G. 1976, J. Atmos. Terr. Phys., 38, 841.

Fahr, H. J. and Shizgal, B. 1983, Rev. Geophys. Space Sci., 21, 75.

Fanale, F. P., Banerdt, W. B., Elson, L. S., Johnson, T. V. and Zurek, R. W. 1982, in Satellites of Jupiter. (Ed. D. Morrison), University of Arizona Press, Tucson, AZ, p. 756.

Fanale, F. P., Johnson, T. V., and Matson, D. L. 1977, in Planetary Satellites (Ed. Joseph A. Burns), University of Arizona Press, Tucson, AZ, p. 379.

Fang, T.-M., Smyth, W. H., and McElroy, M. B. 1976, Planet. Space Sci., 24, 577.

Festou, M. C. 1981a, Astr. Ap., 95, 69.

Festou, M. C. 1981b, Astr. Ap., 96, 52.

Goldberg, B. A., Garneau, G. W., and LaVoie, S. K. 1984, Science, 226, 512.

Goldberg, B. A., Mekler, Yu., Carlson, R. W., Johnson, T. V., and Matson, D. L. 1980, Icarus, 44, 305.

Haff, P. K., Watson, C. C., and Yung, Y. L. 1981, J. Geophys. Res., 86, 6933.

Hartle, R. E. 1971, Phys. Fluids, 14, 2592.

Hartle, R. E. 1973, Planet. Space Sci., 21, 2123.

Hartle, R. E., Ogilvie, K. W., and Wu, C. S. 1973, Planet. Space Sci., 21, 2181.

Hartle, R. E. and Thomas, G. E. 1974, J. Geophys. Res., 79, 1519.

Hartle, R. E., Curtis, S. A., and Thomas, G. E. 1975, J. Geophys. Res., 80, 3689.

Haser, L. 1957, Bull. Acad. Roy. de Belgique, Classe des sci., 5th ser., 43, 740.

Haser, L. 1966, Proc. 13th Liege Symposium, No. 233.

Hilton, D. A. 1987, Ph.D. Thesis, Department of Planetary Sciences, The University of Arizona.

Hilton, D. A. and Hunten, D. M. 1985, Bull. AAS, 17, 696.

Hodges, R. R. 1973, J. Geophys. Res., 78, 8055.

Hodges, R. R., Jr. 1974, J. Geophys. Res., 79, 2881.

Hodges, R. R., Jr. 1980, J. Geophys. Res., 85, 164.

Hodges, R. R., and Tinsley, B. A. 1981, J. Geophys. Res., 86, 7649.

Hodges, R. R., and Tinsley, B. A. 1982, Icarus, 51, 440.

Hodges, R. R., Rohrbaugh, R. P., and Tinsley, B. A. 1981, J. Geophys. Res., 86, 6917.

Hodges, R. R., and Tinsley, B. A. 1986, J. Geophys. Res., 91, 13649.

Hunten, D. M. 1985, Geophys. Res. Letters, 12, 271.

Ingersoll, A. P., Summers, M. E., and Schlipf, S. G. 1985, Icarus, 64, 375.

Ip, W. -H. 1982, Ap. J., 262, 780.

Ip, W. -H. 1985, In Proceedings, International Workshop on the Atmospheres of Saturn and Titan, 16-19 September 1985, ESA SP-241.

Ip, W. -H. 1986, Geophys. Res. Letters, 13, 423.

Ip, W. -H., and Goertz, C. K. 1983, Nature, 302, 232.

Keller, H. U. 1973, Astr. Ap., 27, 51.

Keller, H. U., and Thomas, G. E. 1975, Astr. Ap., 39, 7.

Keller, H. U., and Meier, R. R. 1976, Astr. Ap., 52, 273.

Kliore, A., Cain, D. L., Fjeldbo, G., and Seidel, B. L. 1974, Science, 183, 323.

Kumar, S. 1979, Nature, 280, 758.

Kumar, S. 1980, Geophys. Res. Letters, 7, 9.

Kumar, S. 1982, J. Geophys. Res., 87, 1677.

Kumar, S. 1984, J. Geophys. Res., 89, 7399.

Kumar, S. 1985, Icarus, 61, 101.

Kumar, S., and Hunten, D. M. 1982, in Satellites of Jupiter (Ed. D. Morrison), University of Arizona Press, Tucson, AZ, p. 782.

Lanzerotti, L. J., and Brown, W. L. 1983, J. Geophys. Res., 88, 989.

Lunine, J. I., and Stevenson, D. J. 1985, Icarus, 64, 345.

Macy, W. W., Jr., and Trafton, L. M. 1975a, Icarus, 25, 432.

Macy, W., Jr., and Trafton, L. 1975b, Ap. J., 200, 510.

Macy, W., and Trafton, L. 1980, Icarus, 41, 131.

Matson, D. L., Goldberg, B. A., Johnson, T. V., and Carlson, R. W. 1978, Science, 199, 531.

Matson, D. L., Johnson, T. V., and Fanale, F. P. 1974, Ap. J. (Letters), 192, L43.

Matson, D. L., and Nash, D. B. 1983, J. Geophys. Res., 88, 4771.

McGrath, M. A., and Johnson, R. E. 1987, Icarus, 69, 519.

Morabito, L. A., Synnott, S. P., Kupferman, P. N., and Collins, S. A. 1979, Science, 204, 972.

Münch, G., and Bergstralh, J. T. 1977, Pub. A.S.P., 89, 232.

Nash, D. B., Carr, M. H., Gradie, J., Hunten, D. M., and Yoder, C. F. 1986, in Satellites (Ed. J.A. Burns and M.S. Matthews), University of Arizona Press, Tucson, AZ, p. 629.

Pearl, J., Hanel, R., Kunde, V., Maguire, W., Fox, K., Gupta, S., Ponnamperuma, C., and Raulin, F. 1979, Nature, 280, 755.

Penner, J. E. 1977, Ph.D. Thesis, Harvard University, Cambridge, Massachusetts.

Pilcher, C. B., Smyth, W. H., Combi, M. R., and Fertel, J. H. 1984, Ap. J., 287, 427.

Pilcher, C. B., and Strobel, D. F. 1982, in Satellites of Jupiter (Ed. D. Morrison), University of Arizona Press, Tucson, AZ, p. 807.

Rodriguez, J. M. 1983, Ph.D. Thesis, Dept. of Physics, Harvard University, Cambridge, Massachusetts.

Rodriguez, J. M., Prather, M. J., and McElroy, M. B. 1984, Planet. Space Sci., 32, 1235.

Schneider, N. M., Hunten, D. M., Wells, W. K., and Trafton, L. M. 1987, Science, 238, 55.

Schneider, N. M., Wells, W. K., Hunten, D. M., and Brown, R. A. 1985, Bull. AAS, 17, 699.

Shemansky, D. E. 1984, Private Communication.

Shemansky, D. E., Smith, G. R., Smyth, W. H., and Combi, M. R. 1984, Bull. AAS, 16, 712.

Sieveka, E. M. 1983, Ph.D. Thesis, Dept. of Nuclear Engineering and Engineering Physics, University of Virginia.

Sieveka, E. M., and Johnson, R. E. 1984, Ap. J., 287, 418.

Sieveka, E. M., and Johnson, R. E. 1985, J. Geophys. Res., 90, 5327.

Smith, B. A., and Smith, S. A. 1972, Icarus, 17, 218.

Smith, G. R., Shemansky, D. E., Broadfoot, A. L., and Wallace, L. 1978, J. Geophys. Res., 83, 3783.

Smyth, W. H. 1979, Ap. J., 234, 1148.

Smyth, W. H. 1981, Ap. J., 246, 344.

Smyth, W. H. 1983, Ap. J., 264, 708.

Smyth, W. H. 1986, Nature, 323, 696.

Smyth, W. H., and Combi, M. R. 1983, Bull. AAS, 15, 810.

Smyth, W. H., and Combi, M. R. 1984, Bull. AAS, 16, 663.

Smyth, W. H., and Combi, M. R. 1985, Bull. AAS, 17, 695.

Smyth, W. H., and Combi, M. R. 1988, Ap. J, in press (Paper II).

Smyth, W. H., and McElroy, M. B. 1977, Planet. Space Sci., 25, 415.

Smyth, W. H., and McElroy, M. B. 1978, Ap. J., 226, 336.

Smyth, W. H., and Shemansky, D. E. 1983, Ap. J., 271, 865.

Summers, M. E. 1984, Ph.D. Thesis, Division of Geological and Planetary Sciences, California Institute of Technology.

Summers, M. E., Strobel, D. F., Yung, Y. L., Trauger, J. T., and Mills, F. 1986, Ap. J., submitted.

Summers, M. E., Yung, Y. L., and Haff, P. K. 1983, Nature, 304, 710.

Trafton, L. 1975, Nature, 258, 690.

Trafton, L. 1980, Icarus, 44, 318.

Trafton, L. 1981, Ap. J., 247, 1125.

Trafton, L. and Macy, W., Jr. 1975, Ap. J. (Letters), 202, L155.

Trafton, L., Parkinson, T., and Macy, W. 1974, Ap. J. (Letters), 190, L85.

Trauger, J. T. 1984, Bull. AAS, 16, 712.

Trauger, J. T. 1985, Bull. AAS, 17, 694.

Trauger, J., Roesler, F. and Münch, G. 1976, Bull. AAS, 8, 468.

FIGURE CAPTIONS

Figure 1. Motion of a Neutral Cloud Packet. The mathematical description for the primary population of the neutral cloud based upon the dynamic evolution of neutral cloud packets is depicted. The one neutral cloud packet shown on its trajectory at a flight time $t' > 0$ is ejected from a satellite exosphere area element $d\Omega$ with a velocity $\vec{\omega}$ at flight time $t' = 0$.

Figure 2. Motion of a Neutral Cloud Subpacket. The mathematical description of the secondary population of the neutral cloud based upon the dynamic evolution of neutral cloud subpackets is depicted. The one neutral cloud subpacket shown on its trajectory at flight time $t'' > 0$ is ejected at flight time $t'' = 0$ with initial velocity $\vec{\xi}$ from the neutral packet. The location of the neutral packet at the later time ($t'' > 0$) is also indicated.

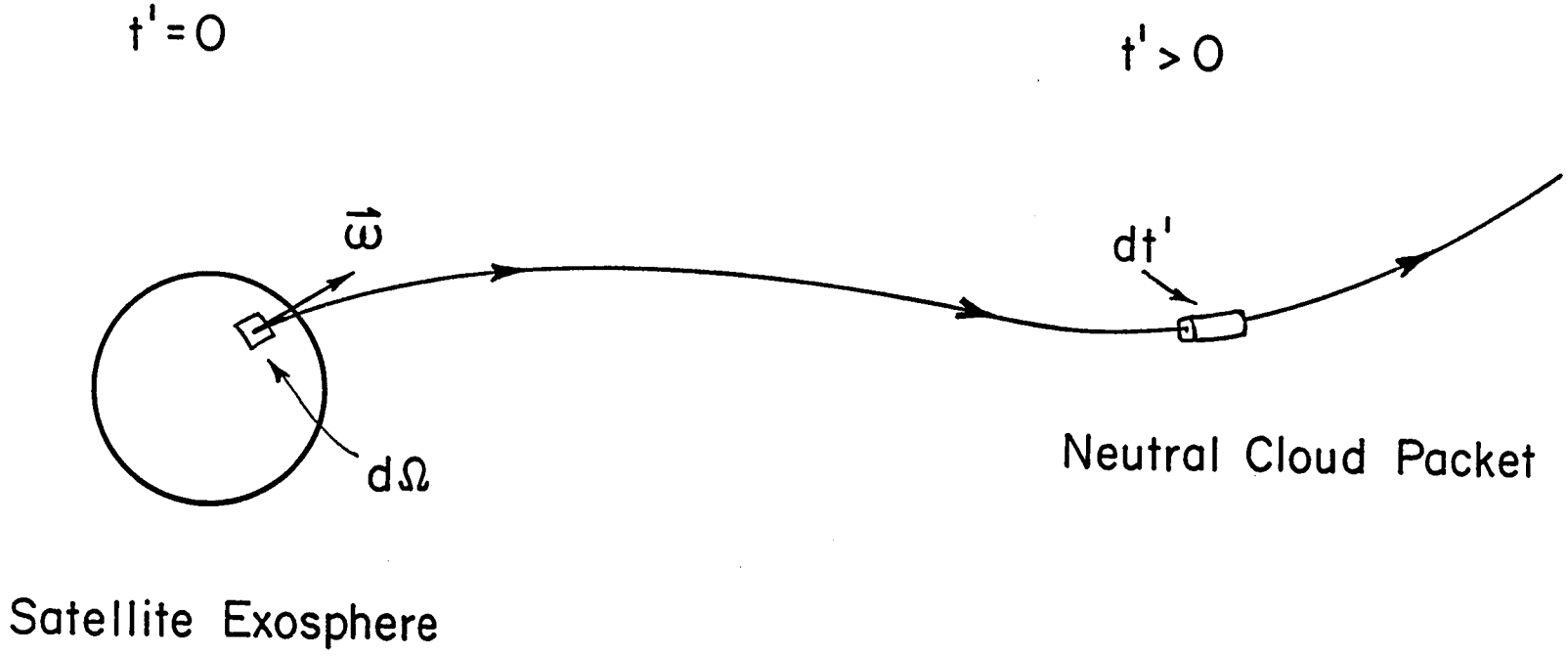

Figure 1

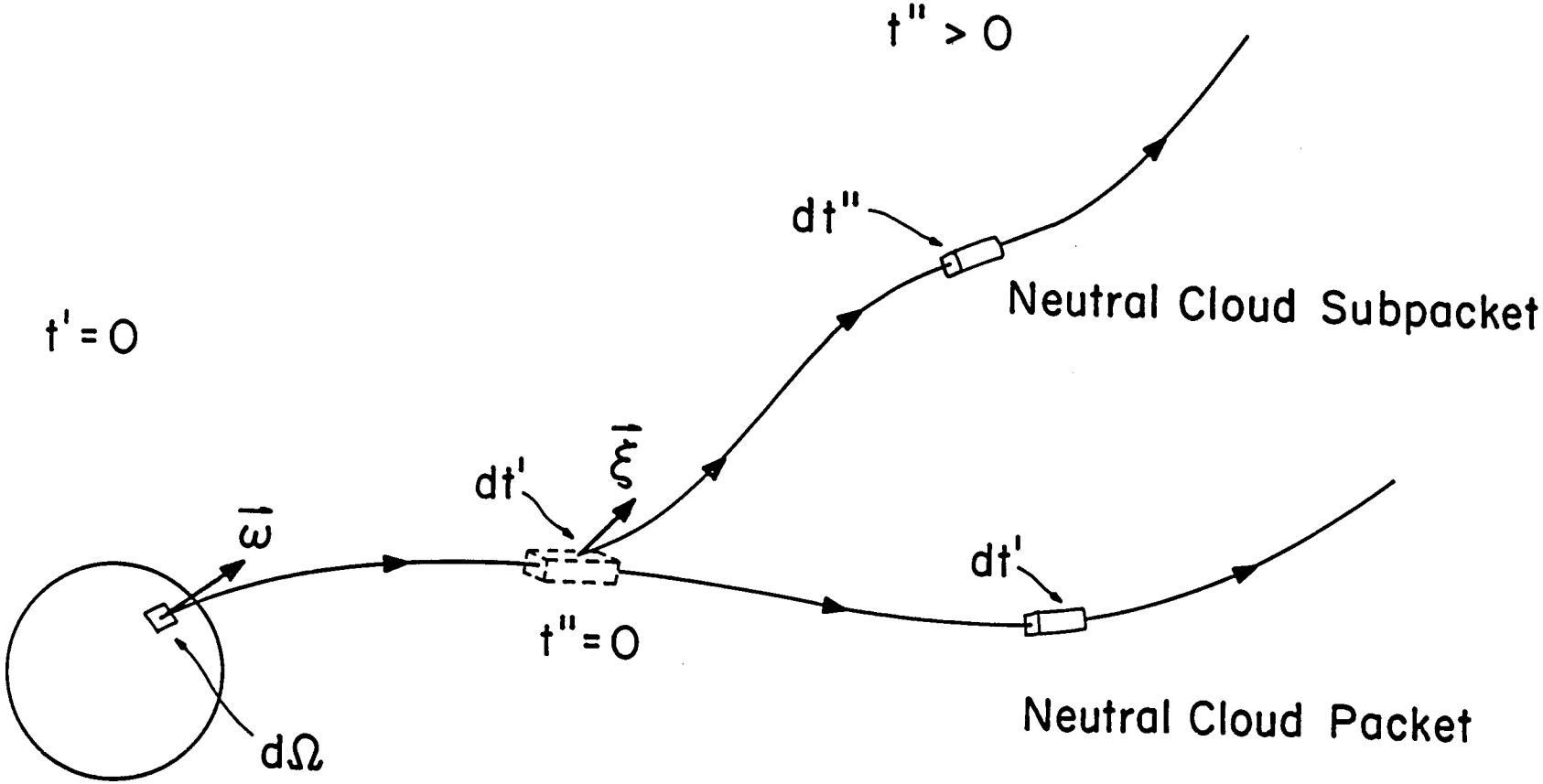
t'' > 0
dt''
Neutral Cloud Subpacket
t' = 0
dt'
ω
ω
dt'
t'' = 0
dΩ
Neutral Cloud Packet
Satellite Exosphere

Figure 2

Michael R. Combi and William H. Smyth
Atmospheric and Environmental Research, Inc.
840 Memorial Drive
Cambridge, MA 02139-3758

Appendix VII

A General Model for Io's Neutral Gas Clouds. II. Applications to the Sodium Cloud

A General Model for Io's Neutral Gas Clouds.I.

Application to the Sodium Cloud

by

W. H. Smyth

M. R. Combi

To appear in

The Astrophysical Journal

15 May 1988

Atmospheric and Environmental Research, Inc.

840 Memorial Drive, Cambridge, Massachusetts

Abstract

The general model for Io's neutral gas cloud developed in Paper I is applied to the sodium cloud. It includes realistic spacetime dependent sinks for sodium in the plasma torus, sources for sodium that describe both thermal and nonthermal processes in the satellite exosphere/corona, and forces on sodium atoms exerted by the planetary and satellite masses and by solar radiation pressure. The sodium cloud model provides a natural and consistent physical explanation for the basic morphological character of the cloud and its east-west asymmetries as observed from ground-based telescopes. The emerging physical explanation is understood in terms of a sodium sink based upon Voyager 1 data for a 7° tilted corotating plasma torus with an offset-dipole planetary magnetic field in the presence of an east-west electric field of ~2.8 mV/m, and a nonthermal sodium source peaked at ~3 km sec^{-1} describing an incomplete collisional cascade process driven by the interaction of the corotating plasma torus with Io. The active exobase area for the nonthermal sodium source is intermediate between a spherically symmetric source (~2.7 x 10^{26} atoms sec^{-1}) and a band source (~1.7 x 10^{26} atoms sec^{-1}), where the latter excludes a portion of the leading and trailing hemispheres. The nonthermal source produces a sodium density (in agreement with recent measurements) of ~3.0 x 10^{3} atoms cm^{-3} at the model-adopted exobase of 2600 km radius and implies a collisional exobase that is somewhat below that level. At the model-adopted exobase, the flux of the nonthermal sodium source dominates by roughly an order of magnitude or more the flux of a 1000-2000°K thermal sodium source. By itself such a thermal source is incompatible with the sodium cloud data. The nature of the nonthermal processes in the exosphere/corona and their implications for the other gas clouds of Io are discussed.

1. Introduction

Studies for the four (Na, K, O, S) known neutral gas clouds of Io coupled with observational data provide an excellent remote sensing tool for recovering physical information regarding the local atmosphere/corona of the satellite, the interactions of this atmosphere/corona with the corotating plasma torus, and the processes that shape the properties of the inner magnetosphere of Jupiter. Recognizing this potential, a general model, appropriate to any of the gas clouds of Io, was developed by Smyth and Combi (1988, hereafter Paper I). This general model is applied here to the sodium cloud with physical insights gained that decisively demonstrate the power of this approach.

The sodium cloud is a particularly good first candidate for this application, for two major reasons. First of all, the sodium cloud is significantly brighter (~10^2 to 10^3) than the other neutral clouds and has been observed extensively during most of the last 16 years, with increasingly better image data obtained in the last decade. This not only allows typical characteristics of the cloud to be identified unambiguously, but also provides a long-term data base that, upon understanding its physical basis, gives a direct and unique means of studying the time history of the Io-planetary-magnetosphere system since about 1972. Second, the sodium cloud has interactions with the plasma torus that are less complex than those for the atomic potassium, oxygen, and sulfur clouds. The excitation mechanism for the sodium cloud (and the potassium cloud) is solar resonance scattering, which is independent of the plasma torus properties, in contrast to the primary electron impact excitation mechanism for the oxygen and sulfur clouds. The sodium cloud, furthermore, has a very small cross section for charge exchange reactions with the major oxygen and sulfur ions of the torus but a very short lifetime that depends on the plasma torus electrons through electron impact ionization. Similar results hold for the dimmer Io potassium cloud, although charge exchange cross sections are considerably larger. In comparison, elastic collisions, charge exchange reactions, and electron impact ionization are all important in determining the lifetime of the oxygen and sulfur clouds. Because of these properties, the study of the sodium cloud allows the different plasma-neutral gas processes to be more easily separated and thereby allows a greater level of confidence and certainty to be gained in the analysis of all the observational cloud data for Io.

The studies of the sodium cloud in this paper are restricted to explaining some of the typical or most basic characteristics of the cloud drawn from published and unpublished observational data. The purpose of this is to verify the analytic usefulness of the model and to provide an overall consistent and physical understanding within which the answers to more refined questions may be pursued in future studies of specific observational data. In keeping with this purpose, for example, three successively more complex descriptions of the plasma torus were considered and were sufficient to explain the basic characteristic of the cloud. A yet more complex description for a plasma torus with properties inherently dependent upon the System III magnetic longitude angle was not included, although observational data for the plasma torus suggest that such features are present. Such System III asymmetries in the plasma torus would produce some time-dependent perturbations in the basic morphology of the sodium cloud. The study of such modifications will be pursued in future model investigations of specific sodium cloud observations.

This paper is organized into five remaining sections. In section 2, past models for the sodium cloud are reviewed and the motivation for developing better models is discussed. The general model of Paper I is adapted to the sodium cloud in section 3, and the interactions of sodium in the plasma torus are discussed. In section 4, the model is used to investigate and provide a consistent physical explanation both for the most basic morphological characteristics of the spatially extended sodium cloud and for the east-west intensity asymmetry observed very near Io. This leads to definite conclusions regarding the flux distribution and density of sodium in the exosphere of Io, the level of the collisional exobase in the atmosphere, the nature of the interaction of the corotating plasma torus and the satellite atmosphere/corona, and the presence of an east-west electric field in the planetary system. These results and some of their implications are discussed in section 5. The paper is briefly summarized in section 6. The Appendices contain mathematical expressions to define the plasma torus descriptions developed in section 3 and the sodium atom flux distributions adopted in section 4.

2. Review of Past Models

Models for the Io sodium cloud have evolved over the past decade by gradual refinements in the description of the source, lifetime, and orbital dynamics of sodium atoms in the Jovian environment as summarized in Table 1. These refinements have been introduced in response to improved cloud data and also to new data obtained for Io and the plasma torus. All of the cloud models in Table 1 assume that sodium atoms are initially ejected radially (with specified source conditions) from Io's surface or local atmosphere (non-radial ejection is also considered by Pilcher et al. 1984) and then travel unhindered along trajectories in the circumplanetary space until they are lost from the cloud by some ionizing sink mechanism. The density and brightness of the cloud are determined by appropriately following many sodium atoms along their trajectories, with proper account taken of ionization and excitation phenomena. For most models, these trajectories are determined by solving in three dimensions the circular-restricted three-body equations of motion for the Jupiter-Io-atom system.

The results of early modeling of the sodium cloud were to identify electron impact ionization as the dominant sink mechanism (Carlson, Matson, and Johnson 1975), and to explore the implication of this finite ionization lifetime (assumed to be spatially uniform) on the cloud morphology (Carlson, Matson, and Johnson 1975; Fang, Smyth, and McElroy 1976; Smyth and McElroy 1977), based upon limited slit-average data showing the absence of a symmetric cloud about Jupiter. Upon the acquisition of two-dimensional image data for the sodium cloud in 1976 and 1977 (Murcray 1978; Matson et al. 1978; Murcray and Goody 1978), the character of a bright and predominantly forward cloud of sodium (i.e., a cloud leading Io in its orbit) became evident. In modeling efforts (Matson et al. 1978; Smyth and McElroy 1978), the presence of the predominantly forward cloud was reproduced by restricting the surface from which atoms were ejected from Io to the inner hemisphere (or within ±30° of it) and by limiting the forward-cloud length by selecting a suitably short spatially uniform sodium lifetime (~20-30 hr). The forward cloud was shown to depend primarily on the low speed components (~3 km sec^{-1}) of the initial velocity distribution with a source rate of about 2×10^{25} sec^{-1} (Smyth and McElroy 1978), while a higher velocity tail ($\lesssim$15 km sec^{-1}) was also shown to be important for populating the cloud north and south of Io (Trafton and Macy

1975; Macy and Trafton 1980; Trafton 1980b) and in reproducing the asymmetric character of observed sodium line profiles (Smyth and McElroy 1977; Carlson et al. 1978; Macy and Trafton 1980). East-west shape asymmetries, first observed in the forward cloud by Goldberg et al. (1978) when images of diametrically opposite phase angles were compared, were shown to arise naturally upon incorporating in the orbital dynamics the acceleration of sodium atoms by solar radiation pressure (Smyth 1979, 1983). East-west intensity asymmetries observed very near Io (Bergstralh et al. 1975, 1977) were also shown (Smyth 1983) to be caused at least in part by the action of solar radiation pressure on sodium atoms ejected at slow velocities ($\lesssim$2.2 km sec^{-1}) from Io. More recently, atmospheric shielding of the sunlit surface by SO_2 vapor to vary the efficiency at which sodium may be sputtered from the surface by corotating ions as a function of the satellite geocentric phase angle has been suggested (Thomas 1986) as an alternative mechanism for the east-west intensity asymmetry. Asymmetries in the plasma torus that may more completely explain this intensity asymmetry will be discussed in sections 3 and 4.

Until 1979, a fundamental deficiency in models for the sodium cloud was the lack of any spatial description of the magnetospheric plasma and hence the ionization lifetime of sodium in the circumplanetary space of Jupiter. The encounter of Voyager 1 with Jupiter provided this missing information and indicated the presence of an extremely radially asymmetric plasma torus, spatially including Io's orbit and oscillating about its orbital plane, that yielded a sodium lifetime as small as 1-2 hours near Io. Incorporating a radial, one-dimensional (i.e., vertically time-averaged) spatial description of the sodium lifetime based on early Voyager data to model a forward cloud image obtained on the Voyager encounter day by ground-based observations, Goldberg et al. (1980) obtained a reasonable match for a sodium source rate of about 3×10^{26} atoms sec^{-1} by restricting gas ejection to one hemisphere. This source rate is about an order of magnitude larger than that determined earlier by Smyth and McElroy (1978) and reflects the increased escape of sodium required to supply the forward cloud when sodium ionization by the plasma torus is explicitly included in the model. Incorporating a more realistic two-dimensional oscillating description of the plasma, Smyth and Combi (1983) presented model calculations for the forward sodium cloud suggesting an isotropic source rate of 2×10^{26} atoms sec^{-1} and demonstrating, as suggested earlier by Smyth (1979, 1983), that the predominantly forward cloud was actually caused

by the extremely radial asymmetric lifetime sink of sodium in the plasma torus and not necessarily by a hemispherical sodium source at Io. This subject will be explored further in section 4. The sodium cloud model of Smyth and Combi (1983) was later used (Pilcher et al. 1984) to explain the time-dependent north/south oscillatory nature of less-bright sodium directional features in terms of the oscillating sodium sink and a high-velocity (~20 km sec^{-1}) sodium source of about 1 x 10^{26} atoms sec^{-1} produced by magnetospheric wind-driven escape, preferentially from the equatorial region of Io. The relationship of such a sodium source to the longitudinal and latitudinal distribution of different volcanic plumes (McEwen and Soderblom 1983), thermal emission from hot spots (Johnson et al. 1984; McEwen et al. 1985), and surface composition (Nelson et al. 1980) poses interesting questions which are now beginning to be probed by the neutral cloud models.

The advances anticipated in physical insight by accurately describing the spacetime interactions of the plasma torus with Io and its extended neutral cloud are aptly illustrated by the sodium cloud model of Smyth and Combi (1983). In general, electron impact ionization, ion-neutral charge exchange reactions, and even elastic ion-neutral collisions (Brown, Pilcher, and Strobel 1983) between the corotating magnetospheric plasma and Io's local and extended atmospheres are processes that must be evaluated and included where necessary in developing each new cloud model. For sodium, improved versions of the model of Smyth and Combi (1983) are developed in section 3 which include even more complete descriptions for the plasma torus as illustrated in section 4. Applications of these more complete models to the large JPL Io sodium cloud data base recently reviewed by Goldberg, Garneau, and LaVoie (1984) and to the complementary and novel Io sodium cloud data-cube images (Doppler resolved, two-dimensional sky plane images) recently reported by Trauger (1984, 1985) provide excellent opportunities for answering fundamental questions in future studies.

3. Model Description

The general mathematical formalism developed in Paper I to describe the neutral gas clouds of Io is here explicitly applied to the Io sodium cloud. For a given neutral gas, the formalism divides the cloud into a description for a primary population and a description for a secondary population. The description for the primary population is based upon following the spacetime history of an ensemble packet of atoms initially ejected from the satellite exobase. The description for the secondary population is similarly based upon following the spacetime history of ensemble subpackets that are created in the spatially extended circumplanetary volume about Jupiter from primary cloud atoms or molecules. The spacetime history of an ensemble packet (or subpacket) and the creation of ensemble subpackets depend upon the physical processes by which the neutral gas interacts with the plasma torus.

a. Interactions in the Plasma Torus

The interactions of sodium atoms with the plasma torus are summarized in terms of chemical reactions and their minimum reaction times in Table 2. There are four basic processes: ionization by solar photons and electrons (R1 and R2), charge exchange (R3 - R5), charge transfer (R6 and R7), and elastic ion-neutral collisions (R8).

Ionization is the most important process for removing sodium atoms directly from an ensemble packet or subpacket. Electron impact ionization (R2) has the smallest reaction time in Table 2 by more than an order of magnitude and effectively determines the lifetime of the cloud. This lifetime for sodium in the plasma torus, however, varies significantly both in space and in time. For an assumed longitudinally symmetric plasma torus tilted by 7 degrees relative to Io's orbital plane, the electron impact ionization lifetime of sodium is shown in Figure 1 for plasma properties to be described later that are appropriate to the Voyager 1 encounter epoch. A minimum lifetime of between 1 and 2 hours occurs on the centrifugal equator between 5.7 and 6.1 planetary radii (R_J) from Jupiter (i.e., $\sim\pm$ 0.2 R_J from the place where Io's orbit intersects the centrifugal equator plane at ~110° and 290° System III magnetic longitude). Inside of a radial distance of about 5.4 R_J on the plasma centrifugal symmetry plane, the sodium lifetime increases extremely rapidly because of a very steep decrease primarily in the electron temperature.

Charge exchange reactions (R3-R5) and charge transfer reactions (R6 and R7), in contrast to ionization processes, remove only a small amount of sodium from the cloud. Charge exchange reactions remove sodium from the primary cloud (an ensemble packet) by creating ensemble subpackets of fast neutrals (~60 km sec^{-1}) which effectively escape from the Jupiter system unless they are trapped in the outer magnetosphere. Because of extremely small cross sections for O^+ and S^+ with Na, only fast sodium atoms are effectively produced. Charge transfer reactions remove sodium directly from the primary cloud by creating additional ions. Both charge exchange and charge transfer reactions have their minimum lifetimes between about 5.0 R_J and 6.0 R_J on the centrifugal equator where the corotating ions have their maximum densities. Inside a radial distance of about 5.4, where the electron impact ionization lifetime increases rapidly, charge transfer reactions are, however, still not effective, since the dominant ion species are then S^+ and O^+. In this inner region, charge exchange reactions with Na^+ are also not effective, since the ion densities are contained by the decreasing ion temperature to be very closely (~± 0.1 R_J) confined to the centrifugal equator, thereby minimizing their spatial overlap with the neutral cloud during the nominal 15-20 hours of flight time of sodium atoms in the forward cloud (see Figure 2). Consequently, electron impact ionization is the only lifetime process that will be considered in this paper for calculating the loss of sodium atoms from an ensemble packet. Furthermore, because the ensemble subpackets created by resonance charge exchange (R5) have a relatively low production rate and move so rapidly in the circumplanetary space that they contribute only minimally to the bright forward (Region B) and near-trailing Io (close Region C) portion of the cloud, they may, for purposes of this paper, also be safely neglected. Those charge exchange reactions that occur directly with the local atmosphere within the Lagrange sphere (~ 6 satellite radii in radius) about Io and that are important sources for the fast component of the fainter sodium observed remote from Io by Brown and Schneider (1981) and more recently near Io by Schneider, Hunten, and Brown (1984) and Trauger (1984, 1985) may be properly included in the source characteristics of the ensemble packets.

The fourth process in Table 2, ion-neutral elastic collisions (R8), as noted by Brown, Pilcher, and Strobel (1983), may be either "hard" (resulting from the repulsive core of the interatomic potential) or "soft" (resulting from the attractive force induced by the passing ionic charge). The "hard"

collisions result in significant momentum transfer to the sodium atoms and cause a simple but small loss of material from the primary cloud that creates ensemble subpackets and are, in this way, somewhat similar in effect to the resonance charge exchange reaction (R5). "Soft" collisions will result in much smaller momentum transfer that severs the kinematic connection between the initial escape conditions at Io and the morphological structure of the near (Region B, close Region C) cloud and thereby also create ensemble subpackets. The attractive potential for the soft sodium collisions has recently been shown (Johnson 1985) to be much smaller than earlier estimates (Brown, Pilcher, and Strobel 1983) so that only hard collisions need be considered for sodium. Since the "hard" collision reaction time for R8 listed in Table 2 is similar in magnitude and spatial character to that of reaction R5 and is more than an order of magnitude larger than reaction R2, the creation of ensemble subpackets by reaction R8 can also be safely neglected for purposes of this paper. The explicit development of the ensemble subpacket formalism for the secondary population of sodium atoms will therefore not be considered further in this paper.

b. Primary Cloud Description

The description of the primary population of sodium atoms is based upon following in flight time t' an ensemble packet of atoms ejected initially (t'=0) at an absolute time t_b with a velocity $\vec{\omega}$ from a surface area element $d\Omega$ centered upon the angular direction $\hat{\Omega}$ of the satellite exobase (see Figure 1 in Paper I). The location of the center of the packet at time t'>0 in a coordinate system fixed relative to the satellite is denoted by $\vec{r}(t', t_b|\vec{\omega},\hat{\Omega})$. The packet trajectories $\vec{r}(t', t_b|\vec{\omega},\hat{\Omega})$ for sodium atoms are computed by numerically solving the modified circular-restricted three-body equations of motion (see Smyth 1983). These equations of motion include both the gravitational field of Jupiter and Io and the effects of solar radiation acceleration.

To describe the interactions of the ensemble packet with the plasma torus, a transformation at an absolute time t of a location $\vec{R}$ in the satellite fixed coordinate system to a location $\vec{\tilde{R}}$ in the plasma torus coordinate system is required and denoted by

$$\vec{\tilde{R}} = \overleftrightarrow{T}(t) \cdot \vec{R} + \vec{D}(t). \qquad (1)$$

This transformation is explicitly defined, for purposes of this paper, in Appendix A. The tensor part of the transformation, $\overleftrightarrow{T}(t)$, explicitly includes the tilt angle of the plasma torus and the absolute time dependent angular motion of both the plasma torus and Io about Jupiter. The vector part of the transformation $\vec{D}(t)$ explicitly includes the effects of the magnetic dipole offset distance and also the stretched-offset distance of the plasma torus because of the presence of an east-west field in the Jupiter system. The location $\vec{r}(t', t_b|\hat{\vec{\omega}}, \hat{\Omega})$ in the plasma torus coordinate frame of the packet at flight time t' is therefore given by

$$\vec{r}(t', t_b|\hat{\vec{\omega}}, \hat{\Omega}) = \overleftrightarrow{T}(t_b+t') \cdot \vec{r}(t', t_b|\hat{\vec{\omega}}, \hat{\Omega}) + \vec{D}(t_b+t'). \tag{2}$$

The probability that the ensemble packet of atoms at flight time t' exists is

$$P(t', t_b|\hat{\vec{\omega}}, \hat{\Omega}) = \exp\left[-\int_0^{t'} \hat{\nu}(t'', t_b|\hat{\vec{\omega}}, \hat{\Omega})\, dt''\right] \tag{3}$$

where $\hat{\nu}(t', t_b|\hat{\vec{\omega}}, \hat{\Omega})$ is the packet collision frequency which depends upon the plasma torus properties and is divided into a contribution from ionization (I), charge exchange (CE), and charge transfer (CT),

$$\hat{\nu} = \hat{\nu}^{(I)} + \hat{\nu}^{(CE)} + \hat{\nu}^{(CT)} \tag{4}$$

as discussed in Paper I. As was seen in the above discussion of sodium atom interactions with the plasma torus, $\hat{\nu}^{(I)}$ for electron impact ionization is the only term that needs to be retained in this paper in evaluating expression (4). Three different descriptions for $\hat{\nu}^{(I)}$ varying in spatial complexity will be developed in the next subsection.

The spatial properties of the neutral cloud are obtained by properly integrating the contributions of an ensemble packet over its complete flight time and over all initial and exobase conditions. Expressions for the contributions of the packet to various cloud properties (e.g., number density, brightness, ion input rate to the plasma torus) are defined in Paper I. In general, if such a packet contribution is denoted by $\hat{Q}(t', t_b|\hat{\vec{\omega}}, \hat{\Omega})$, the corresponding spatial property of the neutral cloud in the observer's coordinate

frame $\vec{r}_o$ at an absolute time t_o is denoted by $Q(\vec{r}_o, t_o)$ and is given by the ensemble average $< \hat{Q} >$. The ensemble average $< \hat{Q} >$ is defined by equation (48) in Paper I and the transformation $\overleftrightarrow{T}_o(t)$ required in this definition is given, for purposes of this paper, in Appendix B.

For model calculations presented in the next section, the only sodium cloud property to be calculated is its D-line emission brightness on the sky plane as viewed from Earth. The excitation mechanism for the sodium cloud emission in the D_1 line (λ_1 = 5895.92 Å) and D_2 line (λ_2 = 5889.95 Å) is solar resonance scattering. The rate J_{λ_i} at which a sodium atom absorbs (and then instantaneously emits) photons in the D_1 line (i=1) and D_2 line (i=2) is given by

$$J_{\lambda_i} = \gamma_i(v) \left(\frac{\pi e^2}{m_e c} \right) \frac{(\pi F_{\nu_i})}{h\nu_i} f_i R^{-2}, \tag{5}$$

where R is the Sun-Jupiter distance in astronomical units, f_i is the oscillator strength of the i^{th} line, πF_{ν_i} is the solar continuum-level photon flux between the D_1 and D_2 lines at R=1, $e^2/m_e c$ is the classical electron radius,

$$(\pi F_{\nu_i}) = 6.80 \times 10^{-5} \frac{\lambda_i^2}{c} F_{\lambda'} \tag{6}$$

(see Allen 1976), and $\gamma_i(v)$ is the fraction of this solar continuum flux available to the sodium atom as it is Doppler shifted out of the bottom of the solar D-line Fraunhofer absorption feature by the instantaneous radial velocity v of the sodium atom relative to the Sun. Further discussion of the emission rate (5) is given by Smyth (1979, 1983). The total photon emission rate for the packet is given by using equation (5) in equation (19) of Paper I. The D-line emission brightness on the sky plane is then determined assuming no parallax by the column projection (equation 50 in Paper I) of the ensemble average (equation 48 in Paper I) of this emission rate for the packet.

c. Sodium Lifetime Description

The ensemble packet collision frequency (4) and lifetime τ for sodium are effectively determined by electron impact ionization and are therefore given simply by

$$\hat{\nu} = \hat{\nu}^{(I)} = \tilde{n}_e K(\tilde{T}_e) = \tau^{-1} \tag{7}$$

Here $\tilde{n}_e$ and $\tilde{T}_e$ are the electron density and temperature in the plasma coordinate frame evaluated at the physical location of the ensemble packet, and $K(\tilde{T}_e)$ is the electron impact ionization rate coefficient shown in Figure 3 as a function of electron temperature. For model results to be presented in the next section, it is sufficient to describe the electron density $\tilde{n}_e$ and temperature $\tilde{T}_e$ for three different steady-state physical situations: (1) Case A, a rotating, Jupiter-centered plasma torus tilted 7° with respect to the orbit plane of Io, (2) Case B, a rotating, offset-dipole-centered plasma torus tilted 7° with respct to the orbit plane of Io, and (3) Case C, a rotating, offset-dipole-centered plasma torus tilted 7° with respect to the satellite orbit plane in the presence of an east-west electric field.

The electron density $\tilde{n}_e$ and temperature $\tilde{T}_e$ for Case A and Case B may be expressed as a function of only the position vector, $\vec{\tilde{R}}$, in the plasma torus coordinate frame. The collision frequency $\tilde{\nu}$ and lifetime $\tilde{\tau}$ for sodium in the plasma torus coordinate frame are then given by

$$\tilde{\nu}(\vec{\tilde{R}}) = \tilde{n}_e(\vec{\tilde{R}})\, K(\tilde{T}_e(\vec{\tilde{R}})) = \tilde{\tau}^{-1}(\vec{\tilde{R}}) \tag{8}$$

so that equation (7) becomes

$$\hat{\nu} = \tau^{-1} = \tilde{\nu}(\vec{\tilde{r}}). \tag{9}$$

Here $\vec{\tilde{r}}$ is defined by equation (2), where $\vec{D}(t_b + t')$ is zero for Case A and nonzero for Case B, and the transformation tensor $\overleftrightarrow{T}$ includes both the seven-degree tilt and the relative rotational motion between the satellite and plasma coordinate frames. In particular, for purposes of this paper, the electron description in Case A and Case B will be further limited to Voyager 1 encounter conditions and the plasma torus will be assumed longitudinally symmetric. The resulting two-dimensional lifetime $\tilde{\tau}(\tilde{\rho},\tilde{z})$ is given in Figure 1, where $\tilde{\rho}$ is the radial along, and $\tilde{z}$ is normal to the centrifugal plasma plane. The radial coordinate $\tilde{\rho}$ in Figure 1 is centered on Jupiter in Case A and on the dipole-offset location in Case B. The lifetime of sodium at Io's location for both Case A and Case B is shown in Figure 4 as a function of the System III longitude angle of Io and are seen to be similar in magnitude and to behave approximately like a phase-shifted sine curve with minimum values occurring when the satellite intersects the centrifugal plasma plane.

The lifetime for sodium in Figure 1 is determined as follows. The adopted values for the electron temperature and density along the centrifugal equator are shown respectively in Figures 5 and 6 and reflect the currently best available values. Assuming a longitudinally symmetric plasma torus, a constant value along dipole field lines for the electron temperature and ion temperature (also shown in Figure 5), and relative ion abundances given by unpublished UVS and PLS results (Shemansky 1985; Bagenal 1985a), the electron density $\tilde{n}_e(\tilde{\rho},\tilde{z})$ in Figure 7 is determined by iteratively solving the diffusive equilibrium equations for a multispecies plasma (see Bagenal 1985b). The sodium lifetime in Figure 1 then follows directly by using in equation (8) the electron density of Figure 7 and the electron temperature of Figure 5, assuming $\tilde{T}_e$ is constant along dipole field lines.

A more complex description of the lifetime for the sodium cloud is obtained in Case C, where both the radial offset of the dipole magnetic field from the center of Jupiter and the east-west stretched shift of the plasma torus from the center of the magnetic field caused by an east-west electric field are included. The magnetic dipole offset, which is explicitly included in the packet formalism by the transformation vector $\vec{D}(t)$ in equation (1), makes the lifetime in a Jupiter-centered coordinate frame vary in System III magnetic longitude angle, even if the torus were assumed longitudinally symmetric in the plasma torus coordinate frame. The east-west shift has three distinct effects on the plasma properties: (1) a geometric shift of the plasma torus center toward the east, (2) a decrease in the electron temperature $\tilde{T}_e$ of a plasma volume element as it moves from west to east of Jupiter, and (3) a decrease in the electron number density $\tilde{n}_e$ of a plasma volume element as it moves from west to east of Jupiter. The effect of the geometric shift is explicitly included in the packet formalism by the transformation vector $\vec{D}(t)$ in (1). The second and third effects, however, make the electron density $\tilde{n}_e$ and temperature $\tilde{T}_e$ depend, in addition to their spatial location $\vec{\tilde{R}}$, on their east-west angular orientation (i.e., its "phase angle" Φ) about Jupiter. The collision frequency $\tilde{\nu}$ and lifetime $\tilde{\tau}$ for sodium in the plasma torus coordinate frame therefore have the functional form

$$\tilde{\nu}(\vec{\tilde{R}},\Phi) = \tilde{n}_e(\vec{\tilde{R}},\Phi)\ K(\tilde{T}_e(\vec{\tilde{R}},\Phi)) = \tilde{\tau}^{-1}(\vec{\tilde{R}},\Phi) \qquad (10)$$

so that equation (7) becomes

$$\hat{\nu} = \tau^{-1} = \tilde{\nu}(\vec{r},\Phi(t_b+t')), \tag{11}$$

where $\vec{r}$ is given by equation (2) and Φ is evaluated at the absolute time t_b+t' corresponding to the position of the ensemble packet at flight time t'.

For purposes of this paper, the electron density $\tilde{n}_e$ and temperature $\tilde{T}_e$ shall furthermore be assumed for Case C to be intrinsically symmetric in the plasma torus longitudinal coordinate for any fixed value of Φ. The lifetime $\tilde{\tau}$ in equation (10) will therefore depend only upon three independent variables, i.e., $\tilde{\tau}(\tilde{\rho},\tilde{z},\Phi)$. An explicit function for $\tilde{\tau}(\tilde{\rho},\tilde{z},\Phi)$ is developed in Appendix C. It is given by equation C.9 and is based upon assuming that $\tilde{n}_e$ and $\tilde{T}_e$ used in Figure 1 are valid at western elongation (i.e., for $\Phi = 270°$) near where the Voyager 1 PLS data were acquired. The lifetime for sodium in the plasma torus coordinate frame as determined by equation C.9 is illustrated in Figure 8. The motion of Io in the plasma torus is also shown in Figure 8 as determined by the transformation (1). The complete radial domain of Io in the plasma torus coordinate frame is shown in Figure 9 as a function of System III magnetic longitude. The corresponding lifetime of sodium at Io's location in the plasma torus is also shown in Figure 10 as a function of Io System III magnetic longitude and Io phase angle. Note that the lifetime of sodium for Io at eastern elongation (90° Io phase angle) is significantly longer than at western elongation (270° Io phase angle). This will result in a brighter sodium cloud near the satellite when Io is east of Jupiter, as discussed in the next section.

4. Model Results

The new sodium cloud model developed in the previous section will now be used to explore two different topics: (1) the physical significances of a predominantly forward sodium cloud and its east-west orbital asymmetries (the latter discovered by Goldberg et al. 1978, 1980) and (2) the role of the plasma torus in explaining the east-west intensity asymmetry of the near Io cloud discovered by Bergstralh et al. (1975, 1977) and its extension into the forward cloud (more recently reported by Goldberg, Garneau, and LaVoie 1984).

For all model results to be presented, the sodium D_2-line emission brightness on the sky plane is computed for a satellite exobase of 2600 km in radius that is divided into 326 equal-area elements. An initially radial velocity vector is assumed for the trajectory of each ensemble packet ejected from each active area element. Active area elements are chosen to simulate a uniform flux of sodium ejected from the entire exobase or from a portion of the exobase such as a quadrant, hemisphere or band region. In computing the ensemble average for the sky plane D_2 brightness of the predominantly forward sodium cloud, an initial mean speed of 2.6 km sec^{-1} (i.e., a monoenergetic source, typical of the speed of the peak of the expected velocity distribution for the forward cloud) is chosen for each active area element. For model calculations examining the east-west intensity asymmetry of the sodium cloud, initial speed distributions are in addition assumed for each active area element. The ensemble packet trajectories $\vec{r}(t', t_b | \omega, \hat{\Omega})$ originating from each active area element are calculated including the effects of solar radiation pressure and the gravitational attraction of Io and Jupiter as discussed earlier.

a. Forward Sodium Cloud

The presence of a bright, well developed forward sodium cloud and the absence of an equally bright trailing cloud have been observed for Io for over a decade (Trafton, Parkinson and Macy 1974; Macy and Trafton 1975a,b; Münch and Bergstralh 1977; Trafton and Macy 1978; Murcray and Goody 1978; Murcray 1978; Matson et al. 1978; Goldberg et al. 1980; Morgan, Pilcher, and Fertel 1983; Trauger 1983, 1984; Pilcher et al. 1984; Morgan and Pilcher 1984; Goldberg, Garneau and LaVoie 1984; Trauger 1985). In the absence of knowledge about the spatial structure of the extremely radially asymmetric sodium sink

in Figure 2, pre-Voyager attempts to model the cloud interpreted the forward cloud by limiting a primarily low-velocity sodium source to a hemispherical region about the satellite and assuming a spatially uniform lifetime (Carlson, Matson and Johnson 1975; Smyth and McElroy 1977, 1978; Matson et al. 1978; Smyth 1979; Macy and Trafton 1980). The hemispherical source region, centered more or less on the inner satellite hemisphere, supplied sodium preferentially (because of orbital dynamics and radially ejected atoms) to the forward cloud. The adopted spatially uniform lifetime of about 20 hours both fixed the length of the forward cloud to that roughly observed and spatially limited sodium atoms that would have eventually (in 25-50 hours) overpopulated and over-extended the observed trailing cloud.

As discussed in section 2, the first post-Voyager modeling of the cloud (Goldberg et al. 1980) incorporated the time-averaged radial structure of the oscillating plasma torus to describe the sodium lifetime in a simple one-dimensional fashion. With this model, the same conclusion was drawn, namely, that the sodium source must still be hemispherical to reproduce properly the predominantly forward cloud. More recently, Smyth (1983) suggested that a real-time oscillating torus may enhance the radial asymmetry of the sodium lifetime so that the forward cloud might be consistently modeled with an isotropic sodium source. If this is true, as it shall be shown to be below, the predominantly forward cloud would then reflect the presence of the plasma torus, not the angular character of the sodium source. The new sodium cloud model will be used to explore and further develop this idea.

To understand the impact of the plasma torus on the morphology of the sodium cloud, a number of monoenergetic model calculations are performed for a variety of active sources on the satellite exobase and for the three plasma torus descriptions (Cases A, B, C) discussed in section 3. Low-speed ($\sim$3 km sec^{-1}) monoenergetic model calculations simulate reasonably well the main features of the forward cloud. This is possible, since earlier studies of spectral and spatial data have indicated that the most probable speed of the velocity dispersion at the exobase occurs at this low-speed value and that a significant percentage ($\gtrsim$30-50%) of the velocity dispersion occurs in the speed interval ($\sim$2-5 km sec^{-1}) where atoms can dynamically populate the forward cloud. The velocity dispersion of sodium atoms at the exobase will be discussed in the next subsection.

Simple comparisons of monoenergetic model calculations for the forward cloud and observed D_2-line emission images (Murcray 1978; Murcray and Goody 1978; Matson et al. 1978; Goldberg, Garneau, and LaVoie 1984; Goldberg 1987) suggest a low-velocity (~2.6 km sec^{-1}) satellite source rate of ~0.5-1 x 10^{26} atoms sec^{-1}. This source rate is smaller than the ~2 x 10^{26} atoms sec^{-1} value for the forward cloud noted by Pilcher et al. (1984), because a lower and more accurate electron temperature is adopted here that increases the sodium lifetime near Io by about a factor of 2. This forward cloud source rate of Pilcher et al. (1984) is similar to the ~3 x 10^{26} atom sec^{-1} source rate determined in the earlier modeling by Goldberg et al. (1980) assuming a sputtering velocity dispersion and a simple one-dimensional description of the plasma torus sink, particularly when the higher velocity (~20 km sec^{-1}) source of ~1 x 10^{26} atoms sec^{-1} discussed by Pilcher et al. (1984) is included to simulate properly the fainter sodium directional features observed in the trailing cloud. Considering the larger velocity dispersion, a forward cloud source rate of ~1 x 10^{26} atoms sec^{-1} is also consistent with the sodium D_2 brightness of many tens of kiloRayleighs observed by Bergstralh et al. (1975, 1977) in their 3 x 8 arc second slit centered on Io. This will be discussed in the next subsection.

A forward cloud source rate of ~1 x 10^{26} atoms sec^{-1} is, however, much larger than the earlier model calculations assuming a simple cutoff lifetime and a hemispherical source of only ~2 x 10^{25} atoms sec^{-1} (Smyth and McElroy 1978; Smyth 1983) and reflects the additional flux required to balance the plasma torus sink of Figure 1. For most forward-cloud model results to be presented, then, monoenergetic (2.6 km sec^{-1}) ejection from the active exobase area with a flux of 2.3 x 10^{8} atoms cm^{-2} sec^{-1} (referenced to the surface area of Io and corresponding to a spherically symmetric source rate of ~1 x 10^{26} atoms sec^{-1}) is therefore adopted as a standard source condition. An Io System III magnetic longitude angle of 140 degrees is also adopted for convenience to set the position for the plasma torus, since this is where the largest model-calculated value of the east-west intensity ratio is obtained, as discussed in the next subsection. Other values of the System III magnetic longitude angle of Io assumed in the model will modify the brightness of the sodium emission somewhat but will not alter the basic spatial shape of the predominantly forward cloud under examination here.

Monoenergetic calculations for the D_2 emission brightness of the forward cloud with Io at eastern elongation are presented in Figure 11. The standard exobase source conditions noted above are assumed for five different active exobase areas: symmetric ejection and ejection from each of its four separate quadrants. The simplest plasma torus description of Case A (i.e., a rotating centrifugal plasma symmetry plane inclined 7° with respect to the satellite plane and centered on Jupiter) is also assumed in Figure 11. For symmetric ejection, the absence of an elongated trailing cloud and the presence and length of the predominantly forward cloud occur naturally in Figure 11 because of the spatially nonuniform nature of the sodium sink (see Figure 2) as anticipated by Smyth (1983). Comparisons for the four quadrant and symmetric sources indicate, as expected on dynamical grounds (Smyth and McElroy 1978), that the trailing inner quadrant is critical in populating the forward cloud and that the outer leading quadrant is most important in populating the trailing cloud. Model calculations for hemispherical sources are shown in Figure 12 and are obtained by properly adding model results for quadrant sources in Figure 11. Both trailing and inner hemispherical sources produce a well developed forward cloud as expected from the quadrant results of Figure 11, but the trailing cloud for the inner hemisphere source is underdeveloped and somewhat less extended than typically observed in ground-based images for Io at this phase angle.

The model results of Figures 11 and 12 suggest that the spatial morphology of the bright sodium cloud may be consistent with a symmetric source or other sources that appropriately mix sodium ejection from a portion of both the inner and outer exobase hemispheres. One such alternative source, considered below, is a band source. Such an exobase source for high-velocity sodium (~20 km sec^{-1}) was suggested by Pilcher et al. (1984) to explain the fainter sodium directional features. The active exobase area for the low-velocity (2.6 km sec^{-1}) band source adopted here is ~±40 degrees in width and centered on the great circle formed by the intersection of the exobase sphere and a plane that is perpendicular to the satellite orbit plane and that contains the centers of Io and Jupiter. Sodium is ejected uniformly from the band area, which is about 63% of the active exobase area of the symmetric source.

Model results for the sodium cloud with Io at both eastern and western elongations are shown in Figure 13 for a symmetric and band source. Comparison of the model results at lower brightness levels for the symmetric source indicates a forward cloud that is more elongated at western elongation. This east-west orbital asymmetry follows directly from the combined effects of the orbital perturbation by solar radiation pressure of sodium atoms (Smyth 1979, 1983) and the spatially nonuniform lifetime of sodium in the plasma torus. The typical east-west orbital asymmetry observed in ground-based images (Goldberg et al. 1980; Goldberg, Garneau, and LaVoie 1984) is, however, generally more pronounced, and the forward cloud is not this extended in the west. For the band source, this preferential elongation of the west forward cloud is more enhanced and the west cloud is furthermore foreshortened. These additional effects occur because the band source restricts atom trajectories to those which are more strongly influenced by the acceleration of solar radiation pressure. Typically observed east-west orbital asymmetries are probably best matched by a source that is somewhat intermediate to the band source and symmetric source. Comparison of model results for the symmetric and band sources in Figure 13 indicates spatial morphologies that are similar at the 1 to 2 kiloRayleigh level, but are significantly brighter very near Io for the symmetric source. Near Io, this increased brightness occurs because the symmetric source is ~1.6 times larger than the band source, while further from Io much of this larger source has since been ionized by the plasma torus and no longer contributes to the forward cloud. Model calculations using the band source and the plasma torus description with a magnetic dipole offset (Case B) are extremely similar to the results in Figure 13, as may be anticipated by the small lifetime differences for Case A and Case B shown in Figure 4.

Model calculations for the band source with a plasma torus description including both the magnetic dipole offset and an east-west electric field offset (Case C) are shown in Figure 14. The nominal value for the east-west stretched offset adopted in Figures 8 and 10 is assumed ($\epsilon = 0.025$ with $\Psi_s = \pi$; see the Appendices). For a plasma torus element 5.9 R_J west of the dipole center, this nominal value corresponds to an east-west L-shell change of ~0.30 R_J (i.e., an effective displacement of ~0.15 R_J). Comparison of the spatial morphology of the model calculations in Figure 14 indicates that at eastern elongation the cloud is significantly brighter (~25%) very near Io and has a brighter and hence more fully developed forward and trailing cloud with-

in a distance of ~1/2 to 1 R_J from the satellite. This character of the sodium cloud is also evident in the observational image data published by Goldberg, Garneau, and LaVoie (1984) and reinforces the idea that the east-west electric field is present in the Jovian system. The brighter cloud for Io at eastern elongation occurs because of the larger lifetime of sodium that exist at eastern phase angles, as was illustrated in Figures 8 and 10. The significantly brighter sodium cloud for Io at eastern phase angles as illustrated in Figure 14 provides a natural explanation for the east-west intensity asymmetry discovered by Bergstralh et al. (1975, 1977) which is discussed below.

b) East-West Intensity Asymmetry

The presence of an east-west intensity asymmetry in the brightness of the D-line emissions from the sodium cloud very near Io was discovered by Bergstralh et al. (1975, 1977) from ground-based observations. These observations, acquired for many different east and west geocentric phase angles of the satellite over two apparitions, measured the brightness of the cloud in a 3 x 8 arc second slit centered on Io with the long dimension oriented perpendicular to the projection of the satellite orbit plane. As illustrated in Figure 15, this viewing slit samples primarily the sodium D-line emissions from the local (i.e., bound) atmosphere of the satellite which is within the Lagrange sphere. The Lagrange sphere is an effective sphere centered on Io inside of which the gravitational field of the satellite dominates the gravitational field of Jupiter. The slit measurements of Bergstralh et al. show that both the D_1-line and D_2-line emission brightnesses for Io east of Jupiter are consistently about 25% larger than for Io west of Jupiter. Furthermore, the slit-averaged D_2 brightness values for Io near eastern elongation were typically ~40-45 kR, with a few measured values in the 50-60 kR range. Modeling results of Smyth (1979, 1983) suggest that a significant part of this east-west intensity asymmetry may be attributed to the acceleration effects of solar radiation pressure on sodium atoms if the velocity distribution at the exobase is sufficiently peaked at low subescape speeds. Results presented below for the sodium cloud model of section 3, however, suggest that the velocity distribution may not be this highly peaked at these very low speeds and that the east-west asymmetries in the plasma torus induced by the east-west electric field are therefore primarily responsible for the observed east-west intensity asymmetry in the sodium cloud.

Model calculations presented below for the D-line emission brightness in the Bergstralh slit are computed for the Case C description of the plasma torus which explicitly includes both the magnetic dipole offset and the east-west offset resulting from a convective east-west directed electric field. For these model results, the east-west brightness ratio in the slit is measured by dividing its calculated brightness for Io at eastern elongation (90° geocentric phase angle) by its calculated brightness for Io at western elongation (270° geocentric phase angle). Calculations are performed for the two Io System III magnetic longitude angles of 140° and 320°. For an Io System III magnetic longitude angle near 140°, the east-west brightness ratio in the slit has a maximum value. For an angle near 320°, the ratio has a minimum value. This dependence of sodium brightness and hence east-west ratio on the Io System III magnetic longitude angle occurs because of the changing space-time lifetime history experienced by sodium atoms near Io (see Figure 10). This changing lifetime dependence is geometric in nature and occurs because Io's position in the plasma torus (see Figure 8) varies as the orientation of the magnetic dipole offset and the east-west offset cycle between alignment and near cancellation. This brightness modulation is exhibited in the data of Bergstralh et al. (1975, 1977), although it was not recognized by them because of an error in properly calculating the Io System III magnetic longitude angle. A detailed analysis of the Bergstralh et al. data augmented by additional slit data acquired more recently by Goldberg (1987) is beyond the scope of this paper and will be published separately. Model computations presented here are selected to illustrate the primary character of the east-west brightness ratio and its relationship to the strength of the electric field and to the speed dispersion of atoms ejected from Io's exobase.

For exobase ejection of sodium, the band source is selected for all model caluclated values of the east-west brightness ratio. This source represents a somewhat minimal active area exobase source (i.e., ~63% of the symmetric source) that was shown in the previous subsection to be needed to simulate reasonably well the basic morphological features of the forward sodium cloud for speeds in the ~2-5 km sec^{-1} range. Both lower speeds (with a likely preference to more symmetric ejection) and higher speeds (that do not contribute significantly to the forward cloud) may also be present in the velocity dispersion of atoms ejected from the exobase and could contribute significantly to the Bergstralh slit brightness. To explore these possibilities, the

character of monoenergetic model calculations is examined first. Model calculations are then performed for different velocity distributions in order to assess whether the observed slit brightnesses and east-west brightness ratio place constraints on the speed dispersion and source strength of sodium atoms ejected from the exobase.

The model calculated dependence of the east-west brightness ratio on the plasma torus shift parameter ϵ (see the Appendices) is shown in Figure 16 for monoenergetic (2.6 km sec^{-1}) ejection of sodium from an exobase band source and for the two Io System III magnetic longitude angles of 140° and 320°. Such a sodium source is, of necessity, required, since the existence of the forward cloud source is well established. The parameter ϵ, which is small, is defined by Barbosa and Kivelson (1983) as the ratio of the magnitude of the east-west electric field to the value of the corotational electric field (~0.113 volt/m) at Io's orbital distance from the magnetic dipole. For increasing values of the east-west electric field (i.e., increasing values of ϵ), the east-west brightness ratio increases for both curves in Figure 16. For an ϵ value of 0.025, the observed ~25% enhancement of the east-west intensity ratio is achieved as an average between the maximum ratio value on the 140° curve and the minimum ratio value on the 320° curve. This value of ϵ implies an effective average east-west offset of ~0.15 R_J for a plasma parcel at Io's distance from the magnetic dipole center and an east-west electric field of ~2.8 mV/m. This value of ϵ is very similar to the ~0.03 value suggested by Barbosa and Kivelson (1983) to produce a ~±10% modulation in the electron temperature that is required in explaining the dawn-dusk plasma torus asymmetry in the EUV S^{++} ion emission intensity measured in 1979 by the Voyager spacecraft (Sandel and Broadfoot 1982; Shemansky and Sandel 1982). Additional analysis of these data (Sandel 1985) has shown that the EUV asymmetry is time variable and corresponds to a time-averaged east-west offset of a plasma torus parcel at Io's distance from the magnetic dipole center of about 0.2 R_J, roughly toward dawn. Further confirmation of an east-west electric field of this magnitude is evident in east-west asymmetries in optical S^+ ion emissions from the plasma torus observed in the 1981-84 time frame (Morgan 1985a,b,c). Analysis of 1981 data by Morgan (1985a,b), when the plasma torus had changed in some important ways from the 1979 Voyager picture, led him to suggest a preferred value of 0.04 for ϵ, with a value near 0.03 still providing a reasonable fit to the intensity asymmetry but a less

preferred fit to differences between the east and west radial profiles of the S^+ emissions. Since the Case C description for the plasma torus used in the sodium model is based upon the Voyager encounter picture, a representative value of 0.025 is adopted for ϵ in subsequent calculations.

The east and west D_2 brightness (per unit sodium atom flux) in the Bergstralh slit is shown in Figure 17 for monoenergetic model calculations with velocities ranging from 0 to 10 km sec^{-1} and for Io System III longitude angles of 140° and 320°. The corresponding east-west brightness ratios are shown in Figure 18. The increase and then decrease of the east and west brightness and their ratio with ejection speed may be understood as follows. For ejection speeds less than about 1.7 to 1.8 km sec^{-1}, the trajectories of sodium atoms are basically ballistic in nature (i.e., confined to the Lagrange sphere; see Figure 15). In this velocity range, the sodium abundance and brightness in the Bergstralh slit increase with increasing speed because the atoms fill an increasing portion of the slit viewing area. Because of the larger sodium lifetime near Io at eastern elongation, this increasing sodium abundance translates directly into a relative increase of the east intensity and hence to an increasing east-west intensity ratio. For ejection speeds larger than about 1.7 to 1.8 km sec^{-1}, sodium atoms may escape the satellite (i.e., the Lagrange sphere) with increasing ease. This reduces both the abundance of sodium near Io and the residence time of sodium atoms in the Bergstralh slit, during which time the differing east-west lifetimes may alter the sodium abundance differently. These two factors cause the D_2 brightness and the east-west ratio to decrease with increasing velocity. In addition, for ejection velocities near 2.0 km sec^{-1}, the abundance of sodium near Io at eastern elongation is also preferentially enhanced by the action of solar radiation pressure (Smyth 1979, 1983), as is particularly evident in the 140° curve of Figure 18.

For the 140° curve and 320° curve in Figure 18, the average east-west brightness ratio is equal to the observed 1.25 value for the ballistic ejection speed of ~1.05 km sec^{-1} and for the escape ejection speed of ~2.6 km sec^{-1}, the latter speed being consistent with the results of Figure 16. For an exobase ejection speed of ~1.05 km sec^{-1}, the sodium atoms and hence D_2 brightness are confined within a spherical shell about 1600 km above the surface of Io, while for the larger speed of 2.6 km sec^{-1}, the sodium escapes Io

and forms a forward cloud as discussed in the previous subsection. In reality, of course, there is a dispersion of sodium atom speeds at the exobase. The slit brightness and corresponding east-west ratio then depend upon the convolution of the exobase flux distribution (as a function of speed) with the monoenergetic model calculated brightness per unit flux results of Figure 17. The nature of the speed dispersion of sodium near Io and its impact on the east-west intensity ratio are addressed in the remainder of this section.

Various components of the speed dispersion of sodium atoms at the exobase of the satellite have been roughly characterized in past analyses of spectral and spatial data for the D-line emissions. Spectral line profile data (Trafton 1975; Trauger 1977; Trafton and Macy 1977, 1978; Carlson et al. 1978; Trafton 1983) have shown that the ejection speeds range from values comparable to the exobase escape velocity of the satellite (~2 km sec^{-1}) to those as large as 15-20 km sec^{-1}, with data of Brown and Schneider (1981) and also more recent unpublished and high signal-to-noise data acquired at Oak Ridge Observatory extending this speed range to beyond 70 km sec^{-1}. The typical line profile has two main characteristics: a low-velocity peak and a high-velocity asymmetric skirt. The peak, which is relatively narrow (FWHM of ~±20-40 ma or ~±1 to 2 km sec^{-1}), is Doppler shifted ~20-50 ma (i.e., an apparent speed of 1 - 2.5 km sec^{-1}) relative to the projected orbital speed of the satellite on the sky plane and may be associated with nonthermal, low-speed (2-3 km sec^{-1}) atoms ejected from the exobase. The skirt, which is attached asymmetrically to the peak in the Doppler direction of velocities larger than the satellite orbit speed, decreases with increasing Doppler displacement from the peak and extends at low D_2 brightness levels to at least ~1400 ma (~70 km sec^{-1}). The peak and skirt may be associated with nonthermal processes involving multicollisional neutral-neutral encounters as well as single ion-neutral elastic and charge exchange encounters that are driven by plasma torus interactions with Io's local atmosphere. Many of these speed components in the spectral data may also be identified in the spatial morphology data for the sodium cloud. The forward cloud may be identified with the ~2-5 km sec^{-1} speed range (Smyth and McElroy 1977, 1978; Matson et al. 1978; Smyth 1979; Goldberg et al. 1980; Macy and Trafton 1980; Smyth 1983), the fainter trailing-cloud directional features with the ~10-25 km sec^{-1} speed range (Pilcher et al. 1984), and the very faint forward-cloud jets with the ~30-80 km sec^{-1} speed range (Trauger 1984, 1985).

To capture the essence of this speed dispersion and to probe the existence of a more traditional thermal source, two different velocity distributions (or, more correctly, flux distributions) are considered as a function of the initial ejection speed v of sodium atoms from the exobase. The first is what shall be called a modified-sputtering flux distribution, denoted by $\phi(v;\ v_b,\ \alpha,\ v_M)$, to describe in an approximate manner the nonthermal source that is produced by the interaction of plasma torus ions with Io's atmosphere and exosphere. For the modified sputtering flux distribution, the velocity v_b is primarily responsible for determining the most probable speed of the distribution, the parameter α regulates the breadth of the dispersion resulting from the composite effects of single ion-neutral collisional ejection of sodium and sodium ejection from ion-neutral, neutral-neutral collisional cascade processes, and v_M is the maximum speed that a stationary atom can acquire by collision with a corotating plasma torus ion. The second distribution is a Maxwell-Boltzmann flux distribution, denoted by $\phi(v;\ T)$, to describe a thermal source and its thermal corona, where T is the exobase temperature. The definitions and properties of these two flux distributions are presented in Appendix D. The two flux distributions are expressed for convenience as a product of the total flux ϕ_0 for all speeds and a normalized flux distribution $\bar{\phi}$

$$\phi(v;\ v_b,\ \alpha,\ v_M) = \left(\frac{R_S}{R_E}\right)^2 \phi_0\ \bar{\phi}(v;\ v_b,\ \alpha,\ v_M) \tag{12.a}$$

$$\phi(v;\ T) = \left(\frac{R_S}{R_E}\right)^2 \phi_0\ \bar{\phi}(v;\ T) \tag{12.b}$$

where $\bar{\phi}$ is constructed so that it is equal to unity when integrated over the complete speed range and where ϕ_0 is referenced to the satellite surface of radius R_S and not the exobase surface of radius R_E.

The normalized modified sputtering distribution is illustrated in Figure 19 for $\alpha = 3$ (classical sputtering) and $\alpha = 7/3$ (Thomas-Fermi-like collisional ejection), where v_b is selected so that the most probable speed is 3 km sec^{-1}. The maximum speed of the flux distribution is $\sqrt{v_M^2 - v_b^2}$, where v_M = 46.62 km sec^{-1} is determined for collision of corotating oxygen ions and stationary sodium atoms. For corotating sulfur ions and stationary sodium atoms, v_M (= 66.16 km sec^{-1}) is larger, but the shapes of the two flux distributions are otherwise very similar to those in Figure 19 and therefore need

not, in addition, be considered for our purposes. The significant difference between the two curves in Figure 19 is that the distribution for $\alpha = 3$ is more populated near the most probable speed and consequently less populated at higher speeds ($\gtrsim$ 12 km sec^{-1}) than the distribution for $\alpha = 7/3$. As noted earlier by Sieveka and Johnson (1984), the approximate two-to-one ratio in the sodium source for the forward cloud and directional feature that was deduced by Pilcher et al. (1984) is more appropriate for the Thomas-Fermi-like flux distribution. In Figure 19, this is illustrated simply by roughly assigning the forward cloud to the 2-5 km sec^{-1} speed range and the directional feature to the 12-25 km sec^{-1} speed range. For the distribution with $\alpha = 3$, the atom flux populations associated with the forward cloud and the directional feature are then 47.2% and 6.8%, respectively, which yield a sodium source ratio of ~7. For the distribution with $\alpha = 7/3$, these two populations are 34.6% and 16.5%, respectively, and yield the desired sodium source ratio of ~2.

The normalized Maxwell-Boltzmann flux distribution is illustrated in Figure 20 for a moderately high exobase temperature of 1500°K and compared with the modified sputtering flux distributions of Figure 19. The Maxwell-Boltzmann flux distribution is highly peaked about the most probable speed of 1.275 km sec^{-1}. About 80% of the flux population is confined below the speed of 1.8 km sec^{-1}, while only 11.7% and 1.4% have speeds in excess of 2.0 km sec^{-1} and 2.6 km sec^{-1}, respectively. Such a flux distribution will produce a sodium corona confined almost entirely within the Lagrange sphere of Io and will consequently contribute to the Bergstralh slit brightness. This Maxwell-Boltzmann flux distribution is, however, clearly not energetic enough to be an appropriate source for supplying sodium to the forward cloud and to the directional features.

Model results for the D_2 brightness per unit atom flux (i.e., normalized by ϕ_0) based upon the band source with a modified sputtering flux distribution are shown for the Io System III longitude angles of 140° and 320° in Figure 21 for $\alpha = 3$ and in Figure 22 for $\alpha = 7/3$. The two corresponding east-west brightness ratios are shown in Figure 23. Both the brightness per unit flux and the ratio values are presented as a function of the most probable speed v_m of the flux distribution, which is related to v_b (see Appendix D) as indicated numerically in Figure 23. In Figure 23 the observed east-west ratio of ~1.25 is matched as an average value between the 140° and 320° curves for a most

probable speed of ~3.2 km sec^{-1} with $\alpha = 3$ and for a most probable speed of ~2.9 km sec^{-1} with $\alpha = 7/3$. Assuming a source rate of 2.3 x 10^8 atom cm^{-2} sec^{-1} for the forward cloud (i.e., in the 2-5 km sec^{-1} speed range), the flux ϕ_0 is then 5.05 x 10^8 atom cm^{-2} sec^{-1} and 6.53 x 10^8 atom cm^{-2} sec^{-1} for $\alpha = 3$ and $\alpha = 7/3$, respectively. With these values for ϕ_0 and the most probable speeds of 3.2 km sec^{-1} and 2.9 km sec^{-1}, the corresponding D_2 brightnesses in the Bergstralh slit from Figures 21 and 22 vary from ~28 kR to 21 kR for $\alpha = 3$ and from ~32 kR to 24 kR for $\alpha = 7/3$. For the favored flux distribution with $\alpha = 7/3$, these D_2 brightness values are similar to, but smaller than, the typical observed values of ~40-45 kR and the less frequently observed values of ~50-60 kR. If, however, a symmetric source had been used instead of the band source, the model calculated D_2 brightness values would be enhanced by about a factor of two, yielding D_2 brightness for $\alpha = 7/3$ in the ~50-60 kR range. A source with active exobase surface area somewhere between the band source and the symmetric source will therefore match both the observed D_2 brightness and the east-west intensity ratio of ~1.25.

Model results for the D_2 brightness per unit atom flux (i.e., normalized by ϕ_0) based upon the band source with a Maxwell-Boltzmann flux distribution are shown in Figure 24 for the Io System III longitude angles of 140° and 320°. The corresponding east-west intensity ratio is shown in Figure 25. In both figures, the model results are presented as a function of the most probable speed v_m of the flux distribution, which is defined in Appendix D and is related to the exobase temperature T as indicated numerically in Figure 25. The average of the 140° and 320° curves in Figure 25 matches the observed ratio of 1.25 for a low most probable speed of 0.71 km sec^{-1} (i.e., T ≃ 460°K) and for a high and thermally unrealistic most probable speed of ~3.65 km sec^{-1} (i.e., T ≃ 12,300°K). For exobase temperatures of 1000°K to 2000°K, which amply cover the range that has been suggested for Io (Kliore et al. 1975; Kumar 1984, 1985; Summers 1985), the east-west ratio in Figure 25 as determined by the average between the 140° and 320° curves is significantly higher than the observed value of ~1.25. This result follows directly from the small dispersion of the Maxwell-Boltzmann flux distribution illustrated in Figure 20 and the monoenergetic model results of Figures 17 and 18 which are significantly peaked near the ejection speeds of 1.6 km sec^{-1} and 1.7 km sec^{-1}.

The fact that the east-west intensity ratio for a Maxwell-Boltzmann flux distribution with an exobase temperature of 1000°K to 2000°K is much larger than the observed value places a constraint on the flux of such a thermal source. For a value of ϕ_0 no larger than 2 x 10^8 atom cm^{-2} sec^{-1}, the D_2 brightness in the Bergstralh slit as determined from Figure 24 varies between ~27 kR and ~18 kR. These brightnesses are comparable to those determined earlier for the modified sputtering flux distribution, and, when added to the contribution for the preferred modified sputtering flux distribution (α = 7/3, v_m = 2.9 km sec^{-1}, ϕ_0 = 6.53 x 10^8 atoms cm^{-2} sec^{-1}), yield an average east-west intensity ratio of 1.31 and a maximum eastern brightness of 59 kR, both of which are already too large. A value of ϕ_0 ~ 1 x 10^8 cm^{-2} sec^{-1} is only slightly more acceptable, producing a maximum eastern D_2 brightness of ~45 kR for the two flux distributions and an average east-west ratio of 1.29. Even for this value of ϕ_0, however, the Maxwell-Boltzmann flux is already dominated by at least a factor of ~7 at the adopted exobase radius (2600 km) by the nonthermal modified-sputtering flux. For a lower exobase temperature, the thermal flux is not so tightly constrained. With an exobase temperature of 460°K, the thermal flux may be as large as $\phi_0 \simeq 2 \times 10^8$ atoms cm^{-2} sec^{-1}, since, when it is combined with the preferred modified sputtering flux distribution, a maximum eastern D_2 brightness of ~45 kR and east-west brightness ratio of 1.25 are produced. This cooler thermal component of the corona is, however, very closely confined near the exobase ($\lesssim$ a few hundred kilometers). Even though the sodium data do not rule out the existence of such a cool thermal component, its presence is not required since, as noted earlier, the nonthermal flux distribution by itself is perfectly capable of matching both the observed brightness and the east-west ratio. These results suggest that the ion-neutral collisional processes produced by the interactions of the corotating plasma torus ions and Io's atmosphere/exosphere dominate over thermal processes in the exosphere and even bring into question the physical possibility that Io's atmosphere can support any appreciable classical thermal exosphere.

The density of sodium at the exobase radius (2600 km) may be approximately estimated from the ϕ_0 values for each flux distribution by using the expressions derived in Appendix D. For the preferred modified sputtering flux distribution (α = 7/3. v_m = 2.9 km sec^{-1}, ϕ_0 = 6.53 x 10^8 atoms cm^{-2} sec^{-1}), the nonthermal sodium density at the exobase is estimated to be ~3.0 x 10^3

cm^{-3}. This value is very similar to the sodium density of $(2.2 \pm 1.1) \times 10^3$ cm^{-3} actually measured at this distance from Io by means of novel eclipse data for Io's sodium atmosphere obtained from ground-based observations (Schneider et al. 1987). Nonthermal model results to also match the radial density gradient of sodium, measured by Schneider et al., look very promising, but such an analysis is beyond the scope of this paper. For the Maxwell-Boltzmann flux distribution, the thermal sodium density is constrained to be $\lesssim 1.7 \times 10^3$ cm^{-3} for a hot thermal exobase (T=1500°K, $\phi_0 \leq 1 \times 10^8$ atoms cm^{-2} sec^{-1}) and $\lesssim 6.0 \times 10^3$ cm^{-3} for a cooler thermal exobase (T = 460°K, $\phi_0 \lesssim 2 \times 10^8$ atoms cm^{-2} sec^{-1}). When compared with the measured sodium density, these model-constrained thermal densities suggest that cooler thermal components are not present at the adopted exobase radius, although they could, of course, exist at a somewhat lower altitude if the true collisional exobase were located there. As has been suggested by the relative ion compositions in the plasma torus (Gehrels and Stone 1983; Bagenal 1985b) and by the relative escape rates of atoms to supply the neutral clouds (Smyth and Combi 1984), the relative abundance of sodium to oxygen and sulfur is $\sim 10^{-2}$. If this is indicative of the mixing ratio at the model-adopted exobase radius, then the density of the major gas species at this distance from Io would be $\sim 10^5$ cm^{-3}. Such a density is, however, at least an order of magnitude smaller than the density required to form a classical collisional exobase, suggesting even more strongly that the true collisional exobase is likely somewhat below the model-adopted exobase radius of 2600 km.

5. Discussion

The new model for Io's neutral gas cloud developed in Paper I has been applied to the Io sodium cloud. Three successively more complex descriptions of the plasma torus were explicitly considered for the sodium sink in addition to sodium sources at Io's exobase that were both thermal and nonthermal in nature. These sink and source signatures have been increasingly more evident in observational data for the sodium cloud in the past several years. A review of earlier sodium cloud models indicated that previous descriptions of the plasma torus and the sodium source have not adequately included these signatures. Model calculations to illustrate the importance of these sinks and sources in the sodium cloud were presented. These calculations were able both to reproduce and to provide a consistent physical explanation for the basic morphological characteristics and east-west intensity asymmetry of the cloud observed from ground-based telescopes. These model results and their physical implications are summarized below.

Model results for the distribution of the D_2-line emission brightness on the sky plane were used to analyze the general observed characteristics of the sodium cloud and to relate them to both the spatial structure of the plasma torus and certain source conditions on Io's exobase. The most basic observed characteristic of the sodium cloud—the absence of a bright, elongated trailing cloud and the presence of a predominantly bright forward cloud—was shown to occur naturally because of the extreme radial gradients in the density and temperature of the plasma torus inside Io's orbit. These gradients produce a sharp increase in the electron impact ionization lifetime for sodium atoms (see Figure 1), so that the forward cloud (which dynamically occupies the interior circumplanetary space) survives much longer than the trailing cloud (which dynamically occupies the external circumplanetary space). The overall shape and brightness of the basic forward and trailing clouds are consistent with an exobase source that contains radial sodium ejection from at least a portion of the inner and outer hemispheres. Both a symmetric source ($\sim 1.0 \times 10^{26}$ atoms sec^{-1}) and a band source ($\sim 0.65 \times 10^{26}$ atoms sec^{-1}) with a mean, nonthermal ejection speed of ~2.6 km sec^{-1} produce a similar and acceptable forward cloud for brightness levels of $\lesssim$ 1-2 kR. In the model calculation, the east-west orbital asymmetry of the forward cloud, which is produced by D-line solar radiation pressure effects on sodium atoms, is, however, more enhanced for the band source than for the symmetric source.

When compared with typical image data (Goldberg et al 1980; Goldberg, Garneau, and LaVoie 1984), a preferred source would appear to be somewhat intermediate to the band and symmetric sources. The generally brighter sodium cloud that has been observed in image data when Io is preferentially east of Jupiter (Goldberg, Garneau, and LaVoie 1984) occurs naturally in the model results for the most complex of the plasma torus descriptions (Case C), where both an east-west electric field offset and a magnetic field dipole offset were included.

Model results were also presented that quantitatively reproduce the observed east-west intensity asymmetry of the sodium cloud (Bergstralh et al. 1975, 1977) and relate it to an east-west (i.e., dawn-dusk) electric field in the Jupiter system and to the flux distribution for sodium atoms at the model-adopted exobase of Io. For a plasma torus description (Case C) with a magnetic field dipole offset and an east-west electric field of ~2.8 mV/m (i.e., an east-west offset of 0.15 R_J at Io's distance from the dipole center), monoenergetic (~2.6 km sec^{-1}) model calculations reproduced the basic structure of the forward cloud and also the average 25% east-to-west brightness enhancement observed in the measuring slit of Bergstralh et al. Larger and smaller values of the electric field produced enhancements that were, respectively, too large or too small when compared with the observed value. A similar value for the east-west electric field has been previously used to explain both the EUV dawn-dusk intensity asymmetry from S^{++} emission in the plasma torus (see Barbosa and Kivelson 1983; Ip and Goertz 1983) measured by the Voyager spacecraft and the optical east-west intensity asymmetry from S^{+} emission measured from ground-based facilities (see Morgan 1985a,b,c). The east-west asymmetries of the plasma torus and the sodium cloud are anticorrelated, as noted earlier by Smyth and Combi (1985 and 1987). To properly simulate the D-line brightnesses in the Bergstralh et al. slit, however, a flux distribution must be used to include the contributions from the speed of all sodium atoms in the exosphere/corona, since the slit is centered on Io and spatially samples the sodium brightness primarily in the Lagrange sphere of the satellite (see Figure 15). A modifed sputtering flux distribution, to describe the nonthermal speeds evident in sodium cloud data, and a thermal Maxwell-Boltzmann flux distribution, to explore the importance of a classical thermal exosphere, were therefore adopted.

For the modifed sputtering flux distribution, two different physical situations were included to describe the nonthermal sodium source produced by interaction of the corotating plasma torus ions and the atmosphere/exosphere of Io. The first is for a sodium source generated by a complete ion-neutral, neutral-neutral cascade process, for which a classical sputtering flux distribution was chosen. The second is for a sodium source generated by a somewhat incomplete cascade process that exhibits at higher speeds ($\gtrsim$ 10 km sec^{-1}) the character of single elastic collisional ejection of atoms by corotational ions, for which a Thomas-Fermi-like flux distribution was constructed. This second flux distribution more accurately reflects the relative speed populations of sodium atoms as roughly deduced from spatial and spectral data for the sodium cloud. Fast ($\gtrsim$ 60 km sec^{-1}) sodium atoms, which are produced by charge exchange with Na^+ and are evident in the very faint sodium jets ahead of Io (Trauger 1984,1985), were not, however, included along with the Thomas-Fermi-like flux distribution, because they are too fast and are too low in population to be important for our immediate purposes. From model calculations, it was shown that the general spatial character of the sodium cloud and both the average ~25% east-to-west intensity enhancement and the absolute brightness measured by Bergstralh et al. were consistently reproduced by a Thomas-Fermi-like distribution with a most probable speed of ~2.9 km sec^{-1}, an exobase source with flux of 6.5×10^8 atoms cm^{-2} sec^{-1} (referenced to Io's surface area), and an active exobase area somewhere between the band source and the symmetric source. This corresponds to a total sodium source between 1.7×10^{26} atoms sec^{-1} and 2.7×10^{26} atoms sec^{-1}. The classical sputtering flux distribution for a symmetric source could just fit both the brightness and 25% east-to-west intensity enhancement, but it is much too deficient in flux in the 12-25 km sec^{-1} speed range to supply adequately the fainter sodium directional feature (Pilcher et al. 1984).

Model results for the Maxwell-Boltzmann flux distribution indicated that for suggested thermal exobase temperatures in the range ~ 1000-2000°K, the calculated east-west intensity ratio is much higher than the observed value of ~1.25. This result constrains the thermal flux to be $\lesssim 1 \times 10^8$ atoms cm^{-2} sec^{-1}, even when a nonthermal Thomas-Fermi-like flux distribution with a minimum band source and flux of 6.5×10^8 is also assumed to contribute simultaneously to the slit D_2 brightness. The thermal flux distribution contributes primarily to the corona density within the Lagrange sphere and is far

too deficient in energetic sodium atoms to contribute any significant sodium to the forward cloud. The near order of magnitude dominance of the nonthermal flux over the thermal flux at the model-adopted exobase (2600 km radius) corresponds to a thermal sodium density of $\lesssim 1.7 \times 10^3$ cm^{-3} and a nonthermal sodium density of ~3.0×10^3 cm^{-3}. The nonthermal density compares very well with the measured value of $(2.2 \pm 1.1) \times 10^3$ cm^{-3} at the model-adopted exobase recently reported by Schneider et al. (1987). A cooler exobase temperature of 460°K is constrained by the sodium data to a thermal flux of $\lesssim 2 \times 10^8$ atoms cm^{-2} sec^{-1} and a corresponding thermal sodium density of $\lesssim 6.0 \times 10^3$ cm^{-3} at the model-adopted exobase. Based upon these sodium densities, the classical collisional exobase would occur somewhat below the model-adopted exobase. Such heights for the collisional exobase are nearer the "minimum" SO_2 atmosphere for Io at the Voyager 1 encounter required by photochemical models of Kumar (1984).

Based upon the sodium results, the escape of oxygen and sulfur from Io should also be characterized by a large, nonthermal flux distribution in the exosphere. In contrast to sodium, however, an equally large and very fast (~60-100 km sec^{-1}) flux distribution will be produced for atomic oxygen and sulfur by charge exchange reactions because the elastic and charge exchange cross sections are comparable (Smyth and Combi 1984). The very fast neutrals will, however, contribute minimally to the corona density, but the corresponding newly created hot oxygen and sulfur ions will provide at Io a major energy source for the plasma torus (Smyth and Combi 1984). This energy source at Io, in contrast to the spatially distributed energy source for the torus produced by the extended neutral clouds, may provide the additional energy required to properly balance the EUV energy radiated primarily by sulfur ions as noted recently by Shemansky (1987). The lower speed, nonthermal flux produced by elastic collisional processes will, however, support an extended nonthermal corona. The density of this nonthermal corona will be determined in a self-consistent manner by a balance between the outward-directed escape flux of collisionally energized neutrals and the upward supply rate from below of gases from Io's lower atmosphere and surface. From simulation of such a corona, McGrath and Johnson (1987) have reached conclusions similar to those of this paper, namely, that these collisional corona processes are the dominant gas escape mechanism for supplying mass to the plasma torus and that single collision ejection of neutrals is, for the "minimum" SO_2 atmosphere of

Io (Kumar 1984), the largest coronal ejection process. These nonthermal collisional processes will penetrate energetically somewhat below the classical collisional exobase level and may modify significantly the gas density and simple diffusive equilibrium (vertical stratification) assumptions used in photochemical models for Io (Kumar 1984, 1985). In this manner, the simple photochemical picture could be replaced in the upper atmosphere by a nonthermal heating layer and an effective global atmospheric blowoff process.

Future studies of the sodium clouds of Io will be able to extend and refine significantly the physical insights for the satellite and the plasma torus gained from the investigations of this paper. Detailed model-data comparisons of the brightness and the east-west brightness ratios near Io can be used to (1) calculate the sodium density profile inside and beyond the Lagrange sphere of Io, (2) estimate the amount of cooling that electrons may have undergone in the upper atmosphere/corona, (3) refine the shape and nonisotropic character of the nonthermal flux distribution of sodium atoms near the exobase and hence the character of the ion-neutral processes in the upper atmosphere/corona, and (4) investigate variations in the strength of the east-west electric field and/or the plasma torus properties over more than a decade time span. Further model-data studies of time variations in the brightness morphologies of the forward sodium cloud and the directional features can be used to investigate inherent System III longitudinal dependence in the plasma torus and probe changes in the sodium source that occur on time scales which depend upon the satellite phase angle, the System III longitude angle of Io, or longer secular changes in the Jovian system. Of particular pertinence to these morphological studies are the massive sodium cloud data set acquired by JPL (Goldberg, Garneau and LaVoie 1984) and the novel Doppler-resolved images for the sodium cloud acquired by Trauger (1984, 1985).

Beyond the sodium cloud, valuable future studies for the potassium, oxygen and sulfur clouds can also be performed. In particular, by using the new gas cloud model of Paper I and cloud emission brightness data acquired for oxygen and sulfur with the aid of rocket (Durrance, Feldman and Weaver 1983; Skinner and Durrance 1986), the IUE satellite (Ballester et al. 1987), and ground-based telescopes (Brown 1981; Mekler 1986), a number of major investigations will be made possible. These investigations will be capable of calculating (1) the density in the upper atmosphere/corona of Io, (2) the loss

rate of gases from the atmosphere, and (3) the three-dimensional spatial character of the ion loading rate, plasma mass loading rate and ion energy input rate for the plasma torus supplied by different gas species lost by Io both very near the satellite and in the spatially extended neutral clouds.

6. Summary

A new general neutral cloud model (Paper I) has been applied to explain various observed phenomena regarding both the local and the extended regions of the neutral sodium cloud produced by Io. These include the predominant forward cloud, the east-west orbital asymmetry of the forward cloud, and the density of sodium in the near Io atmosphere/corona and its east-west intensity asymmetry. The model accounts for the spatially nonuniform and time-dependent sodium sink produced by a 7° inclined corotating plasma torus which in its most general form (as required by the sodium data) includes the physical and geometrical effects of the Jovian offset-dipole magnetic field and an east-west electric field of ~2.8mV/m whose presence and strength are implied by direct torus measurements.

Sodium sources considered for Io include nonthermal atmospheric sputtering and incomplete collisional cascade flux distributions, both produced by collisions between torus ions and atmospheric atoms, as well as a thermal source. For the sodium cloud, a dominant nonthermal source for the incomplete collisional cascade flux distribution (peaked at ~3 km sec^{-1} with a strength between 1.7×10^{26} atoms sec^{-1} and 2.7×10^{26} atoms sec^{-1}) is required from an active exobase area which is basically spherically symmetric with the most forward and backward elements absent.

This first application of the model to the sodium cloud has uncovered a number of important new results regarding the nature of the local Io atmosphere/corona and its interactions with the plasma torus, the escape of material from Io, and the nature of the plasma torus itself. Exciting future applications of the new model to the neutral clouds of potassium, oxygen, and sulfur, as well as detailed time-dependent studies of the wealth of sodium data, were also discussed. The most important of these future studies are (1) the space and velocity distribution of gases in the local atmosphere as it relates to the escaping gas and to torus electron cooling, (2) variations in the east-west electric field, (3) system III longitudinal asymmetries in the plasma torus, and (4) the ion, mass, and energy input rates of the local atmosphere and the extended neutral clouds to the plasma torus.

Acknowledgments

This research was supported by the Planetary Atmospheres Program of the National Aeronautics and Space Administration under grants NASW-3949 and NASW-3387. Acknowledgment is also made to the National Center for Atmospheric Research, which is sponsored by the National Science Foundation, for computational time used in the model computations. The authors also wish to thank F. Bagenal, D.E. Shemansky, and E.C. Sittler for their insightful discussions and unpublished electron and ion data for the plasma torus. In addition, we wish to thank B.A. Goldberg for unpublished sodium cloud image data, L.M. Trafton for unpublished sodium cloud spectral data, C.B. Pilcher and J.S. Morgan for unpublished sodium cloud and plasma torus image data, and R.E. Johnson for helpful information regarding ion-neutral cross sections and collisional cascade processes.

APPENDIX A

PLASMA TORUS COORDINATE FRAME TRANSFORMATIONS

The transformation from a location $\vec{\tilde{R}} = (\tilde{x},\tilde{y},\tilde{z})$ in the magnetic (or, more generally, the plasma torus) frame to a location $\vec{R} = (x,y,z)$ in the satellite fixed coordinate frame at an absolute time t is represented by

$$\vec{\tilde{R}} = \overleftrightarrow{T}(t) \cdot \vec{R} + \vec{D}(t) \qquad \text{A.1}$$

in expression (1) of the text. In matrix form, the transformation A.1 is

$$\begin{bmatrix} \tilde{x} \\ \tilde{y} \\ \tilde{z} \end{bmatrix} = [\overleftrightarrow{T}(t)] \begin{bmatrix} x \\ y \\ z \end{bmatrix} + [\vec{D}(t)] \qquad \text{A.2}$$

where the tensor matrix is given by

$$[\overleftrightarrow{T}(t)] = \begin{bmatrix} \cos(\psi-\theta) & \sin(\psi-\theta) & 0 \\ -\sin(\psi-\theta)\cos\phi & \cos(\psi-\theta)\cos\phi & -\sin\phi \\ -\sin(\psi-\theta)\sin\phi & \cos(\psi-\theta)\sin\phi & \cos\phi \end{bmatrix} \qquad \text{A.3}$$

and the column matrix is given by

$$[\vec{D}(t)] = \begin{bmatrix} 1 & 0 & 0 \\ 0 & \cos\phi & -\sin\phi \\ 0 & \sin\phi & \cos\phi \end{bmatrix} \begin{bmatrix} d\cos\delta_d\sin(\mu_N-\mu_d) + \epsilon\,(x^2+y^2)^{1/2}\sin(\psi-\psi_s) \\ -d\cos\delta_d\cos(\mu_N-\mu_d) + \epsilon\,(x^2+y^2)^{1/2}\cos(\psi-\psi_s) \\ -d\sin\delta_d \end{bmatrix}. \qquad \text{A.4}$$

The tensor transformation A.3 includes the tilt angle ϕ of the plasma torus plane and both the angular motion $\psi = \psi(t)$ of the plasma torus and the angular motion $\theta = \theta(t)$ of Io about Jupiter. The vector transformation A.4 contains the effects of the magnetic dipole offset distance d and the stretched-offset distance $\epsilon(x^2+y^2)^{1/2}$ of the plasma torus proposed by Barbosa and Kivelson (1983) because of the presence of an east-west electric field in the Jupiter system. The definitions of the plasma and satellite coordinate frames as well as a more detailed description of the physical transformation A.2 and its related parameters and variables are discussed below.

The plasma torus is centered at the origin of the $(\tilde{x},\tilde{y},\tilde{z})$ frame with the $\tilde{z}$-axis normal to the centrifugal plasma plane and inclined by an angle ϕ with respect to the direction of the Jupiter spin axis. The Jupiter spin axis is

normal to the equatorial plane of the planet in which Io's orbital motion is assumed to be confined to a circular orbit about the planet. The projection of the positive $\tilde{y}$-axis onto the equatorial plane of the planet occurs at the System III (1965) magnetic longitude μ_N of the projected north magnetic polar axis. The magnetic field is described by an offset tilted dipole. The offset-dipole distance d has a direction vector in System III defined by a latitude angle δ_d and a longitude angle μ_d. The spin axis of the plasma torus is parallel to the Jupiter spin axis but is displaced from the center of the torus by the dipole offset vector. The spin period of the plasma torus is the System III rotation period denoted by T_{III}. The orientation of the rotating plasma torus at an absolute time t is determined by specifying the geocentric phase angle ψ,

$$\psi(t) = \psi_{1965}(t_1) + \frac{2\pi}{T_{III}} (t - t_1) , \qquad A.5$$

of the System III longitude $(\mu_N + \pi/2)$, where $\psi_{1965}(t_1)$ is the phase angle as determined in the System III (1965) Jupiter longitude convention for a conveniently chosen absolute reference time t_1. The System III central median is therefore given by $(\mu_N - \pi/2 + \psi)$.

The spin axis of the plasma torus is furthermore displaced in the equatorial plane from the center of Jupiter by an east-west electric field (Barbosa and Kivelson 1983; Ip and Goertz 1983) assumed to be in the equatorial planet plane. The stretched displacement is given by $\epsilon(x^2 + y^2)^{\frac{1}{2}}$, where ϵ is the ratio of the magnitudes of the east-west electric field and the corotation electric field as defined by Barbosa and Kivelson (1983) and $(x^2 + y^2)^{\frac{1}{2}}$ is the radial displacement from Jupiter in the equatorial plane as measured in the satellite fixed coordinate frame. For generality, the orientation of the electric field is assumed not to be exactly east-to-west as defined by an earth observer. Its orientation is determined by the geocentric phase angle ψ_s of a symmetry line (perhaps solar wind in origin) that is drawn in the equator plane, normal to the electric field and directed toward the sunlit portion of the planetary equator. The orbital motion of Io about the center of Jupiter is in the same direction as the spin of the plasma torus but has a longer rotation period T_{Io}. The satellite fixed coordinate frame (x,y,z) is centered on Jupiter with the (x,y)-plane in the equator plane and Io on the positive x-axis. The angular orientation of Io about Jupiter at an

absolute time t is determined by the geocentric Io phase angle θ referenced to the time t_1 as in A.5:

$$\theta(t) = \theta(t_1) + \frac{2\pi}{T_{Io}} (t - t_1) \ . \qquad \text{A.6}$$

For model calculations in this paper, the following values for the transformation parameters are chosen: $\phi = 7°$, $d = 0.131$, $(\delta_d, \mu_d) = (-8°, 149°)$, $\mu_N = 202°$ and $\psi_s = 180°$. The values for d, δ_d, μ_d and μ_N are for the O_4 offset tilted dipole model of the Jovian magnetic field (see Acuña, Behannon and Connerney 1983). Different values for the parameter ϵ are chosen as discussed in section 4.

APPENDIX B

OBSERVER'S COORDINATE FRAME TRANSFORMATION

The transformation from a location $\vec{R}_o = (x_o, y_o, z_o)$ in the observer's coordinate frame to a location $\vec{R} = (x,y,z)$ in the satellite fixed coordinate frame at an absolute time t is represented by

$$\vec{R}_o = \overleftrightarrow{T}_o(t) \cdot \vec{R} \qquad \text{B.1}$$

and used in expression (46) of Paper I. In matrix form, the transformation B.1 is

$$\begin{pmatrix} x_o \\ y_o \\ z_o \end{pmatrix} = [\overleftrightarrow{T}_o(t)] \begin{pmatrix} x \\ y \\ z \end{pmatrix}, \qquad \text{B.2}$$

where the tensor matrix is given by

$$[\overleftrightarrow{T}_o(t)] = \begin{pmatrix} \cos\bar{\phi}\cos\theta & -\cos\bar{\phi}\sin\theta & -\sin\bar{\phi} \\ \sin\theta & \cos\theta & 0 \\ \sin\bar{\phi}\cos\theta & -\sin\bar{\phi}\sin\theta & \cos\bar{\phi} \end{pmatrix} . \qquad \text{B.3}$$

The observer's frame is centered on Jupiter with x_o-axis directed along the Earth-Jupiter line and the Earth located on the negative x_o axis. The angle $\bar{\phi}$ is the apparent tilt angle of the orbit plane of Io as seen by an Earth observer and $\theta = \theta(t)$ is the geocentric phase angle for Io defined by equation A.6.

APPENDIX C
ELECTRON IMPACT IONIZATION DESCRIPTION FOR SODIUM

The electron impact ionization description of the lifetime of sodium in the plasma torus coordinate frame $(\tilde{x},\tilde{y},\tilde{z})$ is developed below for Case A (a rotating, Jupiter-centered and tilted dipole), Case B (a rotating, dipole-offset-centered and tilted dipole), and Case C (a rotating, dipole-offset and tilted dipole in the presence of an electric field in the planetary equator). These cases are adopted in section 3 and used in section 4. The descriptions developed below are appropriate to the encounter time of the Voyager 1 spacecraft with Jupiter.

Voyager 1 in situ plasma data have been reduced (Sittler 1986; Sittler and Strobel 1986; Bagenal 1985a,b; Bagenal et al. 1985; Bagenal and Sullivan 1981) for each measured position along the spacecraft trajectory to L-shell coordinates, adopting an offset tilted dipole description for the magnetic field. Assuming that the electron and ion temperatures are constant along the magnetic field lines and that the electron and ion density distributions along the field lines are determined by solving the diffusive equilibrium equations for a multispecies plasma (see Bagenal 1985b), the electron temperature and density can be determined in the centrifugal plasma torus equator plane at specific radial and longitudinal locations for each spacecraft measurement. Because of the lack of sufficient longitudinal plasma information, the simplifying assumption has generally been made that these densities and temperatures in the centrifugal plane are independent of magnetic longitude. With this assumption, radial profiles for the electron temperature and density in the centrifugal plasma equator plane follow and are shown, respectively, in Figures 5 and 6. This simplifying assumption, of course, ignores the skewed (i.e., nonnormal) orientation of the field lines to the centrifugal equator plane which varies with system III longitude and causes the real plasma torus description above and below the centrifugal plane to be asymmetric except at the node longitudes ($\sim\mu_N \pm 90°$). This assumption also ignores any intrinsic system III magnetic longitude dependence which has been seen in more recent plasma torus data obtained from ground based observations (Pilcher and Morgan 1985; Pilcher, Fertel, and Morgan 1985; Pilcher and Morgan 1980; Trafton 1980a; Trauger, Münch, and Roesler 1980). Adopting this simplification, a

two-dimensional description for the electron density in the plasma torus is chosen at the node longitude's projection (an average condition) where the density above and below the centrifugal plasma plane is symmetric. This longitudinally symmetric description for the electron density is shown in Figure 7, and the corresponding lifetime description for sodium based on electron impact ionization is shown in Figure 1. In Case A the radial coordinate in Figure 1, which is actually centered on the offset-dipole location, is assumed simply to be centered on Jupiter. In Case B the radial coordinate in Figure 1 is centered on the dipole-offset location.

In Case C the additional presence of an electric field in the equator plane destroys the longitudinal symmetry of the electron temperature and density as depicted in Figures 5-7. As a plasma volume element moves from west to east of Jupiter, its radial displacement $L = (\bar{x}^2 + \bar{y}^2)^{1/2}$ in the centrifugal plane from the dipole centered coordinate frame $(\bar{x},\bar{y},\bar{z})$ increases, resulting not only in a new center for the essentially circular path of the plasma volume element (Barbosa and Kivelson 1983) but also in an expansion in the density and a cooling in the temperature of the plasma volume element. Ignoring the approximate 7° tilt of the centrifugal equator, which because of the rotation of the plasma torus about Jupiter causes the component of the equatorial electric field parallel to the radial coordinate L to be modulated very slightly, the radial displacement of the plasma volume element is given (to first order in ϵ) by

$$\frac{L}{L_w} = 1 + \epsilon[1 + \sin(\Phi - (\psi_s - \pi))] \quad . \qquad C.1$$

Here Φ is the phase angle of the plasma volume element about Jupiter ($\Phi = \pi/2$ at eastern elongation, $\Phi = 3\pi/2$ at western elongation, and $\psi_s = \pi$ for an east-to-west directed electric field), L_w is the radial displacement of the plasma volume element at $\Phi = 3\pi/2 + (\psi_s - \pi)$, and ϵ is the ratio of the uniform east-west convection and corotation electric fields as defined by Barbosa and Kivelson (1983). The radial coordinate $\tilde{L} = (\tilde{x}^2 + \tilde{y}^2)^{1/2}$ in the plasma torus centered coordinate frame $(\tilde{x},\tilde{y},\tilde{z})$ is related (to first order in ϵ) to the dipole centered radial coordinate L by

$$\tilde{L} = L[1 - \epsilon \sin(\Phi - (\psi_s - \pi))] \qquad C.2$$

so that (to first order in ϵ) $\tilde{L}$ is, as required, independent of $\Phi - (\psi_s - \pi)$ for a particular plasma volume element

$$\tilde{L} = (1+\epsilon)L_w \quad . \tag{C.3}$$

To describe the plasma torus in the $\tilde{L}$ centered coordinate, the descriptions of the electron density in Figure 7 and the electron temperature in Figure 5, both deduced from Voyager 1 measurements made west of Jupiter, are adopted as the description of the electron density $n_e^w(L_w,\bar{z})$ and electron temperature $T_e^w(L_w)$ at that phase angle near western elongation $\Phi = \frac{3\pi}{2} + (\psi_s - \pi)$ where the plasma volume element is in the Jupiter meridian plane containing the east-west electric field vector. The electron density $\tilde{n}_e$ and temperature $\tilde{T}_e$ in the plasma-torus centered coordinate system $(\tilde{L},\tilde{z},\Phi)$ are then given by

$$\tilde{n}_e(\tilde{L},\tilde{z},\Phi) = \left(\frac{L_w}{L}\right)^3 n_e^w(L_w,\bar{z}) \tag{C.4}$$

$$\tilde{T}_e(\tilde{L},\tilde{z},\Phi) = \left(\frac{L_w}{L}\right)^3 T_e^w(L_w) \quad , \tag{C.5}$$

where the expansion factor is

$$\left(\frac{L_w}{L}\right)^3 = 1-f \tag{C.6}$$

so that to first order in ϵ

$$f = 3\epsilon\,[1 + \sin(\Phi - (\psi_s - \pi))]\,\nabla \tag{C.7}$$

The expansion factor C.6 for the electron temperature follows from the approximate integral of the motion for the diamagnetic moment of a charged particle in a slowly (space and time) varying magnetic field. This adiabatic invariant also requires that the magnetic flux through a flux tube containing the plasma volume element be invariant for the west-to-east radial displacement. For a dipole field, the cross-sectional area in the symmetry plane of the flux tube is proportional to L^3. Assuming a constant height for the plasma volume element as it is displaced radially, the expansion factor C.6 is therefore also applicable for the density C.4.

The lifetime $\tilde{\tau}$ for sodium atoms in the plasma torus centered coordinate frame is given by the reciprocal of the collision frequency,

$$\tilde{\nu}(\tilde{L},\tilde{z},\Phi) = \tilde{n}_e(\tilde{L},\tilde{z},\Phi)\ K(\tilde{T}_e(\tilde{L},\Phi)) \ , \qquad \text{C.8}$$

where $K(\tilde{T}_e)$ is the electron impact ionization rate coefficient. Combining the expressions C.4-C.8, expanding the rate coefficient $K(\tilde{T}_e)$ about $\tilde{T}_e = T_e^w$ in a Taylor series in ϵ, and retaining terms to first order only in ϵ, the lifetime for sodium atoms $\tilde{\tau} = \tilde{\nu}^{-1}$ is given explicitly by

$$\tilde{\tau}(\tilde{L},\tilde{z},\Phi) = \tau^w(L_w,\bar{z})\ [1 + 3\epsilon\ (1 + \sin\ (\Phi - (\psi_s - \pi)))\ (1 + T_e^w(L_w)\ K'(T_e^w(L_w))\ /\ K\ (T_e^w(L_w)))] \qquad \text{C.9}$$

where $\tilde{L} = (1+\epsilon)\ L_w$ and $\tilde{z} = \bar{z}$. Here,

$$\tau^w(L_w,\bar{z}) = [n_e^w(L_w,\bar{z})\ K\ (T_e^w(L_w))]^{-1} \qquad \text{C.10}$$

is the lifetime at $\Phi = \frac{3\pi}{2} + (\psi_s - \pi)$ as given by Figure 1, $T_e^w(L_w)$ is given by the adopted curve in Figure 5, and K(T) and K'(T) are obtained from Figure 3, where

$$K'(T) = \frac{dK(T)}{dT} \ . \qquad \text{C.11}$$

APPENDIX D

THERMAL AND NONTHERMAL FLUX DISTRIBUTION

The atom flux ejected from the exobase to describe the primary population of the cloud is given by

$$\phi(\vec{\omega},\hat{\Omega},t_b) = \vec{\omega} \cdot \hat{\Omega}\, f^{(\text{primary})}(\vec{\omega},\vec{x}_b,t_b) \qquad \text{D.1}$$

in equation (11.b) of Paper I, where $f^{(\text{primary})}(\vec{\omega},\vec{x}_b,t_b)$ is the one-particle distribution function. The rate at which atoms are ejected at time t_b from a differential surface area element $d\Omega$ ($= R_E^2 \sin\Phi\, d\Phi\, d\theta$) with an outward-directed normal unit vector $\hat{\Omega} = (\theta,\Phi)$ located on the exobase of radius R_E at $\vec{X}_b = (R_E,\theta,\Phi)$ and with initial velocity vectors in the range $\vec{\omega}$ to $\vec{\omega} + d\vec{\omega}$ is then

$$\phi(\vec{\omega},\hat{\Omega},t_b)\, d\Omega\, d\vec{\omega}. \qquad \text{D.2}$$

For purposes of this paper, the atom flux is assumed to be uniform on the active portion of the exobase, zero on the inactive portion of the exobase, and independent of the ejection time t_b. The one-particle distribution function on the active exosphere is also assumed to depend only upon the speed $v = |\vec{\omega}|$, so that dropping the '(primary)' superscript,

$$\phi(\vec{\omega},\hat{\Omega}) = \vec{\omega} \cdot \hat{\Omega}\, f(|\vec{\omega}|), \qquad \text{D.3}$$

where $f(|\vec{\omega}|)$ is normalized so that the number density n of this gas at the exobase is given by

$$n = \int_{\text{all space}} f(|\vec{\omega}|)\, d^3\vec{\omega}, \qquad \text{D.4}$$

where $d^3\vec{\omega} = |\vec{\omega}|^2 d\Omega' dv$ is the volume element in velocity space and $d\Omega'$ is the solid angle element in velocity space. An upward-directed flux distribution, $\phi(v)$, is defined as a function of the speed v by

$$\phi(v) = \frac{1}{R_E^2} \int_{\substack{\text{upward} \\ \text{hemisphere}}} \phi(\vec{\omega},\hat{\Omega})\, d\Omega' = \pi v^3 f(v) \qquad D.5$$

so that the uniform flux of atoms ejected from the active area of the exobase in the speed range v to v+dv is $\phi(v)\, dv$. In this paper, the upward-directed flux distribution is adopted and used in the model calculations, where it is simply assumed that the ejection velocity vectors of all atoms are initially normal to the exosphere (i.e., radial ejection).

For the Maxwell-Boltzmann flux distribution adopted in this paper, the one-particle distribution function depends parametrically on the exobase temperature T and is given by

$$f(v;T) = \frac{1}{\sqrt{\pi^3}} \frac{n}{v_T^3} e^{-(v/v_T)^2} \qquad D.6$$

where

$$v_T = \sqrt{\frac{2kT}{m}} \qquad D.7$$

is the most probable speed of the velocity distribution and where m is the mass of the gas atom. The Maxwell-Boltzmann flux distribution then follows from equation D.5 and is given by

$$\phi(v;T) = \frac{n}{\sqrt{\pi}} \left(\frac{v}{v_T}\right)^3 e^{-(v/v_T)^2} . \qquad D.8$$

The most probable speed for the flux distribution D.8 is denoted by v_m and is given by

$$v_m = \sqrt{\frac{3kT}{m}} . \qquad D.9$$

The total upward flux at the exobase may then be related to the flux ϕ_0, referenced to the surface area of Io, by the expression

$$\int_0^\infty \phi(v;T)\, dv = \frac{nv_T}{2\sqrt{\pi}} = \frac{nv_m}{\sqrt{6\pi}} = \frac{R_S^2}{R_E} \phi_0 \qquad D.10$$

where R_S is the radius of the satellite. The normalized flux distribution $\bar{\phi}(v;T)$ is then defined by

$$\bar{\phi}(v;T) = \phi(v;T) \Big/ \frac{nv_T}{2\sqrt{\pi}} = \frac{2}{v_T}\left(\frac{v}{v_T}\right)^3 e^{-(v/v_T)^2} . \qquad D.11$$

For the modified sputtering flux distribution adopted in this paper, the equivalent one-particle distribution function is given as a function of three parameters (α, v_b, v_M) by

$$f(v;\alpha,v_b,v_M) = \frac{v_b^{2\alpha-3}}{\pi C(\alpha, v_M/v_b)} \frac{n}{(v^2+v_b^2)^\alpha}\left[1 - \sqrt{\frac{v^2+v_b^2}{v_M^2}}\right]. \qquad D.12$$

where the dimensionless function $C(\alpha, v_M/v_b)$ is given by the integral

$$C(\alpha, v_M/v_b) = 4\int_0^{\sqrt{(v_M/v_b)^2 - 1}} \frac{x^2}{(1+x^2)^\alpha}\left[1 - \frac{v_b}{v_M}\sqrt{1+x^2}\right] dx \qquad D.13$$

which is not easily expressed in an analytical form for arbitrary α. The dimensionless parameter α regulates the breadth of the speed dispersion, and describes the composite effects at the exobase of single-collisional encounters and multicollisional encounters (i.e., cascade processes or sputtering) of neutral sodium atoms in the atmosphere/corona with corotating ions in the plasma torus. Classical sputtering, which describes a collisional cascade process that has proceeded to completion, is obtained for $\alpha=3$ (see Sieveka and Johnson 1984). As is indicated by the directional feature data for the sodium cloud (Pilcher et al. 1984; Sieveka and Johnson 1984), incomplete collisional cascade processes for the higher speed ($\gtrsim$10 km sec^{-1}) sodium atoms are evident and are more appropriately represented by its leading term in the cascade chain, which is single elastic collisional ejection. For single elastic collisional ejection of sodium atoms by plasma ions (Johnson 1985), the atom flux distribution is directly proportional to the Thomas-Fermi differential cross section (see Johnson 1982; Sieveka and Johnson 1984), which for the energy range of interest in the plasma torus and for the mathematical form adopted for the modified sputtering flux distribution yields an α value of 7/3. The velocity parameter v_b in the distribution function D.12 is primarily responsible for determining the most probable speed of the velocity

distribution. In the theory of sputtering from surfaces, the speed v_b is determined by the surface binding energy ($mv_b^2/2$) for the ejected atom and also ensures that the distribution is well behaved at low values of the speed v. The velocity parameter v_M is the maximum speed that a stationary sodium atom of mass m can acquire in an elastic collision with a plasma torus ion of mass M and relative speed v_R:

$$v_M = \frac{2M}{(M + m)} v_R. \qquad \text{D.14}$$

The velocity v_M establishes a maximum speed for the velocity distribution which is given by $\sqrt{v_M^2 - v_b^2}$. The form of the term $[1 - \sqrt{v^2 + v_b^2}/v_M]$ in equation D.12 was introduced by Thompson (1968) to limit the distribution to this maximum speed. For model calculations in this paper, v_R is chosen to have the nominal corotational speed of 56.8 km sec^{-1} relative to Io, but this speed is likely to be much larger ($\gtrsim$100 km sec^{-1}) as determined from simulations of Io's interaction with the plasma torus (Wolf-Gladrow, Neubauer, and Lussem 1987).

The modified sputtering flux distribution then follows from equation D.5 and is given by

$$\phi(v;\alpha,v_b,v_M) = \frac{n}{C(\alpha,v_M/v_b)} \frac{v}{v_b}^3 \frac{v_b^2}{v^2+v_b^2}^{\alpha} \left[1 - \sqrt{\frac{v^2+v_b^2}{v_M^2}}\right] \qquad \text{D.15}$$

The most probable speed, v_m, for the flux distribution D.15 is determined by solving the nonlinear expression

$$v_m = \frac{v_b}{\sqrt{\frac{2}{3}\alpha + \frac{1}{3}\xi - 1}} \qquad \text{D.16}$$

where

$$\xi = [v_M/(\sqrt{v_m^2 + v_b^2}) - 1]^{-1}. \qquad \text{D.17}$$

The total upward flux at the exobase is then related to the flux ϕ_0, referenced to the surface area of Io, by the expression

$$\int_0^{\sqrt{v_M^2-v_b^2}} \phi(v;\alpha,v_b,v_M)\, dv = nv_b \frac{D(\alpha,v_M/v_b)}{C(\alpha,v_M/v_b)} = \frac{R_S}{R_E}^2 \phi_0 \qquad \text{D.18}$$

where the dimensionless function $D(\alpha, v_M/v_b)$ is given by

$$D(\alpha, v_M/v_b) = \int_0^{\sqrt{(v_M/v_b)^2 - 1}} \frac{x^3}{(1 + x^2)^\alpha} \left[1 - \frac{v_b}{v_M} \sqrt{1 + x^2}\right] dx \qquad \text{D.19}$$

and can easily be integrated analytically. For the case discussed in this paper ($\alpha = 7/3$, $v_m = 2.9$ km sec^{-1}, $v_b = 2.2159$ km sec^{-1}, $v_M = 46.62$ km sec^{-1}), the dimensionless coefficient in equation D.18 is evaluated to be

$$\frac{D(\alpha, v_M/v_b)}{C(\alpha, v_M/v_b)} = 0.4823. \qquad \text{D.20}$$

The normalized, modified-sputtering flux distribution, $\bar{\phi}(v;\alpha, v_b, v_M)$, is finally defined by

$$\bar{\phi}(v;\alpha, v_b, v_M) = \frac{\phi(v;\alpha, v_b, v_M)}{[n v_b (D(\alpha, v_M/v_b)/C(\alpha, v_M/v_b))]}$$

$$= \frac{1}{v_b D(\alpha, v_M/v_b)} \left(\frac{v}{v_b}\right)^3 \left(\frac{v_b^2}{v^2 + v_b^2}\right)^\alpha \left[1 - \sqrt{\frac{v^2 + v_b^2}{v_M^2}}\right]. \qquad \text{D.21}$$

References

Acuña, M. H., Behannon, K. W., and Connerney, J. E. P. 1983, In Physics of the Jovian Magnetosphere, A. J. Dessler (Ed.), Cambridge University Press, Cambridge, UK, p. 1.

Allen, C. W. 1976, Astrophysical Quantities. The Athlone Press, University of London.

Bagenal, F. 1985a, Private communication.

Bagenal, F. 1985b, J. Geophys. Res., 90, 311.

Bagenal, F., McNutt, R. L., Jr., Belcher, J. W., Bridge, H. S., and Sullivan, J. D. 1985, J. Geophys. Res. 90, 1755.

Bagenal, F., and Sullivan, J. D. 1981, J. Geophys. Res. 86, 8447.

Ballester, G. E., Moos, H. W., Feldman, P. D., Strobel, D. F., Summers, M. E., Bertaux, J.-L., Skinner, T. E., Festou, M. C., and Lieske, J. H. 1987, Ap. J. (Letters). 319, L33.

Barbosa, D. D., and Kivelson, M. G. 1983, Geophys. Res. Letters. 10, 210.

Bergstralh, J. T., Matson, D. L., and Johnson, T. V. 1975, Ap. J. (Letters)., 195, L131.

Bergstralh, J. T., Young, J. W., Matson, D. L., and Johnson, T. V. 1977, Ap. J. (Letters)., 211, L51.

Brown, R. A. 1981, The Jupiter Hot Plasma Torus: Ap. J. 244, 1072.

Brown, R. A. and Schneider, N. M. 1981, Icarus, 48, 519.

Brown, R. A., Pilcher, C. B., and Strobel, D. F. 1983, In Physics of the Jovian Magnetosphere, A. J. Dessler (ed.), Cambridge University Press, New York, NY, p. 197.

Carlson, R. W., Matson, D. L., and Johnson, T. V. 1975, Geophys. Res. Letters., 2, 469.

Carlson, R. W., Matson, D. L., Johnson, T. V. and Bergstralh, J. T. 1978, Ap. J. 223, 1082.

Durrance, S. T., Feldman, P. D., and Weaver, H. A. 1983, Ap. J. (Letters). 267, L125.

Fang, T.-M., Smyth, W. H., and McElroy, M. B. 1976, Planet. Space Sci., 24, 577.

Gehrels, N., and Stone, E. C. 1983, J. Geophys. Res. 88, 5537.

Goldberg, B. A. 1987, Private Communication.

Goldberg, B. A., Carlson, R. W., Matson, D. L., and Johnson, T. V. 1978, Bull. AAS 10, 579.

Goldberg, B. A., Garneau, G. W., and LaVoie, S. K. 1984, Science, 226, 512.

Goldberg, B. A., Mekler, Y., Carlson, R. W., Johnson, T. V., and Matson, D. L. 1980, Icarus, 44, 305.

Ip, W.-H., and Goertz, C. K. 1983, Nature 302, 232.

Johnson, R. E. 1982, Introduction to Atomic and Molecular Collisions. Plenum Press, New York.

Johnson, R. E. 1985, Private communication.

Johnson, R. E., and Strobel, D. F. 1982, J. Geophys. Res. 87, 10385.

Johnson, T. V., Morrison, D., Matson, D. L., Veeder, G. J., Brown, R. H., and Nelson, R. M. 1984, Science, 226, 134.

Kliore, A. J., Fjeldbo, G., Seidel, B. L., Sweetnam, D. N., Sesplaukis, T. T., and Woiceshyn, P. M. 1975, Icarus 24, 407.

Kumar, S. 1984, J. Geophys. Res. 89, 7399.

Kumar, S. 1985, Icarus 61, 101.

Macy, W. W., Jr., and Trafton, L. M. 1975a, Icarus, 25, 432.

Macy, W., Jr., and Trafton, L. 1975b, Ap. J., 200, 510.

Macy, W., and Trafton, L. 1980, Icarus, 41, 131.

Matson, D. L., Goldberg, B. A., Johnson, T. V., and Carlson, R. W. 1978, Science, 199, 531.

McEwen, A. S., Matson, D. L., Johnson, T. V., and Soderblom, L. A. 1985, J. Geophys. Res., 90, 12345.

McEwen, A. S., and Soderblom, L. A. 1983, Icarus, 55, 191.

McFarland, R. H. 1965, Phys. Rev. 139, A40.

McFarland, R. H., and Kinney, J. D., 1965, Phys. Rev. 137, A1058.

McGrath, M. A., and Johnson, R. E. 1987, Icarus 69, 519.

Mekler, Y. B. 1986, Private Communication.

Morgan, J. S. 1985a, Icarus 62, 389.

Morgan, J. S. 1985b, Icarus 62, 243.

Morgan, J. S. 1985c, Private Communication.

Morgan, J. S., and Pilcher, C. B. 1984, Private Communication.

Morgan, J. S., Pilcher, C. B., and Fertel, J. H. 1983, Bull. AAS 15, 811.

Münch, G., and Bergstralh, J. T. 1977, Pub. A. S. P., 89, 232.

Murcray, F. J. 1978, Ph.D. Thesis, Dept. of Physics, Harvard University, Cambridge, Massachusetts.

Murcray, F. J., and Goody, R. 1978, Ap. J., 226, 327.

Nelson, R. M., Lane, A. L., Matson, D. L., Fanale, F. P., Nash, D. B., and Johnson, T. V. 1980, Science, 210, 784.

Pilcher, C. B., Fertel, J. H., and Morgan, J. S. 1985, Ap. J. 291, 377.

Pilcher, C. B., and Morgan, J. S. 1980, Ap. J. 238, 375.

Pilcher, C. B., and Morgan, J. S. 1985, Adv. Space Res. 5, 337.

Pilcher, C. B., Smyth, W. H., Combi, M. R. and Fertel, J. H. 1984, Ap. J., 287, 427.

Rutherford, J. A., Mathis, R. F., Turner, B. R., and Vroom, D. A. 1972, J. Chem. Phys., 56, 4654.

Sandel, B. R. 1985, Bull. AAS 17, 695.

Sandel, B. R., and Broadfoot, A. L. 1982, J. Geophys. Res. 87, 212.

Schneider, N. M., Hunten, D. M., and, Brown, R. A. 1984, Bull. AAS 16, 663.

Schneider, N. M., Hunten, D. M., Wells, W. K., and Trafton, L. M. 1987. Science 238, 55.

Shemansky, D. E. 1985, Private Communication.

Shemansky, D. E. 1987, preprint to be published in J. Geophys. Res.

Shemansky, D. E., and Sandel, B. R. 1982, J. Geophys. Res. 87, 219.

Sieveka, E. M., and Johnson, R. E. 1984. Ap. J. 287, 418.

Sittler, E. C. 1986, Private Communication.

Sittler, E. C., and Strobel, D. F. 1986, J. Geophys. Res. 92, 5741.

Skinner, T. E., and Durrance, S. T. 1986, Ap. J. 310, 966.

Smyth, W. H. 1979, Ap. J., 234, 1148.

Smyth, W. H. 1983, Ap. J., 264, 708.

Smyth, W. H., and Combi, M. R. 1983, Bull. AAS 15, 810.

Smyth, W. H., and Combi, M. R. 1984, Bull. AAS 16, 663.

Smyth, W. H., and Combi, M. R. 1985, Bull. AAS 17, 695.

Smyth, W. H., and Combi, M. R. 1987, Geophys. Res. Letters 14, 973.

Smyth, W. H., and Combi, M. R. 1988, Companion Paper (Paper I) to be published in Ap. J. Supp.

Smyth, W. H., and McElroy, M. B. 1977, Planet. Space Sci., 25, 415.

Smyth, W. H., and McElroy, M. B. 1978, Ap. J., 226, 336.

Summers, M. E. 1985, Ph.D. Thesis, California Institute of Technology.

Thomas, N. 1986, Nature, 332, 343.

Thompson, M. W. 1968, Phil. Mag., 18, 377.

Trafton, L. 1975, Ap. J. (Letters). 202, L107.

Trafton, L. 1980, Icarus 42, 111.

Trafton, L. 1980, Icarus 44, 318.

Trafton, L. 1983, Private Communication.

Trafton, L., and Macy, W., Jr. 1975, Ap. J. (Letters). 202, L155.

Trafton, L., and Macy, W., Jr. 1977, Ap. J. 215, 971.

Trafton, L., and Macy, W., Jr. 1978, Icarus, 33, 322.

Trafton, L., Parkinson, T., and Macy, W. 1974, Ap. J. (Letters)., 190, L85.

Trauger, J. T. 1977, Private Communication.

Trauger, J. T. 1983, Private Communication.

Trauger, J. T. 1984, Bull. AAS 16, 712.

Trauger, J. T. 1985, Bull. AAS 17, 694.

Trauger, J. T., Münch, G., and Roesler, F. L. 1980, Ap. J. 236, 1035.

Wolf-Gladrow, D. A., Neubauer, F. M., and Lussem, M. 1987, J. Geophys. Res., 92, 9949.

Zapesochnyi, I. P., and Aleksakhin, I. S. 1968, Zh. Eksp. Teor. Fiz. 55, 76. [also, Soviet Physics, JETP 28, 41, 1969.]

Table 1

Models for the Io Sodium Cloud

Cloud Region Studied	Sodium Source: Velocity Description	Sodium Source: Initial or Mean Velocity (km/sec)	Sodium Source: Preferred Ejection	Sodium Source: Rate (atoms sec^{-1})	Sodium Lifetime: Spatial Description	Sodium Lifetime: Lifetime (hr)	Orbital Dynamics: Spatial Dimensions	Orbital Dynamics: Io's Mass Included	Orbital Dynamics: Radiation Pressure	Reference
Forward	Monoenergetic	3.5	Isotropic	-	Uniform	30, 47	2	Yes	No	Carlson, Matson and Johnson (1975)
-	Distribution	1.9	Isotropic	-	Uniform	Long-lived	3	No	No	Fang, Smyth and McElroy (1976)
Forward	Monoenergetic	2.0	Isotropic	-	Uniform	50	3	Yes	No	Smyth and McElroy (1977)
Forward	Sputtering	2.8	Hemisphere (centered at 30° Io longitude)	-	Uniform	28	3	Yes	No	Matson et al. (1978)
Forward (line profile)	Sputtering and others	0-15	Leading hemisphere	-	Uniform	28	3	Yes	No	Carlson et al. (1978)
Forward	Monoenergetic	2.6, 3.0	Inner or inner/trailing	2×10^{25}	Uniform	15-20	3	Yes	No	Smyth and McElroy (1978)
Forward	Monoenergetic	2.6	Inner hemisphere	2×10^{25}	Uniform	20	3	Yes	Yes	Smyth (1979, 1983)
Forward	Distribution	3-13	Inner hemisphere	-	Uniform	33	3	No	No	Macy and Trafton (1980)
Forward	Sputtering	~ 3	Hemisphere (centered at 45° Io longitude)	3×10^{26}	1-D (radial)	> 1.4	3	Yes	No	Golberg et al. (1980)
Forward	Monoenergetic	2.6	Isotropic	$\sim 2 \times 10^{26}$	2-D oscillating	$\gtrsim 1$	3	Yes	Yes	Smyth and Combi (1983)
Directional feature	Monoenergetic	~ 15	Band	$\sim 1 \times 10^{26}$	2-D oscillating	$\gtrsim 1$	3	Yes	No	Pilcher et al. (1984)

Table 2

Reactions for Sodium Atoms in the Io Plasma Torus

	Reaction	Reaction Time (hr)
R1.	$Na + h\nu \rightarrow Na^+ + e$	400
R2.	$e + Na \rightarrow Na^+ + 2e$	> 1
R3.	$S^+ + Na \rightarrow S + Na^+$	∞
R4.	$O^+ + Na \rightarrow O + Na^+$	∞
R5.	$Na^+ + Na \rightarrow Na + Na^+$	50*
R6.	$S^{++} + Na \rightarrow S^+ + Na^+$	> 40*
R7.	$O^{++} + Na \rightarrow O^+ + Na^+$	> 300*
R8.	$X^+ + Na \rightarrow X^+ + Na$ (elastic collision)	> 30*

* Assumed an ion density of 50 cm^{-3} for Na^+, 500 cm^{-3} for S^{++}, 100 cm^{-3} for O^{++}, and 1000 cm^{-3} for X^+ with an ion-neutral velocity of 60 km sec^{-1}; cross-sectional information for electron impact ionization is from McFarland (1965), McFarland and Kinney (1965) and Zapesochnyi and Aleksakhin (1968); cross sections for S^+, O^+, S^{++} and O^{++} are from Johnson and Strobel (1982), for Na^+ from Rutherford et al. (1972) and for $X^+ = O^+$ or S^+ from new estimates by Johnson (1985).

FIGURE CAPTIONS

Figure 1. Electron Impact Ionization Lifetime of Sodium. The lifetime in hours is shown as calculated in the plasma torus for plasma conditions appropriate to the Voyager 1 encounter epoch. The radial and vertical distances are given in units of the planetary radius (R_J).

Figure 2. Interaction of the Sodium Cloud and the Plasma Torus. The spatially projected overlap in the satellite plane of the Io plasma torus with the solar radiation perturbed cloud shape (solid boundary with heavy shading) and with the unperturbed cloud shape (short dashed boundary) is indicated for the diametrically opposite satellite phase angles as published by Smyth (1983). The cloud shape illustrates the envelope of sodium after 20 hours of flight time.

Figure 3. Electron Impact Ionization Rate Coefficient for Sodium. The rate coefficient is shown as a function of the electron temperature and has been calculated assuming a Maxwell-Boltzmann distribution and cross-sectional information from McFarland (1965), McFarland and Kinney (1965) and Zapesochnyi and Aleksakhin (1968).

Figure 4. Electron Impact Ionization Lifetime of Sodium at Io. The lifetime as a function of the System III magnetic longitude angle of the satellite is shown at Io's position for a 7° tilted plasma torus that is centered on Jupiter (light line, Case A) and centered on the offset magnetic dipole location (heavy line, Case B).

Figure 5. Temperature in the Io Plasma Torus. The electron temperature as a function of radial distance (L-shell) in units of planetary radii (R_J) is a representative average from inbound and outbound PLS electron data of Voyager 1 (Sittler and Strobel 1986; Sittler 1986). The ion temperature is also shown as obtained from the corrected analysis of the PLS ion data of Voyager 1 (Bagenal et al. 1985; Bagenal 1985b).

Figure 6. Electron Density in the Plasma Torus. The electron density as a function of radial distance (L-shell) in units of planetary radii (R_J) is shown in the centrifugal equator as deduced from the PLS electron data of Voyager 1 (Sittler and Strobel 1986; Sittler 1986) and from Voyager UVS remote sensing data (Shemansky 1985).

Figure 7. Electron Density in the Plasma Torus. The density in units of cm^{-3} is shown in a cross-sectional cut of the plasma torus and is appropriate to the Voyager 1 encounter epoch. See the text for more details.

Figure 8. Electron Impact Lifetime of Sodium in the Plasma Torus. The lifetime in units of hours is shown at eastern and western elongation in the coordinate frame of the plasma torus (Case C) that is tilted by 7°, has a magnetic dipole offset and is in the presence of an east-west electric field of ~2.8 mV/m. The lifetime at Io's location in the plasma torus for these two elongation pictures varies periodically as a function of the System III magnetic longitude of the satellite and is shown by the heavy closed line.

Figure 9. Location of Io in the Plasma Torus. The shaded area shows the domain of Io's location in the plasma torus as a function of the System III magnetic longitude angle and the "effective L-shell" (denoted by L') for a 10-degree tilted and rotating magnetic dipole that is offset from the center of Jupiter and that is in the presence of an east-west electric field of ~2.8 mV/m. The dotted line in the center of the area is the location of Io if the east-west electric field were zero.

Figure 10. Electron Impact Ionization Lifetime of Sodium at Io's Location. The lifetime in units of hours at Io's location for the plasma torus description of Figure 8 is shown as a function of the System III magnetic longitude angle of Io and the geocentric phase angle of Io for Jupiter at opposition. The highest lifetime contour of 15 hours is centered on an Io System III longitude angle of ~160° and an Io geocentric phase angle of 90°.

Figure 11. D_2 Brightness of the Sodium Cloud on the Sky Plane. Monoenergetic (2.6 km sec^{-1}) model calculations for the D_2 emission brightness are shown with Io at eastern elongation for the four labeled quadrant sources and for a symmetric source. A sodium source flux of 2.3×10^8 atoms cm^{-2} sec^{-1} (referenced to the satellite surface area) and the simplest plasma torus description (Case A) are assumed. The D_2 contour brightness levels, in units of kilo-Rayleighs, are, from outside to inside, 0.2, 0.5, 1.0, 2.0, 5.0, 10.0, 20.0 and 50.0. See the text for further discussion.

Figure 12. D_2 Brightness of the Sodium Cloud on the Sky Plane. Monoenergetic (2.6 km sec^{-1}) model calculations for the D_2 brightness are shown with Io at eastern elongation for the four labeled hemispherical sources. The sodium flux, plasma torus description and contour levels are the same as in Figure 11.

Figure 13. East-West Orbital Asymmetry in the Sodium Cloud. Monoenergetic (2.6 km sec^{-1}) model calculations for the D_2 brightness of the cloud on the sky plane with Io at eastern and western elongation are compared for the symmetric source and the band source. The sodium flux, plasma torus description and contour levels are the same as in Figure 11 with the exception that an outer 0.1 kiloRayleigh contour has been added.

Figure 14. East-West Orbital Asymmetry in the Sodium Cloud. Monoenergetic (2.6 km sec^{-1}) model calculations for the D_2 brightness of the cloud on the sky plane with Io at eastern and western elongation are compared for the band model. The sodium flux and contour levels are the same as in Figure 11. The plasma torus description is for Case C. See the text for further discussion.

Figure 15. Bergstralh Slit for the Sodium Cloud. The size of the slit (shaded rectangle) used by Bergstralh et al. (1975, 1977) in measuring the sodium cloud brightness near Io is shown for Jupiter at opposition in relation to the satellite disk (dark circle) and the Lagrange sphere (large circle) of the satellite.

Figure 16. East-West Intensity Ratio. The east-west intensity ratio in the Bergstralh et al. (1975, 1977) slit is calculated as a function of the plasma torus shift parameter ϵ for monoenergetic (2.6 km sec^{-1}) ejection from a band source and for the plasma torus description Case C. The ratio is shown for a System III magnetic longitude angle for Io of 140° (maximum ratio) and 320° (minimum ratio). The dashed line indicates the observed average ratio.

Figure 17. D_2 Brightness in the Bergstralh Slit. The monoenergetic model calculated D_2 brightness in the observing slit expressed in normalized flux units for Io at eastern (east) and western (west) elongation is shown as a function of the sodium ejection speed from a band source. The plasma torus description (Case C) is described in the text and the System III magnetic longitude angle of Io is 140° in (a) and 320° in (b).

Figure 18. East-West Intensity Ratio. The east-west intensity ratio, as determined from the model results of Figures 17a and 17b, is shown. The dashed line indicates the observed average ratio.

Figure 19. Modified-Sputtering Flux Distribution. The normalized modified-sputtering flux distribution, $\bar{\phi}(v;\alpha,v_b,v_M)$, is shown as a function of the sodium ejection speed v for $\alpha = 3$ (classical sputtering) and $\alpha = 7/3$ (Thomas-Fermi-like collisional ejection), where the most probable speed for both distributions is 3.0 km sec^{-1}. See the text for further discussion.

Figure 20. Maxwell-Boltzmann Flux Distribution. The normalized Maxwell-Boltzmann flux distribution, $\bar{\phi}(v;T)$, is shown as a function of the sodium ejection speed v for an exobase temperature of 1500°K. The two flux distributions of Figure 19 are also shown for comparison.

Figure 21. D_2 Brightness in the Bergstralh Slit. The model calculated brightness in the observing slit expressed in normalized flux units for Io at eastern (east) and western (west) elongation is shown as a function of the most probable speed of the modified-sputtering flux distribution for $\alpha = 3$. The band source and the plasma torus description (Case C) assumed in the calculation are described in the text. The System III magnetic longitude angle of Io is 140° in (a) and 320° in (b).

Figure 22. D_2 Brightness in the Bergstralh Slit. Same description as Figure 21, except $\alpha = 7/3$.

Figure 23. East-West Intensity Ratio. The east-west intensity ratio is shown in (a), as determined from the model results ($\alpha = 3$) in Figure 21, and in (b), as determined from the model results ($\alpha = 7/3$) in Figure 22. The horizontal dashed line indicates the observed ratio. The vertical dashed line indicates the most probable speed where the average value between the 140° and 320° curves is equal to the observed average ratio.

Figure 24. D_2 Brightness in the Bergstralh Slit. The model calculated brightness in the observing slit expressed in normalized flux units for Io at eastern (east) and western (west) elongation is shown as a function of the most probable speed of the Maxwell-Boltzmann flux distribution. The band source and the plasma torus description (Case C) assumed in the calculation are described in the text. The System III magnetic longitude angle of Io is 140° in (a) and 320° in (b).

Figure 25. East-West Intensity Ratio. The east-west intensity ratio as determined from the model results in Figures 24 for a Maxwell-Boltzmann flux distribution is shown as a function of the most probable speed (lower scale) and corresponding exobase temperature (upper scale). The range of exobase temperatures from 1000°K to 2000°K is indicated by the shaded area. The dashed line indicates the observed average ratio.

Figure 1

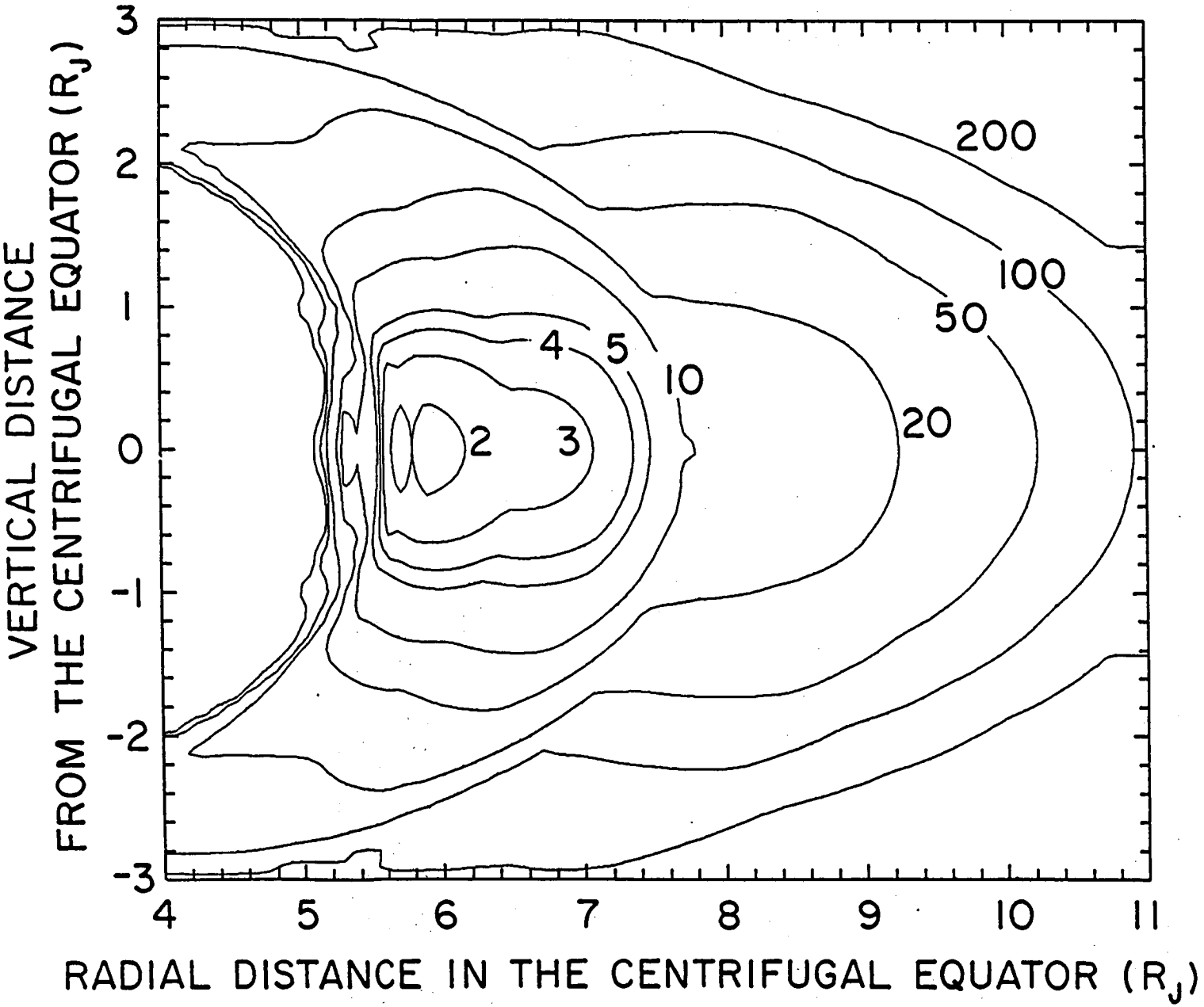
VERTICAL DISTANCE
FROM THE CENTRIFUGAL EQUATOR (R_J)
3
2
1
0
-1
-2
-3
200
100
50
20
10
5
4
3
2
4
5
6
7
8
9
10
11
RADIAL DISTANCE IN THE CENTRIFUGAL EQUATOR (R_J)

Figure 2

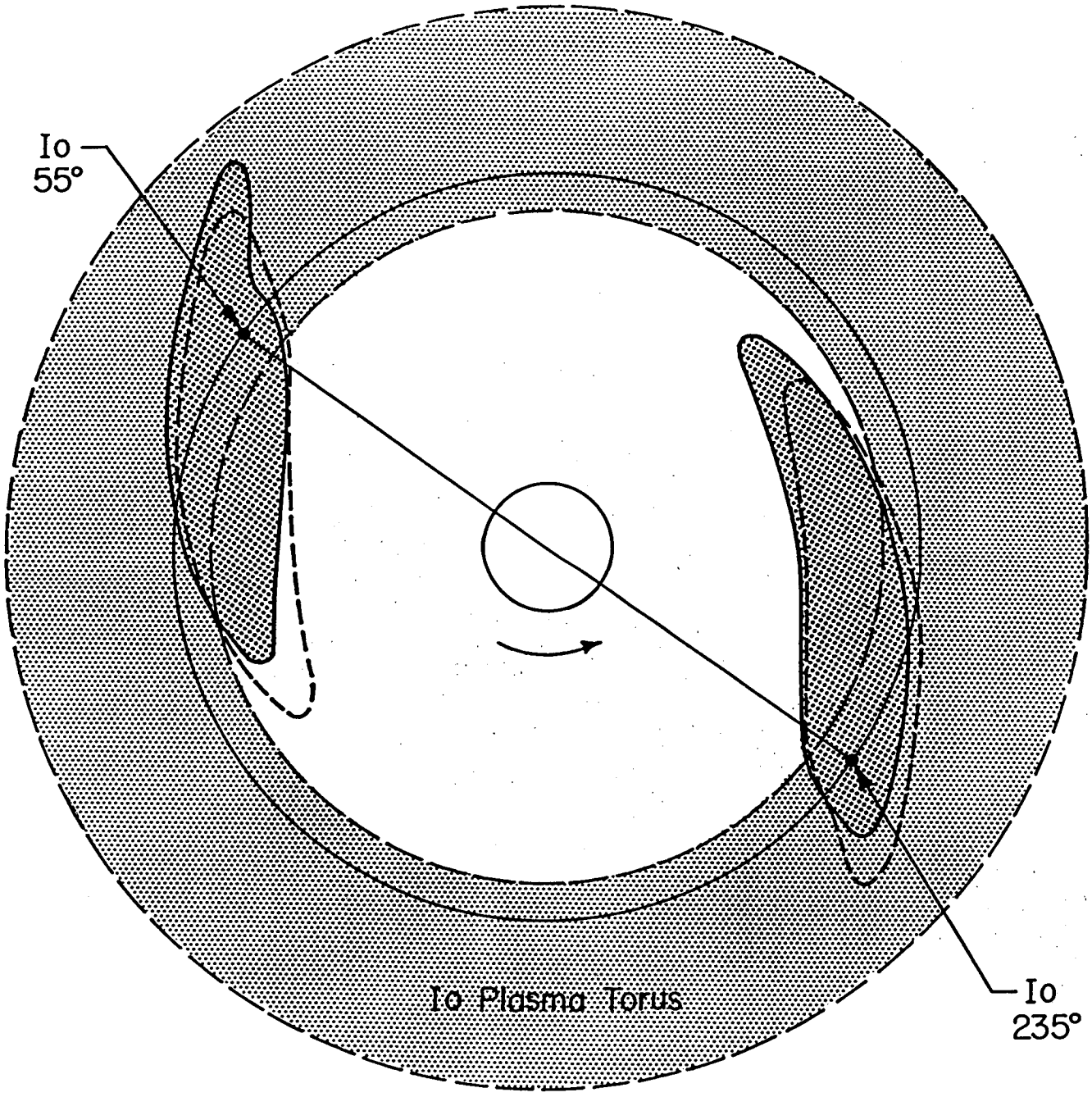

Figure 3

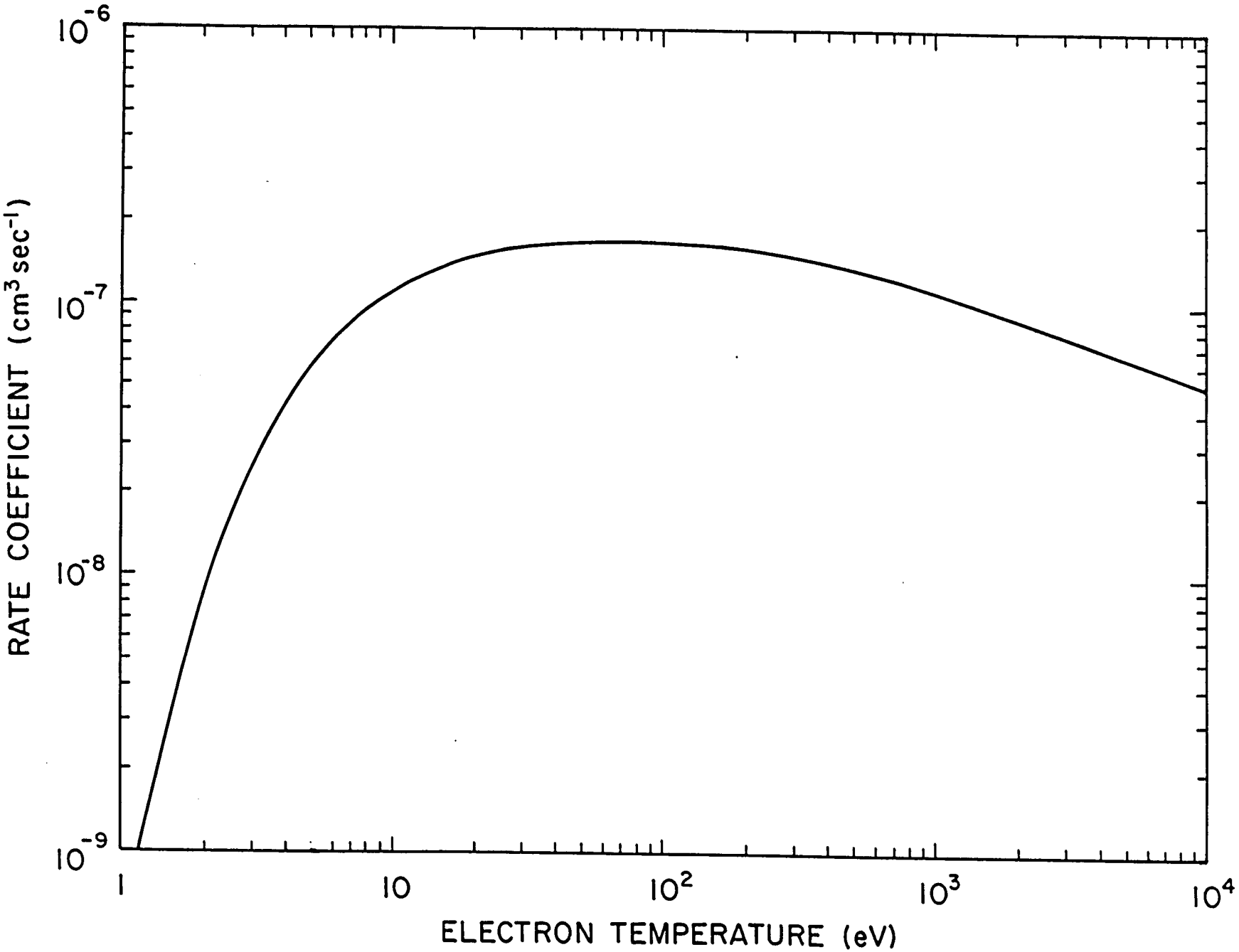
10^{-6}
10^{-7}
10^{-8}
10^{-9}
RATE COEFFICIENT ($cm^3 sec^{-1}$)
1
10
10^2
10^3
10^4
ELECTRON TEMPERATURE (eV)

Figure 4

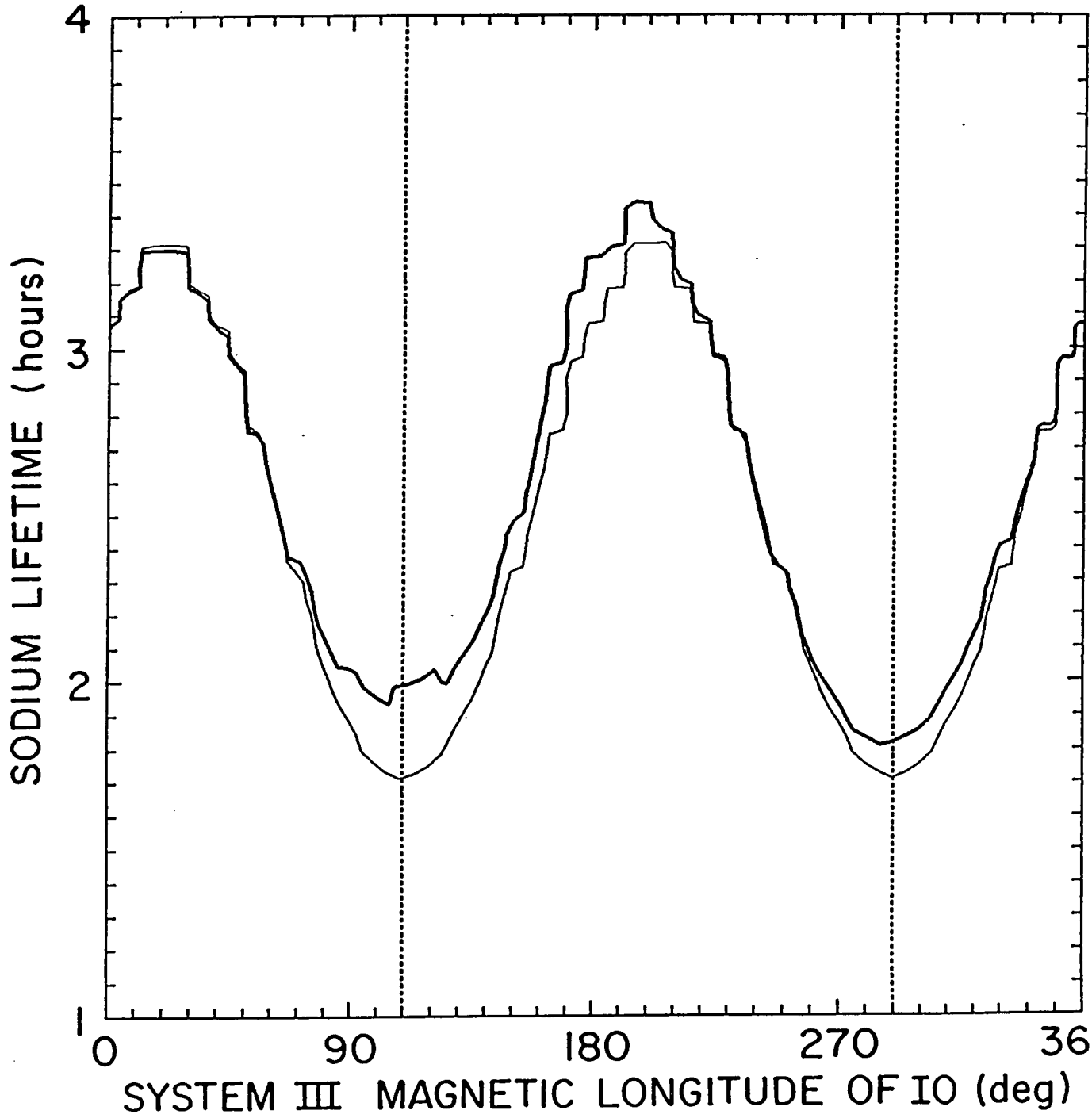
SODIUM LIFETIME (hours)
4
3
2
1
0
90
180
270
360
SYSTEM III MAGNETIC LONGITUDE OF IO (deg)

Figure 5

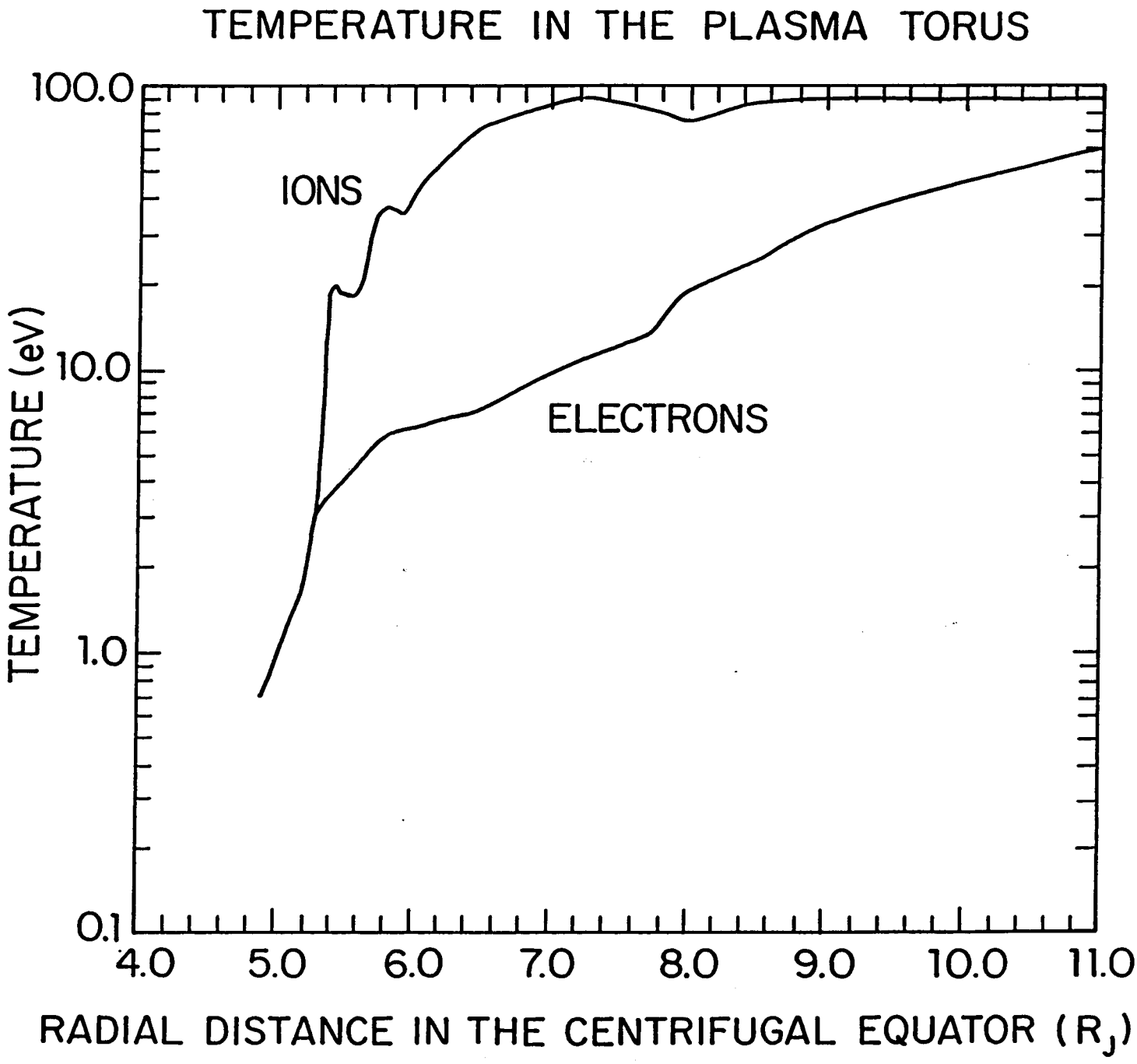
TEMPERATURE IN THE PLASMA TORUS
100.0
10.0
1.0
0.1
TEMPERATURE (eV)
IONS
ELECTRONS
4.0
5.0
6.0
7.0
8.0
9.0
10.0
11.0
RADIAL DISTANCE IN THE CENTRIFUGAL EQUATOR (R_J)

Figure 6

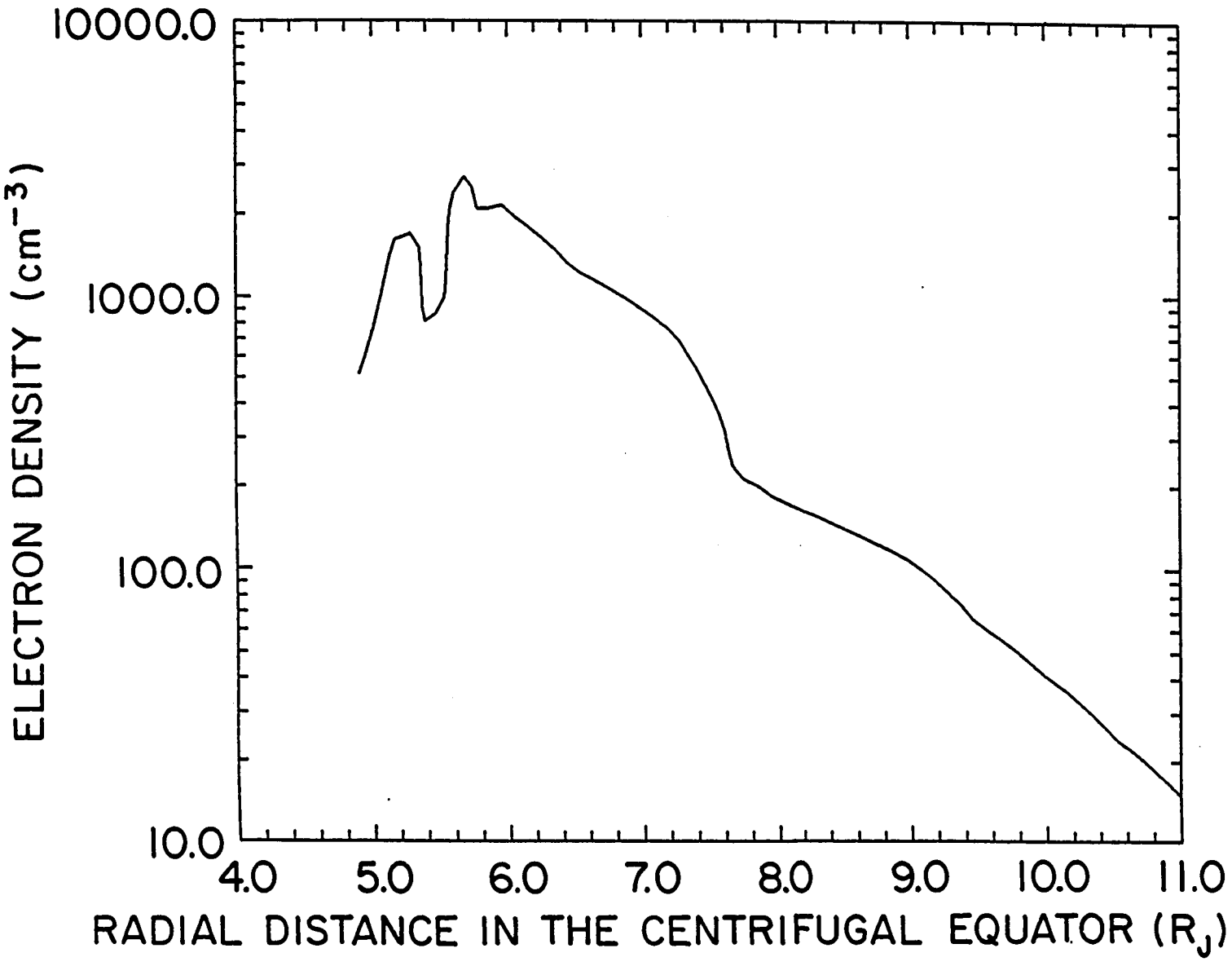
10000.0
1000.0
100.0
10.0
ELECTRON DENSITY (cm^{-3})
4.0
5.0
6.0
7.0
8.0
9.0
10.0
11.0
RADIAL DISTANCE IN THE CENTRIFUGAL EQUATOR (R_J)

Figure 7

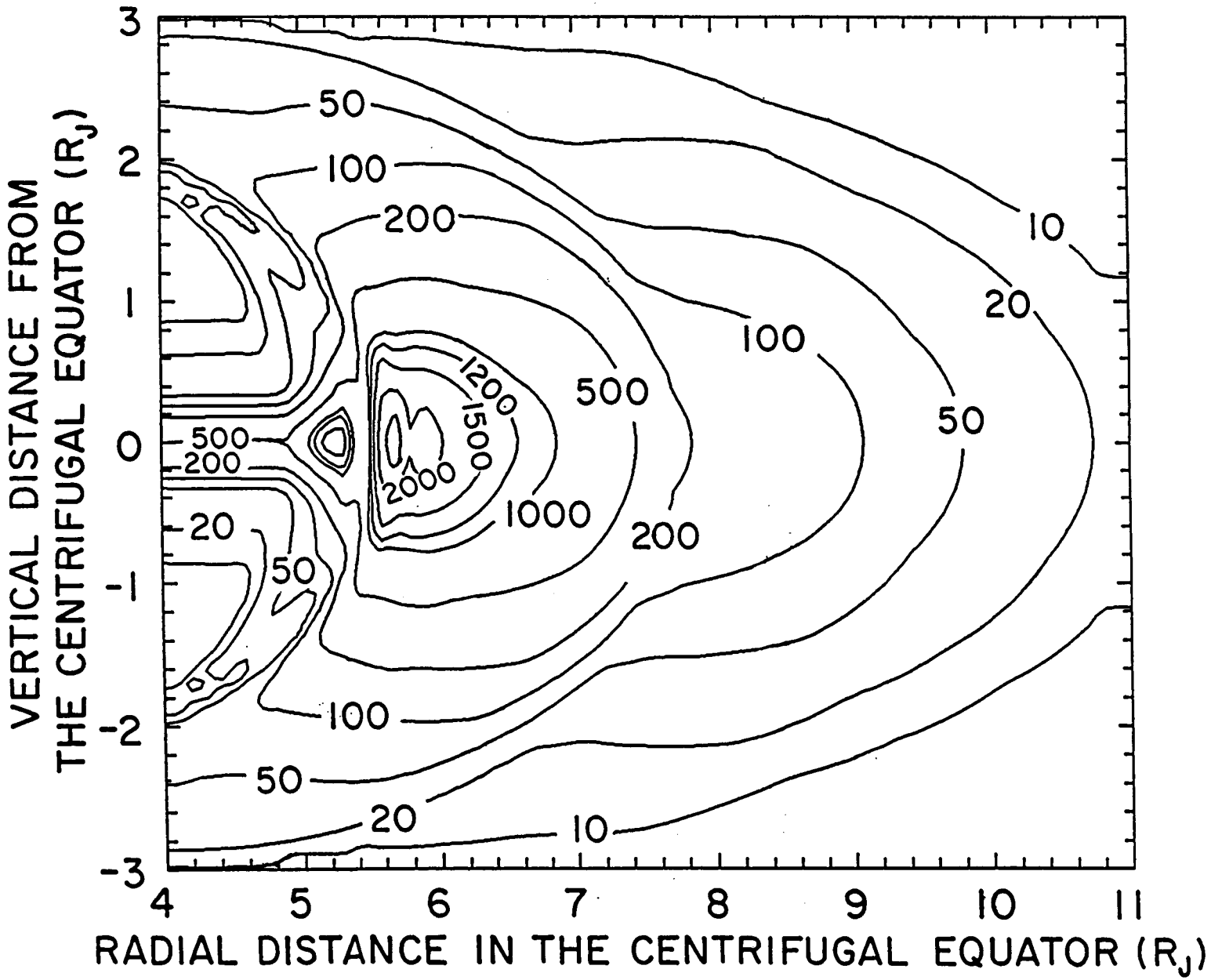
VERTICAL DISTANCE FROM THE CENTRIFUGAL EQUATOR (R_J)
RADIAL DISTANCE IN THE CENTRIFUGAL EQUATOR (R_J)
3
2
1
0
-1
-2
-3
4
5
6
7
8
9
10
11
50
100
200
10
20
100
500
1200
1500
2000
500
200
20
50
1000
200
50
100
50
20
10

Figure 8

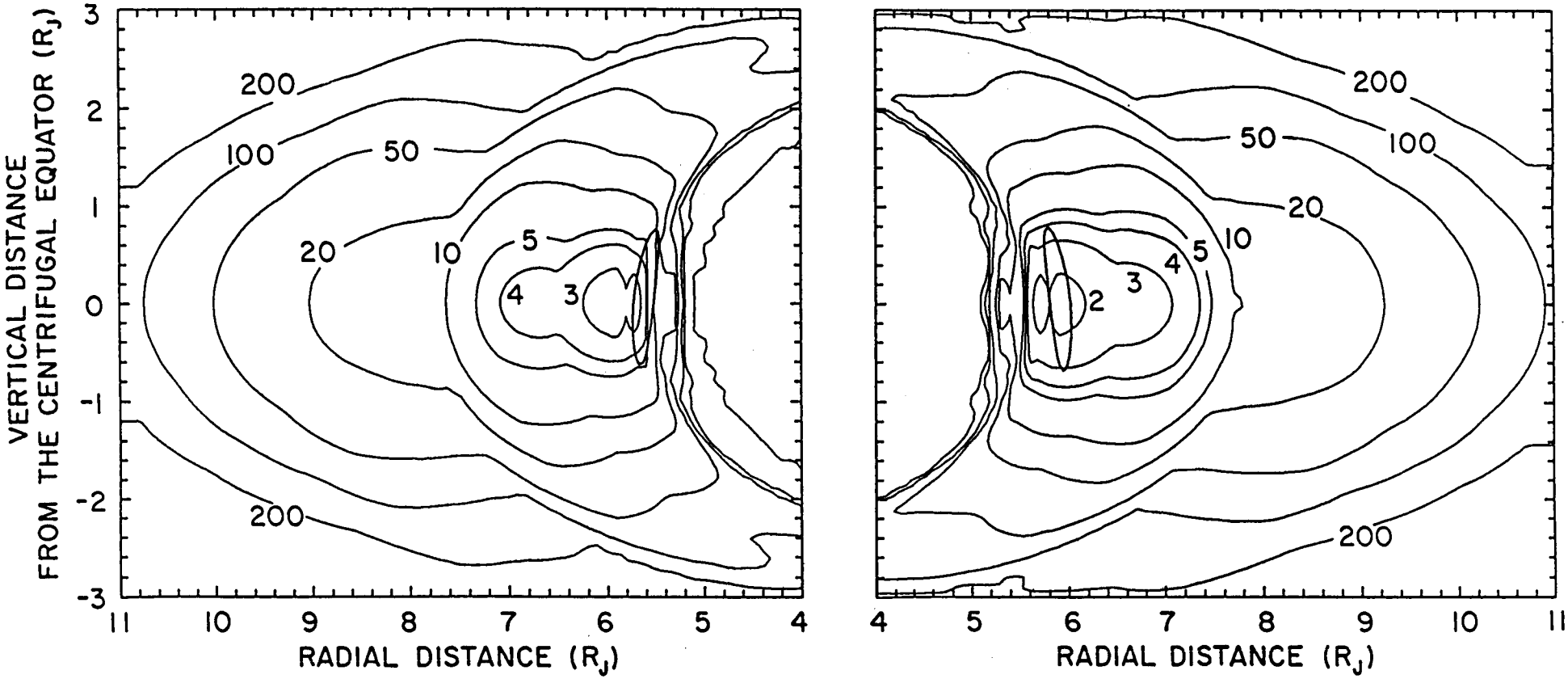
VERTICAL DISTANCE
FROM THE CENTRIFUGAL EQUATOR (R_J)
3
2
1
0
-1
-2
-3
200
100
50
20
10
5
4
3
200
11
10
9
8
7
6
5
4
RADIAL DISTANCE (R_J)
200
50
100
20
10
5
4
3
2
200
4
5
6
7
8
9
10
11
RADIAL DISTANCE (R_J)

Figure 9

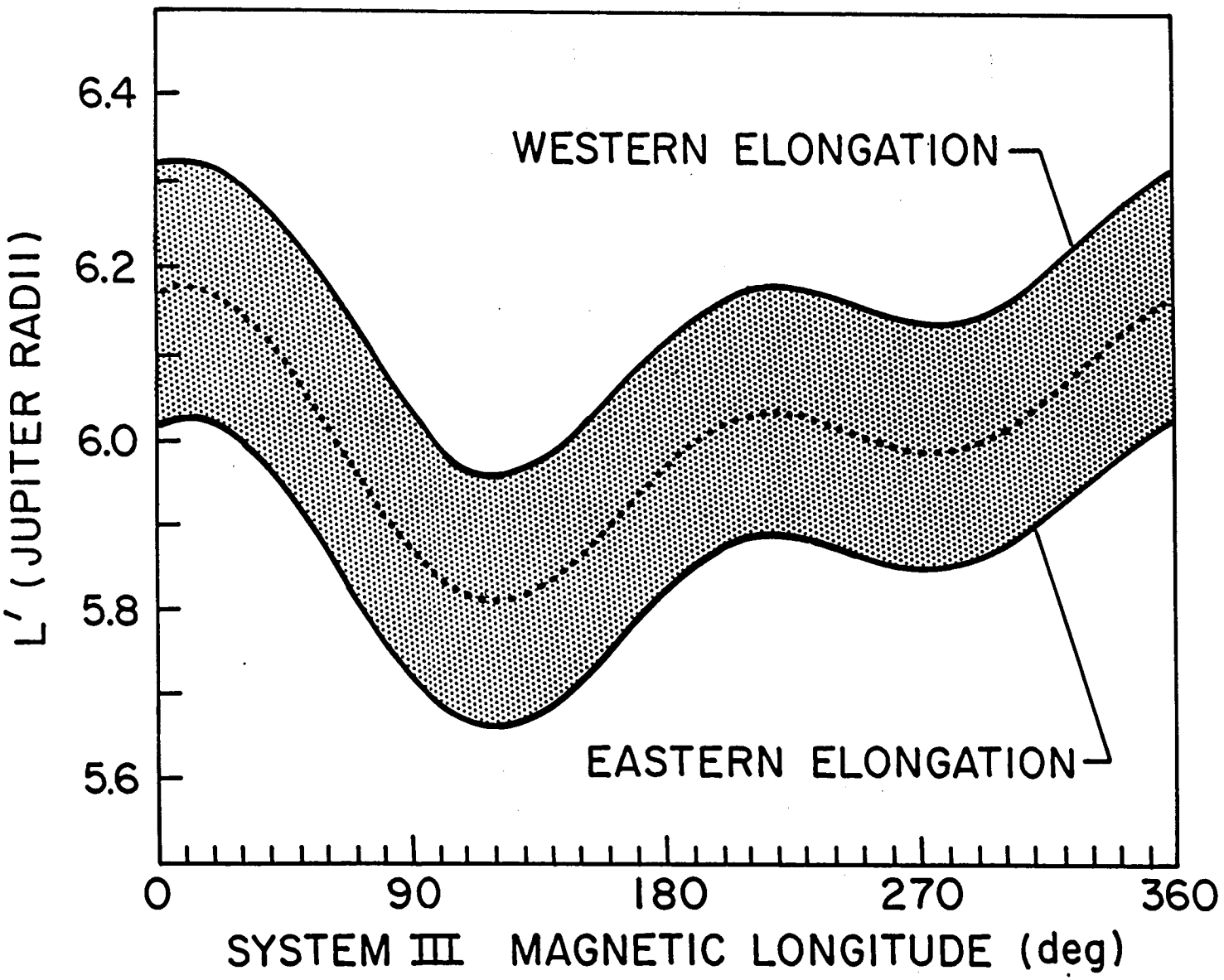
6.4
6.2
6.0
5.8
5.6
L′ (JUPITER RADII)
WESTERN ELONGATION
EASTERN ELONGATION
0
90
180
270
360
SYSTEM III MAGNETIC LONGITUDE (deg)

Figure 10

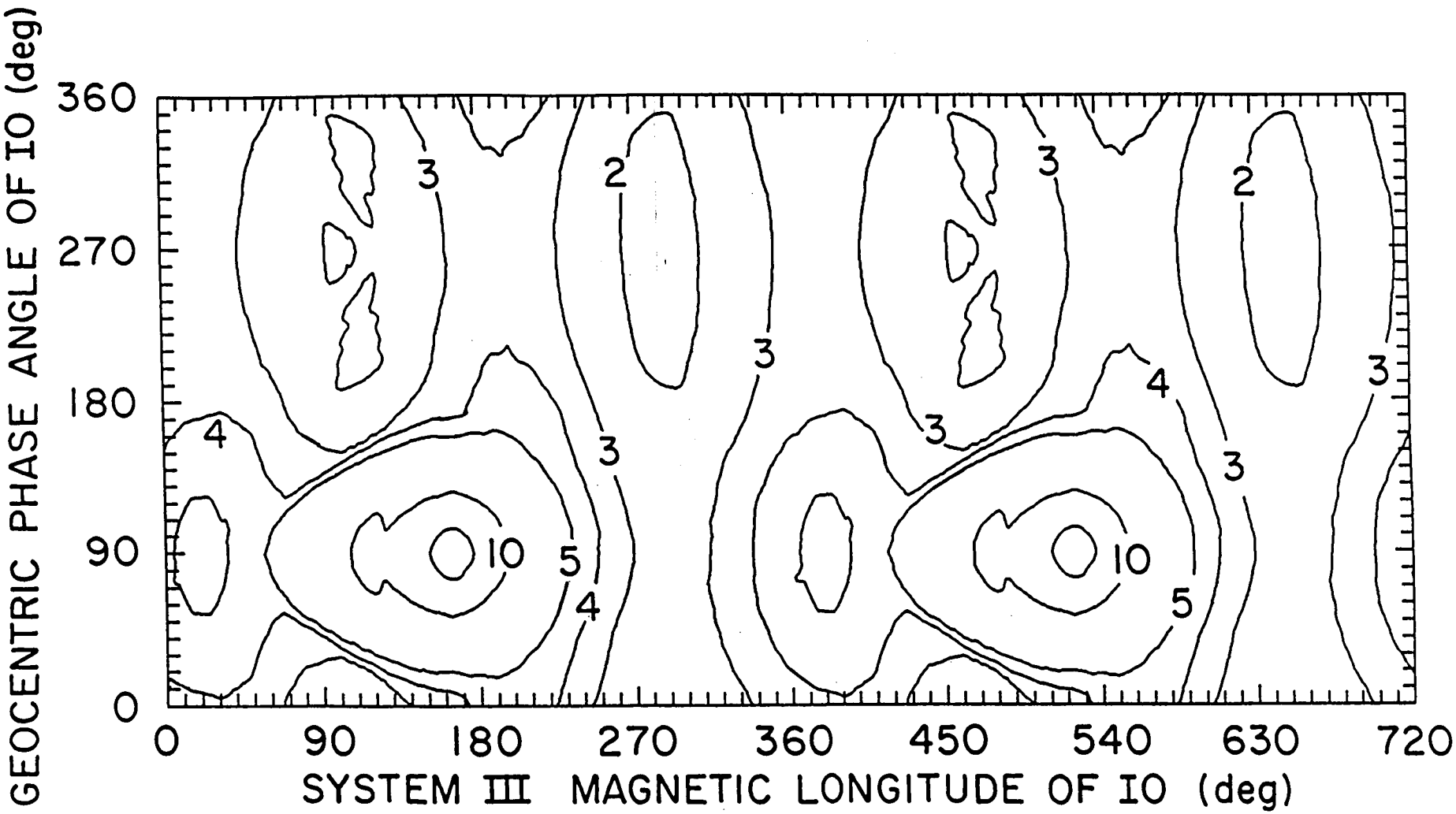
GEOCENTRIC PHASE ANGLE OF IO (deg)
360
270
180
90
0
0
90
180
270
360
450
540
630
720
SYSTEM III MAGNETIC LONGITUDE OF IO (deg)
2
3
4
5
10

Figure 11

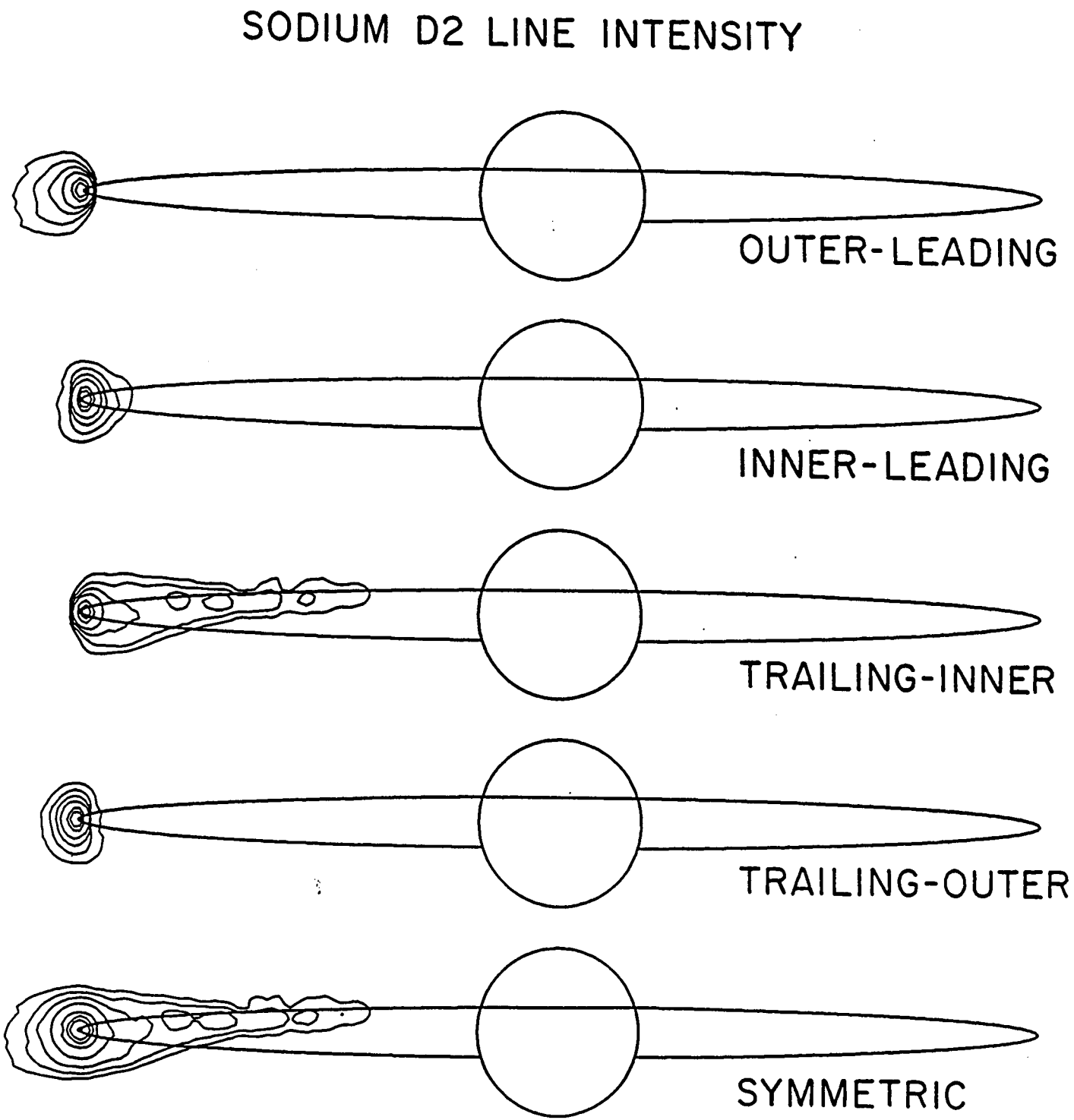
SODIUM D2 LINE INTENSITY
OUTER-LEADING
INNER-LEADING
TRAILING-INNER
TRAILING-OUTER
SYMMETRIC

Figure 12

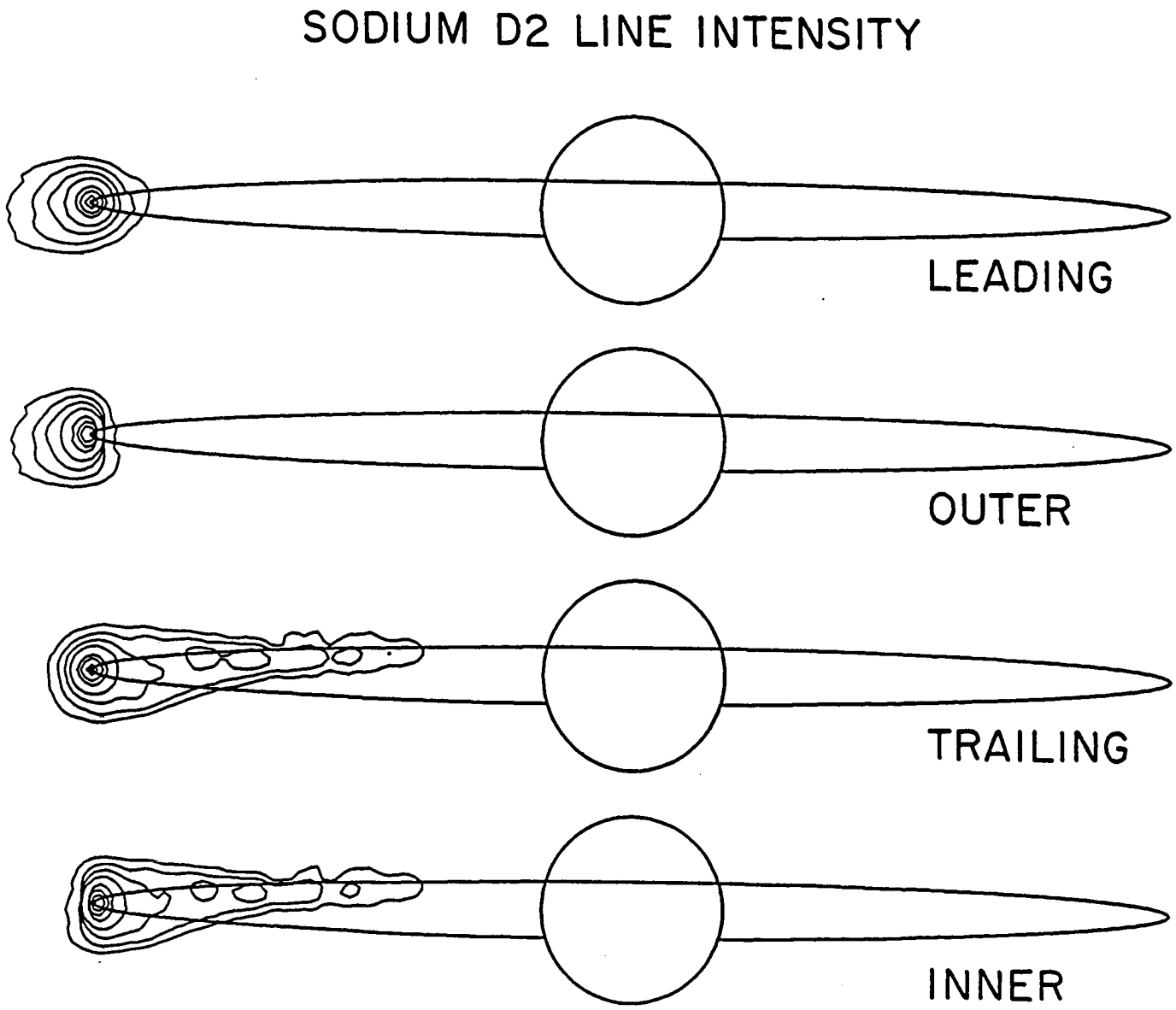

Figure 13

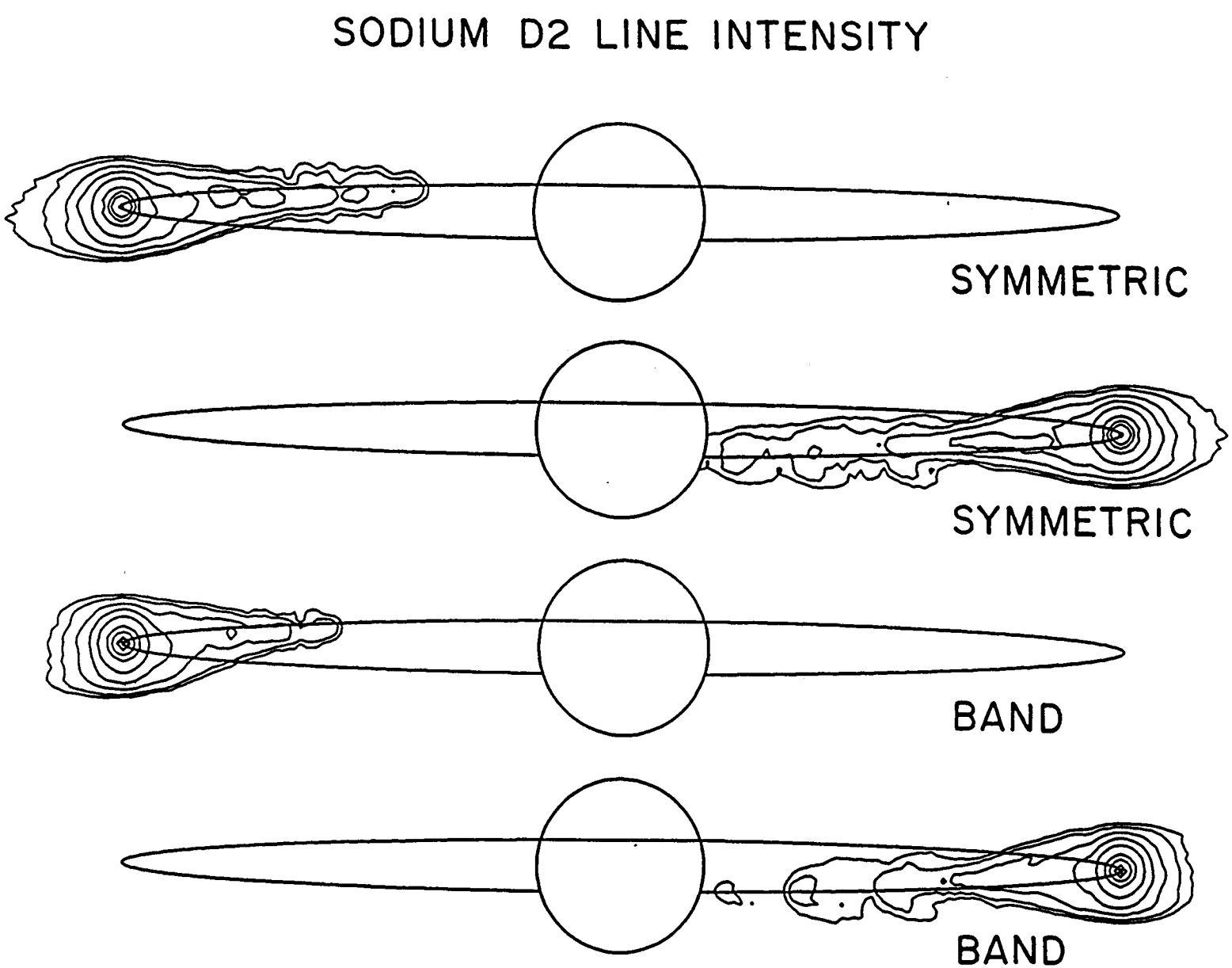

Figure 14

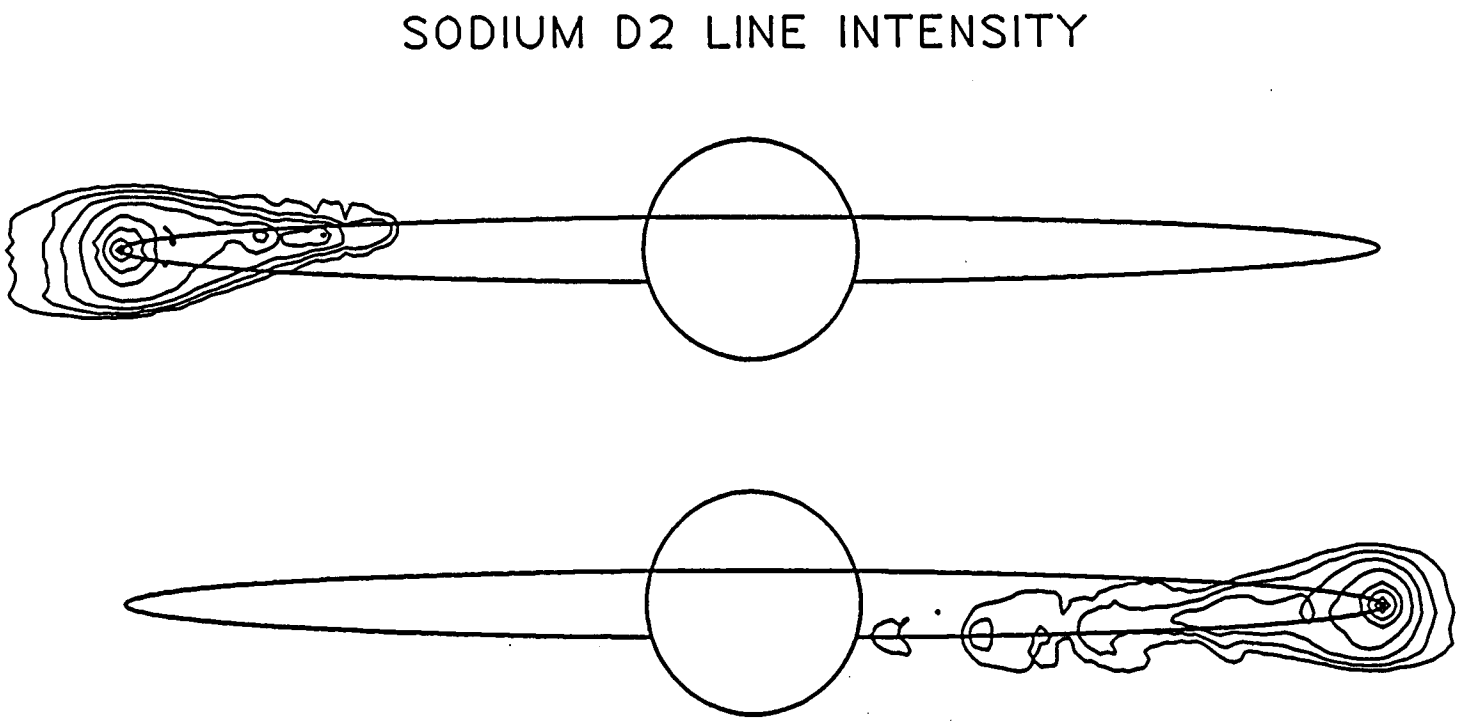

Figure 15

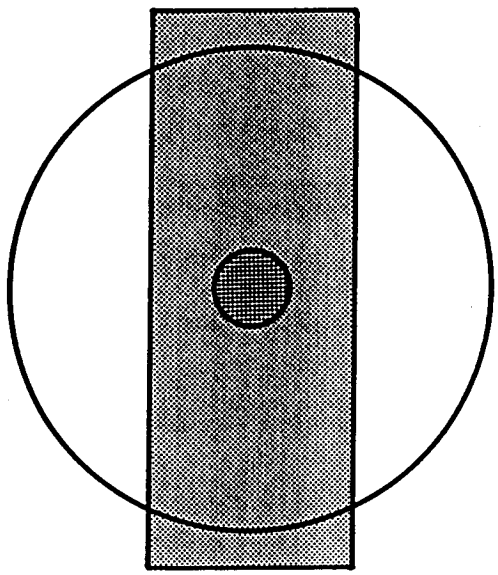

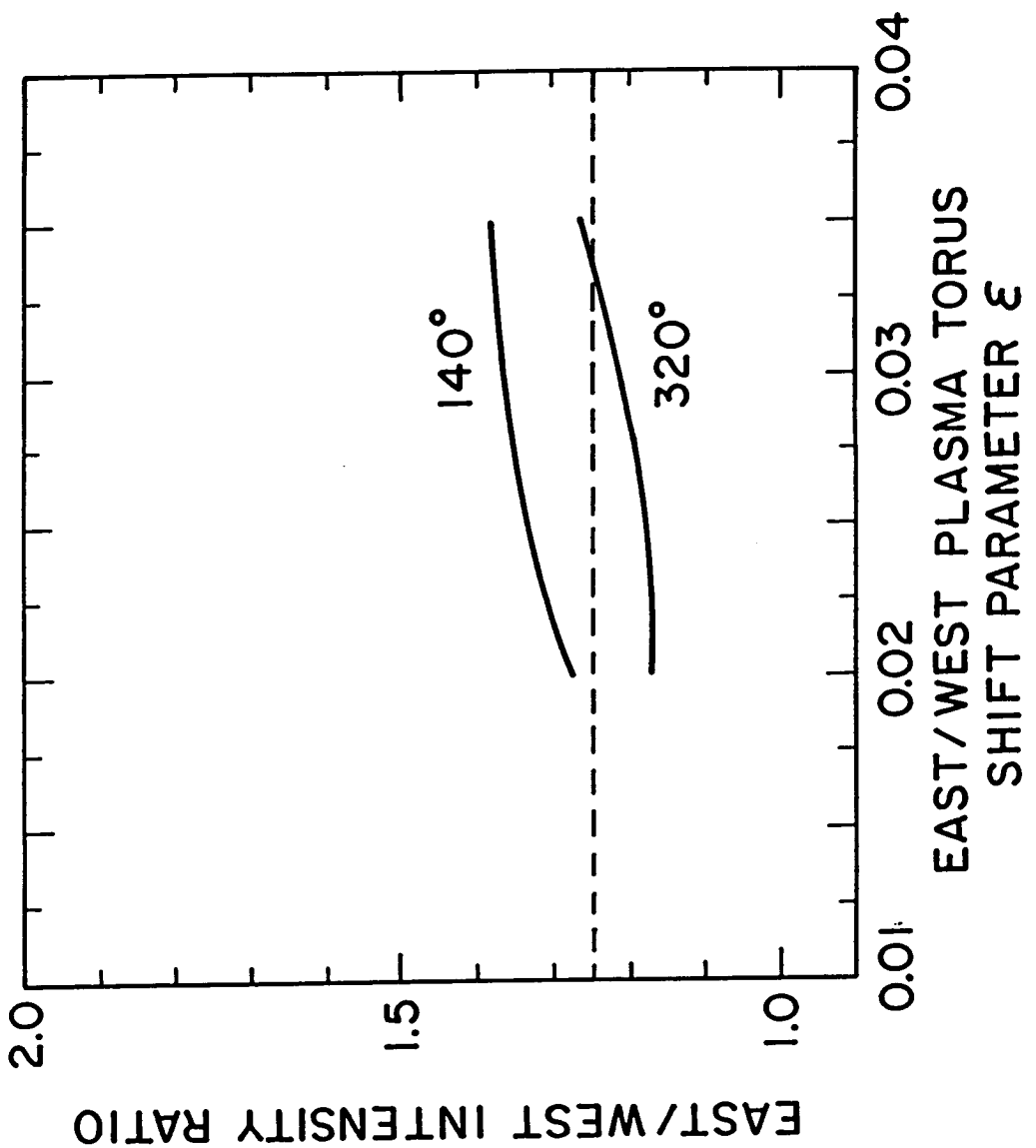
EAST/WEST INTENSITY RATIO
2.0
1.5
1.0
0.01
0.02
0.03
0.04
EAST/WEST PLASMA TORUS
SHIFT PARAMETER ε
140°
320°

Figure 16

Figure 17

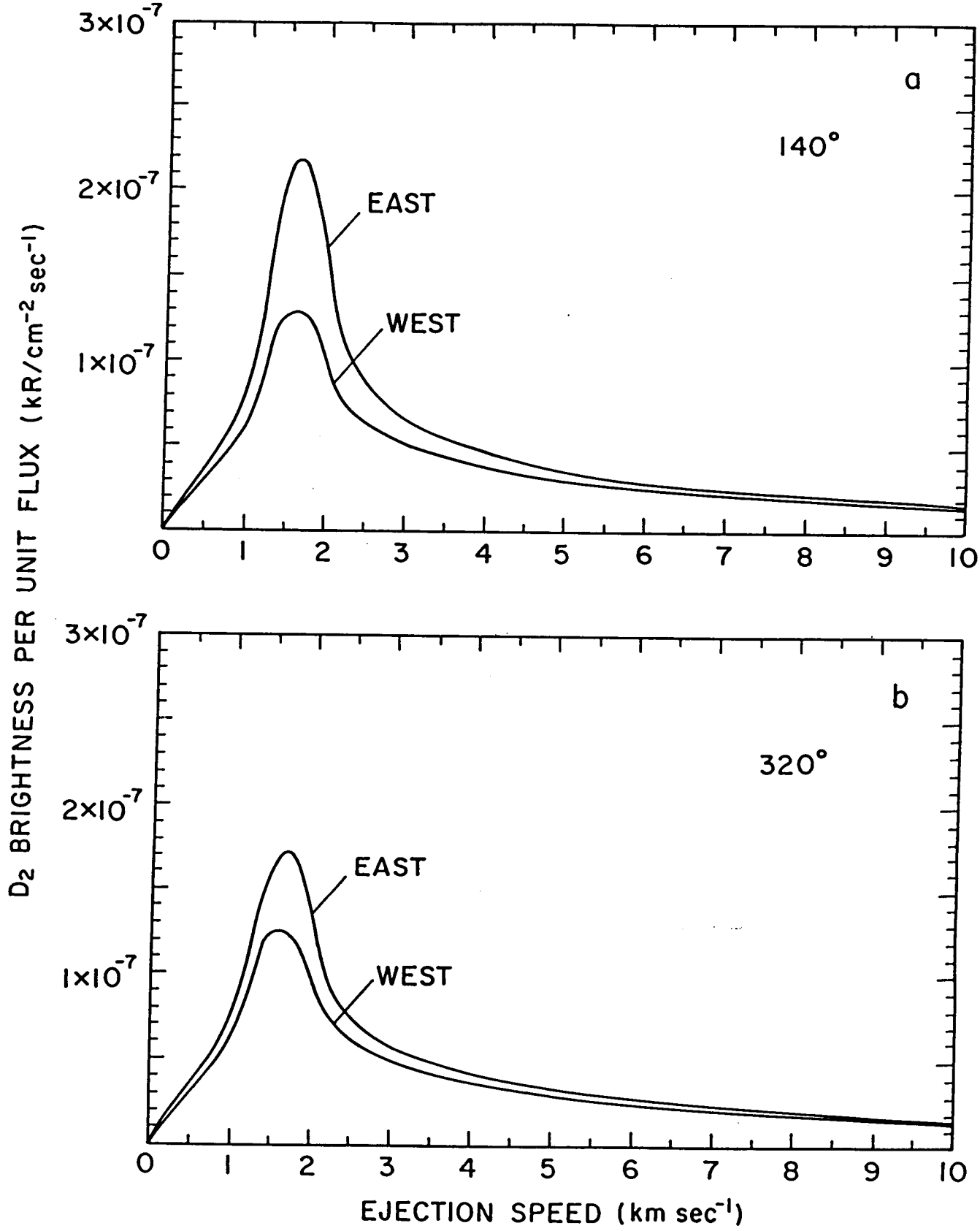
3×10⁻⁷
2×10⁻⁷
1×10⁻⁷
a
140°
EAST
WEST
0
1
2
3
4
5
6
7
8
9
10
b
320°
D₂ BRIGHTNESS PER UNIT FLUX (kR/cm⁻² sec⁻¹)
EJECTION SPEED (km sec⁻¹)

Figure 18

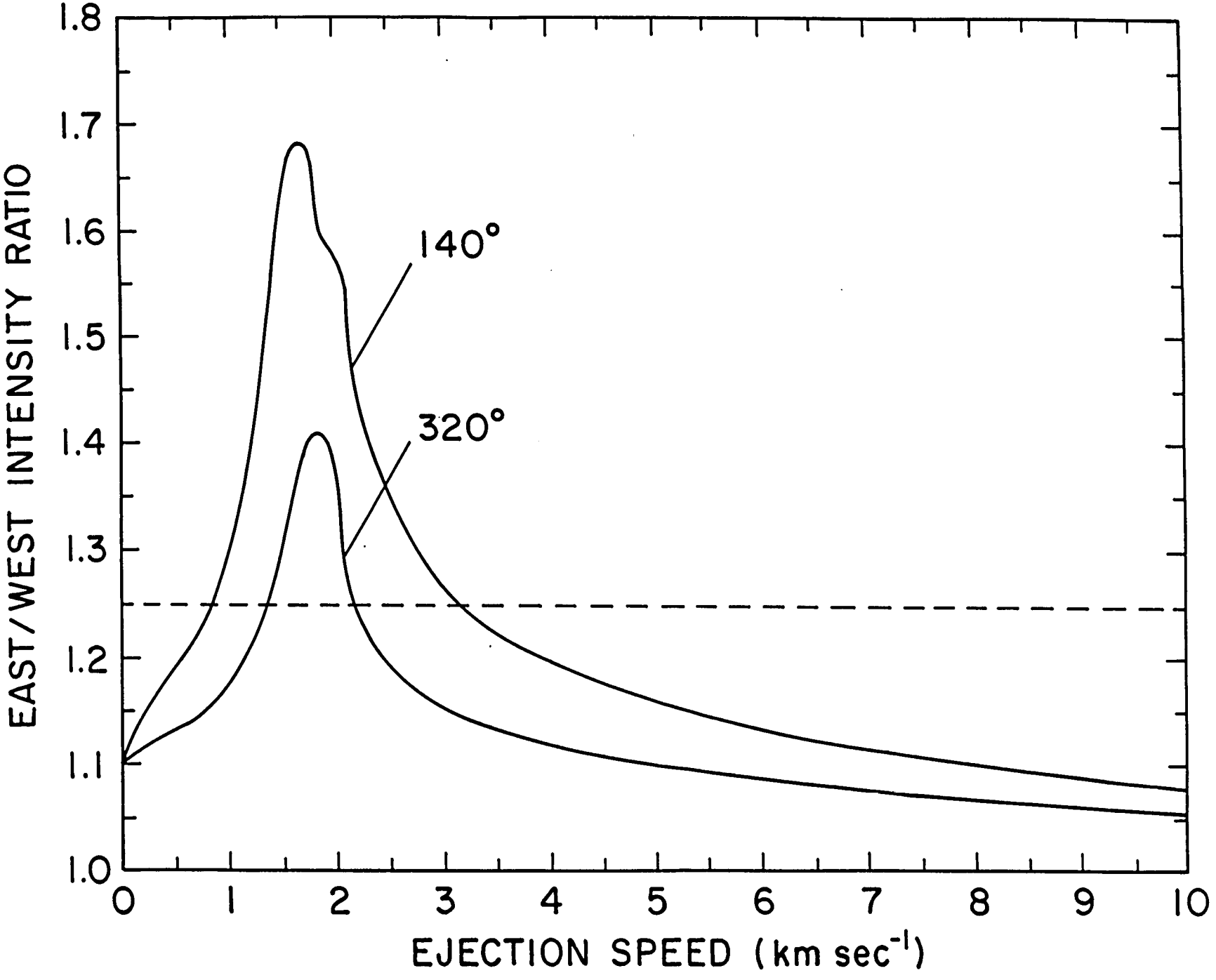
1.8
1.7
1.6
1.5
1.4
1.3
1.2
1.1
1.0
EAST/WEST INTENSITY RATIO
140°
320°
0
1
2
3
4
5
6
7
8
9
10
EJECTION SPEED (km sec⁻¹)

Figure 19

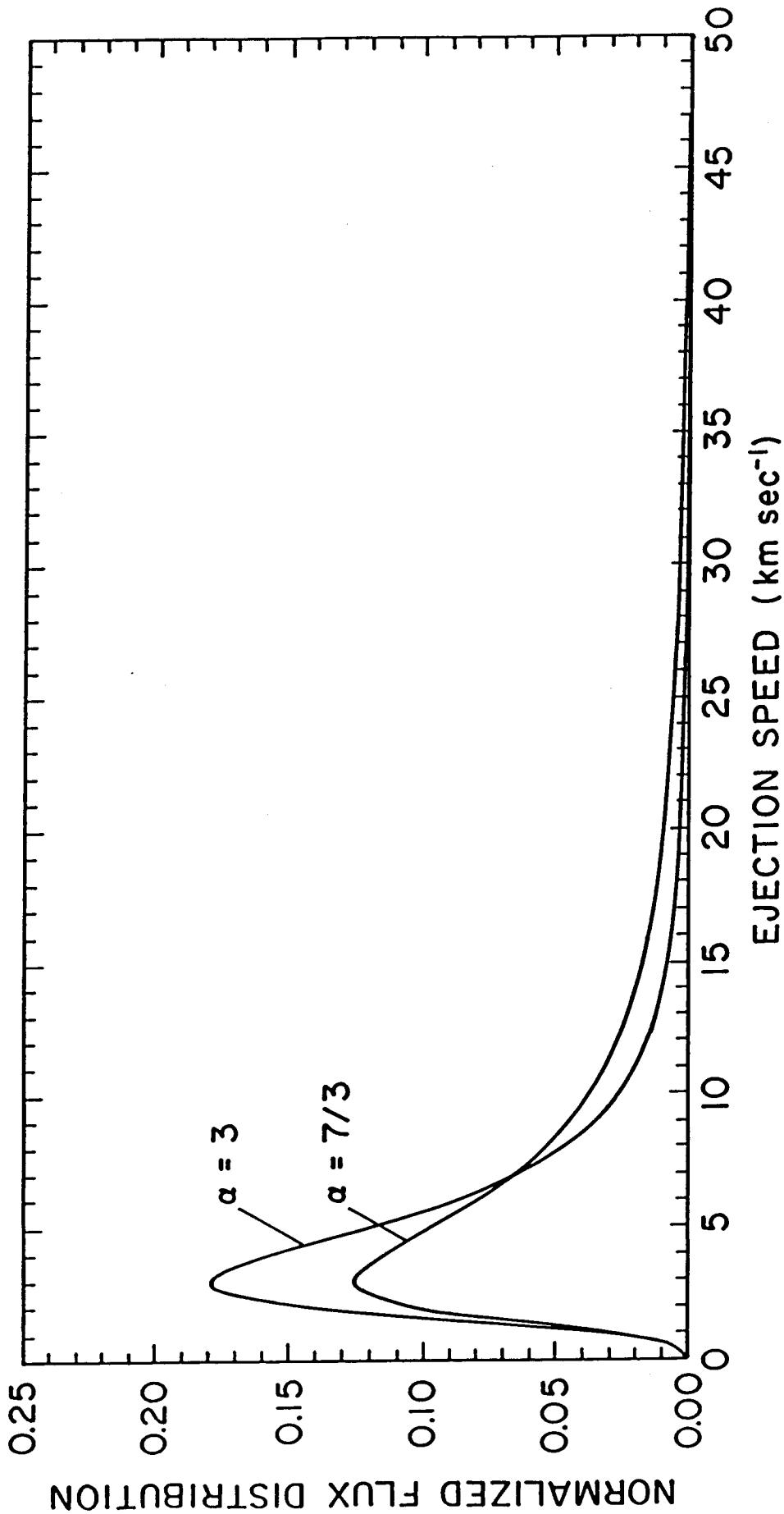
NORMALIZED FLUX DISTRIBUTION
0.25
0.20
0.15
0.10
0.05
0.00
0
5
10
15
20
25
30
35
40
45
50
EJECTION SPEED (km sec⁻¹)
α = 3
α = 7/3

Figure 20

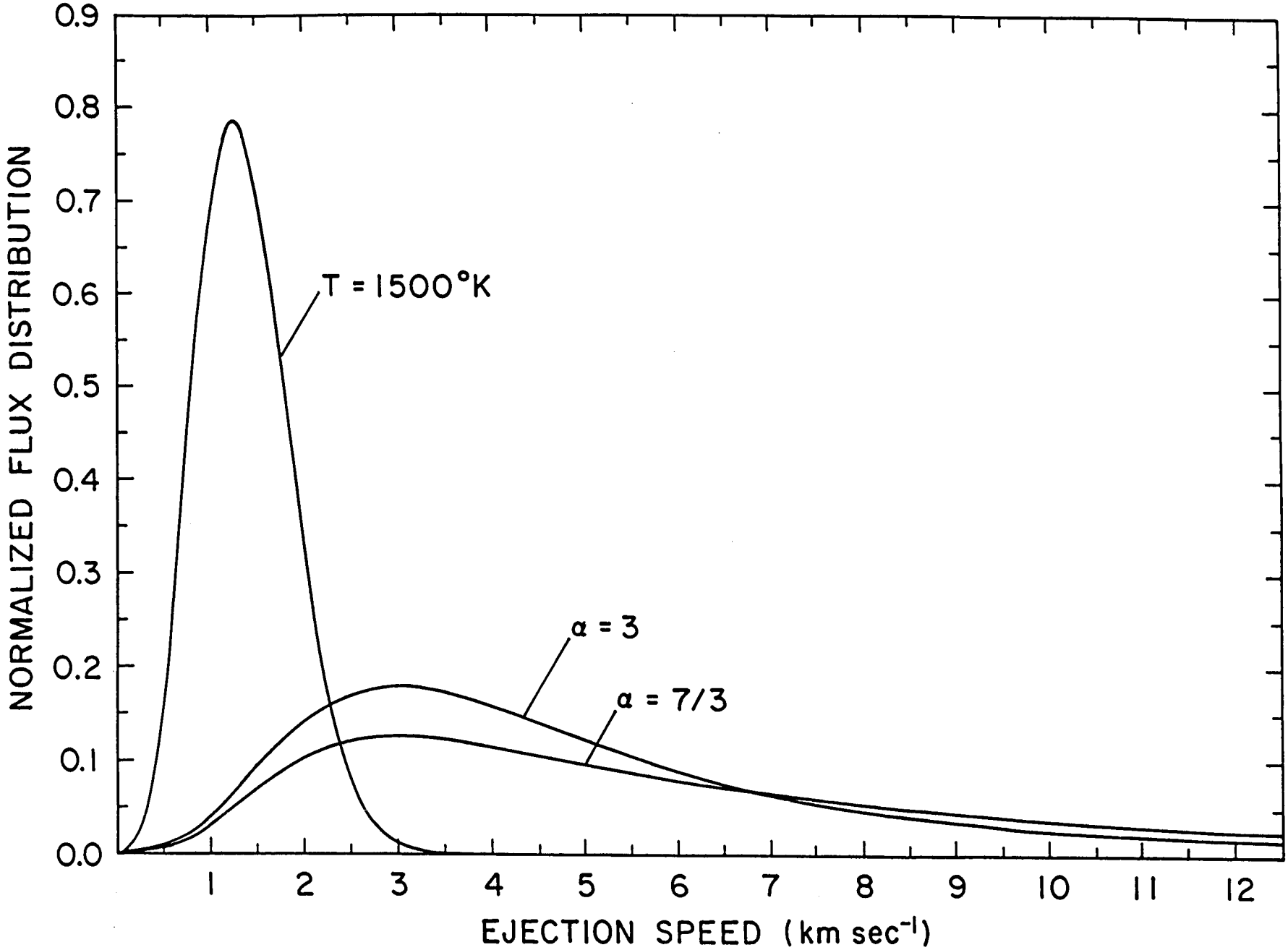
NORMALIZED FLUX DISTRIBUTION
0.0
0.1
0.2
0.3
0.4
0.5
0.6
0.7
0.8
0.9
T = 1500°K
α = 3
α = 7/3
1
2
3
4
5
6
7
8
9
10
11
12
EJECTION SPEED (km sec⁻¹)

Figure 21

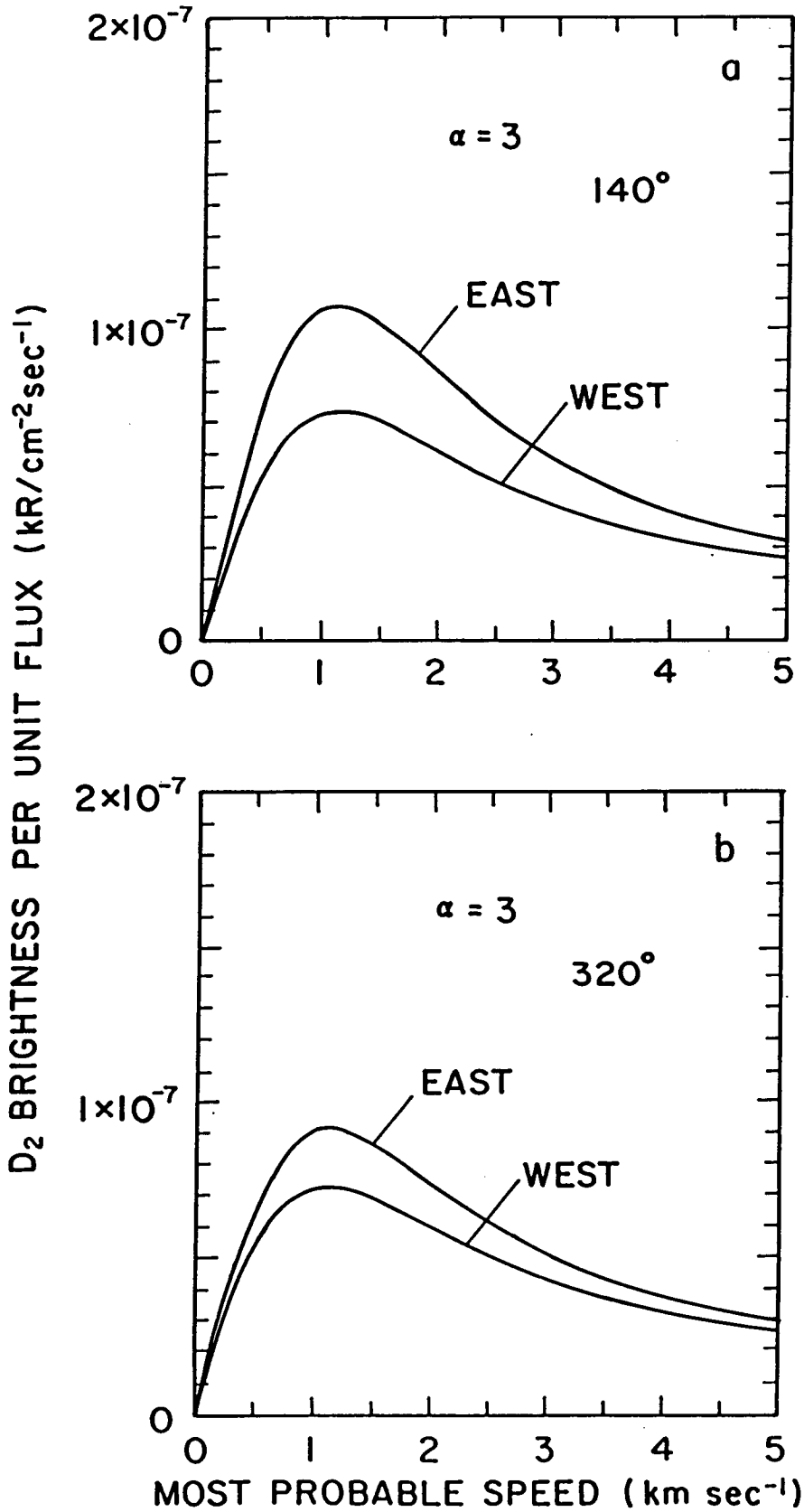
2×10⁻⁷
1×10⁻⁷
0
a
α = 3
140°
EAST
WEST
0
1
2
3
4
5
b
α = 3
320°
EAST
WEST
D₂ BRIGHTNESS PER UNIT FLUX (kR/cm⁻²sec⁻¹)
MOST PROBABLE SPEED (km sec⁻¹)

Figure 22

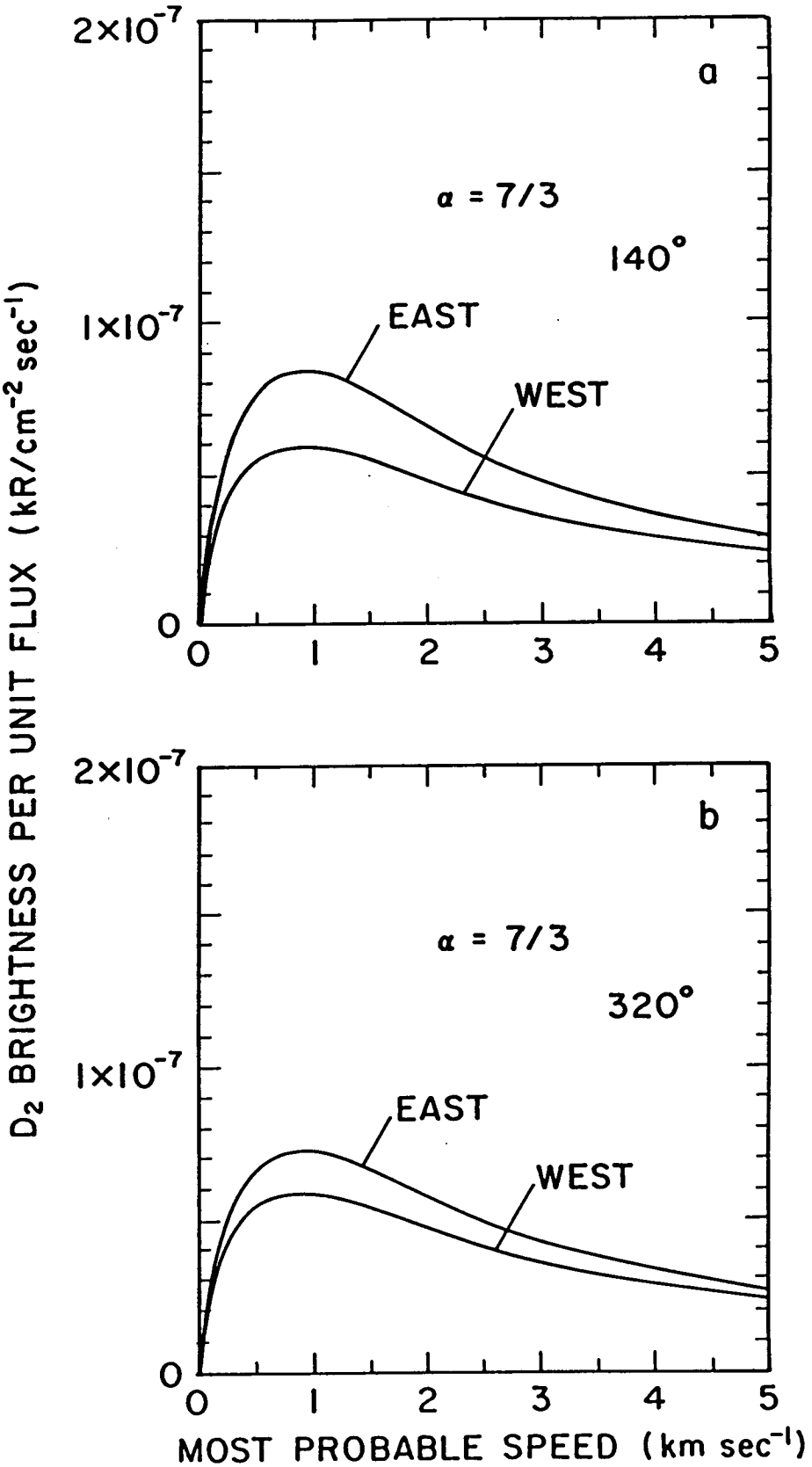
2×10⁻⁷
1×10⁻⁷
0
a
α = 7/3
140°
EAST
WEST
0
1
2
3
4
5
b
α = 7/3
320°
EAST
WEST
D₂ BRIGHTNESS PER UNIT FLUX (kR/cm⁻² sec⁻¹)
MOST PROBABLE SPEED (km sec⁻¹)

Figure 23

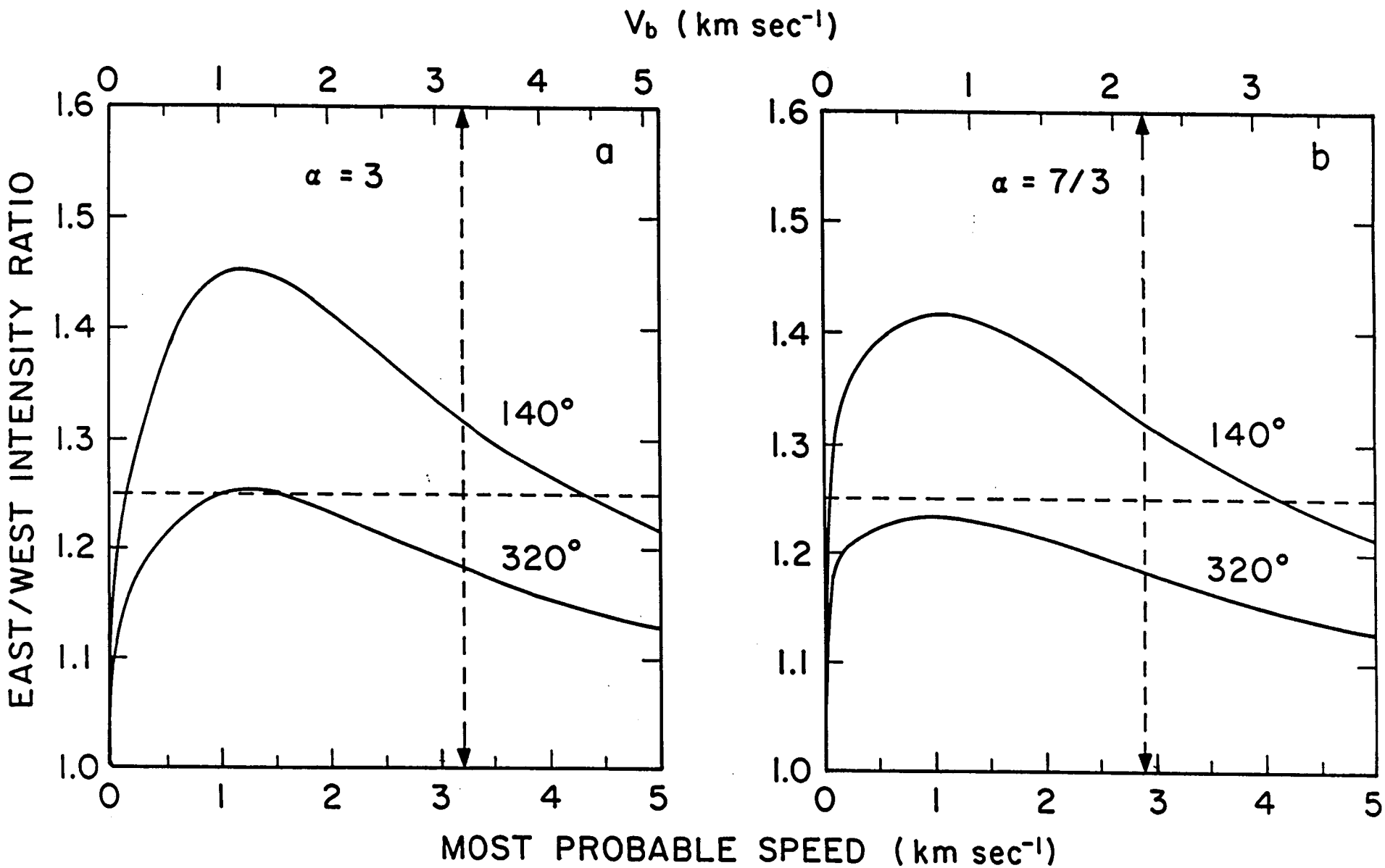
V_b (km sec^{-1})
EAST/WEST INTENSITY RATIO
MOST PROBABLE SPEED (km sec^{-1})
α = 3
a
140°
320°
α = 7/3
b
140°
320°

Figre 24

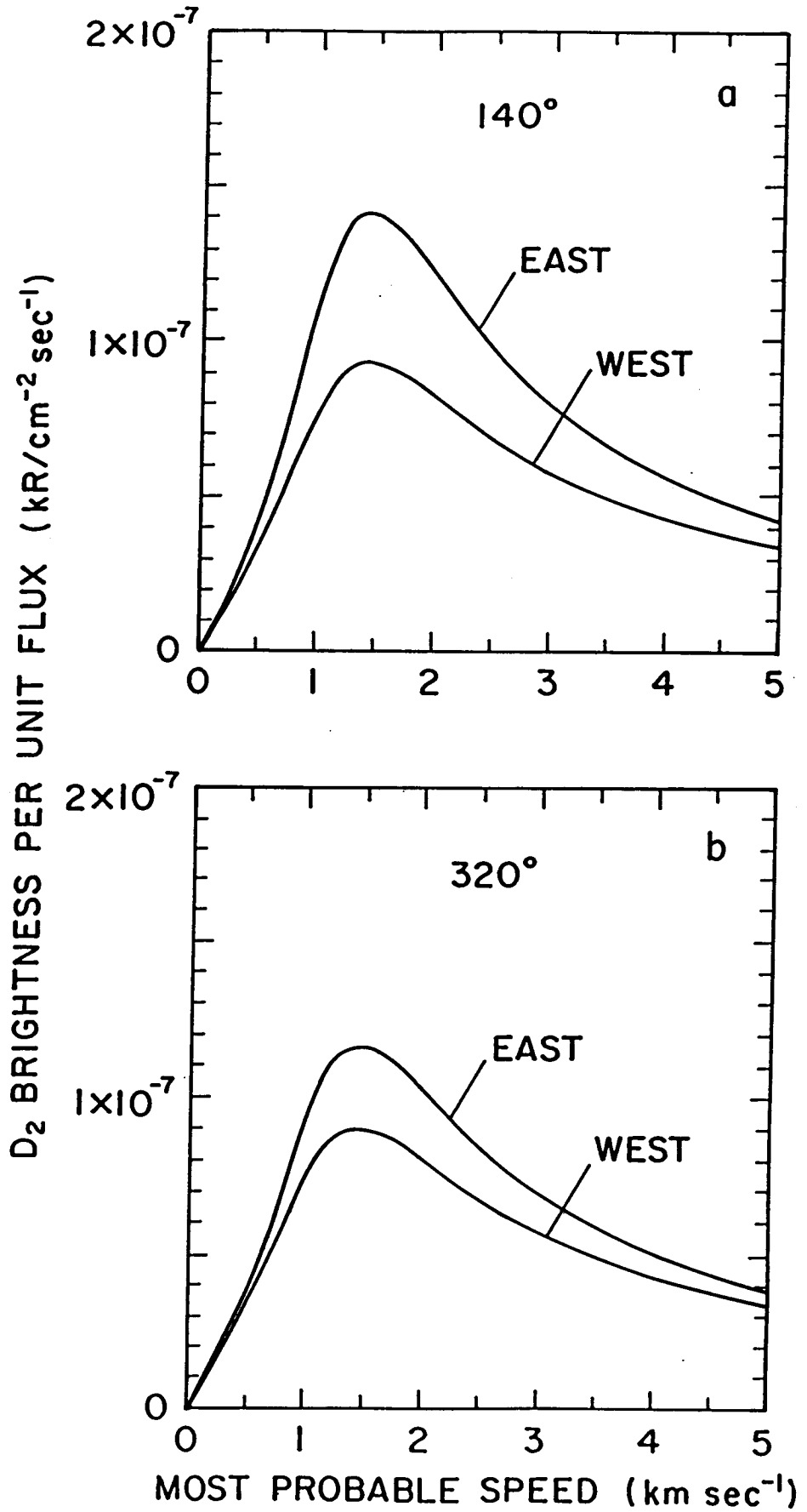
2×10⁻⁷
1×10⁻⁷
0
140°
a
EAST
WEST
0
1
2
3
4
5
2×10⁻⁷
1×10⁻⁷
0
320°
b
EAST
WEST
0
1
2
3
4
5
D₂ BRIGHTNESS PER UNIT FLUX (kR/cm⁻² sec⁻¹)
MOST PROBABLE SPEED (km sec⁻¹)

Figure 25

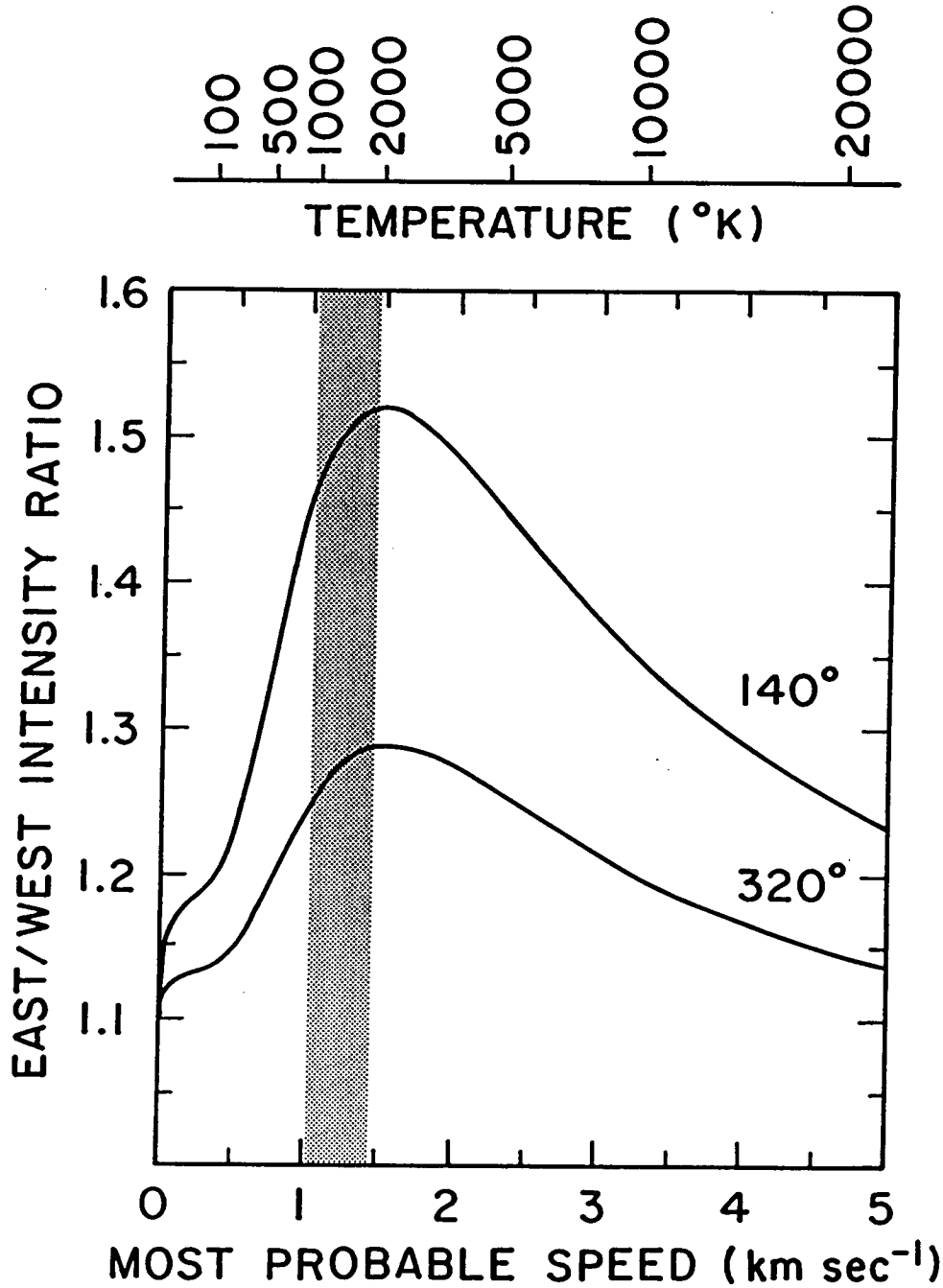
100
500
1000
2000
5000
10000
20000
TEMPERATURE (°K)
1.6
1.5
1.4
1.3
1.2
1.1
EAST/WEST INTENSITY RATIO
140°
320°
0
1
2
3
4
5
MOST PROBABLE SPEED (km sec⁻¹)

Michael R. Combi and William H. Smyth
Atmospheric and Environmental Research, Inc.
840 Memorial Drive
Cambridge, MA 02139-3758

Appendix VIII

Correlating East-West Asymmetries in the Jovian Magnetosphere and the Io Sodium Cloud

TECHNICAL REPORT STANDARD TITLE PAGE

1. Report No.	2. Government Accession No.	3. Recipient's Catalog No.

4. Title and Subtitle	5. Report Date
A Modeling Analysis Program for the JPL Table Mountain Io Sodium Cloud Data	March 1988
	6. Performing Organization Code
7. Author(s)	8. Performing Organization Report No.
William H. Smyth and Bruce A. Goldberg	
9. Performing Organization Name and Address	10. Work Unit No.
Atmospheric and Environmental Research, Inc. 840 Memorial Drive Cambridge, MA 02139	11. Contract or Grant No. NASW-3949
	13. Type of Report and Period Covered
12. Sponsoring Agency Name and Address	Final Report 6/1/84 - 11/30/87
NASA Headquarters Contracts and Grants Division Washington, DC 20546	14. Sponsoring Agency Code
15. Supplementary Notes	

16. Abstract

Research efforts in the third and final year of this project are divided into three main areas: (1) completion of data processing and calibration for thirty-four of the 1981 Region B/C images, selected from the massive JPL sodium cloud data set, (2) identification and examination of the basic features and observed changes in the morphological characteristics of the sodium cloud images, and (3) successful physical interpretation of these basic features and observed changes using the highly-developed numerical sodium cloud model at AER. The modeling analysis has led to a number of definite conclusions regarding the local structure of Io's atmosphere, the gas escape mechanism at Io, and the presence of an east-west electric field and a System III longitudinal asymmetry in the plasma torus. Large scale stability as well as some smaller scale time variability for both the sodium cloud and the structure of the plasma torus over a several year time period are also discussed.

17. Key Words (Selected by Author(s))	18. Distribution Statement
satellite atmospheres planetary magnetospheres	

19. Security Classif. (of this report)	20. Security Classif. (of this page)	21. No. of Pages	22. Price*
Unclassified	Unclassified		

*For sale by the Clearinghouse for Federal Scientific and Technical Information, Springfield, Virginia 22151.